UNIVERSIDADE DA CORUÑA

Doctoral thesis

Crashworthiness analysis and design optimization of hybrid energy absorption devices. Application to aircraft structures

By

Javier Paz Méndez

Ingeniero de Caminos, Canales y Puertos

Supervisors

Luis Esteban Romera Rodríguez

Dr. Ingeniero Industrial

Jacobo Díaz García

Dr. Ingeniero de Caminos, Canales y Puertos

Programa de doctorado en Ingeniería Civil

2018

Preface

The herunder dissertation has been presented for the degree of *doctor en ingeniería civil* (Doctor of Philosophy in civil engineering) at Universidade da Coruña. This investigation was performed under the supervision of Professor Luis E. Romera Rodríguez and Professor Jacobo Díaz García at the Structural Mechanics Group, between October 2014 and May 2018.

This investigation is original to the best of the author's knowledge, except when previous research is cited or recognized. Moreover, all communications arisen from this work are itemized in chapter 1.

Javier Paz Méndez
May 15, 2018

Acknowledgments

Writing a PhD Thesis is often deemed an arduous and lonely journey, albeit the author's own experience differs vastly from this. Dr. Jacobo Díaz García and Dr. Luis Romera Rodríguez not only have sown and nourished the author's love for science, but also have relentlessly provided the perilous guidance, expertise and inspirational talks that undergoing this investigation required. Sincere gratitudes are also beholden to Dr. Miguel Costas Piñó for his experienced advice on simulation and crashworthiness matters throughout this study.

The help and resources provided by the Structural Mechanics Group from Universidade da Coruña and Dr. Santiago Hernandez Ibáñez have also been crucial in achieving this work. The wholesome and comfortable environment provided by coworkers and friends is also acknowledged, mentioning Antonio, Ibuki, Fran and Mario as a small portion of the superb research group. The encouragement from the always-supportive personnel at the UDC is sincerely recognized, particularly remarking that from Miluca and Ana.

During the research stay carried out in Edinburgh during the last trimester of 2016, the counsel and hospitality generously provided by Dr. Filipe Teixeira-Dias and the University of Edinburgh have made this a productive and delightful experience. Roommates Rafa, Sam, Blanca and Gladys are profoundly owed to for turning an old house into a heartwarming and spirited home to endure the hardships of winter. A sincere thank you is also indebted to the Fundación Barrié for the financial support offered during this period.

On a more personal matter, the author is naturally indebted to his parents and siblings, not only for their continuous care and emotional support, but also for lending a helping hand when it was required the most.

As sung by the Beatles, everything is better when "I get by with a little help from my friends". Luis, Xoel, Javi, Majan, Marcos, Andrés, Carlos, Bruno, Laura and Carlota are among those who offered equal parts of strength, wisdom and leisure when times demanded. Your insightful comments will never be forgotten.

Last but not least, the author wants to express his deepest gratefulness towards Elena for her unconditional support and love provided throughout this venture; as well as mutual pets Isidoro, Jet and Candy, source of never-ending and pure joy during the hardest of times.

Abstract

Amid the main research lines for the enhancement of aircraft and automotive designs, structural optimization and crashworthiness studies are at their pinnacle. Means of transport need to be robust and safe, albeit efficiency and lightness cannot be neglected. While active safety systems have avoided innumerable accidents, passive crashworthiness systems need to protect passengers when they do occur. In the event of a crash, modern structures are designed to collapse progressively, dissipating high amounts of kinetic energy and protecting the passengers against abrupt decelerations. Within this broad field of study, the aim of this thesis is that of bettering traditional crash structures by designing and optimizing thin-walled hybrid energy absorbers, and ultimately proving reduced occupant injury levels during representative impact scenarios.

The collapsible energy absorbers studied throughout this research originated by combining square metallic tubes with inner cores made from glass-fiber reinforced polymer (GFRP) and foam structures. Honeycombs are studied in depth, showing their outstanding behavior as load bearing structures and identifying the effects of modifying their cell's shape. Another composite structure investigated was that of an intertwined four-plate star core, slightly less stiff than honeycombs but promising crushing behavior. Foam extrusions are also used as standalone reinforcements and as filling of the inner core's voids, always enhancing the energy absorption capabilities of specimens.

Specimens are characterized according to different crashworthiness metrics, including their energy absorption value, peak force undergone during its collapse and the mass of the components. Moreover, each initial design is subjected to optimization techniques to achieve the utmost from the aforementioned metrics. For that, finite element simulations of axial dynamic loading are parametrized as to obtain variable core heights, material thicknesses and modifiable honeycomb's cell size and shape. These are later coupled with sampling and metamodeling algorithms, constructing a surrogate model which performs accordingly with the simulation during any fluctuation in the design variables. Later on, the metamodels are single- and multi-objectively optimized with genetic algorithms, yielding various sets of designs that excel in one or more of the selected responses.

As a second goals of this work, the previous energy absorber design and the methodology used are to be applied in a significant impact scenario of a passenger vehicle. A drop-test numerical simulation from a Boeing 737-200 fuselage section is developed and correlated with extensive experimental data, later analyzing the crushing behavior of isolated components and their energy absorption trends. The effect of adding hollow thin-walled tubes as vertical struts is studied, expecting a great enhancement of the conventional design response. Surrogate-based optimization methodologies are also applied to this simulation, monitoring various crashworthiness biometrics and the specimen's mass.

Results show that on a coupon basis, the usage of inner reinforcements can modify the tube's collapse patterns and increase its specific energy absorption values by up to 30 %, mainly caused by the interaction between the core and the confining structure. Moreover, reducing the core's height has also shown improved responses, offsetting the triggering loads of each component and yielding peak force values 33 % lower. Topographic optimization of honeycomb cells has revealed that the highest specific energy absorption values for dynamic loads are not achieved with a regular cell but with a pseudo-rectangular one. The usage of foam as cell-filling has also proved superb, increasing energy absorption by another 28 % with minor hindering on the specimen's mass.

As for the validation of the full size aircraft drop-test simulation, numerical and graphical results closely match those of the experimental procedure. It was found

that removing the auxiliary fuel tank from the original section increased occupant injury levels due to high structural deformation and low energy absorption by the main structures. In a later phase, hybrid energy absorbers are added to the fuselage section with an empty cargo area, and a new surrogate model is built with 600 full-scale drop test simulation. The surrogate is then single- and multi-objectively optimized, reducing acceleration peak values by 50 % and injury levels from severe to moderate at different occupant locations.

Contents

Preface **iii**

Acknowledgments **v**

Abstract **vii**

Contents **xi**

List of Figures **xv**

List of Tables **xxi**

1 Introduction **1**

1.1 Motivation 2

1.2 Contributions of this thesis 5

1.3 Research aims and methodology 6

1.4 Outline 7

References 10

2 Structural crashworthiness and numerical methods **13**

2.1 A brief introduction to crashworthiness 13

2.1.1 Origin and purpose 14

2.1.2 Crashworthiness analysis: experiment and simulation . 17

2.1.3 Crasworthiness design 23

2.1.4 Crashworthiness evaluation 31

2.2 Collapsible impact energy absorbers 40
2.2.1 Design of energy absorbers 40
2.2.2 Axial collapse of thin-walled square tubes 48
2.2.3 Hybrid energy absorbers 61
2.3 Finite element analysis of dynamic simulations 67
2.3.1 Formulation of governing equations 67
2.3.2 Finite element discretization 69
2.3.3 Solution methods 70
2.3.4 Stability and other remarks on explicit methods . . . 74
2.4 Optimization procedures 78
2.4.1 Optimization methods 78
2.4.2 Meta-heuristic optimization 80
2.4.3 Surrogate-based methods 82
2.4.4 Design optimization 89
References 96

3 Crushing analysis and crashworthiness optimization of hybrid energy absorbers enclosing GFRP honeycomb structures 123
3.1 Introduction 123
3.2 Model description 125
3.2.1 Specimen 125
3.2.2 Design variables and objective functions 126
3.2.3 Analysis settings 130
3.3 Results and discussion 131
3.3.1 Initial results 131
3.3.2 Parameter study 136
3.3.3 Optimization results 139
3.3.4 Optimum points 143
3.4 Conclusions 144
References 146

4 Size and shape crashworthiness optimization of hybrid energy absorbers enclosing honeycomb and foam structures 149
4.1 Introduction 149

4.2 Materials 150
4.3 Design variables and objective functions 154
4.3.1 Specimen A 155
4.3.2 Specimen B 158
4.3.3 Analysis settings 161
4.4 Results 165
4.4.1 Specimen A 165
4.4.2 Specimen B 170
4.5 Conclusions 180
References 183
References 185

5 Crash response of aircraft structures enhanced with crushable energy absorbers. Crashworthiness analysis and passenger injury assessment 189
5.1 Introduction 189
5.2 Fuselage model description 190
5.2.1 Materials 194
5.2.2 Numerical simulation 195
5.2.3 Analysis settings 200
5.3 Results and discussion 201
5.3.1 Verification 201
5.3.2 Effect of the energy absorbers 204
5.4 Conclusions 214
References 217

6 Optimization of hybrid energy absorbers for crashworty aircraft designs 221
6.1 Introduction 221
6.2 Components description 222
6.2.1 Description of test article 222
6.2.2 Model description 222
6.2.3 Materials 225
6.2.4 Numerical simulation 226

6.2.5 Surrogate-based optimization 227
6.3 Results 231
6.3.1 Surrogate model fitness 231
6.3.2 Baseline model 231
6.3.3 Single-objective optimization 232
6.3.4 Multi-objective optimization 236
6.4 Conclusions 243
References 245

7 Summary, conclusions and future research 247
7.1 Summary 247
7.2 Conclusions 248
7.3 Future research 251

Appendices 253

A Extended summary in Spanish 255
A.1 Introducción y objetivos 255
A.2 Metodología y modelos 257
A.3 Resultados y discusión 259
A.4 Conclusiones y futuras líneas de investigación 261

B Extended summary in Galician 265
B.1 Introdución e obxectivos 265
B.2 Metodoloxía e modelos 267
B.3 Resultados e discusión 269
B.4 Conclusións e futuras liñas de investigación 271

Bibliography 275

List of Figures

1.1 Cessna 172 impact test at NASA Langley's Facility. Taken from [5]. 3
1.2 Schematics of main aircraft fuselage crashworthiness absorption structures. 5

2.1 Ferrari's F310B Formula One® cockpit cutaway (1997) [37]. . . . 15
2.2 Ag-1 agricultural aircraft. Taken from [39]. 16
2.3 Flight of Beechcraft Bonanza 35 N3188V in January 1949. Taken from [41]. 17
2.4 Large transport aircraft model in KRASH. Taken from [56]. . . . 19
2.5 Sikorsky ACAP helicopter as tested by Fasanella et al. [65]. . . . 22
2.6 Hybrid III MADYMO 50^{th} percentile female adult ATDs. Taken from [70]. 23
2.7 Transmission of crash loads in fuselage cross sections. Taken from [75]. 24
2.8 Sub-floor assembly featuring sinewave beams. Taken form [87]. . 26
2.9 Sub-floor structural assembly featuring energy-absorbing foam blocks. Taken form [14]. 27
2.10 Boeing 737 post-test deformation. Plastic hinges circled in white. 28
2.11 Tension crash concept and energy absorption components. Adapted from [107]. 29
2.12 Fokker F28 fuselage section featuring vertical struts. Taken from [111]. 31

2.13 Aircraft longitudinal deceleration profile. 32
2.14 Initial configuration of idealized aircraft vertical drop test. 33
2.15 Energy absorption under force-displacement curve. 34
2.16 Idealized energy absorbing profiles. 35
2.17 Force-displacement curve. Adapted from [123]. 36
2.18 Acceleration integration and its representation in an Eiband diagram. 39
2.19 Tube deformation modes. 43
2.20 Schematic diagrams of tube wall cross-sections for various axial crushing modes. Taken from [155]. 44
2.21 Post-test mild steel samples. Impact velocities (left to right): 385 m/s, 277 m/s, 227 m/s, 173 m/s, 0 m/s Taken from [157]. 45
2.22 Multicorner cross-sectioned tubes from Fan et al. [162]. 46
2.23 Strut with kink. 47
2.24 Frustum crushing evolution. Taken from [170]. 48
2.25 Smart ForTwo body-in-white. Adapted from [177]. 48
2.26 Axial progressive deformation modes of square tubes. Taken from [150, 178]. 50
2.27 Collapse elements for thin-walled square tubes. 50
2.28 Realistic and kinematically admissible type I folding. Adapted from [138]. 51
2.29 Strip resembling traveling hinge. 53
2.30 Shell deformation over toroidal surface. 53
2.31 Theoretical and experimental comparison of square and rectangular tubes. Adapted from [183]. 58
2.32 Force-displacement evolution of aluminum square tube with $C = 100$ mm and $h = 2$ mm. 61
2.33 Sectional cuts of two square steel tubes ($C/h = 50$). 62
2.34 Axially-loaded composite tube splaying process. Taken from [154]. 64
2.35 Nomex® honeycomb ($\rho = 48\,\mathrm{kg/m^3}$). Behavior and test article. . 66
2.36 Illustrative examples of three sampling strategies for a two-dimensional problem. 84
2.37 Depiction of an evolutionary algorithm. 93
2.38 Depiction of crossover and mutation. 94

2.39 Depicted effect of crossover and mutation to the population members. 95

3.1 Hybrid energy absorber. 124
3.2 Three-dimensional cut of the finite element mesh of the specimen. 127
3.3 Three-dimensional cut of the specimen. All dimensions in millimeters. 129
3.4 Top view of the specimen. All dimensions in millimeters. 130
3.5 Variation of the R^2 indicator with the maximum number of MARS bases for different objective functions. 132
3.6 Influence of the maximum number of MARS maximum basis functions on the cross-validated mean absolute error for different objective functions. 133
3.7 Force-displacement curves of the complete specimen, separate parts, and both parts added together. 134
3.8 Post-test deformation and sectional cut of reinforced and hollow square steel tubes ($C/h = 50$). 135
3.9 Force-displacement curves of the complete specimen and a hollow tube with equal mass. 135
3.10 Parameter study results in term of SEA and peak load. 138
3.11 Pareto fronts obtained after multi-objective optimization. 141
3.12 Force-displacement curves of the initial and optimum specimens. 145

4.1 Airbus A300 fuselage section featuring vertical struts. Taken from [23]. 150
4.2 Stress-strain curve of the AA7075-T651 aluminum at a strain rate of 0.035 s^{-1}. 152
4.3 Numerical and experimental tensile stress-strain curves of the Ultramid A3WG10 BK00564 up to fracture at a strain rate of $3.25 \times 10^{-4} s^{-1}$ 153
4.4 Yield surface and flow potential in the meridional plane for the crushable foam model with isotropic hardening. 154
4.5 Stress-strain curve of the ArmaFORM PET/W AC 135. 155
4.6 Top view of the specimen. All values in millimeters. 156
4.7 Different honeycomb cell shape configurations. 157
4.8 Significant cell shapes for specimen B. 159
4.9 Comparison of the collapse modes of specimen A. 162

4.10 Force - displacement curves of the non-triggered and triggered collapse schemes for specimen A. 163
4.11 Three-dimensional cut of the baseline model for specimen B. . . 164
4.12 Cell shape of the optimum for the single-objective constrained optimization of specimen A. 167
4.13 Objective function evolution. 168
4.14 Force - displacement curves of the unconstrained and constrained optima of specimen A. 169
4.15 Force - displacement curves of the initial design constrained optima of specimen A. 170
4.16 *SEA* - P_{peak} Pareto front of specimen A. 171
4.17 Mass - E_{a} Pareto front of specimen A. 172
4.18 Top view of the optimum model for the single-objective *SEA* unconstrained optimization of specimen B. 173
4.19 Baseline component compared to the model without foam, the model with only a foam filling, and the constrained and unconstrained optima of specimen B. 174
4.20 Evolution of the cost function during the single-objective optimization of specimen B for the SC4 case. 175
4.21 Mass - E_{a} Pareto fronts of specimen B. Designs with and without foam extrusions. 177
4.22 *SEA* - P_{peak} Pareto front of specimen B. 179
4.23 *SEA* - C_{t} Pareto front. 180
4.24 Variables' evolution for SC1 in the *SEA* - C_{t} Pareto front of specimen B. 181
4.25 Component configuration for some points from the *SEA* - C_{t} Pareto frontier from table 4.18. 182

5.1 Dynamic drop test facility diagram as presented by Abromowitz et al. [299]. 191
5.2 Boeing 737-200 test section. Taken from [299]. 192
5.3 Boeing 737-200 test article. Taken from [67]. 193
5.4 Numerical model in Abaqus 2016. 196
5.5 Detail of the energy absorbers and the connecting part developed. 196

5.6 Detail of the lower aircraft structures. 197
5.7 Detail of cargo door and upper fuselage structures. 198
5.8 Radial displacements obtained in the static load case. All displacements in meters. 202
5.9 Comparison between the real [67] and numerical specimens at 20 ms, 60 ms and 100 ms. 203
5.10 Left and right floor velocities. Analytic and numerical results. . . 205
5.11 Left and right floor accelerations. Analytic and numerical results 206
5.12 Model energies throughout the simulation. 207
5.13 Aircraft acceleration responses with the auxiliary fuel tank, with and without energy absorbers. 208
5.14 Vertical acceleration loads in Eiband diagram. Fuselage with the auxiliary fuel tank, with and without energy absorbers. 209
5.15 Vertical strut after impact and response. 210
5.16 Aircraft collapse evolution of main structures. 212
5.16 *(Continued).* 213
5.17 Final deformation of the specimen without the auxiliary fuel tank, without and with energy absorbers. 214
5.18 Aircraft acceleration responses without the auxiliary fuel tank, with and without energy absorbers. 215
5.19 Vertical acceleration loads in Eiband diagram. Fuselage without the auxiliary fuel tank, with and without energy absorbers. 216

6.1 Post-test deformation of honeycomb- and foam-filled hybrid energy absorber featured as vertical strut. 223
6.2 Mesh detail of hybrid energy absorber with load-transmitting bars and rigid plates. 224
6.3 Two-millimeter trigger on lower edges of HEA. 224
6.4 Three-dimensional cut of the hybrid energy absorber. 225
6.5 Top view of meshed specimen. 226
6.6 Numerical model in Abaqus 2016. 228
6.7 Post-impact deformation of HEA under location **1b**. 232
6.8 Acceleration history of original, baseline and optimum models at location **1**. 234

6.9 Eiband diagrams for vertical accelerations at locations 1 and 1b. 235
6.10 Deformation comparison of crushed fuselage section with and without HEAs. 237
6.11 Pareto front and sampling values for ${A_1}^{\max}$ and ${A_{1b}}^{\max}$. 238
6.12 Eiband injury criteria of original fuselage and HEA optimum from table 6.6. 239
6.13 Post-test deformation of hybrid energy absorber under location **1b** for model in table 6.6. Complete specimen and inner core. 240
6.14 Force-displacement evolution of energy absorber from figure 6.13. . 241
6.15 Internal energy for model in table 6.6, divided by significant structural components. 242
6.16 Energy dissipation by plastic deformation for original model and optimum from table 6.6. 243

List of Tables

2.1 Human tolerance limits. Adapted from [124]. 38
2.2 Head injury criteria and tolerance limits. Adapted from [124]. . . 40

3.1 S-275 J0H steel properties and Mises plasticity model values for equation (3.1). Taken from [304]. 125
3.2 Material properties of Ultramid A3WG10 BK00564. 126
3.3 Characteristics of design variables from figures 3.3 and 3.4. All dimensions in millimeters. 128
3.4 Points from the energy-mass Pareto front shown in figure 3.11a. . 139
3.5 Points from the energy-peak load Pareto front shown in figure 3.11b. 142
3.6 Comparison between initial design and optimum designPositive values between brackets designate improvement of an objective function from the optimum over the baseline design. 143

4.1 AA7075-T651 aluminum properties and Mises plasticity model values for equation (4.1). Taken from Børvik et al. [25]. 151
4.2 Material properties of Ultramid A3WG10 BK00564. 152
4.3 Material properties of ArmaFORM PET/W AC 135. 154
4.4 Bounds and initial values of design variables for specimen A. All dimensions in millimeters. 157
4.5 Bounds and initial values of design variables for specimen B. All dimensions in millimeters. 160
4.6 Different weight factors for the cost function from equation (4.6). . 161

4.7 Energy absorbed values for different mesh sizes. 162
4.8 Experiment and impact velocity correlation for FEM simulations. 164
4.9 Configuration parameters for the JEGA library optimization algorithms. 165
4.10 R^2 and RMSE values for the different metrics of two surrogate models for specimen A. 166
4.11 Single-objective optimization results of specimen A. 167
4.12 Points from SEA - P_{peak} Pareto front of specimen A. 169
4.13 Points from mass - E_{a} Pareto front of specimen A. 171
4.14 Single-objective SEA optimization results of specimen B. 173
4.15 Single-objective C_{t} optimization results of specimen B. 175
4.16 Points from mass - E_{a} Pareto front of specimen B. 178
4.17 Points from SEA - P_{peak} Pareto front of specimen B. 179
4.18 Points from SEA - C_{t} Pareto front of specimen B for SC1. Model with an * depicted in figures 4.25a to 4.25d. 181

5.1 Material properties of the AA2024-T3 [301], AA7075-T6 [302] aluminium alloys, the tank material [67] and the impacting block. . 194
5.2 Geometrical properties of significant fuselage structures. 199
5.3 Type, number and size of the finite elements used. 199
5.4 Comparison of masses (in kg) between the test article and the computer model. 200

6.1 Bounds and initial values of design variables. All dimensions in millimeters. 229
6.2 Configuration parameters for the JEGA library optimization algorithms. 230
6.3 MLS surrogate model fitness. C-V* refers to the cross-validation value of RMSE. 231
6.4 Design variables and response metrics of original fuselage without absorbers, with baseline absorbers, and with the single-objective optimum specimen designs. 233
6.5 Design variables and response metrics of Pareto front. 236

6.6 Design variables and response metrics of the closest specimen to utopia point. 239

1

Introduction

This thesis is enclosed amid the research field of crash safety and occupant protection, primarily focused on aircraft structures. The hereunder investigation verses on the design and analysis of the crashworthiness performance of thin-walled collapsible energy absorbers intended for aeronautical applications. Steel and aluminum square tubes filled with composite and foam structures are modeled and crushed under axially-dominated loads. Optimization procedures are used seeking components with low mass values and reduced levels of passenger injury. Although these devices can be used in several transportation systems, a Boeing 737-200 fuselage section is chosen to determine the level of improvement obtained when fitting the studied absorbers as vertical struts given the broad experimental data available. In this chapter, the crashworthiness field of study that has driven this investigation is introduced, with special focus on the advances made by the aircraft industry, while a more exhaustive review is offered in chapter 2. Later on, the aims sought with the research and the methodology employed are listed and briefly described, as well as a short introduction to the contents from each of the following chapters. Finally, a record of the author's main peer-reviewed publications, proceedings and congress communications stemming from this work is offered.

1.1 Motivation

Society's increasing demand of lower fuel consumption and higher safety for vehicle occupants has significantly conditioned the aerospace, automotive and railroad industries. This field of study, namely, vehicle crashworthiness, gained importance in the 1960s, when the US army studied the survivability of low speed helicopter crashes which were causing serious injuries or resulting fatal. Conclusions agreed that the vertical force transmitted to the occupant significantly affected the injury level in many impact scenarios [1].

Soon after, the knowledge gained with these studies performed by the military was adopted by the commercial aircraft industry [2], and in the 1980's, it also became a must for the automotive design engineers. The deformation mechanisms and energy dissipation trends determine the forces transmitted to the occupants, so by establishing crashworthiness standards and certification requirements, the survivability of aircrafts and automobiles crash scenarios is continuously improving. Incidentally, bettering the active and passive safety systems would result in a major reduction of the crash rates and their damaging consequences, alleviating one of today's major problems of society.

In order to assess and improve the crashworthiness of a vehicle, numerical and experimental tests are performed. In the automotive industry, full vehicle testing under impact conditions is frequent given the relatively inexpensive experiment procedures. The European New Car Assessment Programme (Euro NCAP) is a voluntary seven-test car safety rating developed to assess the injury level on occupants and pedestrians during collisions [3]. The tests performed by the Euro NCAP and other safety programs (ASEAN NCAP, ANCAP or Latin NCAP [4]) are later on coupled with numerical simulations used to study the impact dynamics and energy absorption behavior of vehicles and humans.

However, full testing of aircraft models is laborious and expensive, thus limiting experimental programs to few private institutions. To address this issue, research programs by the Federal Aviation Administration (FAA), the U.S. Department of Defense and the National Aeronautics and Space Administration

Figure 1.1: Cessna 172 impact test at NASA Langley's Facility. Taken from [5].

(NASA), have conducted hundreds of crashworthiness tests of helicopter and aircraft impact scenarios. NASA alone has performed full-scale crash tests of over 150 specimens, including prototypes from the Bell and Sikorsky rotorcraft from the ACAP US Army program [6], and over a hundred military, general aviation and commercial airplanes [7]. The data extracted from these tests was used to characterize the response of both the primary fuselage structures and specific cabin components, as well as passenger-injury levels. In the example from figure 1.1, a Cessna 172 was dropped nose-up from 30 meters for measuring post-test performance of emergency location transmitters (ELT) [5], later using this data for improved ELT placement inside the craft.

Furthermore, since the test specimens had been thoroughly instrumented, finite element analyses and scaled models were developed and verified with the large experimental database created from the dynamic crashworthiness tests. These models not only require significantly less resources than full-scale experiments, but they can also provide insight on the behavior of the aircraft in situations where tests cannot be performed. Moreover, given a validated baseline model, a large number of impact conditions and design alternatives can be studied with little or no extra cost, complementing and supporting the experimental impact tests.

The initial numerical models developed were build using simplifications that sped up the calculations, with passengers being modeled as point masses and ignoring cutouts, fasteners and finer details. These models were able to predict the global response of the aircraft, although the behavior of localized features (as the stress level on a particular component during impact) was not adequately captured. However, and with the concurrent rise of computer power, models have become more detailed, allowing the implementation of more realistic features that draw the response of numerical and experimental specimens ever closer.

With the usage of finite element models, the study of the crashworthiness response of aircraft structures became far more economic. Material resources and man-hours at workshops are traded by computer clusters and code lines, ultimately addressing the design and test processes more efficiently. This technological leap, backed with all the previous ones before it, aided in providing a deeper knowledge on the impact dynamics of complex structures. In the case of an aircraft crash, the optimum response would be provided given that all the primary and secondary airframe structures work simultaneously, maximizing the energy absorption and dissipation. The necessary livable space after the impact must also be maintained, reducing cargo damage and passenger injuries by avoiding collisions with detached objects or the aircraft's inside features.

Different approaches are followed to obtain this crashworthiness improvement of a structure. In the case of automobiles, the usage of energy absorbers behind the bumper structure or reinforced B-pillars for frontal and side impacts respectively, is now of common practice in the automotive industry. Pedestrians are also considered in crashworthiness analyses, and flexible bumpers and bonnets have been used since. As a result of these and other enforced measures, the average Euro NCAP rating rose from a mere two stars in 1998 to four out of five in 2005 [8].

In the case of aircraft structures, the approach for bettering the response in crash scenarios resembles that of the automotive industry. The vertical kinetic energy is dissipated via deformation of the main frames, the sub-floor structures, the sub-cargo area, and the vertical struts depicted in figure 1.2. The last are axially-loaded during hard landing and water ditching scenarios, and have proved

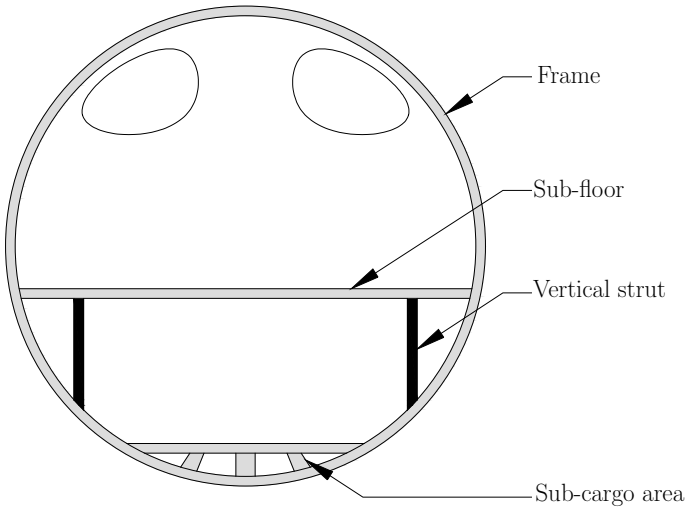

Figure 1.2: Schematics of main aircraft fuselage crashworthiness absorption structures.

to dissipate up to 15 % of the craft's vertical kinetic energy. However, few current designs include these structures, and those that feature them do not exhibit and efficient collapse according to crashworthiness standards. Chapter 2 offers a more in-detail review of the state of the art of these and other energy absorbing devices for transport applications, as well as showing that the door for improvement is still ajar. The benefits offered by the usage of composite materials, bio-inspired structural configurations and optimization techniques are here combined to ultimately enhance the crashworthiness response of energy absorbing structures intended for the aircraft industry.

1.2 Contributions of this thesis

This research is focused on the design and optimization of hybrid energy absorbers for aircraft applications according to crashworthiness criteria. The following contributions are offered:

1. This thesis uses finite element modeling and simulation to analyze the dynamic axial collapse of thin-walled square tubes complemented by inner cores from honeycomb and star-shaped composite structures and foam extrusions. Different devices are studied and optimized under crashworthiness criteria, including mass, cost and passenger injury metrics.

2. A fuselage section from a frequently-tested aircraft is modeled and verified, obtaining a sensible agreement between the numerical and experimental drop-test results; later constituting a benchmark for testing the performance of hybrid energy absorbers.

3. The structural and biometric performance of collapsible energy absorbers in an aircraft hard-landind scenario is analyzed, as well as characterizing the effect on the crushing evolution, energy trends and effect on passenger injury levels caused by the auxiliary fuel tank located in the cargo area.

4. Surrogate-based optimization techniques are successfully applied to the aforementioned specimens, both as standalone tested items and as part of a fuselage vertical drop test, efficiently obtaining devices with enhanced crashworthiness responses.

1.3 Research aims and methodology

This investigation was set out with two well-defined aims as contribution to the field of crashworthiness, namely:

1. Gaining scientific knowledge on the behavior of collapsible energy absorbers under dynamic axial loads and during a representative impact simulation. Metallic tubes are to be complemented with untested combinations of various shapes and materials that enhance crashworthiness performance, including honeycomb composite structures and high-density foam extrusions. Specimens are also numerically tested in a validated fuselage section under a drop test scenario, assessing whether passenger injury levels and other biometric indicators.

2. Successfully coupling and applying surrogate-based multi-objective optimization techniques in full-scale impact simulations, combining the robustness of metamodeling with the response enhancement yielded by optimization. Finite element experiments are parametrized and coupled with algorithms for sampling execution, surrogate model construction and metaheuristic optimization; eventually obtaining sets of designs and responses with higher crashworthiness performance than initial configurations.

Achieving the aforementioned aims has been solely based on numerical techniques, although the drop test simulation of the fuselage section has been correlated with experimental test data. As for computational methods, the following tools have been required:

- Finite element modeling of materials and components involved, using Abaqus Explicit and parametrized Python scripts for automatized simulations and user-defined material subroutines in Fortran 90.
- Dynamic testing of the aforementioned models; coupled with Python code for sorting, filtering and post-processing the extracted data.
- The DAKOTA framework offers the algorithms required for performing samplings, metamodel construction, and robust genetic optimization algorithms; all of which have been used with each sample constituting a finite element simulation.

1.4 Outline

The work here presented is based on aseries of publications produced by the author. Chapters 3 to 6 correspond to adapted self-contained journal articles, some of which are already published, while others are to be submitted for publication. A brief content summary of each chapter is now presented.

- **Chapter 2** introduces the crashworthiness concept, tracing the origins and following its evolution until today's state of the art. Collapsible energy

absorbers are also presented, with special attention to square thin-walled tubes and the assortment of reinforcing structures used for enhancing their response. Finally, the reader is presented with numerical methods and basic notions of surrogate-based optimization techniques, two of the cornerstones throughout the investigation.

- **Chapter 3** studies and optimizes the response under axial impact loading of steel tubes filled with a GFRP honeycomb structure with variable cell size and ply thickness.
- **Chapter 4** deepens into the behavior of similar components from chapter 3, adapting them towards the aircraft industry. Steel is replaced by aluminum, foam extrusions are added for higher energy absorption efficiency, and the honeycomb's cell undergoes size and shape optimization procedures.
- **Chapter 5** verses on the simulation, validation and crashworthiness analysis of an aircraft's fuselage section in a drop-test scenario; as well as examining the effects of featuring crushable absorbers as vertical struts.
- **Chapter 6** combines the methodologies and findings derived from previous chapters, ultimately lessening passenger injury for aircraft vertical impacts by optimizing the overall response of a fuselage enclosing collapsible hybrid energy absorbers.
- **Chapter 7** draws the investigation to a close, offering a summary of the work, the conclusions to which it led, and future lines of research that could arise from it.

Moreover, the extended summaries of this work in Spanish and Galician can be respectively found in appendices A and B as to comply with the content requirements from Universidade da Coruña.

Five peer-reviewed publications as the main author have arisen from this investigation, namely:

- J. Paz, J. Díaz, L. Romera, and M. Costas. "Crushing analysis and multi-objective crashworthiness optimization of GFRP honeycomb-filled energy

absorption devices". *Finite Elements in Analysis and Design* 91 (2014), pp. 30–39 [9].

- J. Paz, J. Díaz, L. Romera, and M. Costas. "Size and shape optimization of aluminum tubes with GFRP honeycomb reinforcements for crashworthy aircraft structures". *Composite Structures* 133 (2015), pp. 499–507 [10].

- J. Paz, L. Romera, and J. Díaz. "Crashworthiness optimization of aircraft hybrid energy absorbers enclosing honeycomb and foam structures". *AIAA Journal* 55.2 (2017), pp. 652–661 [11].

- J. Paz, L. Romera, J. Díaz, and F. Teixeira-Dias. "Drop test numerical simulation and crashworthiness enhancement of an aircraft fuselage section". *To be submitted for publication* (2018)

- J. Paz, L. Romera, J. Díaz. "Optimization of hybrid energy absorbers for crashworty aircraft designs". *To be submitted for publication* (2018)

Furthermore, this and other closely related work have also been presented in three international proceedings:

- L. Romera, J. Paz, M. Costas, J. Díaz, and S. Hernández. "Crashworthiness response of honeycomb metallic-GFRP energy absorption devices". In: *The 2014 International Conference on High Performance and Optimum Design of Structures and Materials. Ostend, Belgium.* (2014) [12].

- J. Díaz, M. Costas, L. Romera, J. Paz, and S. Hernández. "Surrogate-based multi-objective optimization of glass-fiber-steel crash absorbers". In: *The 2014 International Conference on High Performance and Optimum Design of Structures and Materials. Ostend, Belgium.* (2014) [13].

- J. Paz, F. Teixeira-Dias, L. Romera and J. Díaz. "Crashworthiness improvement of aircraft fuselage sections using hybrid energy absorbers". In: *The 20th International Conference on Composite Structures. Paris, France.* (2017).

Finally, this investigation is enclosed within two national research projects:

- "Optimización probabilista topológica y topométrica de estructuras aeronáuticas en régimen lineal y no lineal"; OPTOPAER. Grant agreement: DPI 2013-41893-R
- "Optimización probabilista de estructuras aeronáuticas intactas y dañadas frente a cargas dinámicas y de impacto"; OPTISAFE. Grant agreement: DPI 2016-76934-R.

References

[1] Laananen, DH and Winkelman, KL. "Analysis of energy-absorbing seat configurations for aircraft". *International journal of crashworthiness* 1.4 (1996), pp. 355–368.

[2] Snyder, Richard G. *Civil Aircraft Restraint Systems: State-of-the-Art Evaluation of Standards, Experimental Data, and Accident Experience*. Tech. rep. SAE Technical Paper, 1977.

[3] European New Car Assessment Programme (Euro NCAP). *Frontal Impact Testing Protocol, Version 6.0.2*. Tech. rep. European New Car Assessment Programme (Euro NCAP), 2013.

[4] Global NCAP. *List of NCAPS*. `https://goo.gl/dWvokW`.

[5] NASA. *1974 Cessna 172 drop test at NASA Langley's Landing and Impact Research Facility. August 26ht, 2015*. `https://goo.gl/x8U3hc`.

[6] Jackson, Karen E, Fasanella, Edwin L, Boitnott, Richard, McEntire, Joseph, and Lewis, Alan. "Occupant Responses in a Full-Scale Crash Test of the Sikorsky ACAP Helicopter". *Journal of the American Helicopter Society* 49.2 (2004), pp. 127–139.

[7] Jackson, Karen E, Boitnott, Richard L, Fasanella, Edwin L, Jones, Lisa E, and Lyle, Karen H. "A history of full-scale aircraft and rotorcraft crash testing and simulation at NASA Langley Research Center" (2004).

[8] *Barómetro de Seguridad Vehicular del Parque de Automoción.* Tech. rep. Fundación FITSA, 2007.

[9] Paz, J, Díaz, J, Romera, L, and Costas, M. "Crushing analysis and multi-objective crashworthiness optimization of GFRP honeycomb-filled energy absorption devices". *Finite Elements in Analysis and Design* 91 (2014), pp. 30–39.

[10] Paz, J., Díaz, J., Romera, L., and Costas, M. "Size and shape optimization of aluminum tubes with GFRP honeycomb reinforcements for crashworthy aircraft structures". *Composite Structures* 133 (2015), pp. 499–507.

[11] Paz, J., Romera, L., and Diaz, J. "Crashworthiness optimization of aircraft hybrid energy absorbers enclosing honeycomb and foam structures". *AIAA Journal* 55.2 (2017), pp. 652–661.

[12] Romera, L, Paz, J, Costas, M, Dıaz, J, and Hernandez, S. "Crashworthiness response of honeycomb metallic-GFRP energy absorption devices". *High Performance and Optimum Design of Structures and Materials. Ostend, Belgium.* 137 (2014), p. 225.

[13] Díaz, J., Costas, M., Romera, L., Paz, J., and Hernández, S. "Surrogate-based multi-objective optimization of glass-fiber-steel crash absorbers". *High Performance and Optimum Design of Structures and Materials. Ostend, Belgium.* 137 (2014), p. 225.

2

Structural crashworthiness and numerical methods

Hereunder, the reader is introduced to the main branches of study dominating this investigation. After a brief account on the notions of aircraft crashworthiness, the focus deepens into the characteristics of collapsible energy absorbers and their behavior under impact loads. As this dissertation heavily relies on numerical simulations, the fundamentals of finite element methods and optimization techniques applied in crashworthiness are also described. Although concise, this foreword intents to cover the basics of each subject, also providing a path towards more exhaustive sources when a thorough review is sought.

2.1 A brief introduction to crashworthiness

The general public is ever more aware of transport safety and its role in minimizing accidents' burden on society. Automobiles, aircrafts, and other means of transport are designed according to efficiency and occupant protection criteria, both comprised in a field named crashworthiness. The following section introduces the crashworthiness concept, the methods used for its assessment, and how passengers and transport industries have benefited from this field of study.

2.1.1 Origin and purpose

The ethos of the crashworthiness concept can be traced back to the 1920s. After surviving a plane crash during WWI, Hugh DeHaven, considered by many the "father of crash survivability", started an investigation that resulted in the Crash Injury Research project in Cornell in 1942. He would later on publish the book 'Mechanical analysis of survival in falls from heights of fifty to one hundred and fifty feet' [34], where he stated that many injuries could be avoided via structural designs with enhanced pressure distribution and better impact responses. This investigation led in 1952 to DeHaven's four basic crashworthiness principles, where passenger aircraft transport is compared with the freight industry. Bearing in mind that the fuselage, restraint systems and occupants are referred to as container, interior packaging and contents respectively, the principles are [35]:

1. "The package should not open up and spill its contents and should not collapse under reasonable or expected conditions of force and thereby expose objects inside it to damage".
2. "Packaging structures which shield the inner container must not be made of brittle or frail materials; they should resist force by yielding and absorbing energy applied to the outer container so as to cushion and distribute impact and thereby protect the inner container".
3. "Articles contained in the package should be held and immobilized inside the outer structure by what packaging engineers call interior packaging [...] for it prevents movement and resultant damage from impact against the inside of the package itself".
4. "The wadding, blocks, or means for holding an object inside a shipping container must transmit forces to the strongest parts of the contained objects".

Modern crashworthiness in automotive and aircraft design still abides by this principles, ultimately seeking the highest protection of occupants against harm in the event of a crash [36]. Injuries are classified as either environmental (caused by

threats as fire, water intrusion or chemical exposure) or traumatic, which include contact and acceleration injuries. To minimize the former, and following the crashworthiness' first and second rules, the occupants compartment is built with strong materials as to create a survivable volume. This cell structure is featured in most modern transport systems, including airplanes and automobiles. In motor racing this structure is called cockpit (see figure 2.1), and by combining carbon fiber reinforced polymers (CFRP), Kevlar and an aluminum honeycomb extrusions has withheld the survivable volume in crashes with up to 75-g acceleration peaks.

Figure 2.1: Ferrari's F310B Formula One® cockpit cutaway (1997) [37].

Besides reinforcing shielding structures against external perils, the existence of a safe crushing stroke, the crushing distance upon jeopardizing the occupant area, also increases the vehicle's safety by reducing acceleration and contact contusions. Thus, the stiff cockpit is ideally protected by more ductile structures that gradually collapse, dissipating and absorbing the kinetic energy during the collision. In automobiles, these weaker elements include the bumper, crash boxes and front rails; while in aircrafts they comprise sub-cargo reinforcements, vertical struts and the main frames. The lower and less stiff crushing stroke found in general aviation crafts results in a faster exhaustion of the available crushing distance and a sudden force increase in vertical impact scenarios. This event, called 'bottom-out effect' is one of the main reasons why fatal crashes per flight hour are 50 times higher in general aviation than in commercial aviation [38].

Figure 2.2: Ag-1 agricultural aircraft. Taken from [39].

Once a safe compartment is ensured, the immobilization of the passenger inside it is crucial. Moreover, this restraint must redirect the pressure transmitted to the occupant so that it is transfered through strong skeleton structures, as well as preventing impact with other inner objects. The final step of a crashworthiness design deals with the post-crash safety , including fire prevention and safe egress.

Fred Weick's agricultural aircraft, the Ag-1 from figure 2.2 (1950), was the first to be designed according to DeHaven's recommendations [40]. It was developed with a 40-g resistant cockpit and weaker bow structures, which would fail progressively before damaging the occupant survivable cell. The first major manufacturer to include crashworthiness in the design process was the Beechcraft Company with the Bonanza [2]. This craft, shown in figure 2.3, included a long nose for gradual deceleration in front impacts, a reinforced cockpit to protect the passengers and strong longitudinal floor beams to minimize the penetration on the impacting surface.

During the 1970's and 1980's, the FAA focused on updating the Federal Aviation Regulations concerning crashworthiness features. As an example, shoulder harnesses became mandatory for all occupants in light airplanes due to the

Figure 2.3: Flight of Beechcraft Bonanza 35 N3188V in January 1949. Taken from [41].

survivability improvement obtained when they are used [42]. Another measure was applied in 1988, as the FAR amendment 23-36 established that injury criteria was required to be measured by standardized anthropomorphic test devices (ATD) in emergency landing conditions [43].

A substantial increase in the crashworthiness of vehicles has been obtained since DeHaven's principles were first stated. However, and despite all the efforts made up to date, the general opinion is that much more can be done. Fatalities in 2015 in the US territory surpassed 35 000 for motorcars and almost 400 in general aviation crashes [38, 44], of which over 40% are estimated to be preventable via crashworthy structural designs [45].

2.1.2 Crashworthiness analysis: experiment and simulation

When designers and engineers assess a vehicle's response in impact scenarios, it is done either experimentally or through numerical simulations. Up until the 1990s, most of the studies were performed using real specimens, but with the ever

increasing computer resources, methodologies have swerved towards a higher usage of validated numerical models rather than the initial experimental methods. The automotive industry still performs frequent full-scale experimental tests, albeit aircraft testing under dynamic crash conditions in still rather atypical. Moreover, since complete aircraft numerical models require vast computer resources, most studies have been conducted with single components or representative fuselage sections.

Experiments have been performed by the FAA and other aircraft safety administrations since the 1950s. The findings extracted helped create a database of dynamic tests ranging from commercial airplanes to military helicopters. The validation step, vital both in aircraft and automobiles [46–48], is performed comparing the experimental results with numerical simulations; also consisting in an essential tool for gaining confidence in the simulation's prediction capabilities. If a component does not behave realistically in the simulation, the crash response and kinematics of the whole model can be strongly compromised [49].

In the early stages, numerical models were developed using lumped-mass spring damper systems. These simulations were performed combining non-linear springs, lumped masses and beam elements, with the equations of motion integrated explicitly in the code to obtain the kinematic behavior of the model [50]. The number of elements usually ranged between five and fifty, seldom surpassing the barrier of a hundred, accordingly with the computational resources available at the time. Therefore, small parameter changes, such as modifying the non-linear spring responses, critically influenced the crushing evolution of energy dissipating structures, including the sub-floor area, landing gear or the main frames [51]. Thus, experimental data and good engineering judgment is necessary in the simplification and modeling processes in order to obtain accurate model responses from these kinematic models.

The beginning of non-linear finite element codes is mainly linked to the US government, starting with the NASTRAN structural analysis code in the 1960s [52]. Among the many hybrid codes developed, KRASH [53] probably was the most used of them all. KRASH was developed under U.S. Army sponsorship and made public in 1979, with following updates that bettered the code's predictions

for aircraft dynamic and impact simulations. The FAA, a major sponsor in the project, used this code to simulate and fine tune the models built from the experimental tests of rotorcraft, general aviations and commercial aircraft (see figure 2.4), making KRASH the most validated code with full-scale experiments [54]. The validated models still are used as fast tool for predicting the global impact dynamics of the global model in the early design stages, although localized component responses are not reliably predicted. Even today, a library of aircraft KRASH models is regularly employed by the Air Accident Investigation Tool (AAIT) to understand aircraft crash dynamics [55].

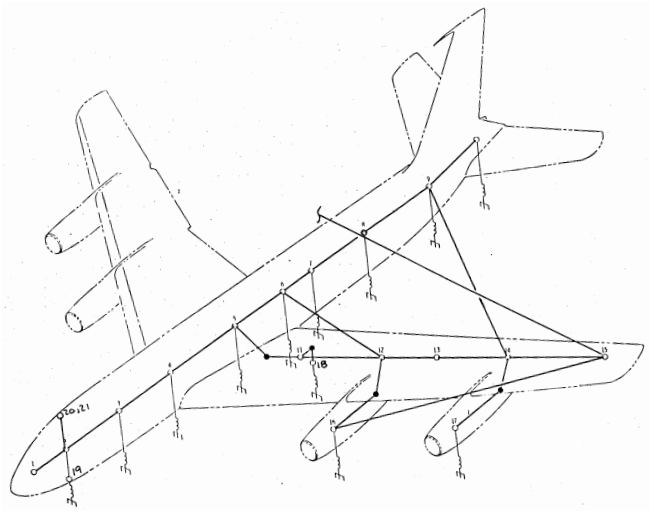

Figure 2.4: Large transport aircraft model in KRASH. Taken from [56].

However, these kinematic models were affected by certain shortcomings. Most of the codes used implicit time integration, which lagged computer performance even for small models. Implicit techniques also lacked robustness in nonlinear problems, often failing to converge at certain time steps and requiring experienced personnel to edit the code if a reliable final solution was to be obtained. Moreover, kinematic simulations are not first-principles models, requiring considerable experimental testing during the fine-tuning of the model and being only suitable for a limited range of impact conditions.

As computational power evolved, so did the crash analysis codes and the level of detail in the simulations [57]. With funding from the US Department of Energy, a varied suite of nonlinear dynamic structural codes were developed during the 1970s and 1980s at the Lawrence Livermore National Laboratories. Hallquist and Whirley [58] originally created the DYNA3D code to simulate nuclear bomb release at low heights, as no 3D software was able to achieve this at the time. The code was vectorized for higher efficiency when running on the Cray-1 vector computer, and it featured efficient explicit time integration, two element formulations and several libraries for materials and equations of state (EOS).

In 1973, the US National Highway Transportation and Safety Authority (NTHSA) also drew its efforts towards accurately assessing passenger safety only through simulation techniques. The joint venture involved automobile models developed in the University of Michigan, occupant models from the Naval Civil Engineering Laboratories, and the WRECKER computer code for impact simulation developed by IIT Research Institute [59]. This program was an adaptation of Belytschko and Marchertas' WHAMS code for reactor safety studies [60], which featured explicit time integration for more robustness and faster computation times in crash simulations.

By 1978, DYNA3D's source code was made public and established itself as a cornerstone for many of modern commercial codes, including its successor LS-DYNA [61], MSC.Dytran [62] and PAMCRASH [63]. As codes evolved, finite element analyses (FEA) allowed for better modeling of components and material responses, eventually changing the approach for today's dynamic nonlinear simulations.

Nowadays, with a correct characterization of the model's shape, material and simulation conditions, results accurately mimic the experimental process without previous adjustment required. FEAs are considered first-principles or fully predictive methods, although experimental testing for validation is still considered necessary and of common practice [50]. The automotive industry, driven by consumer pressure for safety and safety legislations, continued exploiting the predictive capabilities of numerical methods adopting an early usage of FEA

into their design process. Crash simulations evolved to include full vehicle models with accurate representation of complex features such as airbag detonation, fuel sloshing in the tank or injury assessment via anthropomorphic test devices (ATDs).

However, it was not until the establishment of structural design requirements, shortly after the beginning of the 21st century, that aircraft numerical simulations were used to predict the airframe's response during impact, consequently reducing development costs. Finite element models aided in the inception, testing and certifying of isolated components, such as seat restraints or overhead stowage bins. Thus, embracing finite element methods for full-scale evaluation and certification would not only translate into less expenses, but also allows assessing a wider range of working or impact conditions, many of which cannot be experimentally tested. Moreover, the detailed crush behavior and energy dissipated by each single component can be effortlessly retrieved in a numerical simulation, data not so easily obtained from experimental methods [64]. Consequently, critical design features can be identified easier, which can later be addressed by efficient crashworthiness optimization of the component's design.

Seeking a wider usage of FEM, Fasanella and Jackson [66] described several full-scale crash modeling and simulation guidelines for aircraft impact numerical simulations, including advice for the development, execution, and validation of finite element analyses. The report also contains experimental data from two Boeings 737-100 and a Sikorsky ACAP helicopter (figure 2.5a) full-scale drop tests performed at the FAA William J. Hughes Technical Center at the beginning of the 2000s. As a first approach, a full-scale nonlinear MSC.Dytran simulation of the first specimen was developed and correlated with the experimental results (figure 2.5b). Structural deformation values and floor-level acceleration responses closely matched the drop-test data. Before the second experiment was conducted, a pretest simulation was performed to assess the accuracy of FEA as a predictive tool. Results proved outstanding, successfully anticipating acceleration values at the component level as well as the fuselage's collapse process [67].

Many advancements have been implemented in FEA and improved simulation's computational time, robustness and accuracy. Belytschko's subcycling procedures

(a) Pretest helicopter test article.

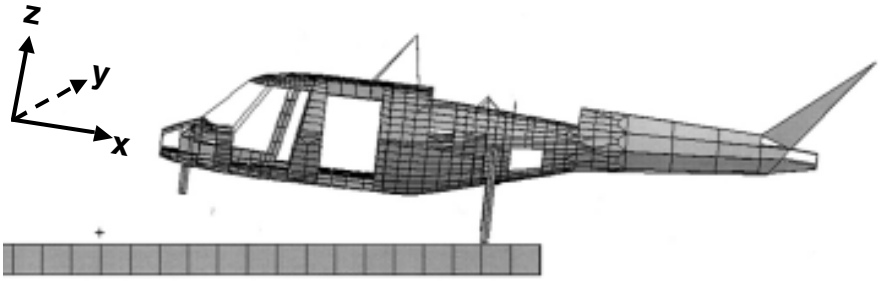

(b) Finite element model in MSC.Dytran.

Figure 2.5: Sikorsky ACAP helicopter as tested by Fasanella et al. [65].

allow for different stable time increments in explicitly-integrated models, bettering overall computational time in model with differentiated mesh sizes [68]. The usage of improved adaptive meshing techniques refines mesh density during the simulation based on accuracy, yielding more precise results with little effect on the computational cost [69]. Extended material and equation-of-state formulations widen the number of test conditions simulated, while new element formulations increase robustness through specifically designed codes.

Concerning the crashworthiness field, the development of numerical human body models provided a better understatement of passenger injuries than the traditional physical dummies. The Articulated Total Body (ATB) program from 1975 developed by the US Air Force was one of the pioneers in the simulation of human responses, combining join-connected elements into multi-body systems [71]. Although efficient and accurate, these models have been outcompeted by modern numerical designs offering higher accuracy capabilities. Depending on the level of detail required and the computational power at disposal, ATDs

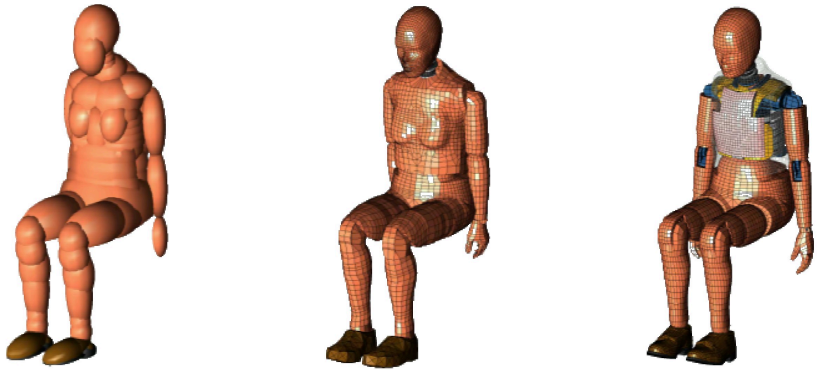

(a) Ellipsoid model **(b)** Facet-based model **(c)** Finite element model

Figure 2.6: Hybrid III MADYMO 50^{th} percentile female adult ATDs. Taken from [70].

are modeled either with ellipsoids, facets or finite elements. Ellipsoid models, based on the multi-body systems, are the most computer efficient; whereas facet dummies allow a better geometric representation of human characteristics [72]. Finite element dummy models, however, produce the best results on the ATDs kinematic behavior and local and global deformation levels, with the drawback of being the most computer-costly of the three. A wide variety of models are offered for the various FEM softwares, with MADYMO offering the broadest database [73] ranging from a six-week infant to the standard adult female from figure 2.6.

2.1.3 Crasworthiness design

When a crashworthiness improvement is sought for hard-landing or water-ditching scenarios, the aircraft's kinetic energy before impact is divided into its horizontal and vertical components. The longitudinal deceleration, with exception of sudden impact against solid objects, is usually of least concern. The highest acceleration peak occurs in the first third of the pulse duration, and most of the energy is dissipated through friction with the ground [74]. After that, during the slide out phase, acceleration loads are significantly lower.

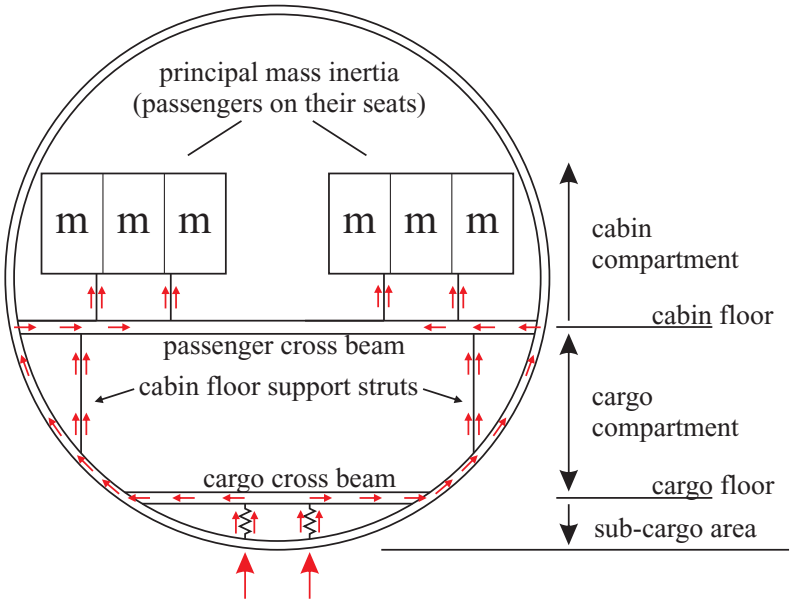

(a) Single-isle transport aircraft.

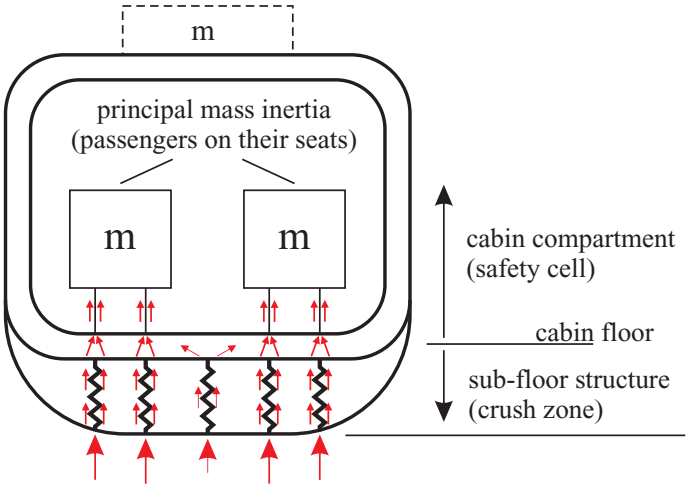

(b) Helicopters and light fixed-wing aircraft.

Figure 2.7: Transmission of crash loads in fuselage cross sections. Taken from [75].

The vertical energy fraction is absorbed by the landing gear [76], deformation of the aircraft structural components and the occupant seat system [50]. Unlike with the horizontal pulses, vertical deceleration is critically influenced by the sub-floor structures. In helicopters and general aviation, the landing gear is the first structure to contact the ground [77] as shown in figure 2.7. The sole plastic deformation and friction with the ground dissipates a significant amount of energy in hard landing scenarios, although the contribution from this component is negligible in water ditching. In the commercial aircraft range, the highest contribution for kinetic energy dissipation stems from deformation of the main fuselage. After the sub-cargo area impacts the ground, the crushing process then stresses the main circumferential frames, which collapse locally in the form of plastic hinges. Some aircraft designs include vertical struts for floor support, which also play an important role in energy dissipation and maintaining structural integrity [78]. Seat design and certification is also vital for avoiding passenger injuries, with extensive ongoing research concerning the topic [79–81]. Seat crashworthiness requirements include two dynamic tests [82], combining vertical, longitudinal and lateral loads as to comply with dynamic standards FAR § 23.562 and § 25.562 [83–86]. As for the other three different energy-dissipating structures —sub-cargo enhancements, main frames and struts —a more detailed description and some significant advances for each component are now offered.

2.1.3.1 Sub-cargo area

Helicopters and aircrafts have benefited from sub-floor enhancements since the 1980s. According to Kindervater et al. [74]'s "controlled load concept", a crashworthy sub-floor structure should, at least:

- Distribute uniformly ground reactions and seat loads.
- Exhibit moderate initial stiffness and gradually increase the crushing force levels.
- Have load bearing capability for normal operation and dissipate energy during crashes.

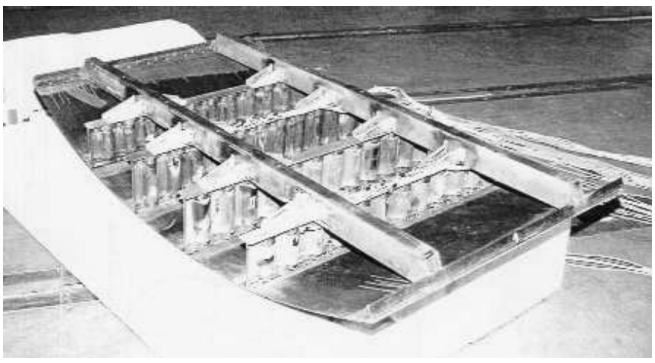

Figure 2.8: Sub-floor assembly featuring sinewave beams. Taken form [87].

Following a similar approach, Carden and Hayduk [88] studied the crash dynamics of five aircraft sub-floor structures, analyzing energy absorption and structural integrity. The usage of sinusoid or conusoid beam structures as the ones from figure 2.8 has also proved an effective method of attenuating acceleration loads in helicopters and aircrafts [89–93]. Posterior enhancements on these structures, as including chamfer triggers [94, 95] or inducing an eccentric load transmission to the main structures [96, 97], ease the crushing initiation and further reduce peak load values. More recently, Waimer et al. [98] also added composite thin-walled half-tubes in the sub-cargo area, which collapse between the cargo cross-beam and main frame.

Farley [99] studied the response of four designs (honeycomb, sinusoid beams, and circular and rectangular stiffened beams), obtaining the best results with a graphite/epoxy sine-wave configuration. Foams are also a recurrent material for energy dissipation in this area [14, 100], commonly featured as solid blocks as shown in figure 2.9. Bisagni [101] found that by adding 12 kilograms of foam blocks in the cargo area, passenger accelerations were lowered by 33% in a vertical impact test; later stating the need for optimization of crushable elements in this industry. The usage of cellular arrangements, including honeycombs [15] and folded-cores [102], has also delivered outstanding crashworthy results under impact scenarios. By means of example, Jackson and Fuchs [103] designed honeycomb absorbers that reduced by one order of magnitude the occupant

acceleration loads in a water ditching scenario, offering a more stable crushing of the structure and better energy transfer to water.

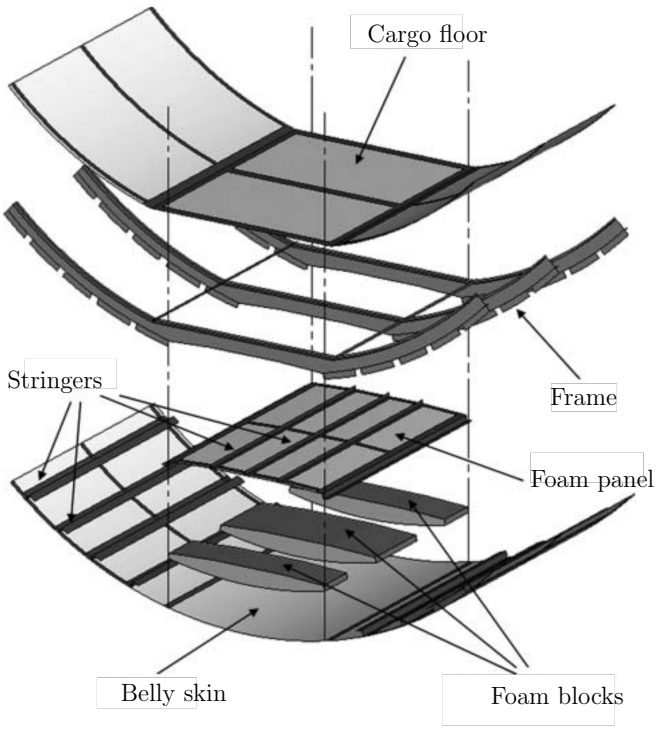

Figure 2.9: Sub-floor structural assembly featuring energy-absorbing foam blocks. Taken form [14].

2.1.3.2 Frames

During the collapse process of the fuselage structures in a vertical crash the main frames flatten, usually forming a series of plastic hinges in the sub-floor region (four are formed in the section from figure 2.10). The location of these hinges affects the overall crushing of the aircraft, as shown by Ren and Xiang [104]. Improving the main frames response can be approached on a single component basis or as a complete structure. Heimbs et al. [105] simulated and tested joint

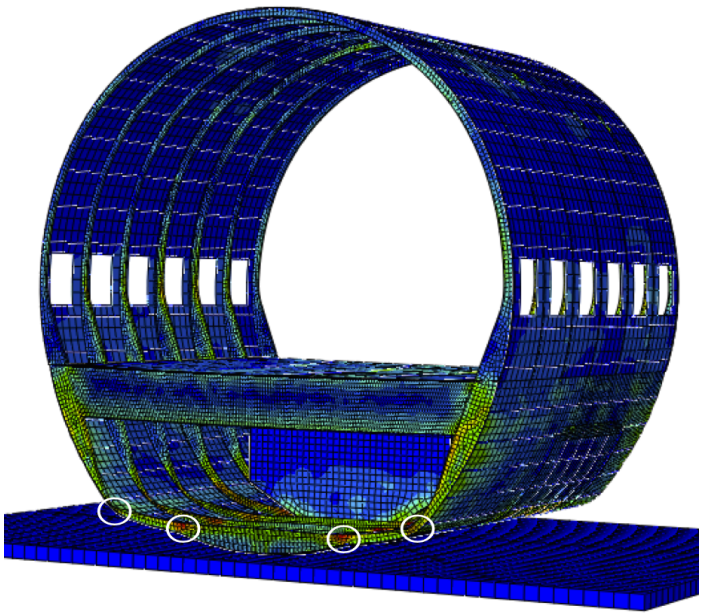

Figure 2.10: Boeing 737 post-test deformation. Plastic hinges circled in white.

failure and skin and frame bending under various load conditions on components made from carbon fiber and epoxy, concluding that fastener failure exclusively can dissipate up to 15 % of the initial vertical kinetic energy. Similar findings were obtained for reinforced sections at the main hinge locations, as the composite laminate made of carbon fiber, PEEK and titanium designed by Waimer et al. [106].

The efficient combination of different crashworthy elements can lead to an overall improvement in performance of the frames. Gransden and Alderliesten [108] examined the crash scenario of a metallic A350-like fuselage section, later compared to a similar specimen with frames, stringers and skin made from composite materials. Results showed slight increase in occupant injury for the latter, although the structural mass was reduced. The conclusion reached points towards capitalizing on the high stiffness-to-weight of composites joined with efficient crash concepts. Schatrow and Waimer [109] combined progressive failure on a cabin floor bearing with energy dissipation by bending at the frame hinges,

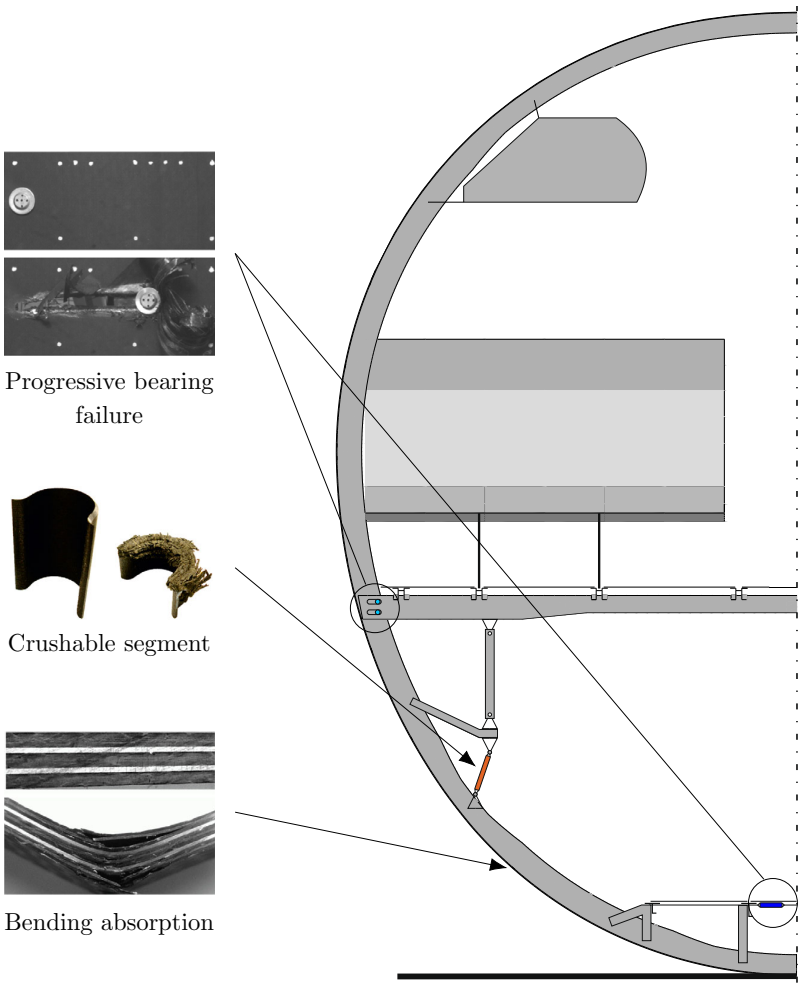

Figure 2.11: Tension crash concept and energy absorption components. Adapted from [107].

crushing of floor-supporting struts and plastic elongation at the cargo floor, as shown in figure 2.11. This tension crash concept for the frames collapse not only offers a smoother response than typical crushing mechanisms, but also allows parallel activation of all energy dissipation components, thus reducing the harmful peak loads of cascading crash concepts [107].

2.1.3.3 Struts

Vertical struts are used in some civil aircraft designs, as the Airbus A320 [110] or the Fokker F28 [111] from figure 2.12, with the main purpose of providing vertical support for the cabin floor. However, following the idea of the "controlled load concept" mentioned earlier, several investigations have assessed the effect of struts as crashworthy elements [112, 113]. Yiru et al. [114] determined that the strut's stiffness was a key factor for damping acceleration loads and maintaining a livable crush space. While stiff struts avoid excessive crushing of the sub-floor area and reduce the risk of bottoming-out, they also transmit higher force peaks to the occupants; thus suggesting the need for a trade-off between the two desired responses [115, 116]. The position and angle of the struts in the fuselage is also critical for occupant protection, as they influence the aforementioned plastic hinge location [104]. By discretely modifying the insertion angles with the floor beams and the main frames, Ren and Xiang [104] concluded that best energy absorption and acceleration trends where obtained for oblique struts, although sacrificing cargo space.

Concerning the geometry and materials of the strut, several options have arisen. Ren and Xiang [16] analyzed the effect of including triggered quadrangular oblique struts in a generic civil aircraft, showing that optimum performance was achieved with material thicknesses slightly under one millimeter. Heimbs and Middendorf [117] proved that composite struts forced to pass through a deflection and cutting device not only showed a robust and effective crushing, but they also are adjustable for different needs by modifying composite ply configurations, the design of shear pins or the number of cutting holes. As in the sub-cargo

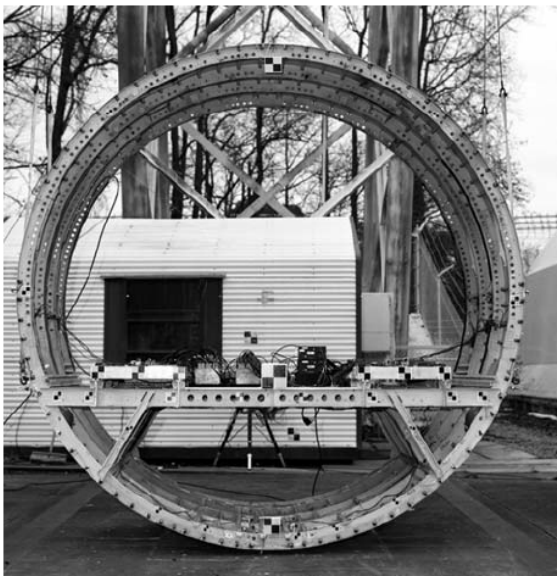

Figure 2.12: Fokker F28 fuselage section featuring vertical struts. Taken from [111].

region, continuous sine-wave beams replacing vertical struts also offer an efficient solution for stable energy dissipation [118].

The crash response of struts and other collapsible energy absorbers is later detailed in section 2.2.1.3.

2.1.4 Crashworthiness evaluation

Crashworthiness studies include information concerning acceleration, displacement and velocity plots, energy absorption values and biometric parameters for injury level assessment on passengers. Some basic concepts for impact dynamic experiments are now reviewed, as well as stating the connection between all the aforementioned data. The following description of crash kinematics is particularized for an aircraft's vertical impact against solid grounds. This example is used to introduce the reader to the impact physics of an idealized aircraft hard-landing crash, albeit most of the information here presented is homologous to other impact scenarios, as are vehicle frontal collision with rigid barriers.

2.1.4.1 Impact physics

During an aircraft hard-landing scenario, the initial non-zero vertical V_z and horizontal V_x velocities progressively decrease until the vessel comes to a complete stop. The horizontal kinetic energy is primarily dissipated via friction and soil deformation. This deceleration process peaks during the first third of the pulse duration, followed by a slide out phase with significantly lower acceleration levels, as shown in figure 2.13.

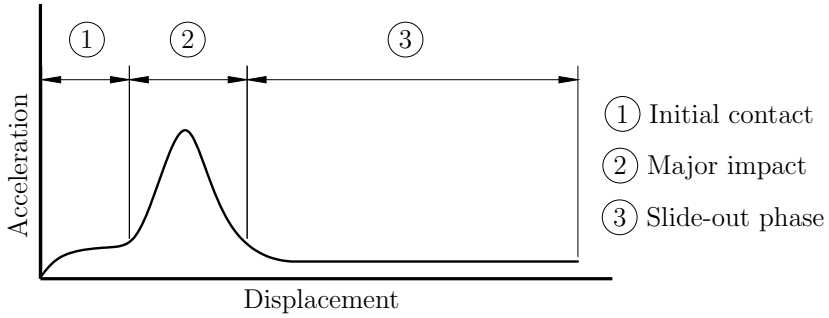

Figure 2.13: Aircraft longitudinal deceleration profile.

On the other hand, a typical vertical acceleration pulse has a triangular shape with harmful acceleration peaks during the sub-floor crushing and seat stroking phases. However, as the vertical energy component is dissipated by structural deformation, the acceleration trends can vary when modifying the aircraft's structural design in a quest for a lower load plateau for longer periods of time.

2.1.4.2 Energy absorption

Modifying the aircraft's structures seeking lower acceleration levels entails progressively dissipating the initial kinetic crash energy. Let's consider an isolated system in which the fuselage from figure 2.14 with a downwards vertical velocity V_{z_0}[1] and a mass m_a impacts a rigid surface. Since the fuselage has non-zero

[1] V_{z_0} is negative as the positive Z-axis direction is that opposed to the aircraft's displacement direction.

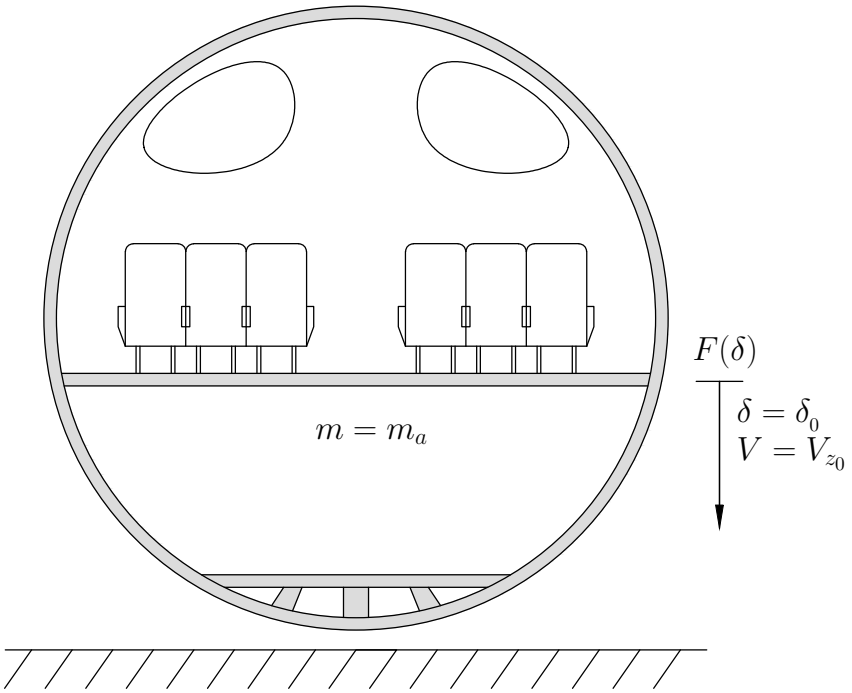

Figure 2.14: Initial configuration of idealized aircraft vertical drop test.

velocity and mass, its kinetic energy E_{k_0} at the initial time δ_0 is calculated by

$$E_{k_0} = \frac{1}{2} m_a {V_{z_0}}^2 . \tag{2.1}$$

This energy is absorbed by different components until the fuselage stops, when $E_{k_f} = 0$. The force $F(\delta)$ required to decelerate the system is given by Newton's Second Law,

$$F(\delta) = m_a a , \tag{2.2}$$

where a is the acceleration of the aircraft at each instant. Moreover, the energy absorbed during a small time increment $\Delta\delta$ can be obtained by multiplying $\Delta\delta$ and the average force during this period, as shown in figure 2.15. If the force is integrated along the whole crushing distance δ as

$$E_a = \int F \, d\delta , \tag{2.3}$$

the resulting value matches the energy absorbed by the system and the area under the aforementioned force-displacement curve. In this idealized scenario, all the kinetic energy is dissipated by material plasticity and failure, thus $E_{k_0} = E_a$. However, real crash cases also exhibit energy dissipation by other processes as friction, heat or material failure.

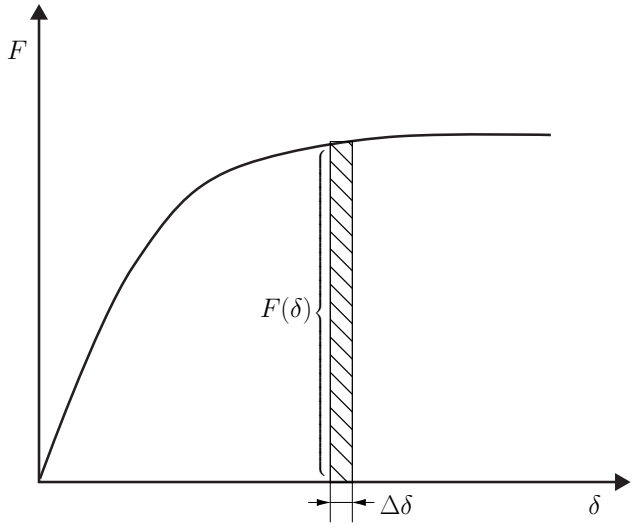

Figure 2.15: Energy absorption under force-displacement curve.

This is also true for impact studies on a coupon basis, as is the case of collapsible impact energy absorbers. The ideal energy absorber is defined as one that offers a constant crushing resistance and thus also a constant deceleration [119]. However, real life energy absorbers exhibit two different force profiles in terms of shape, as shown in figures 2.16a and 2.16b. Type I profiles are characterized by a constant increase in force until it reaches a plateau (figure 2.16a), while those from type II offer an initial peak force value followed by a descending curve. Another significant difference between them was found by Calladine [120] and Booth et al. [121], indicating that type II profiles are more sensible to impact speeds, thus requiring shorter crushing strokes as impact velocity increases.

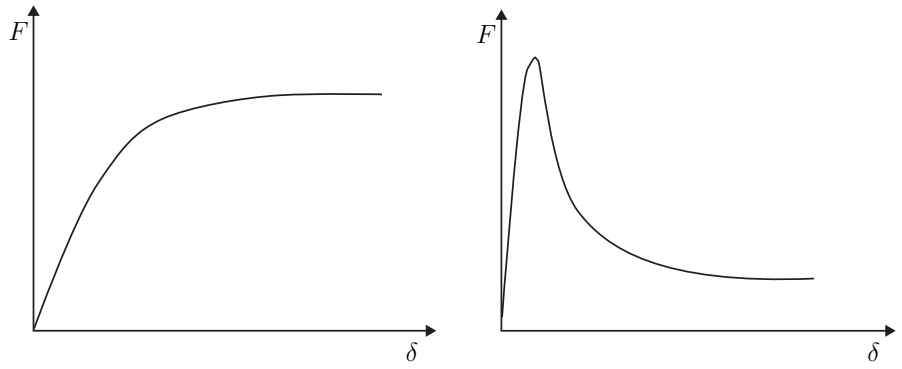

(a) Type I profile. **(b)** Type II profile.

Figure 2.16: Idealized energy absorbing profiles.

2.1.4.3 Data filtering

Whether data is obtained from experiments or simulations, it must undergo a thorough examination to identify any inaccurate or misleading information. When experimental data is acquired, electrical anomalies can generate spurious pulses even after filters are applied, while data that over-ranges the amplifiers can lead to underestimation of the highest acceleration pulses. Moreover, in complex structures such as those of aircrafts and automobiles, the superposition of each component's own mode of oscillation yields acceleration trends where the fundamental low-frequency pulse can be hard to identify.

The SAE recommendation practices [122] address different issues concerning the post-processing of acceleration data, including the usage of their own-defined channel frequency classes (CFC) for vehicle impacts. The CFC algorithms are 2-pole Butterworth filters applied forward and backwards in time to avoid phase shifts, resulting into a 4-pole variation. There are four available (SAE 60, SAE 180, SAE 600 and SAE 1000) where the identifying number approximately corresponds to 1.667 times the filter's cut-off frequency. Moreover, the document classifies the location types on a filter basis, where a SAE 60 is recommended for belt restraint loads and SAE 600 filters are chosen in component coupon-based analyses. An

interested reader is referred to [122] and [17] for a more in-depth explanation on filters and common data filtering practices.

2.1.4.4 Crashworthiness metrics

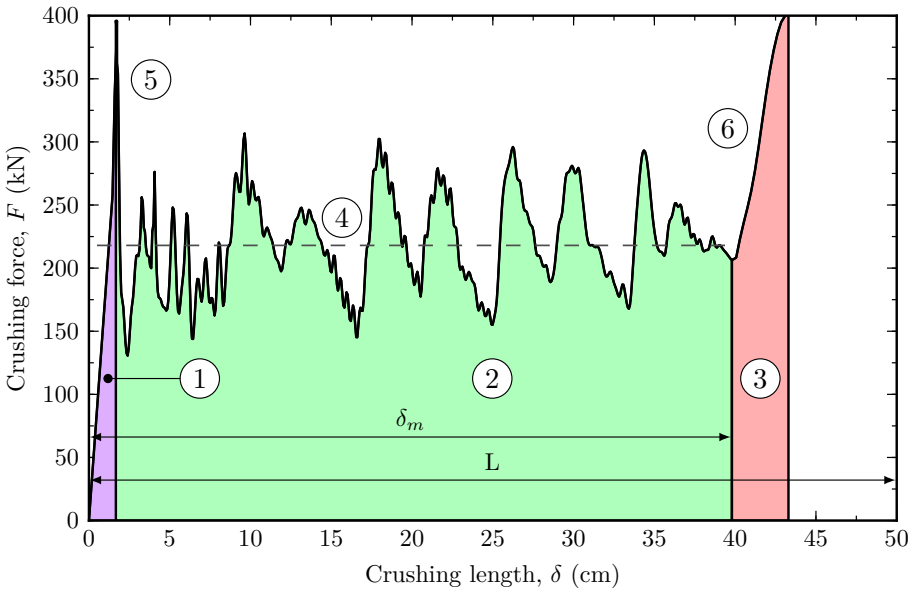

Figure 2.17: Force-displacement curve. Adapted from [123].

A further approximation for accurately understanding the force-displacement behavior of energy dissipating structures is provided by figure 2.17. The area under the curve is divided into three regions, corresponding to elastic, plastic and rebound (or bottoming-out) energies. If the structure is loaded along the elastic curve confining the area designed by (1), all the energy is given back when unloading occurs. However, after the crush initiation load (5) is surpassed, the specimen enters the post-buckling region (2), dissipating energy until exhausting the crush stroke δ_{m}. In this situation, the energy of the elastic and plastic regions ((1) and (2) respectively) is truly dissipated, whereas the area identified by (3) is given back when the force ceases. Thus, for truly assessing the **energy absorbed**

by the structure, equation (2.3) is modified to

$$E_{\mathrm{a}} = \int_{\delta_{\mathrm{m}}} F \, \mathrm{d}\delta \,, \tag{2.4}$$

The bottoming-out effect is identified in figure 2.17 by the curve segment designated by (6), implying that the energy absorbed only comprises the sum of the areas identified by (1) and (2).

For evaluating the efficiency of the device, the mass can also be taken into account in the **specific energy absorption** (SEA) ratio, defined as

$$SEA = \frac{E_{\mathrm{a}}}{m} \,. \tag{2.5}$$

This value is influenced by the absorber shape, material and collapse process undergone. Another factor that is usually taken into account is that of the **stroke efficiency** St_{e}, which provides a ratio between the crush stroke and the total length of the absorber as

$$St_{\mathrm{e}} = \frac{\delta_{\mathrm{m}}}{L} \,. \tag{2.6}$$

Typical values for axially loaded tubes range between 0.7 and 0.8, while $St_{\mathrm{e}} = 1$ is achieved with wire bending energy absorbers [119].

As seen in equation (2.2), forces and accelerations are directly proportional to each other by a factor of the mass. Thus, it is common in crashworthiness the evaluation force-related metrics. The **mean crushing force** P_{m}, defined as the mean value of the force throughout the crushing stroke, can be calculated by

$$P_{\mathrm{m}} = \frac{E_{\mathrm{a}}}{\delta_{\mathrm{m}}} \,, \tag{2.7}$$

being depicted in figure 2.17 by the dashed line (4). Meanwhile, the **peak force** value during the crash (identified as (5) in figure 2.17) is given by

$$P_{\mathrm{peak}} = \max \left\{ F(\delta) \, \forall \delta \in [0, \delta_m] \right\} \,. \tag{2.8}$$

This peak value is also critical in cascading collapse processes, as the progressive activation of each absorbing device is primarily controlled by this load. Moreover, the closer P_{m} and P_{peak} are, the nearer the response is to the ideal energy absorber.

2.1.4.5 Biometrics: passenger injury assessment

All the aforementioned metrics are an useful tool for efficiently designing a crashworthy absorber. However, in complex structures such as those from aircrafts or automobiles, the overall effectiveness from the combination of crashworthy elements is also assessed by biometrics. Anthropomorphic test devices are placed in the occupants seats while accelerometers record data for comparison with human tolerance limits. Human tolerance is defined as a condition of deceleration loading for which survival without major injuries is expected. A common manner of processing this is by monitoring the peak acceleration pulse, its duration and the direction in which the force actuates; later comparing this data with occupant whole-body tolerances. Table 2.1 offers the limit values of voluntary exposure for 20 millisecond pulses in the six main directions. It is important to comment the discrepancy between limits for different directions, as human tolerance to decelerations is three times higher in the back-chest direction than tailwards. Also note that for easier interpretation of data, accelerations are often divided by the value of gravity and offered as a multiple of g = 9.81 m/s^2.

Direction of acceleration		Occupant response	Tolerance
Headward	$+G_z$	Eyeballs down	25 g
Tailward	$-G_z$	Eyeballs up	15 g
Lateral right	$+G_y$	Eyeballs left	20 g
Lateral left	$-G_y$	Eyeballs right	20 g
Sternumward	$+G_x$	Eyeballs in	45 g
Spineward	$-G_x$	Eyeballs out	45 g

Table 2.1: Human tolerance limits. Adapted from [124].

Another method for whole-body injury evaluation was developed by A. Martin Eiband [125], and is based on plotting the acceleration pulses and their duration in logarithmic diagrams. These graphs are tailor-made for each direction and divided into a voluntary exposure area, and moderate and severe injury regions. Figure 2.18 shows a headward Eiband diagram and a graphic depiction of how acceleration pulses are added for its construction.

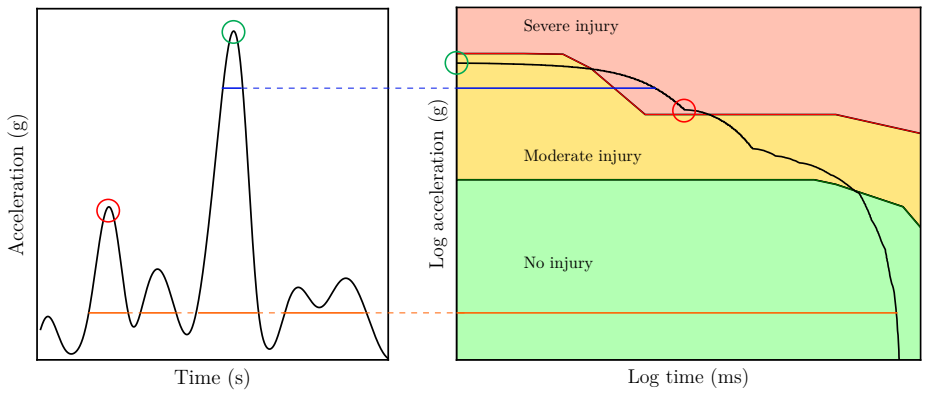

Figure 2.18: Acceleration integration and its representation in an Eiband diagram.

Complementing the whole-body tolerance limits, body part based criteria are also available, including head, spinal and leg injury criteria. Head injuries are identified attending to four criteria: peak deceleration, peak transmitted force, the severity index (SI) and the head injury criterion (HIC); all of which are extracted from the head's linear accelerations at its center of gravity, neglecting the angular component. The last two biometrics are evaluated as

$$\mathrm{SI} = \int_0^T a_\mathrm{h}\,\mathrm{d}t \tag{2.9}$$

and

$$\mathrm{HIC} = \max\left[\frac{1}{t_2 - t_1}\int_{t_1}^{t_2} a_\mathrm{h}(t)\,\mathrm{d}t\right]^n (t_2 - t_1)\,, \tag{2.10}$$

where a_h is the acceleration at the head, t_1 and t_2 any two points in time during the crash, T the complete deceleration duration and n is a weighting factor usually taking the value of $n = 2.5$ [126]. This HIC value is usually limited to 1000 for $t_2 - t_1 = 36\,ms$ and to 700 when $t_2 - t_1 = 15\,ms$ [127]. The human tolerance limits for short pulse durations of all four criteria were extracted by Desjardins et al. [124] from helmeted head impacts, and are presented in table 2.2.

Criterion	Human tolerance
Peak head acceleration (g)	150
Peak force level (kN)	6.7
Severity index	600
Head injury criterion	500

Table 2.2: Head injury criteria and tolerance limits. Adapted from [124].

2.2 Collapsible impact energy absorbers

One of the main objectives of this investigation is the development of crashworthy energy absorbers under axially-dominated loads for aircraft structures. The ultimate goal in using collapsible energy absorbers is that of converting the highest amount of kinetic energy into another form of energy [128]. When this process is reversible (pressure energy in a compressible fluid or elastic deformation in solids) injuries can originate during the release of the converted energy. However, if the energy is irreversibly converted, occupant injuries and cargo damage are reduced. Energy dissipation can be achieved by means of different mechanisms, including friction, shear, tension or torsion; while in this investigation, plastic dissipation through folding of metallic collapsible energy absorbers is studied. Several options to achieve this have been investigated across the years, with some solutions receiving more acceptance than other. Throughout this section, some of these designs are presented and briefly described.

2.2.1 Design of energy absorbers

Many energy absorbers have been designed, all seeking lightness and improvement on the crash responses of transport structures during impact scenarios. As Alghamdi [129] identified, collapsible energy absorbers' shape and thickness-to-weight ratios are similar independently of the scale difference between aircraft, automobile or train structures. Their energy dissipation profile is influenced by many factors, as the magnitude and application of the load, the strain-rate sensitivity of the materials or the deformation mode occurring [130]. However,

there exists a broad need of energy dissipating profiles depending on their ultimate service, leading to the development of several energy absorbers with characteristic behaviors under dynamic loads. Some of these configurations are now offered.

2.2.1.1 Tubes

Thin-walled crushable tubular structures are among the most common energy absorption devices used by the transport industries. They are featured as structural elements in helicopter subfloor structures [131], front deformation areas in cars [132, 133] and trains [134], and even as a roll-over protection structure on construction machinery [135]. Crushable tubes dissipate kinetic energy through plastic deformation, which can unfold under several modes depending on their cross-section shape, load direction, and the ratios between cross-sectional inertia, length and wall thickness [136].

The first studies on collapsible tubes are attributed to J. M. Alexander [137], after obtaining the approximate theoretical expression of the mean axial crushing force in thin-walled circular tubes back in the 1960s. Almost 20 years later, Wierzbicki and Abramowicz [138] developed the super folding element theory which investigated theoretical predictions for the axial mean crushing strength of rectangular tubes. In the experimental models from Abramowicz and Wierzbicki [139], Abramowicz and Jones [140], Pugsley [141], and Singace and Elsobky [142]; Alexander's tube was redesigned by shaping it with rectangular, circular and multi-corner sections; which was later axially crushed, loaded both statically and dynamically. They also carried out multiple studies dealing with the different collapse modes, obtaining an excellent resemblance between the theoretical predictions and the experimental results [143]. Hereafter, the most recurrent deformation modes for square and circular thin-walled tubes are presented.

- **Tube inversion.** During this axial collapse mode, the tube walls progressively turn inside out or outside in aided by a mold located on one end, as shown in figure 2.19a. The die's knuckle radius is critical for obtaining a stable inversion, as small radii lead to progressive buckling and values too

large could result in tube splitting [144]. With the right die, however, tube inversion occurs as in figure 2.19a, delivering stable crushing loads with constrained initial peak forces [145].

- **Tube splitting.** This is a special case of the previous mode in which the die's radius is too large for inversion to occur, leading to fractures in the tube along the longitudinal direction (see figure 2.19d). Ezra [119] also studied the behavior of the split ends, as they can be constrained or allowed to curl yielding higher energy dissipation values.

- **Lateral indentation.** This failure mode starts as a local denting under the applied load, followed by global buckling and bending until the tube reaches structural collapse (figure 2.19b). It is particularly interesting as automobile bumpers or boat structures can be subjected to point lateral loads [146], although only a limited section of a laterally indented tube undergoes plastic deformation.

- **Lateral flattening.** The lateral flattening of tubes between two plates dissipates a higher amount of energy than lateral indentation [147]. Many studies have sought an enhancement of this collapse mode, with Reddy and Reid [148] proving that lateral constraints can triplicate the energy dissipation values of free systems. Later on, Wu and Carney [149] showed that the configuration from figure 2.19c, with an elliptic cross-section and tension bracing, increases even more the energy dissipated by the system.

- **Axial crushing.** It is the most common energy dissipating method, primarily due to its high capabilities as an energy dissipation device [152]. When compared to other deformation modes, energy dissipation values can be up to ten times higher for the same tube, as proved by Reid [153]. Axial crushing in tubes can develop under three different modes, with the progressive crushing from figure 2.20a being inherent of metallic specimens; and the splaying and fragmentation mechanisms shown respectively in figures 2.20b and 2.20c characteristic of those made from composites [154].

  Moreover, progressive folding is further subdivided according to the collapse evolution; which is in turn determined by the geometry of the absorber

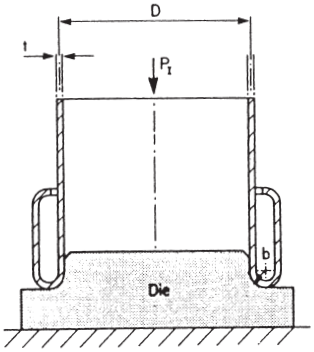

(a) Tube inversion. Taken from [150].

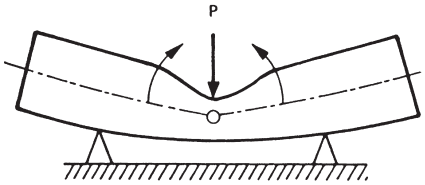

(b) Lateral indentation. Taken from [146].

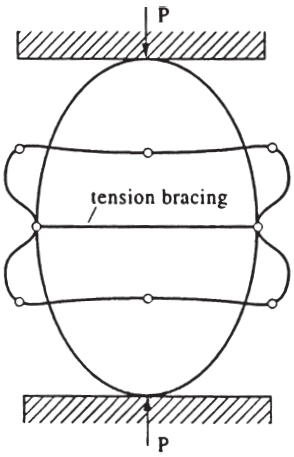

(c) Lateral flattening. Taken from [149].

(d) Tube splitting. Taken from [150].

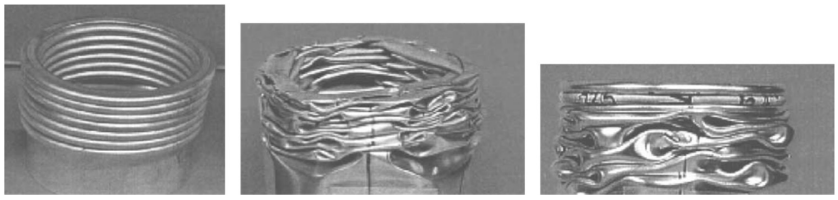

(e) Concertina, diamond and mixed axial modes. Taken from [151].

Figure 2.19: Tube deformation modes.

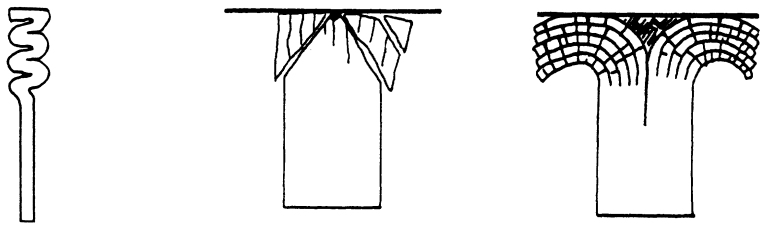

(a) Progressive folding. **(b)** Fragmentation. **(c)** Splaying.

Figure 2.20: Schematic diagrams of tube wall cross-sections for various axial crushing modes. Taken from [155].

and the load conditions. Andrews et al. [156] classified the progressive crushing of circular tubes under quasi-static loading into three categories, of which the concertina and diamond modes of deformation are the most recurrent. The concertina mode is axisymmetric and typical of tube with diameter-to-thickness ratios under 50 [151]. Diamond collapse modes are non-axisymmetric and exhibit specific energy absorption values slightly lower than in the concertina mode [156]. This mode occurs when the diameter-to-thickness ratio is over a hundred, with mixed collapse modes in the 50 to 100 range. The concertina, diamond and mixed modes are shown in figure 2.19e. Wang and Lu [157] found a fourth plastic deformation mode for impact speeds over 100 m/s, named "mushrooming" honoring the post-test shape resulting (see figure 2.21. Square-section thin-walled tubes experience different collapse modes than their circular relatives, although force-displacement trends are similar when undergoing progressive crushing. Section 2.2.2 provides a more in-detail study of square tubes and their response during axial loading, one of the main recurring topics analyzed throughout this investigation.

2.2.1.2 Multicorner columns

During the crushing of square tubes, the areas adjacent to the corners experience higher deformation values and, consequently, higher energy dissipation [158]. Therefore, a higher number of corners could results in enhanced energy absorption

Figure 2.21: Post-test mild steel samples. Impact velocities (left to right): 385 m/s, 277 m/s, 227 m/s, 173 m/s, 0 m/s Taken from [157].

without any additional material. Multicorner structures were first studied by Abramowicz and Wierzbicki [139] as a particular case of square thin-walled tubes in which the adjacent plates do not meet at a right angle. They were found to collapse under a generalized folding mechanism, obtained from the combination of the extensional and inextensional collapse of square tubes.

As described by Zhang and Huh [159], the angle between walls ultimately determines the deformation mode. Inextensional collapse is found for acute angles, extensional mode for values over 120 degrees, and mixed modes for any angle in between. The addition of corners to regular polygons does indeed improve the energy absorption until the 11-corner threshold, as energy dissipation efficiency is reduced in angles too obtuse [160]. New designs have overcome this limitation by including acute and obtuse angles in the same cross-section, leading to star or criss-cross sectioned elements [161]. Fan et al. [162] obtained specific energy absorption values nearly 50% higher with the 12- and 16-sided star sections from figure 2.22 compared to hexagons and octagons with equal sectional area.

2.2.1.3 Struts

The first usage of struts as crashworthiness devices is credited to Postlethwaite and Mills [163], when they analyzed the crushing characteristics of mild steel

Figure 2.22: Multicorner cross-sectioned tubes from Fan et al. [162].

struts for energy absorption purposes. As in the case of laterally loaded tubes, the plastic dissipation of the structure is limited to a hinge at the middle, thus yielding low energy absorbing values. More advanced configurations have been investigated, including the usage of kinks as in figure 2.23 to reduce initial peak forces [164] or the enforcement of lateral constraints for higher energy dissipation. They are featured as floor-supporting elements in several aircraft designs as well as aiding to maintain structural integrity in crash scenarios [165]. By designing struts with composite materials, Heimbs et al. [166] obtained an effective manner of dissipating energy through delamination processes, obtaining a wide range of trigger loads and stable crush forces.

2.2.1.4 Frusta and tapered tubes

Frusta elements and tapered tubes are modified thin-walled tubes that include one or more inclined faces with respect to the longitudinal axis [163]. Interest in these structures has arisen since their are less prone to global buckling and behave better under oblique loads [167]. Furthermore, energy is absorbed in a more regular manner and initial crushing loads are lower than in an equivalent straight tube, although frustra exhibit a slightly lower specific energy absorption performance [168]. Guler et al. [169]'s comparison of force-displacement curves of various straight and tapered specimens resulted in tapered circular tubes displaying the best response. Mamalis et al. [170] studied the crushing of frusta, concluding that their deformation mode is not only determined by the ratios between thickness, diameter and length, but also by the semi-apical angle. As

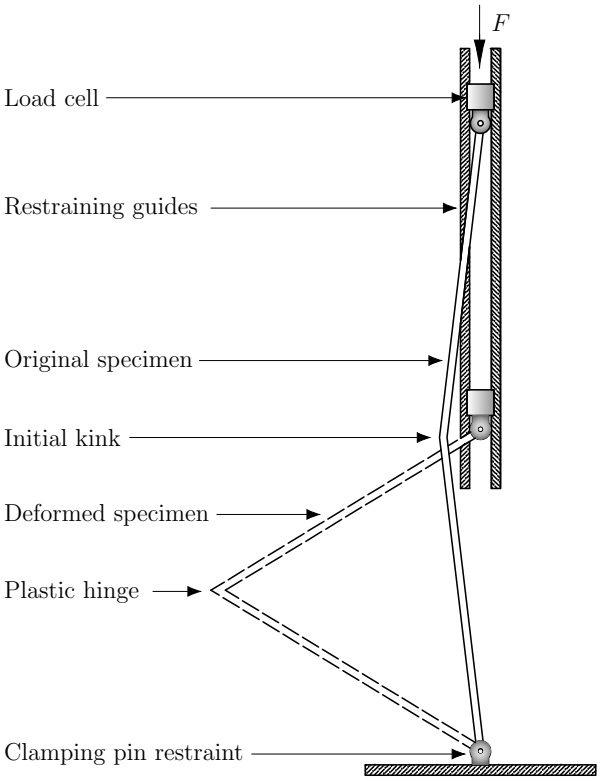

Figure 2.23: Strut with kink.

the diameter varies along the crushing stroke, the mixed collapse modes from figure 2.24 can occur, starting with a concertina mode only to change to diamond collapse after some folds. This also implies that the buckling load tends towards higher values as the crushing evolves, as folds have a larger diameter and more material undergoes plastic deformation.

2.2.1.5 Other collapsible impact energy absorbers designs

Several new thin-walled crushable absorbers have been investigated in the past decades. Novelties can originate from the cross-sectional shape [171], thickness

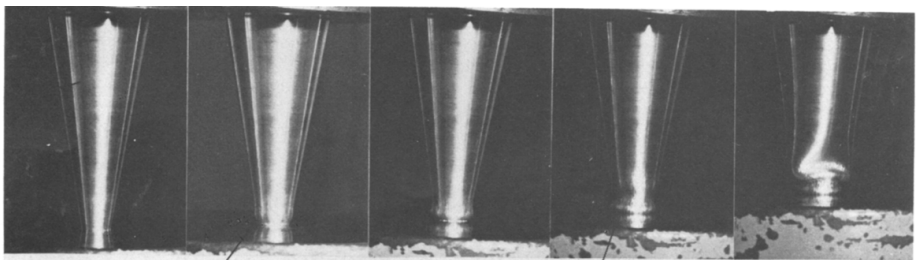

Figure 2.24: Frustum crushing evolution. Taken from [170].

gradation along any direction [172] and usage of stiffeners [173] or corrugations [174, 175]. Menouer et al. [176] devised a system that turns axial loading into a mixed axial-torsion load, obtaining a 47% increase in energy absorption. These more complex devices often are much harder to build, limiting their application in the mass-producing transport industries, although there are some examples as the Smart's corrugated tapered crash boxes from figure 2.25.

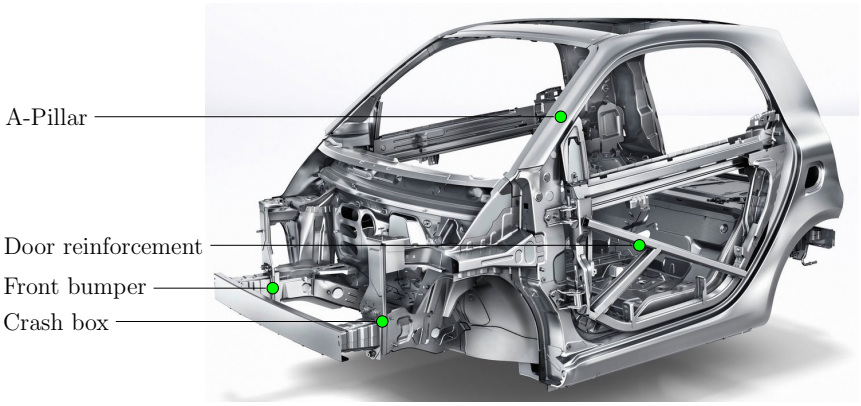

Figure 2.25: Smart ForTwo body-in-white. Adapted from [177].

2.2.2 Axial collapse of thin-walled square tubes

Thin-walled square tubes are regarded as excellent energy dissipating structures under axial loads. Their collapse patterns are different to the ones exhibited by circular tubes, albeit force-displacement responses are fairly similar between

them. In order to understand how a square tube behaves under axial loading, a detailed description of the collapse mechanisms, force-displacement curves and energy dissipation is now presented. The geometric dimensions are generalized, where C is the edge length, h is the wall thickness and L is the total length of the structure.

2.2.2.1 Idealized collapse mechanism[2]

Square tubes collapse can exhibit symmetric, asymmetric, extensional and non-compact collapse modes, mainly dependent on their edge-to-thickness ratio (C/h). According to Jones [178], the extensional mode from figure 2.26a appears on thick-walled specimens where $C/h < 7.5$, the symmetric mode in figure 2.26b is given if $C/h > 40.8$, and mixed or asymmetric modes results from any C/h values in-between (see figure 2.26c). Moreover, when square tubes are too thin ($C/h > 100$), the non-compact collapse from figure 2.26d or Euler-type global buckling can occur, harming the energy dissipation capabilities of the structure [179]. All of the three deformation modes can be explained with Wierzbicki and Abramowicz [138] inextensional and extensional primary collapse mechanisms from figures 2.27a and 2.27b respectively, with the former being the most recurrent.

The deformed quarter-section from figure 2.27a is characterized by the existence of two stationary horizontal hinges (EF and FG) and two inclined traveling hinges (KF and FQ). In this idealized mechanism, the angle between two adjacent plates $2\psi_0$ and the side length $C/2$ remain constant during the collapse.

Following figure 2.27a, the crushing distance δ, can be expressed as

$$\delta = 2H(1 - \cos\alpha)\,, \tag{2.11}$$

where $2H$ is the initial height of the element and α the angle between LR and LG. As for the horizontal displacement, S, it is defined as

$$S = H\sin\alpha\,. \tag{2.12}$$

[2]The idealized mechanism here described has been adapted from the versions offered by Wierzbicki and Abramowicz [138] and Jones [178]. Images, notation and other subtleties have been slightly adapted from the originals to improve clarity for the reader in the context of this document.

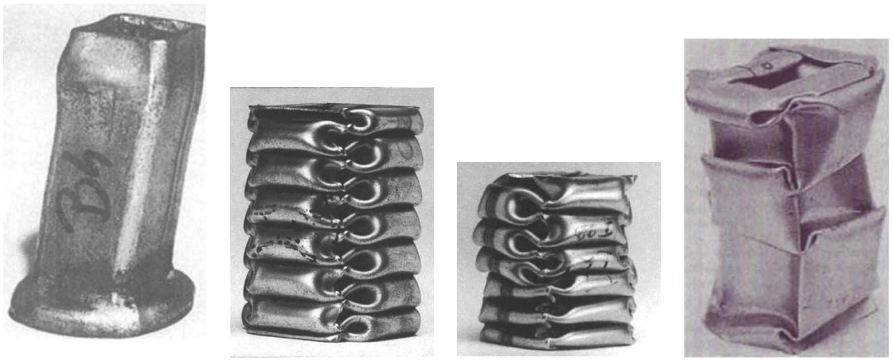

(a) Extensional mode. **(b)** Inextensional symmetric mode. **(c)** Asymmetric mixed mode. **(d)** Non-compact mode.

Figure 2.26: Axial progressive deformation modes of square tubes. Taken from [150, 178].

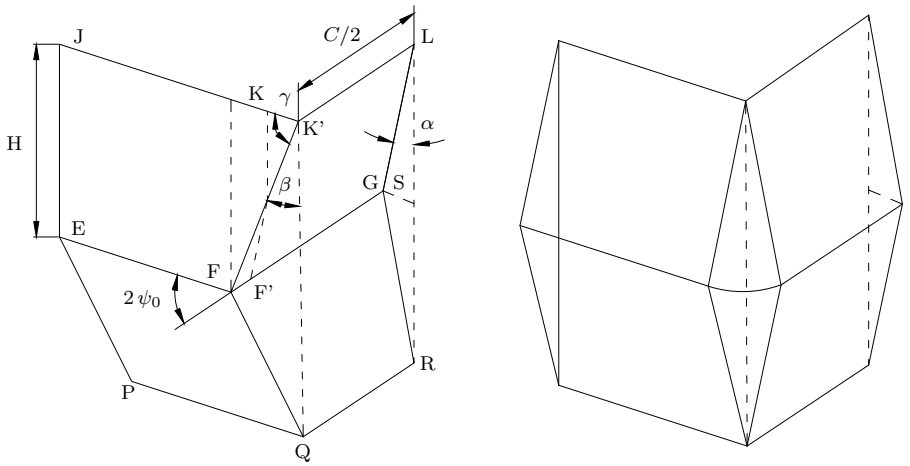

(a) Inextensional folding mechanism (type I).

(b) Extensional folding mechanism (type II).

Figure 2.27: Collapse elements for thin-walled square tubes.

The two other angles shown in figure 2.27a, γ and β, are related as follows:

$$\tan\gamma = \frac{\tan\psi_0}{\sin\alpha}, \quad \tan\beta = \frac{\tan\alpha}{\sin\psi_0}\,. \tag{2.13}$$

The crushing vertical velocity is obtained by differentiating equation (2.11), yielding

$$\dot{\delta} = 2H\,\dot{\alpha}\,\sin\alpha\,, \tag{2.14}$$

while the horizontal component of the velocity at point G is

$$V = \dot{S} = H\,\dot{\alpha}\,\cos\alpha\,. \tag{2.15}$$

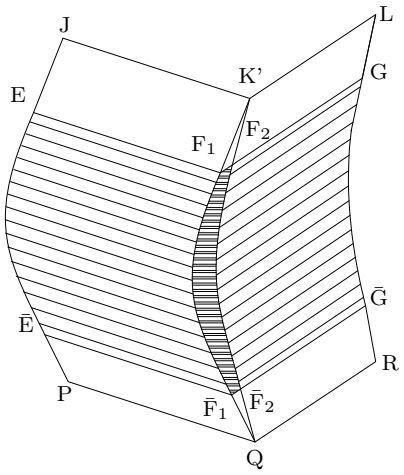

Figure 2.28: Realistic and kinematically admissible type I folding. Adapted from [138].

However, the deformation evolution from figure 2.27a is idealized, showing hinges with infinite curvature which would absorb an infinite amount of energy. The fully consistent and realistic collapse from figure 2.28 shows each plastic hinge influencing a surrounding shaded area, with all four deforming sections connected by a toroidal shell. As the hinge travels it moves from the zero Gaussian curvature of a cylindrical shell into the non-zero curvature toroidal shell delimited by the edges connecting vertices $\mathrm{F}_1 - \mathrm{F}_2 - \bar{\mathrm{F}}_2 - \bar{\mathrm{F}}_1$ in figure 2.28, leading to in-plane stretching [180].

2.2.2.2 Energy dissipation

Computing the energy dissipated by the complete mechanism entails obtaining the quantity absorbed by each of the three types of plastic zones. Traveling hinges can be analyzed by considering the bent strip from figure 2.29. Calculating the energy required to move it a distance Δs entails dividing the process into three stages. Section AB is initially curved, and the energy required for unbending can be expressed as

$$W_{AB} = \overline{AB}\frac{1}{r}M_p = M_{\mathrm{p}}(\pi - \beta)\,, \tag{2.16}$$

with M_{p} being the fully plastic bending moment. Segment BC, however, is first bent and then unbent, doubling the amount of energy as

$$W_{BC} = 2\overline{BC}\frac{1}{r}M_p\,. \tag{2.17}$$

The last segment is equally calculated as

$$W_{CD} = \overline{CD}\frac{1}{r}M_p\,. \tag{2.18}$$

Therefore, the final energy for this hinge traveling a distance Δs is

$$\begin{aligned} W &= W_{AB} + W_{BC} + W_{CD} \\ &= (\overline{AB} + 2\overline{BC} + \overline{CD})\frac{1}{r}M_{\mathrm{p}} \\ &= 2\frac{1}{r}M_{\mathrm{p}}\Delta s\,. \end{aligned} \tag{2.19}$$

For calculating the continuous deformation of a shell over the toroidal surface (figure 2.30), a local coordinate system $[\theta, \phi]$ is defined, where θ is the meridional coordinate and ϕ is the circumferential.

Minding the collapse mechanism, the angles θ and ϕ are limited by

$$\frac{\pi}{2} - \phi \leqslant \theta \leqslant \frac{\pi}{2} + \phi\,, \tag{2.20}$$

$$-\beta \leqslant \phi \leqslant \beta \tag{2.21}$$

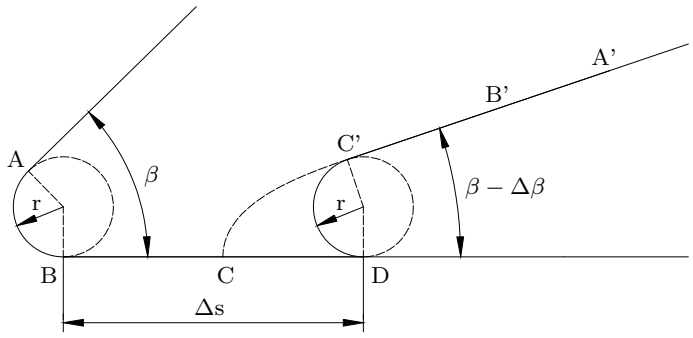

Figure 2.29: Strip resembling traveling hinge.

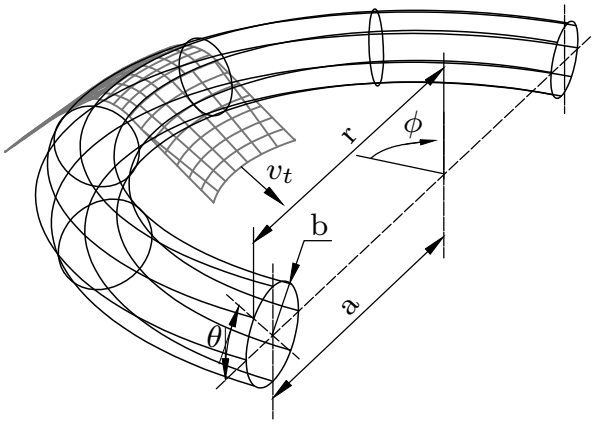

Figure 2.30: Shell deformation over toroidal surface.

while the distance r in figure 2.30 is defined by

$$r = b\cos\theta + a\,. \tag{2.22}$$

When the shell is forced to pass over the toroid, the circumferential strain on the shell is proportional to the tangential velocity v_t, defined as

$$v_\mathrm{t} = \frac{\dot{S}}{\tan\psi_0} = \frac{H\,\dot{\alpha}\,\cos\alpha}{\tan\psi_0}\,. \tag{2.23}$$

yielding a circumferential strain of

$$\dot{\varepsilon}_\phi = \frac{v_\mathrm{t}\sin\theta}{r} = \frac{H\,\dot{\alpha}\,\cos\alpha}{\tan\psi_0}\,\frac{\sin\theta}{b\cos\theta + a}\,, \tag{2.24}$$

In the toroidal shell, plastic flow is representative in the ϕ component, as the energy from the circumferential bending equals zero [138]. Considering a membrane force $N_0 = \sigma_0 h$, where σ_0 is the plastic stress, the plastic energy dissipation rate is

$$\dot{W}_1 = \int_S N_0 \dot{\varepsilon}_\phi \, \mathrm{d}s = \int N_0 \dot{\varepsilon}_\phi r \, \mathrm{d}\phi b \, \mathrm{d}\theta \,. \tag{2.25}$$

Substituting equations (2.22) to (2.24) into equation (2.25) yields

$$\begin{aligned} \dot{W}_1 =& 4N_0 \, bH \frac{\pi}{(\pi - 2\psi_0)\tan\psi_0} + \\ & \cos\alpha \left[\cos\phi_0 - \cos\left(\phi_0 + \frac{\pi - 2\phi_0}{\pi}\beta \right) \right] \dot{\alpha} \,, \end{aligned} \tag{2.26}$$

which after integration with respect to α gives

$$W_1 = 4N_0 bH \, \mathrm{I}_1(\psi_0) = 16 M_0 \frac{Hb}{h} \, \mathrm{I}_1(\psi_0) \,, \tag{2.27}$$

with $M_0 = 1/4\sigma_0 h^2$, and where

$$\begin{aligned} \mathrm{I}_1(\psi_0) =& \frac{\pi}{(\pi - 2\psi_0)\tan\psi_0} \int_0^{\frac{\pi}{2}} \cos\alpha \\ & \left\{ \sin\psi_0 \sin\left(\frac{\pi - 2\psi_0}{\pi} \right)\beta + \cos\psi_0 \left[1 - \cos\left(\frac{\pi - 2\psi_0}{\pi} \right)\beta \right] \right\} \, \mathrm{d}\alpha \,. \end{aligned} \tag{2.28}$$

Since β is a function of α, $\mathrm{I}_1(\psi_0)$ can be evaluated for different values of ψ_0. For square tubes, where $\psi_0 = \frac{\pi}{4}$, $\mathrm{I}_1\left(\frac{\pi}{4}\right) = 0.58$.

On the other hand, the plastic energy dissipation rate by the two hinges AC and CD is

$$\dot{W}_2 = 2M_0 \, c \, \dot{\alpha} \,, \tag{2.29}$$

which after integration with respect to α gives

$$W_2 = 2 \int_0^{\frac{\pi}{2}} M_0 \, c \, \mathrm{d}\alpha = \pi M_0 \, c \,. \tag{2.30}$$

Finally, the inclined hinges dissipation varies with their length, which in turn is dependent of the angle γ as

$$L = \frac{2H}{\sin\gamma}\,. \tag{2.31}$$

Thus, the dissipation rate of the traveling hinges is obtained as

$$\dot{W}_3 = 2M_0\,L\frac{v_\mathrm{t}}{b} = 4M_0\,\frac{H^2}{b}\frac{1}{\tan\psi_0}\frac{\cos\alpha}{\sin\gamma}\,, \tag{2.32}$$

which, after integration, has the form

$$W_3 = 4M_0\,\mathrm{I}_3(\psi_0)\frac{H^2}{b}\,, \tag{2.33}$$

where

$$\mathrm{I}_3(\psi_0) = \frac{1}{\tan\psi_0}\int_0^{\frac{\pi}{2}}\frac{\cos\alpha}{\sin\gamma}\,\mathrm{d}\alpha\,. \tag{2.34}$$

In the case of square tubes, $\mathrm{I}_3\left(\frac{\pi}{4}\right) = 1.11$

Now, all the energy dissipated through plastic deformation is equaled to the external work crushing the element. Considering that the rate of external work is defined by

$$\dot{W}_\mathrm{ext} = P\dot{\delta} = 2PH\,\dot{\alpha}\,\sin\alpha\,, \tag{2.35}$$

where P represents the instantaneous crushing load. The integration of $\dot{W}_\mathrm{ext}$ yields

$$W_\mathrm{ext} = 2PH\,. \tag{2.36}$$

If P_m is defined as the average crushing load, the work balance then requires that

$$2P_\mathrm{m}\,H = W_1 + W_2 + W_3\,. \tag{2.37}$$

Now, substituting equations (2.27), (2.30) and (2.34) in equation (2.36) leads to

$$\frac{P_\mathrm{m}}{M_0} = A_1\frac{b}{h} + A_2\frac{c}{H} + A_3\frac{H}{b}\,, \tag{2.38}$$

where the values of A_1, A_2 and A_3 are known by the type of problem.

It can be reasonably assumed that the collapse mechanism unraveling is the one that requires the lowest possible value of P_{m}. Thus, by minimizing the average crushing load with respect to both H and b as

$$\frac{\partial P_{\mathrm{m}}}{\partial H} = 0, \quad \frac{\partial P_{\mathrm{m}}}{\partial b} = 0 \tag{2.39}$$

the following solutions are obtained:

$$b = \sqrt[3]{\frac{A_2 A_3}{A_1^2}}\,\sqrt[3]{C h^2}\,, \tag{2.40}$$

$$H = \sqrt[3]{\frac{A_2^2}{A_1 A_3}}\,\sqrt[3]{C^2 h}\,. \tag{2.41}$$

Introducing the solutions from equations (2.40) and (2.41) in equation (2.38), we obtain

$$\frac{P_{\mathrm{m}}}{M_0} = 3\,\sqrt[3]{A_1 A_2 A_3}\,\sqrt[3]{\frac{C}{h}}\,. \tag{2.42}$$

A closer examination of equation (2.42) shows how each of the three mechanisms equally contributes to the energy dissipation of the system. Two thirds of the energy are dissipated by the stationary and moving hinge lines, while the remaining is attributed to the small extensional deformations; independently of the values of the coefficients A_i.

In a rectangular section of dimensions $c_1 \times c_2$, $C = \dfrac{1}{2}(c_1 + c_2)$, the coefficients from equations (2.28) and (2.34) for an angle $\psi_0 = \pi/4$ take the values of $\mathrm{I}_1 = 0.58$ and $\mathrm{I}_3 = 1.11$. Given that the section is composed by four corners, the energies from equations (2.27), (2.30) and (2.34) should be multiplied by four. Moreover, considering clamped boundary conditions on the upper and lower ends, more hinges are formed, doubling the value of W_2 in equation (2.30). The energy balance in this case reads

$$2HP_{\mathrm{m}} = M_0 \left(64\,\mathrm{I}_1 \frac{BH}{h} + 8 + 16\,\mathrm{I}_3 \frac{H^2}{b} \right). \tag{2.43}$$

Comparing equations (2.38) and (2.43), the values of the A_i coefficients are

$$A_1 = 32\,\mathrm{I}_1 = 18.56\,, \tag{2.44}$$

$$A_2 = 4\pi\,, \tag{2.45}$$

$$A_3 = 8\,\mathrm{I}_3 = 8.91\,, \tag{2.46}$$

which substituted in equation (2.42) give

$$\frac{P_\mathrm{m}}{M_0} = 38.27\sqrt[3]{\frac{C}{h}}\,. \tag{2.47}$$

However, if this equation is particularized for a square tube, where $c_1 = c_2 = C$, then

$$P_\mathrm{m} = 9.56\,\sigma_0\,h^{\frac{5}{3}}\,C^{\frac{1}{3}}\,. \tag{2.48}$$

The reason behind the exponent in $h^{\frac{5}{3}}$ is explained by the presence of both bending and stretching in the mechanism. In a bending-only deformation, P_m is proportional to h^2, while in a membrane-only deformation it is proportional to h [181]. Thus, in this mechanism, varying at a rate of $h^{\frac{5}{3}}$, the contribution of bending is twice that of stretching, consistent with the findings from equation (2.42).

2.2.2.3 Structural effectiveness and solidity ratio

Studies on crushing of thin-walled tubes usually relate their test results to the adimensional structural effectiveness and solidity ratio. The structural effectiveness, a non-dimensional crushing stress, is defined as

$$\eta = \frac{P_\mathrm{m}}{\sigma_0\,A_\mathrm{N}}\,, \tag{2.49}$$

where A_N is the net cross-sectional area of the tube, taking the values of $A_\mathrm{N} = 4hC$ for square tubes. On the other hand, the solidity ratio is

$$\phi = \frac{A_\mathrm{N}}{A_\mathrm{E}}\,, \tag{2.50}$$

with $A_{\mathrm{E}} = C^2$, representing the area enclosed by the tube's cross-section.

Introducing this two parameters in equation (2.48) leads to

$$\eta = 0.948\,\phi^{\frac{2}{3}}\,. \tag{2.51}$$

This equation reveals that thin-walled tubes behave equally regardless of their aspect ratio, as experimentally observed by Aya and Takahashi [182]. Figure 2.31 shows a comparison between this theoretical model, the empirical approximation by Magee and Thornton [183] ($\eta = 1.4\,\phi^{0.8}$), and experimental results from Magee and Thornton [183], Macaulay and Redwood [184], and Dewalt and Herbein [185].

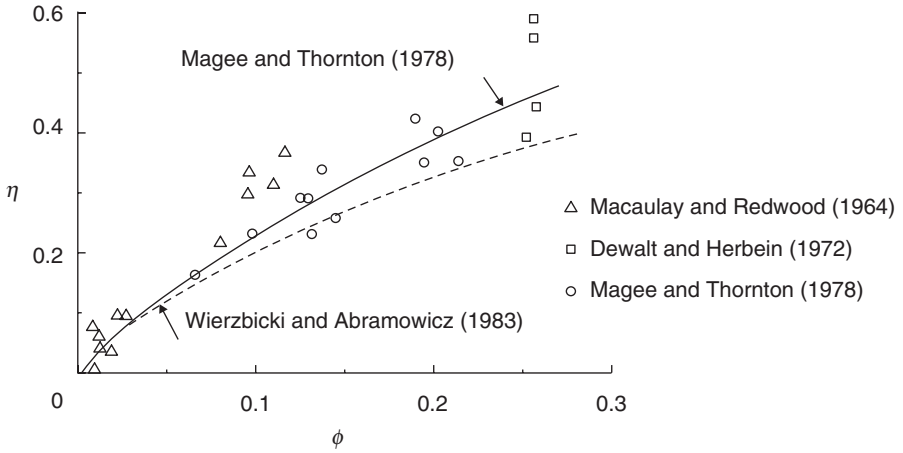

Figure 2.31: Theoretical and experimental comparison of square and rectangular tubes. Adapted from [183].

The theoretical deformation mode described constitutes a trustworthy prediction for the behavior of square-sectioned tubes. However, as research deepened into this field, adjustments have been proposed for even more accurate predictions. To begin with, the effective crushing distance δ_{m} is, in practice, smaller than $2H$. Abramowicz and Jones [140] showed that

$$\frac{\delta_{\mathrm{m}}}{H} = 0.73\,, \tag{2.52}$$

modifying equations (2.47) and (2.51) to

$$\frac{P_{\mathrm{m}}}{M_0} = 52.42 \sqrt[3]{\frac{C}{h}} \tag{2.53}$$

and

$$\eta = 1.3\,\phi^{\frac{2}{3}}\,. \tag{2.54}$$

Another model enhancement highly significant for this research is the effect of dynamic loading. Abramowicz and Jones [186] approximated the value of the strain-rate of a tube impacted at a initial velocity V_0 by

$$\dot{\varepsilon} = 0.33\frac{V_0}{C}\,, \tag{2.55}$$

which added to the empirical Cowper-Symonds uniaxial constitutive equation [187]

$$\begin{aligned} \sigma_0^d &= \sigma_0 \left[1 + \left(\frac{\dot{\varepsilon}}{D}^{\frac{1}{q}}\right)\right] \\ &= \sigma_0 \left[1 + \left(\frac{0.33\,V_0}{CD}^{\frac{1}{q}}\right)\right]\,, \end{aligned} \tag{2.56}$$

where σ_0^d is the strain-rate sensitive yield stress, and D and q are the Cowper-Symonds model parameters.

Finally, merging equations (2.53) and (2.54) and equation (2.56) gives

$$\frac{P_{\mathrm{m}}}{M_0} = 52.42\sqrt[3]{\frac{C}{h}}\left[1 + \left(\frac{0.33\,V_0}{CD}^{\frac{1}{q}}\right)\right] \tag{2.57}$$

and

$$\eta = 1.3\phi^{\frac{2}{3}}\left[1 + \left(\frac{0.33\,V_0}{CD}^{\frac{1}{q}}\right)\right]\,. \tag{2.58}$$

Impact speed not only affects the energy dissipation, but can also change the collapse mode undergone by the tube. Abramowicz and Jones showed that there is a critical length L_{cr} after which the tube undergoes global bending instead of

progressive deformation [143]. This length is influenced by material properties, the tube's dimensions and the initial velocity at which the specimen is struck [188]. To ensure progressive folding during the dynamic axial loading of square tubes, Abramowicz and Jones [143] stated that L should comply with

$$\left(\frac{L}{C}\right)_{\text{cr}} < 3.423\, exp\left(0.04\frac{C}{h}\right); \tag{2.59}$$

while specimens with

$$3.423\, exp\left(0.08\frac{C}{h}\right) \leqslant \left(\frac{L}{C}\right)_{\text{cr}} < 2.453\, exp\left(0.04\frac{C}{h}\right) \tag{2.60}$$

are on the transition are from progressive collapse to global bending. The latter is experienced when

$$\left(\frac{L}{C}\right)_{\text{cr}} \geqslant 2.453\, exp\left(0.08\frac{C}{h}\right). \tag{2.61}$$

2.2.2.4 Force-displacement curves

Understanding the behavior of thin-walled collapsible tube also requires analyzing the force displacement curves originated from the crushing process. The representative graph from an axially compressed aluminum thin-walled tube is presented in figure 2.32. The graph is characterized by an initial peak force, corresponding to the initial triggering load required to start the crushing process. After that, as progressive collapse initiates, its value lowers rapidly, waving periodically around the mean crushing force. Slightly higher values are found every $2H$ distance, corresponding with the initiation of a new fold development.

As presented in section 2.1.4.2, the energy absorption capabilities of an absorber can be assessed by the area under the force-displacement curve. Ideally, the tube would crush under a constant force and protecting occupants or other structures from sudden acceleration peaks. For enhancing the energy absorption capabilities of a tube without modifying its geometrical properties, authors have experimented with the addition of reinforcing cores [129], proving to be an effective solution as hereafter described.

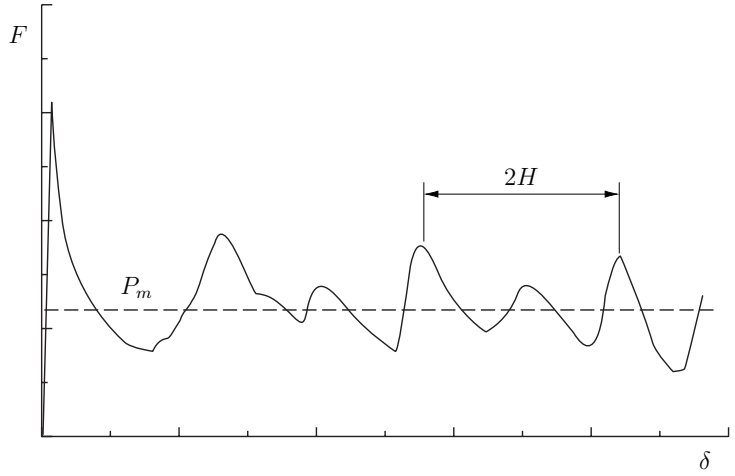

Figure 2.32: Force-displacement evolution of aluminum square tube with $C = 100$ mm and $h = 2$ mm.

2.2.3 Hybrid energy absorbers

One of the main objectives of this research aims at developing an efficient and robust hybrid energy absorber (HEA) for axially-dominated loads. A HEA is a device composed of an outer structure and a inner core, improving the overall crashworthiness performance of the original specimen while maintaining a low mass [167]. Thin-walled metallic tubes are of common usage when designing crushable energy absorbers, usually working as the confining structure. Steel and aluminum are common given their ductility and high energy absorption capabilities. Despite their brittle nature, composite tubes [189] or metal-composite combined tubes [190] have also delivered outstanding crashworthiness results.

As for the inner reinforcement, many materials and designs have been explored over the last years, including cork [191–193], wood [194], fiber-reinforced polymers (FRPs) [155, 195], metals [196], and foams of various natures [197–201]. In the same way that architectural bracing changes the buckling modes of a steel beam by reducing its buckling length, the collapse process of metallic tubes is constrained

by these inner reinforcements. Compared with a hollow tube, HEAs normally provide a better crush response with higher specific energy absorption and less tendency to global buckling [202]. This improvement is attributed to the shorter fold wavelength as it is constrained by the core and the interfacial frictional dissipation between the components [203, 204]. Consequently, higher values of the total absorbed energy are reached, compared to the sum of the responses obtained from crushing all parts separately, this receiving the name of "interaction effect" [9, 205]. An example of this behavior is presented in the post-test sectional cuts from figure 2.33; where the hollow steel tube only develops one complete fold, compared to the three folds from a similar specimen filled with a honeycomb core.

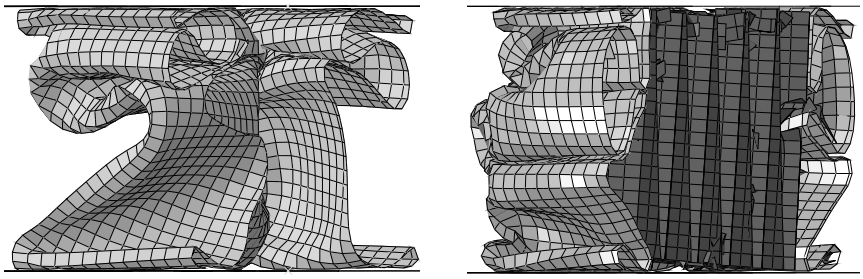

(a) Empty tube. **(b)** Honeycomb-reinforced tube.

Figure 2.33: Sectional cuts of two square steel tubes ($C/h = 50$).

2.2.3.1 Foam-filled tubes

The first studies on hybrid components are attributed to Reid and Reddy [206] and foam-filled thin-walled structures, complementing square and rectangular tubes with polyurethane foam for static and dynamic tests. Many investigations have been performed since to study the effect of foam-filling in different cross-sections, with all achieving improved crashworthiness performance by using foam as a filler material [207–209]. Polymeric and metallic foams are mainly characterized by their cell microstructure and the cell density of the material [210]. Crushing cells inside foam initially deform by bending and stretching, followed by buckling and tearing after the post-yield stage [211]. Thus, foams with small and regular cells

exhibit higher crushing resistance and energy dissipation than those larger and more irregular [212, 213].

A foam's cell density is usually given by the foam relative density, whose increase leads to a increase in bulk material within the foam and the consequent gain in crushing strength [214]. Moreover, as proved by Yi et al. [215], foams with high relative densities are more sensitive to strain-rate variations, a significant factor in all foam materials. Although still not clear, this distinctive strain-rate sensitivity has been attributed to the material rate-dependent behavior [216], micro-inertia effects of the cell walls [217], pressure built inside the cells as crushing initiates [218], and shock-wave effects under high impact loads [219].

Considering equal tubes, the HEAs response is mainly defined by the foam's relative density. As this value increases, so do the specific energy absorption, the number of folds developed, and the critical length for global buckling [208]. Hanssen et al. [207] also proved that the original deformation mode can be altered towards a more effective crushing process, as circular tubes collapsing under diamond mode swerved to concertina after a certain foam density. However, as relative foam densities surpass the 200 kg/m^3 threshold, undesired effects may arise. Reid et al. [179] proved that square tubes filled with polyurethane foams of over 320 kg/m^3 were more prone to global bending, as there was an increase in the force required to initiate collapse. For the same foams, Onsalung et al. [220] and Thornton et al. [221] showed that the HEAs specific energy absorption decreased when densities were over 200 kg/m^3 and 220 kg/m^3 respectively, suggesting the existence of a value for optimum performance neighboring that range.

Nowadays, foam-filled tube studies have drawn their focus towards the usage of the functionally graded foams (FGFs) [222], which have a variable density along the axial or longitudinal direction. Gupta and Ricci [223] introduced functionally graded foams with an also variable volume fraction, reducing non-uniform stress distributions along the foam and triplicating the energy dissipated by the HEA. Another trend deepened into the behavior of filler with negative Poisson ratios, as is the case of the auxenitic foam. Mohsenizadeh et al. [224] recently proved that thin-walled tubes filled with this material offer higher energy absorption values and a more stable deformation than empty or polyurethane-filled specimens.

2.2.3.2 Composite materials and honeycomb structures

Carruthers et al. [225] identified in 1998 the superb behavior of composite materials for crashworthiness enhancement, with special attention to fiber-reinforced polymers (FRPs). These composites, made from short or long fibers blended into a polymer matrix, are ever more used in the aircraft and automobile industries [226], accounting for up to 53% of the new Airbus A350 XWB weight [227, 228]. Great effort has been made to identify their unstable and non-uniform collapsing modes, as composite dissipate energy mostly through delamination, splaying, fracture and degradation processes [229–231]. Concerning the design of collapsible energy absorbers, this material has been used both as inner reinforcement [232] and as a tube [233], which also protects the metal from environmental inclemencies. Hull [154] studied the different failure modes of axially-loaded composite tubes, concluding that with chamfers and certain tube dimensions, the splay collapse from figure 2.34 could be obtained. By crushing absorbers under similar splaying modes, Ramakrishna and Hamada [234] obtained a major increase in SEA performance over metallic absorbers, with Carbon-PEEK components reaching 200 kJ/kg compared to aluminum's mere 30 kJ/kg.

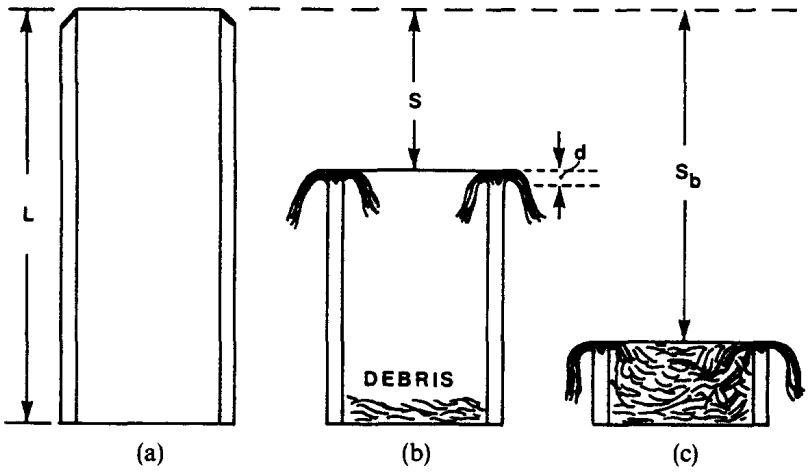

Figure 2.34: Axially-loaded composite tube splaying process. Taken from [154].

Since the crushing behavior is also influenced by other factors, including the initial impact velocity or the inner ply configuration [235], research also evolved towards complementing the existing thin-walled metallic tubes. Wierzbicki et al. [236] developed a theoretical model for assessing the energy absorption and mean crushing load of circular metallic tubes covered with glass fiber and epoxy resin. After correlating with experiments, composite-wrapped tubes showed that energy dissipation could triplicate that of conventional metallic specimens.

Honeycomb and other cellular structures have also proved to deliver excellent energy absorption capabilities as core reinforcements [239–242] , also earning a high consideration among the transport industry under various combinations of materials and shapes. Nomex® sandwich panels are used in several aircraft cabin components [243], aluminum honeycomb structures were developed for vehicle crash attenuating purposes [244], and Olympio and Gandhi [245] designed a honeycomb core for a morphing wing that resisted global strains ten times larger than the original material. Honeycomb structures offer excellent specific energy absorption values with minor strain-rate sensitivity (see figure 2.35), while maintaining a stable crushing load until the compaction phase. Santosa and Wierzbicki [200] proved that thin-walled tubes filled with aluminum honeycombs offered higher specific energy absorption than those filled with aluminum foam, suiting the weight-limited aircraft industry. Moreover, variations from the regular hexagonal cell have also been studied, showing that hourglass-like shapes [246] and square cells [247] also offer excellent crushing behavior. However, to the author's knowledge, no cell-shape crashworthiness optimization has been carried out so far, as they may be optimum patterns for improved energy dissipation. Furthermore, the capabilities of fiber-reinforced polymer honeycomb structures as a thin-walled tube inner reinforcement are yet to be tested, offering the opportunity of combining the high strength of composites with the solidity of honeycombs.

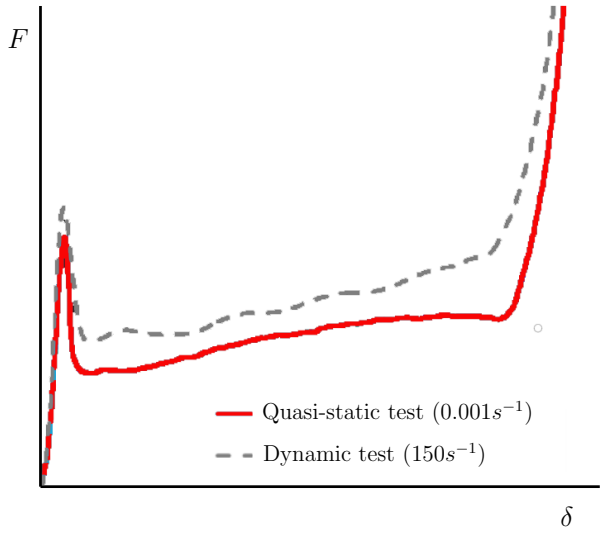

(a) Illustrative quasi-static and dynamic honeycomb behavior. Adapted from [237].

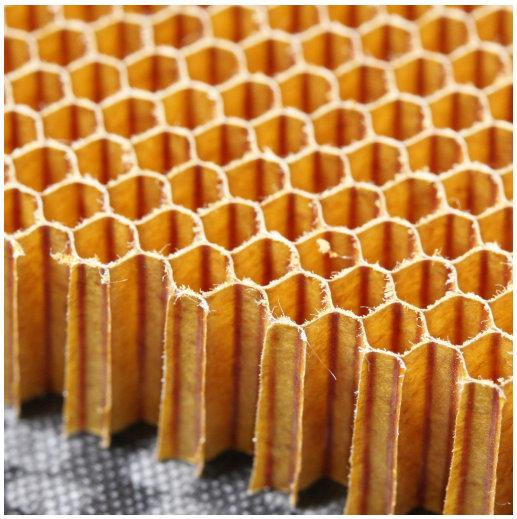

(b) Nomex® honeycomb panel. Taken from [238].

Figure 2.35: Nomex® honeycomb ($\rho = 48\,\mathrm{kg/m^3}$). Behavior and test article.

2.3 Finite element analysis of dynamic simulations

Finite element analyses have proved a powerful and effective tool for accurately predicting the behavior of structures under many boundary conditions and load situations, as shown in section 2.1.2. Moreover, these simulations are first-principle models, theoretically mimicking experimental results without requiring previous adjustments. For the execution of any finite element problem, the below steps are followed:

1. Development of a numerical model.
2. Formulation of the equations governing the model.
3. Discretization of the governing equations.
4. Solution of the equations.
5. Interpretation of the results obtained.

There exist two time-integration schemes for the solution of the equations governing the model, namely implicit and explicit. Implicit methods would produce prohibitively expensive calculation times and many convergence problems with the simulations here proposed. Thus, this section introduces the formulation, discretization and solution of the governing equations for explicit time integration in finite element analyses. Formulas are particularized for a central difference explicit method, the most frequent among finite element codes and featured in the ABAQUS/Explicit software used for this research.

2.3.1 Formulation of governing equations

The equations governing the mechanical behavior of a continuous body include the conservation of matter, momentum and energy, and the constitutive and strain-displacement equations. Much work has been required to couple these equations and laws, of which only the equations of motion are here described.

Any reader eager to discover the mysteries of this fascinating world is referred to [248] for an exhaustive clarification.

The discrete momentum equations of motion are obtained by combining the internal, external and inertial forces at each node. The general equation has the form:

$$\mathbf{Ma} + \mathbf{f}^{\text{int}} = \mathbf{f}^{\text{ext}} \,, \tag{2.62}$$

where $\mathbf{a}$ and $\mathbf{f}$ are column matrices of node's accelerations and forces, and $\mathbf{M}$ is the mass matrix for the unconstrained degrees of freedom. The matrix $\mathbf{f}^{\text{int}}$ refers to the stress inside the material arisen from resistance to deformation, whereas $\mathbf{f}^{\text{ext}}$ corresponds to the external forces applied. In the case of explicit methods, equation (2.62) is re-written as:

$$\mathbf{Ma}^n = \mathbf{f}^n = \mathbf{f}^{\text{ext}}\left(\mathbf{d}^n, t^n\right) - \mathbf{f}^{\text{int}}\left(\mathbf{d}^n, t^n\right) \,, \tag{2.63}$$

with the superscript n denotes the time step number for accelerations, forces, displacements ($\mathbf{d}$) and time t. Furthermore, equation (2.63) is subject to

$$g_I\left(\mathbf{d}^n\right) = 0 \,, \quad I = 1, \cdots, n_{\text{C}} \,, \tag{2.64}$$

where n_{C} is the number of boundary conditions g_I for nodal displacements and other conditions. It is important to note that equation (2.63) is formed by ordinary differential equations of second order in time, yielding a truncation error of second order in the displacements. Moreover, these equations have been discretized in space but not in time, earning the name of semidiscrete equations of motion.

In the case of Lagrangian meshes, the mass matrix $\mathbf{M}$ is only build once, as it remains constant throughout the simulation. This matrix is usually converted into a diagonal matrix, called the *lumped mass matrix*, which is used to directly obtain nodal accelerations from equation (2.63) as:

$$\mathbf{a}^n = \mathbf{M}^{-1}\mathbf{f}^n \tag{2.65}$$

2.3.2 Finite element discretization

After the numerical model is developed and the governing equations have been established, the model is discretized, covering this three procedures:

- **Mesh creation:** the structure is divided into smaller portion via meshing techniques. The global domain Ω is divided into smaller elements Ω_e so that $\Omega = \cup_e \Omega_e$.
- **Definition of shape functions:** solutions between the discrete nodal values are obtained through the interpolation functions N_I, usually taking the form of first or second order polynomials. In the updated Lagrangian formulation, they are expressed in terms of the material coordinates.
- **Mapping of elements:** reference elements are mapped onto the elements in the mesh.

Concerning the mesh definition, traditional methods include the Eulerian and Lagrangian approaches, where the former is characterized by fixed node coordinates and the latter has time-invariant nodes coincident with material points. Consequently, Eulerian meshes must be designed to confine the deformed structures, while their elements do not always coincide with geometrical features of the structure, with the losses in accuracy derived. On the other hand, Lagrangian meshes do follow boundary lines and surfaces, resulting in an easier computation. Moreover, constitutive equations in Langrangian formulation are evaluated at fixed material points all through the analysis, easing the evaluation of history-dependent materials; thus being featured in most finite element codes for the analysis of explicit nonlinear simulations.

In the numerical discretization of a structure, the Eulerian or spatial coordinates are denoted by $\mathbf{x}$, while the Lagrangian or material coordinates are represented by $\mathbf{X}$. At a time $t = 0$, $\mathbf{x} = \mathbf{X}$, but as the structure deforms, its motion is defined the function $\mathbf{\Phi}(\mathbf{X}, t)$ in which $\mathbf{X}$ and t are independent variables. The vector function $\mathbf{\Phi}$ yields the Eulerian location of each material point at a

time t by:

$$\mathbf{x} = \mathbf{\Phi}\left(\mathbf{X}, t\right) \tag{2.66}$$

from which the displacement $\mathbf{u}$ of a material point can be obtained as:

$$\mathbf{u}\left(\mathbf{X}, t\right) = \mathbf{\Phi}\left(\mathbf{X}, t\right) - \mathbf{X}\,. \tag{2.67}$$

Extrapolating this notation towards finite element approximations, the coordinates of the n_N nodes is denoted by $x_{iI} \equiv \mathbf{x}_I$, where i is the component number and I the node number. Thus, motion is approximated by:

$$\mathbf{x}\left(\mathbf{X}, t\right) = N_I\left(\mathbf{X}\right)\mathbf{x}_I\left(t\right)\,, \tag{2.68}$$

with $\mathbf{x}_I$ representing the position vector of node I. By combining equations (2.67) and (2.68), nodal displacements are expressed as:

$$\mathbf{u}_I\left(t\right) = \mathbf{x}_I\left(t\right) - \mathbf{X}_I\,, \tag{2.69}$$

while the displacement field is represented by:

$$\mathbf{u}\left(\mathbf{X}, t\right) = \mathbf{u}_I\left(t\right) N_I\left(\mathbf{X}\right)\,, \tag{2.70}$$

This definition can now be derived in time, yielding nodal velocities and accelerations as:

$$\mathbf{v}\left(\mathbf{X}, t\right) = \dot{\mathbf{u}}_I\left(t\right) N_I\left(\mathbf{X}\right) \tag{2.71}$$

and

$$\mathbf{a}\left(\mathbf{X}, t\right) = \ddot{\mathbf{u}}_I\left(t\right) N_I\left(\mathbf{X}\right)\,. \tag{2.72}$$

2.3.3 Solution methods

There exist different methods for solving equation (2.63), albeit the central difference integration featured in ABAQUS/Explicit is the most common of them for computational mechanics.

Let's consider a simulation with a total time t_E divided into $n = n_{TS}$ time steps, Δt^n. In an algorithm with a variable time step, featured in most codes, time increments are defined by:

$$\begin{aligned} \Delta t^{n+1/2} &= t^{n+1} - t^n \,, \\ t^{n+1/2} &= \frac{1}{2}\left(t^{n+1} + t^n\right) \,, \\ \Delta t^{n+} &= t^{n+1/2} - t^{n-1/2} \,, \end{aligned} \tag{2.73}$$

Thus, the central difference formula for the velocity is expressed as

$$\dot{\mathbf{d}}^{n+1/2} \equiv \mathbf{v}^{n+1/2} = \frac{\mathbf{d}^{\mathrm{n}+1} - \mathbf{d}^{\mathrm{n}}}{t^{n+1} - t^n} = \frac{1}{\Delta t^{n+1/2}}\left(\mathbf{d}^{\mathrm{n}+1} - \mathbf{d}^{\mathrm{n}}\right) \,. \tag{2.74}$$

By rearranging the terms in equation (2.74), it can be written as

$$\mathbf{d}^{n+1} = \mathbf{d}^n + \Delta t^{n+1/2}\mathbf{v}^{n+1/2} \,. \tag{2.75}$$

Since $\mathbf{v}^{n+1/2}$ can also be expressed by

$$\mathbf{v}^{n+1/2} = \mathbf{v}^{n-1/2} + \Delta t^n \mathbf{a}^n \,, \tag{2.76}$$

the acceleration matrix at the time step n is

$$\begin{aligned} \ddot{\mathbf{d}}^n \equiv \mathbf{a}^n &= \left(\frac{\mathbf{v}^{n+1/2} - \mathbf{v}^{n-1/2}}{t^{n+1/2} - t^{n-1/2}}\right) = \\ &= \frac{\Delta t^{n-1/2}\left(\mathbf{d}^{n+1} - \mathbf{d}^n\right) - \Delta t^{n+1/2}\left(\mathbf{d}^n - \mathbf{d}^{n-1}\right)}{\Delta t^{n+1/2}\Delta t^n \Delta t^{n-1/2}} \,, \end{aligned} \tag{2.77}$$

which is reduced to

$$\ddot{\mathbf{d}}^n \equiv \mathbf{a}^n = \frac{\left(\mathbf{d}^{n+1} - 2\mathbf{d}^n + \mathbf{d}^{n-1}\right)}{\left(\Delta t^n\right)^2} \tag{2.78}$$

when the time steps are equal.

For updating the nodal velocities and displacements, equation (2.63) is substituted into equation (2.76), yielding:

$$\mathbf{v}^{n+1/2} = \mathbf{v}^{n-1/2} + \Delta t^n \mathbf{M}^{-1}\mathbf{f}^n \,. \tag{2.79}$$

For explicit methods, the displacements $\mathbf{d}^n$ at the time step n are always known, while $\mathbf{f}^n$ is obtained by sequentially evaluating the strain-displacement and constitutive equations, and the external forces at the nodes. This information is required for obtaining $\mathbf{v}^{n+1/2}$ in equation (2.79), which can later determine $\mathbf{d}^{n+1}$ in equation (2.75). Thus, providing that the mass matrix $\mathbf{M}$ is in the diagonal form, nodal displacements and velocities can be determined without equation solving.

The implementation of such an explicit time integration code has been adapted from [248] and presented hereafter. For this example, velocities are updated in two substeps, enabling the evaluation of the energy balance at integer time steps.

The subroutine *getforce* is responsible for calculating the nodal forces. Nodal velocities and displacements of the element are gathered from the global arrays in step *a)*, strains and stresses are computed at each quadrature point in *ii* and *iii*, while the internal forces are evaluated in *iv*. Another remark is given about the numerical nature of this algorithm, from which first-order errors are expected for the approximation of the gradient. Under certain conditions, however, the gradient can be obtained with errors of second-order, as proved by Barbeiro [249].

Pseudo-code for central difference explicit time integration [248]

1. Initial conditions and initialization:
   set $\mathbf{v}^0$, $\boldsymbol{\sigma}^0$, and initial values of other material state variables;
   $\mathbf{d}^0 = 0, n = 0, t = 0$; compute $\mathbf{M}$
2. Call *getforce*
3. Compute accelerations $\mathbf{a}^n = \mathbf{M}^{-1}\mathbf{f}^n$
4. Time update: $t^{n+1} = t^n + \Delta t^{n+1/2}$, $t^{n+1/2} = \frac{1}{2}\left(t^{n+1} + t^n\right)$
5. First partial update of nodal velocities:
   $\mathbf{v}^{n+1/2} = \mathbf{v}^n + \left(t^{n+1/2} - t^n\right)\mathbf{a}^n$
6. Enforce velocity boundary conditions:
   if node I on Γ_{v_i} : $v_{iI}^{n+1/2} = \bar{v}_i\left(\mathbf{x}_I, t^{n+1/2}\right)$
7. Update nodal displacements $\mathbf{d}^{n+1} = \mathbf{d}^n + \Delta t^{n+1/2}\mathbf{v}^{n+1/2}$
8. Call *getforce*
9. Compute $\mathbf{a}^{n+1}$
10. Second partial update of velocities:
    $\mathbf{v}^{n+1} = \mathbf{v}^{n+1/2} + \left(t^{n+1} - t^{n+1/2}\right)\mathbf{a}^{n+1}$
11. Check energy balance at time step $n + 1$
12. Update counter: $n \leftarrow n + 1$
13. Output; if simulation not complete, go to 4.

Subroutine *getforce*

0. Initialization: $\mathbf{f}^n = 0\,, \Delta t_{\text{crit}} = \infty$
1. Compute global external forces $\mathbf{f}^{\text{ext},n}$
2. Loop over elements e
   a) Gather element nodal displacements and velocities
   b) $\mathbf{f}_e^{\text{int},n} = 0$
   c) Loop over quadrature points ξ_Q
      i. If $n = 0$, go to 4
      ii. Compute measures of deformation $\mathbf{D}^{n-1/2}\left(\xi_Q\right)\,, \mathbf{F}^n\left(\xi_Q\right)\,, \mathbf{E}^n\left(\xi_Q\right)$
      iii. Compute stress $\boldsymbol{\sigma}^n\left(\xi_Q\right)$, by constitutive equation
      iv. Update $\mathbf{f}_e^{\text{int},n}$ by corresponding equation
   d) Compute $\mathbf{f}_e^{\text{ext},n}$
   e) Evaluate $\mathbf{f}_e^n = \mathbf{f}_e^{\text{ext},n} - \mathbf{f}_e^{\text{int},n}$
   f) Compute $\Delta t^e{}_{\text{crit}}$, if $\Delta t^e{}_{\text{crit}} < \Delta t_{\text{crit}}$ then $\Delta t_{\text{crit}} = \Delta t^e{}_{\text{crit}}$
   g) Scatter $\mathbf{f}_e^n$ to global $\mathbf{f}^n$
3. $\Delta t = \alpha \Delta t_{\text{crit}}$

2.3.4 Stability and other remarks on explicit methods

The previous pseudo-code is not only easy to implement, but also inherits the expected robustness of explicit methods, rarely aborting by failure in the algorithm. However, one drawback hinders the usage of explicit algorithms, identified as *the conditional stability of explicit methods.* This condition construes that if the time step exceeds the critical or stable time step Δt_{crit}, the solution will continue to

grow endlessly. Remarks on the stability and other particularities of explicit time integration are now presented.

2.3.4.1 Stable time increment

The analysis of the stable time increment is crucial to evaluate the stability of the integrator for the linear equations of motion. Such values depend on the highest frequency of the linearized system $\omega_{\max}$ according to

$$\Delta t = \alpha \Delta t_{\text{crit}} \,, \qquad \Delta t_{\text{crit}} = \frac{2}{\omega_{\max}} \leqslant \min_{e,l} \frac{2}{\omega_I^e} = \min_e \frac{l_e}{c_e} \,, \tag{2.80}$$

where l_e and c_e respectively are the characteristic length and wavespeed of element e and α is the Courant number. This last factor is accountable for the instabilities derived from nonlinearities, usually ranging between $0.8 \leqslant \alpha \leqslant 0.98$ [250]. Another approach for evaluating the stability limit is that of relating it to the smallest element length in the model $l_{e,\min}$ and the stress wavespeed c_{d} by:

$$\Delta t_{\text{crit}} \approx \frac{l_{e,\min}}{c_{\text{d}}} \,. \tag{2.81}$$

In turn, this wavespeed is influenced by the material's density ρ, and Young modulus E [251]. Its value is obtained as:

$$c_{\text{d}} = \sqrt{\frac{E}{\rho}} \,, \tag{2.82}$$

which coupled with equation (2.80) results in:

$$\Delta t \leqslant \min \left\{ l_e \sqrt{\frac{\rho}{E}} \right\} \,, \tag{2.83}$$

from which is deduced that the value of Δt is reduced for stiffer and lighter materials or high mesh densities.

For the dynamic analysis of both energy absorbers and the fuselage drop test from , the magnitude order for Δt fluctuated around $\Delta t \approx 10^{-7}$. However, as the simulation progresses and elements undergo severe deformation, values for the stable time increment tends to decrease, even up to an order of magnitude.

2.3.4.2 Energy balance

Even if the integrator complies with equation (2.80), instabilities still may arise from other sources, such as the geometric stiffening identified by Belytschko [252]. In this case, a large overprediction of the nodal displacements could go unnoticed even after careful analysis of the results. However, such an instability would unsettle the model's energy balance, consequently violating the conservation of energy. For the central difference method, the internal and external energies are often integrated by low-order methods as:

$$W^{\text{int},n+1} = W^{\text{int},n} + \frac{1}{2}\Delta\mathbf{d}^T\left(\mathbf{f}^{\text{int},n} + \mathbf{f}^{\text{int},n+1}\right) \tag{2.84}$$

and

$$W^{\text{ext},n+1} = W^{\text{ext},n} + \frac{1}{2}\Delta\mathbf{d}^T\left(\mathbf{f}^{\text{ext},n} + \mathbf{f}^{\text{ext},n+1}\right)\,, \tag{2.85}$$

with $\Delta\mathbf{d} = \mathbf{d}^{n+1} - \mathbf{d}^n$. Lastly, by calculating the kinetic energy as

$$W^{\text{kin},n} = \frac{1}{2}\left(\mathbf{v}^n\right)^T\mathbf{M}\mathbf{v}^n\,, \tag{2.86}$$

the energy balance can be stated, following the form

$$W^{\text{kin}} + W^{\text{int}} - W^{\text{ext}} \leqslant \epsilon_w \max\left(W^{\text{kin}}, W^{\text{int}}, W^{\text{ext}}\right)\,, \tag{2.87}$$

where ϵ_w is a small tolerance in the order of 10^{-2}. This balance is recommended to be performed in subdomains if the number of nodes exceeds 10^5, treating the internal forces from adjacent subdomains as external forces for each subdomain.

Energy checks were frequently performed by the author to determine the level of accuracy provided by the ABAQUS/Explicit software. For the components developed in chapters 3 and 4, $\epsilon_w \leqslant 1.6\%$; while $\epsilon_w \leqslant 9\%$ for the fuselage simulations in chapters 5 and 6. However, this last value still abides by the boundaries for accepting as valid the numerical simulation [253].

2.3.4.3 Further enhancements for explicit methods

As the usage of explicit methods became widespread, efforts were drawn towards increasing their efficiency by means of increasing Δt. Three of the most common enhancements are now presented.

- **Mass scaling.** By using this procedure, masses of the stiffer elements are augmented as to increase Δt. This technique is useful for simulations in which high-frequency effects can be neglected, as mass scaling influences inertia effects as increasing loading rates would. As shown in equation (2.83), increasing the material density by γ_m leads to a time step $\sqrt{\gamma_m}$ times higher.
- **Time scaling.** This method is based on reducing the time scale of the process, and hence the number of time steps required. Loading rates must be enlarged accordingly, which can lead to flawed results if strain-rate sensitive materials are involved.
- **Mixed time integration.** This technique, also called *subcycling*, allows different time increments for individual sets of nodes within a model. By doing so, no stiff, small or light elements drag the calculation of those with a higher Δt. Early subcycling techniques were only stable for first-order systems [254], leading to instabilities in those of second-order [255]; although this setback had already been addressed before the end of the 90s [256, 257].

Regarding the usage of these techniques, the author encourages performing convergence tests to accurately determine the limit at which results diverge significantly. For the dynamic analyses computed throughout this research, mass and time scaling were discarded given the nature of the simulation and the usage of strain-rate sensitive materials. However, subcycling was used in the last stages of the investigation, when four hybrid energy absorbers were split into a separate subdomain and mesh with finer elements. This set was later subcycled, as its time increment was over ten times smaller than the non-subcycled model, yielding time gainings of over ten hours for the original 37-hour fuselage drop test simulation.

2.4 Optimization procedures

Efficiently addressing competing needs in the motor vehicle industry is often a trade-off between improving performance, reducing costs and enhancing safety. The detailed finite elements analyses of partial or full designs have proven effective for predicting crashworthiness metrics; ultimately calling for optimization techniques to produce structures with enhanced responses.

Yang et al. [258] showed in 1994 that direct coupling between finite element analyses and optimization algorithms was possible. In the scope of energy-absorbing structures, several authors have used this method to optimize the response of thin-walled tubes and other structures [259]. Some of those designs already studied include several hollow [260–262] and reinforced sections [263, 18], functionally-graded structures [264, 265] and multi-cell or honeycomb arrangements [266–268]. Crashworthiness optimization of components in the aircraft industry is now a reality, with studies on the post-buckling responses of structural panels, seat and restraint performance, or reinforced sub-floor structures. By means of example, Bisagni et al. [269] optimized the response of helicopter sub-floor components under crush force efficiency and specific energy absorption criteria, while Astori and Impari [270] also minimized injury levels by optimizing seat and sub-floor structures.

All through this investigation, the optimization of energy-absorbing structures relies on nonlinear finite element simulations. The devices are first enhanced on a coupon basis; being later on optimized as part of a full-scale fuselage section. In this last section on structural crashworthiness, the reader is offered a brief introduction to the field of optimization, later followed by a more in-depth explanation of surrogate-based meta-heuristic techniques as used by the author.

2.4.1 Optimization methods

Optimization processes are defined as the minimization or maximization of a given set of objective functions by choosing the input values for the variables

from within an allowed design space. Moreover, another set of given functions, the design constraints, need to perform between specified boundaries, otherwise rejecting the design. The final result is a set of elements obtained that best the function responses according to the criteria specified [271].

In general, any optimization problem can be written as:

$$\text{minimize} \quad f_1(\boldsymbol{x}), \cdots, f_i(\boldsymbol{x}), \cdots, f_l(\boldsymbol{x}), \quad \boldsymbol{x} = (x_1, \cdots, x_d)\,, \tag{2.88}$$

subject to the conditions:

$$\begin{aligned} h_j(\boldsymbol{x}) &= 0, (j = 1, 2, \cdots, J)\,, \\ g_k(\boldsymbol{x}) &\leqslant 0, (j = 1, 2, \cdots, K)\,, \end{aligned} \tag{2.89}$$

where $f_1(\boldsymbol{x}), \cdots, f_l(\boldsymbol{x})$ are the objective functions, h_j the equality constraints and g_k the inequality constraints. In the event of $l = 1$, the problem is single-objective, and the solution is a point. However, when $l \geqslant 2$, this becomes a multi-objective problem, which requires a different solving approach and results consist of a set of points. If no h_j or g_k exist in the problem, it is considered an unconstrained optimization, otherwise constrained.

To solve an optimization problem, several search and optimization algorithms are available, but each method's characteristics suit different types of problems. One major division can be made according to the usage of derivate information, yielding gradient-based and gradient-free methods. The first group is often regarded as highly efficient, although their robustness is compromised in functions with expensive derivative calculations, discontinuities or an intractable noise.

Other criteria also divide the procedures according to:

- **Path**
  - Trajectory-based: the initial and final points can be linked with a line or trajectory.
  - Population-based: use multiple agents that sketch out several paths.
- **Nature**

  - Deterministic: no randomness.
  - Stochastic: randomness.

- **Search capability**
  - Local: converge towards local optimum.
  - Global: search for global optima.

Different methods have been effectively used for the crashworthiness optimization of nonlinear finite element simulations. Gradient-based methods were the first employed [258], although the noisy responses yielded by these simulations hindered the computation of gradients [272] and led to premature convergence failures. The development of surrogate modeling and gradient-free optimization methods circumvented this limitations, as algorithms only requires information on the function's value; proving an effective alternative from traditional methods [273, 274].

2.4.2 Meta-heuristic optimization

According to Glover [275], all modern nature-inspired algorithms fall into the meta-heuristics group. The term originates from the Greek terms 'meta' (higher level) and 'heuristics' (discovery by trial and error); and they are regarded as a "master strategy that guides and modifies other heuristics to produce solutions beyond those that are normally generated in a quest for local optimality" [276]. Meta-heuristic methods yield fast and quality solutions in complex problems with high non-linearities and discontinuities, although convergence to the optimal solution cannot be guaranteed.

Two of the pivoting points for these algorithms are intensification and diversification. The diversification factor plays an important role in exploring the global design space, while intensification refers to focusing in a certain region when a promising solution is found [277]. The right combination of the aforementioned factors is critical for achieving global optimality.

Many metaheuristic algorithms exist, both in their original and in combination with other heuristic and classic methods. The most popular and a brief description of their working principles are now introduced:

- **Simulated annealing (SA).** This method is based on the metal annealing processing [278]. It resembles the drop of bouncing balls over a certain topography. When the correct energy loss rate is chosen, the bouncing balls converge and fall in the global minimum.

- **Genetic algorithms (GA).** Considered the most widespread and versatile evolutionary algorithms, this population-based method stems from Darwin's theory of natural selection. The algorithm encodes solutions as individuals and bits as chromosomes, and with the adequate adjustment of the crossover, mutation and selection parameters, global optima can be rapidly obtained [279]. Two genetic algorithms are thoroughly detailed in section 2.4.4.1.

- **Differential evolution (DE).** Developed by Storn and Price [280], the differential evolution method also uses genetically-inspired mutation, crossover and selection to obtain global optima. Section 2.4.4.1 offers a deeper explanation of these techniques as part of a genetic algorithm optimization procedure.

- **Ant colony optimization (ACO).** It is based on the foraging behavior of social ants, which lay scents and chemicals to communicate with each other when a food source [281]. This positive feedback mechanism converges into a state in which the shortest or more efficient routes are selected.

- **Particle swarm optimization (PSO).** PSO searches the space of an objective function by adjusting the trajectory of individual agents in the same way swarms of fish or birds seek nourishment [282]. Several variants of this method and hybrid algorithms using PSO have been developed given its versatility and capabilities in many research fields.

- **Tabu search.** Considered as an intensive local search algorithm, Tabu search uses search history to avoid revisiting local solutions and explore

new areas [276]. Tabu search is implemented in several hybrid algorithms given its efficient allocation of computing power [283].

- **Other metaheuristic algorithms.** New and efficient metaheuristic methods have been developed in the last two decades, among which the Harmony Search [284], the Firefly Algorithm [285] and the Cuckoo Search [286] are the most noteworthy due to their efficiency and wide range of applications.

These and more optimization methods existent in literature are used to optimize complex engineering problems. In some cases, this entails the simulation of a complex numerical model that requires several hours to compute. Thus, regardless of how efficient the optimization algorithm is, the evaluation of each function could severely hinder the process. With the development of surrogate-based methods, however, this is no longer a critical drawback.

2.4.3 Surrogate-based methods

Surrogate-based methods replace an expensive and complex physical models by another physical or mathematical model, the surrogate- or meta-model, with the purpose of reducing the time required to evaluate the former. For this reason, the original objective functions f_i are replaced by other functions, $\hat{f}_i$, which are less costly to evaluate. This surrogate model is faster when computed as it is usually constructed with more tractable functions. These functions, like n-th order polynomials or sets of basis functions such as splines or Gauss functions, avoid the singular, discontinuous, and non-differentiable points from the original model. The similarity of the approximation between the real and surrogate models will condition the results obtained in a later phase.

Before beginning with the construction of the surrogate model, the inputs that have a significant impact on f_i need to be identified through a certain number of observations. The objective is finding the shortest design variable vector $\boldsymbol{x} = \{x^{(1)}, x^{(2)}, \ldots, x^{(n)}\}$ but still being able to obtain the most diverse responses from the model when sweeping the ranges of its variables. The ranges

of the selected design variables are also set in this stage, considering both the behavior and the adequacy for the model.

Another task usually performed is the scaling of the variable vector $\boldsymbol{x}$ so that all variables are in the same magnitude order. Not doing so could greatly interfere with the final results obtained due to malfunction of the surrogate model construction or later on during the optimization process. One of the common approaches for this step consists in carrying out a parameter study with different design variables, obtaining both the fitness of the objective functions for the study and their behavior as the design variables are changed.

2.4.3.1 Sampling strategy

The first step for obtaining the surrogate model consists in defining a sampling plan. This sampling is crucial, since the number of points chosen N_s will condition later on the suitability of the surrogate model. Although sampling techniques as full factorial sampling or Montecarlo methods are available, only the latin hypercube sampling (LHS) developed by McKay et al. [287] is used in this research. This stratified method creates a set of data points that have homogeneous projections onto each variable axis. The design space is split into equally-sized hypercubes, and points are placed into them so that no superimposed projections exist onto the variables' axes. This is achieved by applying the following technique. If $\boldsymbol{X}_\mathrm{s}$ denotes the $N_\mathrm{s} \times \Omega_\mathrm{s}$ matrix in which we want to build the sampling plan on N_s points and Ω_s dimensions (each row is a point) we fill $\boldsymbol{X}_\mathrm{s}$ with random permutations of $\{1,2,\ldots,N_\mathrm{s}\}$ in each column and we normalize our plan into the $[0,1]^{\Omega_\mathrm{s}}$ box.

Figure 2.36 shows some examples of the three different sampling schemes presented for a two-dimensional problem: random sampling (figure 2.36a), full factorial sampling (figure 2.36b), and latin hypercube sampling (figure 2.36c), for a simple case of N equal to 10 samples. As it was predicted before, in random sampling, there are regions of the parameter space that are not sampled and other regions that are heavily sampled. In full factorial sampling, a random value is chosen in each interval for each parameter and every possible combination

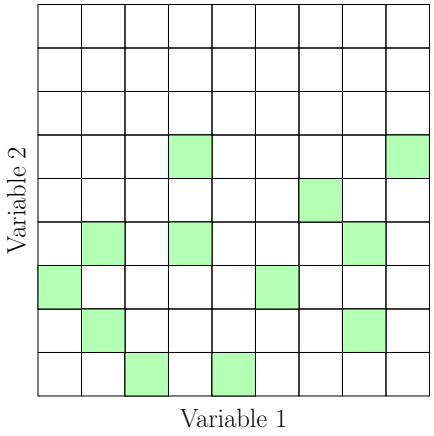

(a) Random sampling strategy.

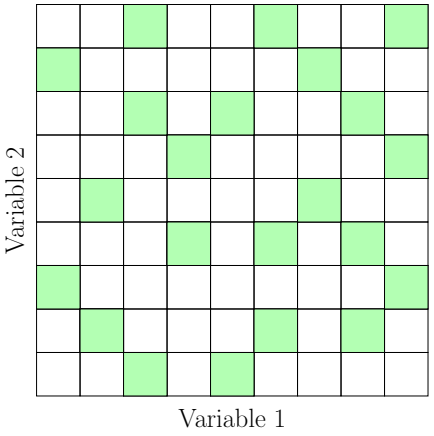

(b) Full factorial sampling strategy.

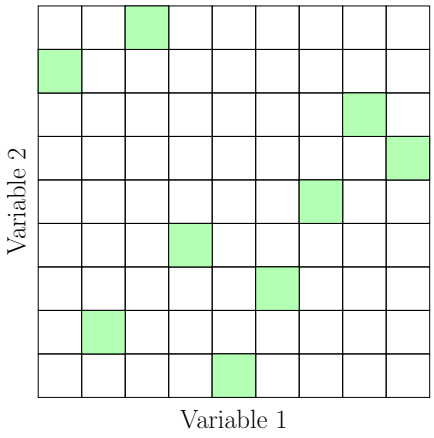

(c) Latin hypercube sampling strategy.

Figure 2.36: Illustrative examples of three sampling strategies for a two-dimensional problem.

of parameter values is chosen. The heavy point-cloud suggests that a higher computer power is required for computing all points. With the latin hypercube sampling, a value is chosen once and only once from every interval of each parameter, being efficient and adequately sampling the entire design space.

2.4.3.2 Construction of surrogate models

The second step when constructing a surrogate model is the building process itself, which consists in adjusting the proper functions to the data points obtained. Three different strategies are used throughout this research, as some surrogate models yielded better results depending on the sampling data profiles. Those techniques are:

- **Gaussian process (Kriging).** This method was developed by Matheron [288] in the 1960s after the thesis of Krige [289]. The interpolation is performed through a Gaussian process governed by prior covariances; predicting the value of a function at a point by weighing and averaging the known values of the function in the neighboring space. Kriging metamodels yield the best linear unbiased prediction of the intermediate values, although the main trend of the function may not be captured on account of adjusting to the known data. The approximation follows the structure

$$\hat{f}(\boldsymbol{x}) = \boldsymbol{g}(\boldsymbol{x})^T \boldsymbol{\beta} + \varepsilon(\boldsymbol{x}) \tag{2.90}$$

  where $\boldsymbol{x}$ is the current point, $\boldsymbol{g}(\boldsymbol{x})$ is the vector of basis functions at $\boldsymbol{x}$ and $\boldsymbol{\beta}$ is a vector containing the least squares estimates of the basis function coefficients. In this research, quadratic polynomials were used as the trend basis functions. The last term, $\varepsilon(\boldsymbol{x})$, is the stationary gaussian process error model, and it is used to correct the trend functions $\boldsymbol{g}(\boldsymbol{x})$. The stationary gaussian process error model, with a mean equal to 0 and a constant variance σ^2, contains a stationary autocorrelation function $r\left(\boldsymbol{x}, \boldsymbol{x'}\right)$ so its autocovariance function is of the form equation (2.91). This error $\varepsilon(\boldsymbol{x})$ adjusts the trend function guaranteeing that at the given sampling points the overall error is zero.

$$\sigma_{\hat{\boldsymbol{f}}(\boldsymbol{x})\hat{\boldsymbol{f}}(\boldsymbol{x'})} = \sigma_{\hat{\boldsymbol{\varepsilon}}(\boldsymbol{x})\hat{\boldsymbol{\varepsilon}}(\boldsymbol{x'})} = \sigma^2 r\left(\boldsymbol{x}, \boldsymbol{x'}\right) \tag{2.91}$$

An anisotropic generalized exponential model equation (2.92) was used for the $r\left(\boldsymbol{x}, \boldsymbol{x'}\right)$ function:

$$r\left(\boldsymbol{x}, \boldsymbol{x'}\right) = exp\left(-\sum_{k=1}^{\Omega} \theta_k |x_k - {x_k}'|^{\gamma}\right), \tag{2.92}$$

where Ω is the number of input dimensions, $0 < \gamma < 2$ and $0 < \theta_k$. For the gaussian correlation function $\gamma = 2$, which is infinitely differentiable, the correlation parameters $\boldsymbol{\theta}$ are related to the correlation lengths L_k by equation (2.93). The correlation lengths are analogous to standard deviation in the normal distribution.

$$\theta_k = \frac{1}{2L_k^2} \tag{2.93}$$

- **Multivariate adaptive regression splines (MARS).** This non parametric regression technique was developed in 1991 by Friedman [290], using splines as base functions for the surrogate model. MARS metamodels are build in two stages, the forward and the backward pass, in which the design space is sequentially partitioned into subregions. For each subregion, regression methods are applied to create a local surface fit in each one. An optimum number of base functions and subregions is selected and joined together to produce a $\mathcal{C}^2$ continuous surface model. The surrogate may not pass through all data, although by selecting a maximum number of base functions the behavior and noise of the function can be adjusted. The model is mathematically expressed as

$$\hat{f}\left(\boldsymbol{x}\right) = \sum_{m=1}^{M} a_m B_m\left(\boldsymbol{x}\right), \tag{2.94}$$

where B_m are the power basis functions (cubic splines were used in this research), a_m the coefficients of the functions, and M is the number of functions. The design space is partitioned into subregions, and for each

subregion regression methods are applied to create a local surface fit in each one. The subregions are joined together to produce a $\mathcal{C}^2$ continuous surface model. At first, the algorithm adjusts a single cubic spline to the design region. This design space is afterward divided into two subregions at a split point, called knot. The location of the knot is optimized so that the highest goodness of fit is obtained. With the design space divided in two sub-regions, a second spline is added to fit this new subregion. The process continues by adding knots and subsequently adjusting new splines until the maximum number of functions M is reached. The model with M splines enters a new phase in which each iteration removes a base function from the model. The function selected for removal needs to improve the most the fit of the model or, if that were not possible, harm the model the least. The only function that cannot be removed is the first spline, since its deletion could produce a hole in the model. At the end of this second phase, a new set of $M-1$ different models are obtained, and the algorithm now chooses the best one. A more thorough explanation is offered by Friedman and Roosen [291].

- **Moving Least Squares (MLS).** The MLS regression model combines polynomial functions to build a surrogate model according to the weighted least squares measure. This approach selects the function's coefficients so the least-square error from the interpolated values is minimized, considering different point weights in view of their proximity. With this approximation, the surrogate model is adjusted with polynomials according to the following formula:

$$\hat{f}\left(\boldsymbol{x}\right) = \sum_{m=1}^{M} c_m B_m\left(\boldsymbol{x}\right), \tag{2.95}$$

where B_m are the polynomial basis functions, c_m are the coefficients of the functions, M is the number of functions and $\boldsymbol{x}$ is the design variables' vector. To adjust the c_m coefficients, the sum of the squared residuals is minimized. Each residual is also assigned a point-specific weight ω_h that considers its relevance to the overall model as follows:

$$\min_{\hat{f}\epsilon\Pi_M} \sum_{h=1}^{n} \omega_h \left(\left\| \hat{f}\left(\boldsymbol{x}_h\right) - f\left(\boldsymbol{x}_h\right) \right\| \right), \tag{2.96}$$

where Π_M is the space of the polynomials used. This method and its working principles are more thoroughly explained by Nealen [292] and Lancaster and Salkauskas [293].

2.4.3.3 Model selection and validation

Surrogate models are an effective tool for addressing the lagging computation of objective functions, although its fine-adjustment for trustworthy results is not straightforward. After the surrogate is constructed, it needs to be established whether the surrogate model will produce reliable results and, additionally, how reliable. The suitability of the metamodel is determined through its trend functions, and in order to judge their accuracy, the goodness of fit R^2 is looked into. This indicator is defined as

$$\begin{aligned} R^2 &= \left(\frac{\sigma_{\boldsymbol{f}\hat{\boldsymbol{f}}}}{\sqrt{\sigma_{\boldsymbol{f}}^2 \sigma_{\hat{\boldsymbol{f}}}^2}} \right)^2 \\ &= \left(\frac{N\sum_{i=0}^{N} f_i \hat{f}_i - \sum_{i=0}^{N} f_i \sum_{i=0}^{N} \hat{f}_i}{\sqrt{\left[N\sum_{i=0}^{N} f_i^2 - \left(\sum_{i=0}^{N} f_i \right)^2 \right] \left[N\sum_{i=0}^{N} \hat{f}_i^2 - \left(\sum_{i=0}^{N} \hat{f}_i \right)^2 \right]}} \right)^2 . \end{aligned} \tag{2.97}$$

For the following research, it was established than surrogate models with a $R^2 \leqslant 0.90$ would not be accepted, as lower values would not provide confident results after the optimization process. However, this indicator is only useful for the MARS and MLS approximations, since Gaussian processes have an error equal to zero in the sampling points, thus always yielding $R^2 = 1$.

In order to test the accuracy of the emulator, the root mean squared error (RMSE) metric is also evaluated, which is defined as

$$RMSE = \sqrt{\frac{\sum_{i=0}^{M} \left(f_i - \hat{f}_i\right)^2}{M}}. \tag{2.98}$$

In some cases, the sole evaluation of the error can lead to misleading results. However, when the error is evaluated using a cross-validation strategy, the predictive capability of the surrogate comes into play. The cross-validation technique consists in splitting the sample of data into k roughly equal subsets called folds. Later on, one of the subsets is removed and the model is fitted to the remaining $k-1$ subsets. The model is then compared to the data points in the fold that was discarded, allowing to test the model predictive capabilities.

If we call Υ to a mapping so that $\Upsilon : \{1, ..., n\} \rightarrow \{1, ..., k\}$, this mapping allocates the n training points to one of the k subsets. The value of the surrogate model obtained by removing the fold Υ_i is defined $\hat{f}^{-\Upsilon_i}(\boldsymbol{x})$. The cross-validation measure, used to estimate the error of the prediction, is

$$\xi(c) = \frac{1}{2} \sum_{i=1}^{N} \left[f_i(\boldsymbol{x}) - \hat{f}^{-\Upsilon_i}\left(\boldsymbol{x}^i, \boldsymbol{c}\right) \right]^2. \tag{2.99}$$

The results from evaluating the R^2 or $RMSE$ indicators during cross-validation help identify the predictive capabilities of the surrogate. By means of example, a MARS metamodel with $R^2 = 0.93$ and $R^2_{cw} = 0.62$ can indicate that the model has excessive noise and the main trend is not well captured.

2.4.4 Design optimization

With the surrogate-based model created, any metaheuristic optimization strategy from section 2.4.2 could be used. However, genetic algorithms provided outstanding results throughout the whole investigation and no other method was used. The calculations required by single-objective optimization are relatively simple

once the proper surrogate model has been built. Single-objective optimization searches for the minima of the function within the limits of the design space.

One of the advantages of a single-objective optimization is the simplicity of its procedure and results. The latter is just a point yielding the optimum performance for the selected function. If no other design criterion is enforces, this technique is known as 'unconstrained optimization'. However, other functions can be forced to perform under specified boundaries, discarding unwanted solutions and narrowing the responses obtained, known as 'constrained optimization'. Optimization is performed for one metric, and then the function used as the constraint, either as an equality or inequality, is also evaluated. If this second function does not comply with the threshold value for the constraint, the former optimum point is discarded, and another optimum point is sought.

Multi-objective optimization was also a part of this investigation, albeit this procedure involves more resources for the calculations. Instead of a single point, the results are conformed by a Pareto front, corresponding to a range of results. The set of all Pareto optimal design configurations, P^*, is defined as:

$$P^* := \left\{ x \in \Pi \mid \nexists x' \in \Pi \; \hat{f}_i \left(\boldsymbol{x'} \right) \leqslant \hat{f}_i \left(\boldsymbol{x} \right) \right\} \tag{2.100}$$

and the Pareto front, which is the set of optimal objective functions from the Pareto design configurations, PF^*, is defined as:

$$PF^* := \left\{ \overline{\boldsymbol{u}} = \left(\hat{f}_1 \left(\boldsymbol{x} \right), \ldots, \hat{f}_k \left(\boldsymbol{x} \right) \right), x \in P^* \right\} \tag{2.101}$$

In the end, each point from the Pareto front has as many components as objective functions were optimized, each constituting a feasible solution to the problem. This Pareto front points cannot improve the value of one objective function without worsening the value of at least one other objective function.

2.4.4.1 Single-objective evolutionary algorithm

As the name suggests, an evolutionary algorithm (EA) is based on processes similar to those that occur during biological evolution. Consequently, most of the terms regarding EAs have their origin in biology and, even though they are simplified, the understanding of the evolutionary process is highly relevant. The variables are encoded and referred to as chromosomes, and each digit of the variable is a gene [294–296].

The EA used in this research is part of the SCOLIB library [19], a collection of C++ nongradient-based optimizers that are derived directly from the common optimization library interface (COLIN). Historically, SCOLIB is derived from the SGOPT library, which was renamed 'Coliny' when the COLIN library was created. The Coliny library was renamed SCOLIB when it became clear that there were many COLIN optimization libraries.

The basic steps of the evolutionary algorithm are shown graphically in figure 2.37, and can be enumerated as follows:

1. Selection of a random initial population. The typical binary encoding scheme is used, and each gene takes either the value of 0 or 1, both with equal probability. The chromosomes are decoded and this first generation undergoes the evaluation of the objective functions.

2. Selection of parents for the next generation based on relative fitness. The fitness of an individual i is denoted F_i. This goodness measure is maximized, and only the top percentage of individuals are selected for the subsequent generations.

3. Application of crossover and mutation to generate a new generation of individuals stemming from the selected parents. This techniques are applied to increase variability and avoid falling into local minima. Figure 2.38 shows graphically how these techniques affect the genes.

    - Crossover is a simple procedure for combining the genetic material of two individuals, consisting in cutting the chromosomes at randomly

selected crossover points, and then interchanging the rest of the chromosome with each other. The crossover probability value controls the crossovers performed every hundred genes.

- Mutation consists in flipping some bit in randomly selected genes. They are carried out in a gene-by-gene basis, in which the probability of mutation is given by the mutation rate indicator.

4. Evaluation of the objective functions on the new individuals. This is performed by assessing the relative fitness of the individuals as in step 1.

5. Application of replacement to determine the new population. After selection, crossover and mutation, there are two populations of individuals, the parents and the offspring. In generational replacement, the parents are discarded, and the offspring will become the parents for the next generation. In order not to lose the best individuals from the parents generation, a few copies of the best individuals are made and transfered directly to the children population, This procedure is known as elitism, and the number of this best individuals selected is determined by the elitism indicator.

6. Evaluation of step 2 and the algorithm until convergence criteria are met or the maximum number of evaluations is reached.

2.4.4.2 Multi-objective genetic algorithm

The method selected for the multi-objective optimization is the multi-objective genetic algorithm (MOGA) from the JEGA Library, developed by Eddy and Lewis [297]. This method performs Pareto optimization supporting general constraints as well as mixtures of real and discrete variables. Unlike other multi-objective algorithms, MOGA has been specifically designed to avoid aggregating and scaling function values to transform the original problem into a single objective problem. The variables are also encoded and referred to as chromosomes, and each digit of the variable is a gene. The steps followed by the algorithm are very much alike the steps from the evolutionary algorithm, but with some adaptations.

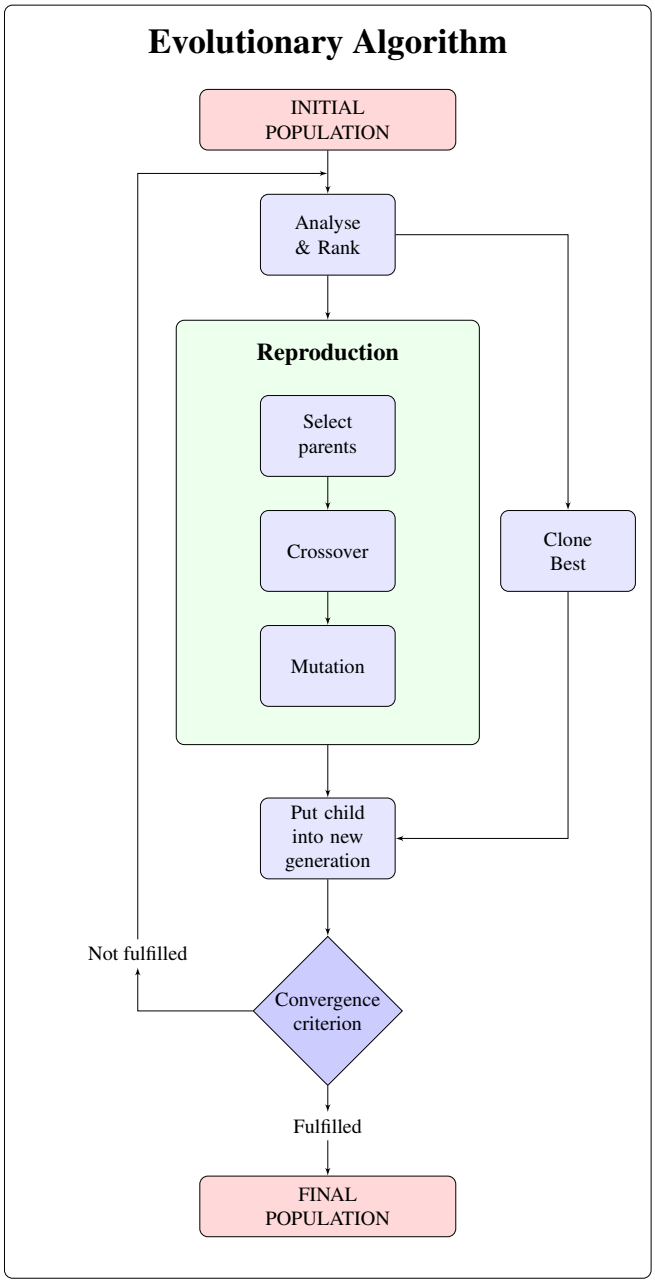

Figure 2.37: Depiction of an evolutionary algorithm.

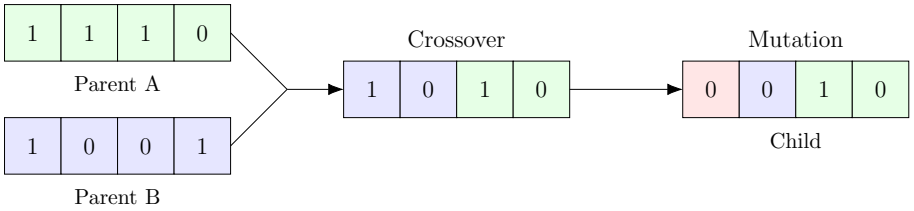

Figure 2.38: Depiction of crossover and mutation.

1. The initial population —the first set of N_c chromosomes —is initialized. For this, an initial number is required, called the seed. This seed has great influence on the results of the algorithm, and can even determine whether it does or does not work.

2. The initial population is evaluated and the values for the objective functions and constraints are calculated. The population members are ranked and then accepted or discarded depending on the number of other designs that dominate them. If the design is beyond the fitness frontier it is accepted and lives on to the next generation, where it will be evaluated again. Otherwise, it is discarded.

3. Perform crossover, combining the genetic material of every two individuals.

4. Perform mutation, randomly changing numbers in order to produce a greater diversity in the population.

5. Evaluate the new population members.

6. Assess the fitness of each member in the population (as in step 2)

7. Replace the population with the members selected to continue in the next generation. The pool of potential members is the current population and the current set of offspring.

8. Apply niche pressure to the population. This niche pressure promotes the formation and maintenance of stable subpopulations in the genetic algorithm.

9. Test for convergence. If the value meets the requirements initially set (or a maximum number of evaluations is reached) the algorithm continues to the next step. Otherwise, jumps to step 2 until the requirements are met.

10. Perform post processing, reducing the final solution set size such that a minimum distance in each direction exists between any two designs.

Note that crossover and mutation are performed each generation to increase variability and dodge local optima. This way, even if a certain population tends to go to a certain local optimum, the member that suffers the mutation will move on to another point in the function and go on with the optimization approaching another optimum, thus avoiding premature convergence (figure 2.39).

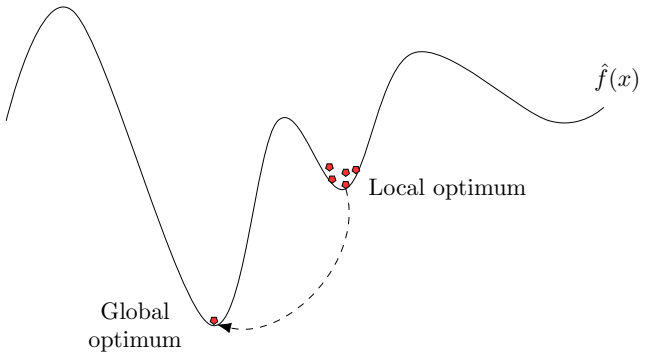

Figure 2.39: Depicted effect of crossover and mutation to the population members.

The replacement type available is the 'below limit replacement', meaning that only the individual within a radius of the best continue to the next generation. If for some reason there were not enough, the shrinkage percentage guarantees the minimum percentage of individuals that need to go on with the process, even though they are not fit enough.

The MOGA also supplies the closest point to the utopia point (point that minimizes all objective functions) and generates the Pareto front. In the end, the

set of points from the Pareto front constitutes the solution to the problem. This Pareto front points cannot improve the value of one objective function without worsening the value of at least another objective function.

References

[2] Snyder, Richard G. *Civil Aircraft Restraint Systems: State-of-the-Art Evaluation of Standards, Experimental Data, and Accident Experience*. Tech. rep. SAE Technical Paper, 1977.

[9] Paz, J, Díaz, J, Romera, L, and Costas, M. "Crushing analysis and multi-objective crashworthiness optimization of GFRP honeycomb-filled energy absorption devices". *Finite Elements in Analysis and Design* 91 (2014), pp. 30–39.

[34] De Haven, Hugh. *Mechanical analysis of survival in falls from heights of fifty to one hundred and fifty feet*. Tech. rep. 1980.

[35] De Haven, Hugh. *Accident survival-airplane and passenger automobile*. Crash Injury Research Project, 1952.

[36] Shanahan, Dennis F. "Basic principles of crashworthiness". *Pathological Aspects and Associate Biodynamics in Aircraft Accident Investigation* (2004).

[37] *Ferrari's F310B cockpit*. `https://goo.gl/sGxXMN`.

[38] National Transportation Safety Board. *2014–2015 US Transportation Fatalities*. `https://goo.gl/VNAJLt`.

[39] Unknown. *AG-1 Airplane*. Digital: Cushing Memorial Library and Archives, Texas A & M University, College Station, Texas; Physical: Graphic Services, Texas A & M University. Available electronically from `https://goo.gl/FdYimq`.

[40] Waldock, William D. "A brief history of" Crashworthiness". In: *1997 SAFE Association Symposium, Phoenix, AZ*. 1997.

[41] Larkins, Bill. *Beech 35 N3188V Jan1949*. `https://flic.kr/p/hX3Zvf`.

[42] Clark, John C. *Summary report on the National Transportation Safety Board's general aviation crashworthiness project findings*. Tech. rep. SAE Technical Paper, 1987.

[43] "Airworthiness Standards: Transport Category Airplanes". *Title 14, Federal Aviation Administration Code of Federal Regulations, Part 23, Washington D. C.* (2012).

[44] Research and Innovative Technology Administration, Bureau of Transportation Statistics. *Transportation Statistics Annual Report 2015*. Tech. rep. U.S. Department of Transportation, Washington DC, 2016.

[45] O'Neill, Brian. "Preventing passenger vehicle occupant injuries by vehicle design—a historical perspective from IIHS". *Traffic injury prevention* 10.2 (2009), pp. 113–126.

[46] Fasanella, Edwin L., Widmayer, E., and Robinson, Martha P. "Structural analysis of the controlled impact demonstration of a jet transport airplane." *Journal of Aircraft* 24.4 (1987), pp. 274–280.

[47] Waimer, M, Kohlgrüber, D, Hachenberg, D, and Voggenreiter, H. "The kinematics model–a numerical method for the development of a crashworthy composite fuselage design of transport aircraft". In: *Sixth triennial international aircraft fire and cabin safety research conference*. 2010.

[48] Byar, Alan and Tan, Tein-Min. "A crashworthiness study of a Boeing 737 fuselage section". PhD thesis. Drexel University Philadelphia, PA, 2003.

[49] Siromani, Deepak. *Crashworthy design and analysis of aircraft structures*. Drexel University, 2013.

[50] Noor, Ahmed K and Carden, Huey D. "Computational methods for crashworthiness" (1993).

[51] Hajela, P and Lee, Eoo. "Topological optimization of rotorcraft subfloor structures for crashworthiness considerations". *Computers & structures* 64.1-4 (1997), pp. 65–76.

[52] Lahey, Robert S, Miller, Mark P, and Reymond, Michael. "MSC/NASTRAN Reference Manual, Version 68". *The MacNeal-Schwendler Corporation* (1994).

[53] Gamon, MA. *KRASH User's Manual: Thoery Volume I.* Tech. rep. FAA-RD-77-1891, Lockheed-California Company, 1979.

[54] Kindervater, CM, Kohlgrüber, D, and Lützenburger, M. "Crash simulation methodologies for aircraft structures used within european crashworthiness research" (1998).

[55] Walton, Andrew, Whayeb, Shakir, and Sadeghi, Majid. *The Air Accident Investigation Tool.* Tech. rep. Second International KRASH User's Seminar, Cranfield Impact Centre, 1995.

[56] Gamon, Max A, Wittlin, Gil, and LaBarge, Bill L. *KRASH 85 User's Guide-Input/Output Format.* Tech. rep. FAA-RD-77-1891, Lockheed-California Company, 1985.

[57] Maia, Leandro Guimarães and Oliveira, Paulo Henriques Iscold Andrade de. *A review of finite element simulation of aircraft crashworthiness.* Tech. rep. SAE Technical Paper, 2005.

[58] Hallquist, John O and Whirley, Robert G. "DYNA3D User's Manual". *LLNL, Livermore, CA, UCID-19592* (1989).

[59] Welch, RE, Bruce, RW, and Belytschko, Ted. *Finite element analysis of automotive structures under crash loadings.* National Highway Traffic Safety Administration, 1976.

[60] Belytschko, T and Marchertas, AH. "Nonlinear finite-element method for plates and its application to dynamic response of reactor fuel sub-assemblies". *Journal of Pressure Vessel Technology* 96.4 (1974), pp. 251–257.

[61] Hallquist, John O et al. "LS-DYNA keyword user's manual". *Livermore Software Technology Corporation* 970 (2007).

[62] MSC DYTRAN User's Manual. "DB/CD". *Los Angeles, USA: MSC Corporation* (2002).

[63] PAM-CRASH. "Solver Reference Manual". *ESI Group Software product company. Rungis (France)* (2000).

[64] Altenhof, William, Paonessa, Saverio, Zamani, Nader, and Gaspar, Robert. "An experimental and finite element investigation into the energy absorption characteristics of a steering wheel armature in an impact". *International journal of impact engineering* 27.2 (2002), pp. 197–212.

[65] Fasanella, EL, Boitnott, RL, Lyle, KH, and Jackson, KE. "Full-scale crash test and simulation of a composite helicopter". *International journal of crashworthiness* 6.4 (2001), pp. 485–498.

[66] Fasanella, Edwin L and Jackson, Karen E. "Best practices for crash modeling and simulation" (2002).

[67] Fasanella, Edwin L and Jackson, Karen E. "Crash simulation of vertical drop tests of two Boeing 737 fuselage sections". In: *U.S. Army Research Laboratory, Vehicle Technology Center, Langley Research Center*. 2002.

[68] Belytschko, T. "Partitioned and adaptive algorithms for explicit time integration". In: *Nonlinear Finite Element Analysis in Structural Mechanics*. 1981, pp. 572–584.

[69] Plewa, Tomasz, Linde, Timur, and Weirs, V Gregory. "Adaptive mesh refinement-theory and applications". *Lecture notes in computational science and engineering* 41 (2005), pp. 3–5.

[70] *MADYMO Dummy models brochure*. TASS International. 2018.

[71] Obergefell, Louise A, Gardner, Thomas R, Kaleps, Ints, and Fleck, John T. *Articulated Total Body Model Enhancements. Volume 2. User's Guide*. Tech. rep. HARRY G ARMSTRONG AEROSPACE MEDICAL RESEARCH LAB WRIGHT-PATTERSON AFB OH, 1988.

[72] Happee, R, Janssen, AJ, Fraterman, E, Monster, JW, Happee, R, and Automotive, TNO. "Application of MADYMO occupant models in LS-DYNA/MADYMO coupling". In: *4th European LS-DYNA Users Conference*. 2003, pp. 3–10.

[73] Fountain, M A, Koppens, W P, and Lupker, H A. "Flexible body modelling in MADYMO". *Proceedings of the 6th International MADYMO Users' Meeting* (1996), pp. 175–186.

[74] Kindervater, CM, Kohlgruber, D, and Johnson, Allen. "Composite vehicle structural crashworthiness-A status of design methodology and numerical simulation techniques". *International Journal of Crashworthiness* 4.2 (1999), pp. 213–230.

[75] Waimer, Matthias, Feser, Thomas, Schatrow, Paul, and Schueler, Dominik. "Crash concepts for CFRP transport aircraft–comparison of the traditional bend frame concept versus the developments in a tension absorbers concept". *International journal of crashworthiness* 23.2 (2018), pp. 193–218.

[76] Lyle, Karen H, Jackson, Karen E, and Fasanella, Edwin L. "Simulation of aircraft landing gears with a nonlinear dynamic finite element code". *Journal of Aircraft* 39.1 (2002), pp. 142–147.

[77] Zhangping, Luo and Jinwu, Xiang. "Crashworthiness performance evaluation to helicopter landing gear by finite element simulation". *Acta Aeronautica et Astronautica Sinica* 24 (2003), pp. 216–219.

[78] Xue, P., Wang, L., and Qiao, C.F. "Crashworthiness study on fuselage section and struts under cabin floor". *International Journal of Protective Structures* 2.4 (2011), pp. 515–526.

[79] Nicholson, Colin R, Turnour, Stephen R, and Chapman, Helen E. *The design and testing of buckling monocoque seating structures for aircraft.* Tech. rep. SAE Technical Paper, 1999.

[80] Cheng, ZQ, Pilkey, Walter D, Balandin, Dmitry V, Bolotnik, Nikolai N, Crandall, Jeffrey R, and Shaw, C Gregory. "Optimal control of helicopter seat cushions for the reduction of spinal injuries". *International journal of crashworthiness* 6.3 (2001), pp. 321–338.

[81] Desjardins, Stanley P. "The evolution of energy absorption systems for crashworthy helicopter seats". *Journal of the American Helicopter Society* 51.2 (2006), pp. 150–163.

[82] Hooper, SJ and Ellis, DR. "Aviation safety and crashworthy seat design". *International journal of crashworthiness* 2.1 (1996), pp. 39–54.

[83] Federal Aviation Administration, Advisory circular 23.562-1. *Dynamic Testing of Part 23 Airplane Seat/Restraint System and Occupant Protection*. 1989.

[84] Federal Aviation Regulations. *Part 23 Airworthiness Standards: Normal, Utility, Acrobatic and Commuter Category Airplanes*. 1991.

[85] Federal Aviation Administration, Advisory circular 25.562-1A. *Dynamic Evaluation of Seat Restraint Systems and Occupant Protection on Transport Airplanes*. 1996.

[86] Federal Aviation Regulations. *Part 25-Airworthiness Standards: Transport Category Airplanes*. 1970.

[87] Mahé, M, Ribet, H, and Le Page, F. "Composite fuselage crash FE modelling dedicated to enhance the design in correlation with full scale drop test". *Mécanique & industries* 2.1 (2001), pp. 5–17.

[88] Carden, Huey D and Hayduk, Robert J. *Aircraft subfloor response to crash loadings*. Tech. rep. SAE Technical Paper, 1981.

[89] Wiggenraad, JFM. *Development of a crashworthy composite fuselage structure for a commuter aircraft*. 1999.

[90] McCarthy, MA and Wiggenraad, JFM. "Numerical investigation of a crash test of a composite helicopter subfloor structure". *Composite structures* 51.4 (2001), pp. 345–359.

[91] Kindervater, C. M. and Georgi, H. "Composite strength and energy absorption as an aspect of structural crash resistance". *Structural Crashworthiness and Failure* (1993).

[92] Delsart, David, Joly, Didier, Mahe, Michel, and Winkelmuller, Gérard. "Evaluation of finite element modelling methodologies for the design of crashworthy composite commercial aircraft fuselage". *Office National d'Etudes et de recherches aerospatiales* 188 (2004).

[93] Littell, Justin D, Jackson, Karen E, Annett, Martin S, Seal, Michael D, and Fasanella, Edwin L. "The Development of Two Composite Energy Absorbers for Use in a Transport Rotorcraft Airframe Crash Testbed (TRACT 2) Full-Scale Crash Test". In: *Proceedings of the 71st Annual American Helicopter Society Forum, Virginia Beach, VA, Mat.* 2015, pp. 5–7.

[94] Duan, Shuyong, Tao, Yourui, Han, Xu, Yang, Xujing, Hou, Shujuan, and Hu, Zhangping. "Investigation on structure optimization of crashworthiness of fiber reinforced polymers materials". *Composites Part B: Engineering* 60 (2014), pp. 471–478.

[95] Sokolinsky, Vladimir S, Indermuehle, Kyle C, and Hurtado, Juan A. "Numerical simulation of the crushing process of a corrugated composite plate". *Composites Part A: Applied Science and Manufacturing* 42.9 (2011), pp. 1119–1126.

[96] Kermanidis, Th, Labeas, G, Apostolopoulos, C, and Michielseif, Louis. "Numerical simulation of composite structures under impact". *WIT Transactions on The Built Environment* 35 (1970).

[97] McCarthy, MA, Harte, CG, Wiggenraad, JFM, Michielsen, ALPJ, Kohlgrueber, D, and Kamoulakos, A. "Finite element modelling of crash response of composite aerospace sub-floor structures". *Computational Mechanics* 26.3 (2000), pp. 250–258.

[98] Waimer, Matthias, Siemann, MH, and Feser, Thomas. "Simulation of CFRP components subjected to dynamic crash loads". *International Journal of Impact Engineering* 101 (2017), pp. 115–131.

[99] Farley, Gary L. "Crash energy absorbing subfloor beam structure". *Journal of the American Helicopter Society* 32.4 (1987), pp. 28–38.

[14] Zheng, Jianqiang, Xiang, Jinwu, Luo, Zhangping, and Ren, Yiru. "Crashworthiness design of transport aircraft subfloor using polymer foams". *International Journal of Crashworthiness* 16.4 (2011), pp. 375–383.

[100] Jackson, KE. "Impact testing and simulation of a crashworthy composite fuselage concept". *International Journal of Crashworthiness* 6.1 (2001), pp. 107–122.

[101] Bisagni, Chiara. "Computational Fluid and Solid Mechanics 2003 || Development of a crashworthy subfloor concept for a commuter aircraft". In: 2003.

[15] Meng, F X, Zhou, Q, and Yang, J L. "Improvement of crashworthiness behaviour for simplified structural models of aircraft fuselage". *International Journal of Crashworthiness* 14.1 (2009), pp. 83–97.

[102] Heimbs, S, Mehrens, T, Middendorf, P, Maier, M, and Schumacher, A. "Numerical Determination of the Nonlinear Effective Mechanical Properties of Folded Core Structures for Aircraft Sandwich Panels". *6th European LS-DYNA Users' Conference* (2011), pp. 1–14.

[103] Jackson, Karen E and Fuchs, Yvonne T. "Comparison of ALE and SPH simulations of vertical drop tests of a composite fuselage section into water" (2008).

[104] Ren, Yiru and Xiang, Jinwu. "A comparative study of the crashworthiness of civil aircraft with different strut configurations". *International Journal of Crashworthiness* 15.3 (2010), pp. 321–330.

[105] Heimbs, Sebastian, Hoffmann, Marco, Waimer, Matthias, Schmeer, Sebastian, and Blaurock, Jörg. "Dynamic testing and modelling of composite fuselage frames and fasteners for aircraft crash simulations". *International Journal of Crashworthiness* 18.4 (2013), pp. 406–422.

[106] Waimer, Matthias, Kohlgrüber, Dieter, Keck, Rüdiger, and Voggenreiter, Heinz. "Contribution to an improved crash design for a composite transport aircraft fuselage—development of a kinematics model and an experimental component test setup". *CEAS Aeronautical Journal* 4.3 (2013), pp. 265–275.

[107] Schatrow, Paul and Waimer, Matthias. "Investigation of a crash concept for CFRP transport aircraft based on tension absorption". *International journal of crashworthiness* 19.5 (2014), pp. 524–539.

[108] Gransden, Derek I and Alderliesten, René. "Development of a finite element model for comparing metal and composite fuselage section drop testing". *International Journal of Crashworthiness* 22.4 (2017), pp. 401–414.

[109] Schatrow, Paul and Waimer, Matthias. "Crash concept for composite transport aircraft using mainly tensile and compressive absorption mechanisms". *CEAS Aeronautical Journal* 7.3 (2016), pp. 471–482.

[110] Kindervater, Christof M, Johnson, Alastair F, Kohlgrüber, Dieter, Lützenburger, Marius, and Pentecote, Nathalie. "Crash and impact simulation of aircraft structures-hybrid and FE based approaches". In: *European congress on computational methods in applied sciences and engineering. Barcelona, Spain: ECCOMAS*. 2000.

[111] Lyle, Karen H, Stockwell, Alan E, and Hardy, Robin C. "Application of probability methods to assess airframe crash modeling uncertainty". *Journal of aircraft* 44.5 (2007), pp. 1568–1573.

[112] Kumakura, Ikuo, Minegishi, Masakatsu, Iwasaki, Kazuo, and HOSOKAWA, Takefumi. "Impact simulation of simplified structural models of aircraft fuselage". *SAE transactions* 109.1 (2000), pp. 1238–1243.

[113] Shoji, Hirokazu, Minegishi, Masakatsu, and Aoki, Takahira. "Channel Section Short Column with Fixed Ends under Axial Impact Load". In: *47th AIAA / ASME / ASCE / AHS / ASC Structures, Structural Dynamics, and Materials Conference*. 2006, p. 1760.

[114] Yiru, Ren, Jinwu, Xiang, Zhangping, Luo, and Jianqiang, Zheng. "Effect of Cabin-floor Oblique Strut on Crashworthiness of Typical Civil Aircraft Fuselage Section". *Acta Aeronautica Et Astronautica Sinica* 2 (2010), p. 012.

[115] Kumakura, I., Minegishi, M., and Iwasaki, K. "Impact simulation of simplified structural models of aircraft fuselage". *2000 World Aviation Conference* (2000).

[116] Shoji, H., Minegishi, M., and Aoki, T. "Impact characteristics estimation of channel section short column under axial impact load". *Structural Dynamics and Materials Conference* 4 (2007), pp. 3967–3976.

[16] Ren, Yiru and Xiang, Jinwu. "The crashworthiness of civil aircraft using different quadrangular tubes as cabin-floor struts". *International Journal of Crashworthiness* 16.3 (2011), pp. 253–262.

[117] Heimbs, S and Middendorf, P. "Design, analysis and testing of a composite crash absorber for aeronautic applications". In: *3rd ECCOMAS thematic conference on the mechanical response of composites*. 2011, pp. 537–544.

[118] Perez Galan, J. L., Climent, H., and Le Page, F. "Non-linear response of metallic and composite aeronautical fuselage structures under crash loads and comparison with full scale test". In: *European Congress on Computational Methods in Applied Sciences and Engineering, ECCOMAS, Barcelona*. 2000.

[119] Ezra, Arthur A. "An assessment of energy absorbing devices for prospective use in aircraft impact situations". In: *Dynamic response of structures*. Pergamon Press. 1972.

[120] Calladine, CR. "An investigation of impact scaling theory" (1983).

[121] Booth, E, Collier, D, and Miles, J. *Impact scalability of plated steel structures*. 1983.

[122] SAE, SAE. "J211-1 Instrumentation for Impact Test—Part 1—Electronic Instrumentation". *SAE International* (2007).

[17] Huang, M. *Vehicle Crash Mechanics*. CRC Press, 2002.

[123] Costas Piñó, Miguel. "Crashworthiness analysis and design optimization of hybrid impact energy absorbers" (2015).

[124] Desjardins, SP, Zimmerman, RE, Bolukbasi, AO, and Merritt, NA. "Aircraft crash survival design guide". *US Army Aviation Systems Command TR* 89 (1989).

[125] Eiband, A Martin. "Human tolerance to rapidly applied accelerations: a summary of the literature". *National Aeronautics and Space Administration (NASA)* (1959).

[126] Henn, Hans-Wolfgang. "Crash tests and the head injury criterion". *Teaching mathematics and its applications* 17.4 (1998), pp. 162–170.

[127] King, Albert I. "Fundamentals of impact biomechanics: part I-biomechanics of the head, neck, and thorax". *Annual review of biomedical engineering* 2.1 (2000), pp. 55–81.

[128] Stronge, William James. *Impact mechanics*. Cambridge university press, 2004.

[129] Alghamdi, AAA. "Collapsible impact energy absorbers: an overview". *Thin-walled structures* 39.2 (2001), pp. 189–213.

[130] Johnson, W. "Metallic energy dissipating systems". *Appl. Mech. Rev.* 31 (1978), pp. 277–288.

[131] Bisagni, Chiara. "Crashworthiness of helicopter subfloor structures". *International Journal of Impact Engineering* 27.10 (2002), pp. 1067–1082.

[132] White, M.D. and Jones, N. "Experimental quasi-static axial crushing of top-hat and double-hat thin-walled sections". *International Journal of Mechanical Sciences* 41.2 (1999), pp. 179–208.

[133] White, M.D., Jones, N., and Abramowicz, W. "A theoretical analysis for the quasi-static axial crushing of top-hat and double-hat thin-walled sections". *International Journal of Mechanical Sciences* 41.2 (1999), pp. 209–233.

[134] Marsolek, J and Reimerdes, H-G. "Energy absorption of metallic cylindrical shells with induced non-axisymmetric folding patterns". *International Journal of Impact Engineering* 30.8 (2004), pp. 1209–1223.

[135] Ahmad, Zaini and Thambiratnam, David Pathmaseelan. "Application of foam-filled conical tubes in enhancing the crashworthiness performance of vehicle protective structures". *International journal of crashworthiness* 14.4 (2009), pp. 349–363.

[136] Lu, Guoxing and Yu, TX. *Energy absorption of structures and materials*. Elsevier, 2003.

[137] Alexander, J. M. "An approximate analysis of the collapse of thin cylindrical shells under axial loading". *Quarterly Journal of Mechanics and Applied Mathematics* 13.1 (1960), pp. 10–15.

[138] Wierzbicki, Tomasz and Abramowicz, Wlodzimierz. "On the crushing mechanics of thin-walled structures". *Journal of Applied mechanics* 50.4a (1983), pp. 727–734.

[139] Abramowicz, W and Wierzbicki, T. "Axial crushing of multicorner sheet metal columns". *Journal of Applied Mechanics* 56.1 (1989), pp. 113–120.

[140] Abramowicz, Wlodzimierz and Jones, Norman. "Dynamic progressive buckling of circular and square tubes". *International Journal of Impact Engineering* 4.4 (1986), pp. 243–270.

[141] Pugsley, A.G. "On the crumpling of thin tubular struts". *Quarterly Journal of Mechanics and Applied Mathematics* 32.1 (1979), pp. 1–7.

[142] Singace, A.A. and Elsobky, H. "Further experimental investigation on the eccentricity factor in the progressive crushing of tubes". *International Journal of Solids and Structures* 33.24 (1996), pp. 3517–3538.

[143] Abramowicz, W. and Jones, N. "Transition from initial global bending to progressive buckling of tubes loaded statically and dynamically". *International Journal of Impact Engineering* 19.5-6 (1997), pp. 415–437.

[144] Kinkead, AN. "Analysis for inversion load and energy absorption of a circular tube". *The Journal of Strain Analysis for Engineering Design* 18.3 (1983), pp. 177–188.

[145] Al-Hassani, STS, Johnson, W, and Lowe, WT. "Characteristics of inversion tubes under axial loading". *Journal of Mechanical Engineering Science* 14.6 (1972), pp. 370–381.

[146] Thomas, SG, Reid, SR, and Johnson, W. "Large deformations of thin-walled circular tubes under transverse loading—I: an experimental survey of the bending of simply supported tubes under a central load". *International journal of mechanical sciences* 18.6 (1976), 325in3327–326in6333.

[147] DeRuntz, John A and Hodge, PG. "Crushing of a tube between rigid plates". *Journal of Applied Mechanics* 30.3 (1963), pp. 391–395.

[148] Reddy, T Yella and Reid, SR. "Lateral compression of tubes and tube-systems with side constraints". *International Journal of Mechanical Sciences* 21.3 (1979), pp. 187–199.

[149] Wu, Lan and Carney, John F. "Initial collapse of braced elliptical tubes under lateral compression". *International Journal of Mechanical Sciences* 39.9 (1997), pp. 1023–1036.

[150] Reid, SR. "Plastic deformation mechanisms in axially compressed metal tubes used as impact energy absorbers". *International Journal of Mechanical Sciences* 35.12 (1993), pp. 1035–1052.

[151] Guillow, SR, Lu, G, and Grzebieta, RH. "Quasi-static axial compression of thin-walled circular aluminium tubes". *International Journal of Mechanical Sciences* 43.9 (2001), pp. 2103–2123.

[152] Sadeghi, MM. "Design of heavy duty energy absorbers". *Structural Impact and Crashworthiness,* 2 (1984), pp. 588–604.

[153] Reid, SR. "Metal tubes as impact energy absorbers". *Metal forming and impact mechanics* (1985), p. 249.

[154] Hull, D. "A unified approach to progressive crushing of fibre-reinforced composite tubes". *Composites science and technology* 40.4 (1991), pp. 377–421.

[155] Hamada, H. and Ramakrishna, S. "A FEM method for prediction of energy absorption capability of crashworthy polymer composite materials". *Journal of Reinforced Plastics and Composites* 16.3 (1997), pp. 226–242.

[156] Andrews, KRF, England, GL, and Ghani, E. "Classification of the axial collapse of cylindrical tubes under quasi-static loading". *International Journal of Mechanical Sciences* 25.9-10 (1983), pp. 687–696.

[157] Wang, B and Lu, G. "Mushrooming of circular tubes under dynamic axial loading". *Thin-walled structures* 40.2 (2002), pp. 167–182.

[158] Tang, Zhiliang, Liu, Shutian, and Zhang, Zonghua. "Analysis of energy absorption characteristics of cylindrical multi-cell columns". *Thin-Walled Structures* 62 (2013), pp. 75–84.

[159] Zhang, Xiong and Huh, Hoon. "Crushing analysis of polygonal columns and angle elements". *International Journal of Impact Engineering* 37.4 (2010), pp. 441–451.

[160] Yamashita, Minoru, Gotoh, Manabu, and Sawairi, Yasuhiko. "Axial crush of hollow cylindrical structures with various polygonal cross-sections: Numerical simulation and experiment". *Journal of Materials Processing Technology* 140.1 (2003), pp. 59–64.

[161] Reddy, Sekhar, Abbasi, Milad, and Fard, Mohammad. "Multi-cornered thin-walled sheet metal members for enhanced crashworthiness and occupant protection". *Thin-Walled Structures* 94 (2015), pp. 56–66.

[162] Fan, Z, Lu, G, and Liu, K. "Quasi-static axial compression of thin-walled tubes with different cross-sectional shapes". *Engineering Structures* 55 (2013), pp. 80–89.

[163] Postlethwaite, HE and Mills, B. "Use of collapsible structural elements as impact isolators, with special references to automotive applications". *Journal of strain analysis* 5.1 (1970), pp. 58–73.

[164] Grzebieta, RH and Murray, NW. "The static behaviour of struts with initial kinks at their centre point". *International Journal of Impact Engineering* 3.3 (1985), pp. 155–165.

[165] Kumakura, Ikuo, Minegishi, Masakatsu, Iwasaki, Kazuo, Shoji, Hirokazu, Yoshimoto, Norio, Terada, Hiroyuki, Sashikuma, Hirofumi, Isoe, Akira, Yamaoka, Toshihiro, Katayama, Noriaki, et al. *Vertical drop test of a transport fuselage section.* Tech. rep. SAE Technical Paper, 2002.

[166] Heimbs, S, Strobl, F, Middendorf, P, and Guimard, JM. "Composite crash absorber for aircraft fuselage applications". *WIT Transactions on the built environment* 113 (2010), pp. 3–14.

[167] Baroutaji, Ahmad, Sajjia, Mustafa, and Olabi, Abdul-Ghani. "On the crashworthiness performance of thin-walled energy absorbers: Recent advances and future developments". *Thin-Walled Structures* 118 (2017), pp. 137–163.

[168] Mamalis, AG and Johnson, W. "The quasi-static crumpling of thin-walled circular cylinders and frusta under axial compression". *International Journal of Mechanical Sciences* 25.9-10 (1983), pp. 713–732.

[169] Guler, Mehmet A, Cerit, Muhammed E, Bayram, Bertan, Gerceker, Bora, and Karakaya, Emrah. "The effect of geometrical parameters on the energy absorption characteristics of thin-walled structures under axial impact loading". *International Journal of Crashworthiness* 15.4 (2010), pp. 377–390.

[170] Mamalis, AG, Johnson, W, and Viegelahn, GL. "The crumpling of steel thin-walled tubes and frusta under axial compression at elevated strain-rates: some experimental results". *International Journal of Mechanical Sciences* 26.11 (1984), pp. 537–547.

[171] Zhang, Xiong and Zhang, Hui. "Energy absorption of multi-cell stub columns under axial compression". *Thin-Walled Structures* 68 (2013), pp. 156–163.

[172] Zhang, Xiong, Wen, Zhuzhu, and Zhang, Hui. "Axial crushing and optimal design of square tubes with graded thickness". *Thin-Walled Structures* 84 (2014), pp. 263–274.

[173] Salehghaffari, S, Tajdari, M, Panahi, M, and Mokhtarnezhad, F. "Attempts to improve energy absorption characteristics of circular metal tubes subjected to axial loading". *Thin-Walled Structures* 48.6 (2010), pp. 379–390.

[174] Singace, Abduljalil Abdulla and El-Sobky, Hobab. "Behaviour of axially crushed corrugated tubes". *International Journal of Mechanical Sciences* 39.3 (1997), pp. 249263267–261265268.

[175] Eyvazian, Arameh, Habibi, Meisam K, Hamouda, Abdel Magid, and Hedayati, Reza. "Axial crushing behavior and energy absorption efficiency of corrugated tubes". *Materials & Design (1980-2015)* 54 (2014), pp. 1028–1038.

[176] Menouer, A, Baleh, R, Djebbar, A, and Abdul-Latif, A. "New generation of energy dissipating systems based on biaxial buckling". *Thin-Walled Structures* 85 (2014), pp. 456–465.

[177] Daimler. *The new smart fortwo 2014: smart fortwo bodyshell*. `https://goo.gl/4Fb2SD`.

[178] Jones, Norman. *Structural impact*. Cambridge university press, 2011.

[179] Reid, S. R., Reddy, T. Y., and Gray, M. D. "Static and dynamic axial crushing of foam-filled sheet metal tubes". *International Journal of Mechanical Sciences* 28.5 (1986), pp. 295–322.

[180] Calladine, Chris R. *Theory of shell structures*. Cambridge University Press, 1989.

[181] Ohokubo, Y, Akamatsu, T, and Shirasawa, K. "Mean crushing strength of closed-hat section members SAE paper 740040". *Automotive Engineering Comgress, Detroit* (1974).

[182] Aya, N and Takahashi, K. "Energy Absorbing Characteristics of Body Structures (Part 1)". *Transactions of Society of Automotive Engineers of Japan* 7 (1974), pp. 60–66.

[183] Magee, CL and Thornton, PH. *Design considerations in energy absorption by structural collapse*. Tech. rep. SAE Technical Paper, 1978.

[184] Macaulay, MA and Redwood, RG. "Small scale model railway coaches under impact". *The Engineer* 218 (1964), pp. 1041–1046.

[185] Dewalt, WJ and Herbein, WC. "Energy Absorption by Compression of Aluminum Tubes". *Alcoa Research Laboratories Engineering Design Division, Report* 12-72 (1972), p. 23.

[186] Abramowicz, W. and Jones, N. "Dynamic axial crushing of square tubes". *International Journal of Impact Engineering* 2.2 (1984), pp. 179–208.

[187] Cowper, G Rr and Symonds, Paul Southworth. *Strain-hardening and strain-rate effects in the impact loading of cantilever beams*. Tech. rep. Brown Univ Providence Ri, 1957.

[188] Karagiozova, D and Alves, Marcılio. "Transition from progressive buckling to global bending of circular shells under axial impact—-Part I: Experimental and numerical observations". *International Journal of Solids and Structures* 41.5 (2004), pp. 1565–1580.

[189] Mamalis, AG, Robinson, M, Manolakos, DE, Demosthenous, GA, Ioannidis, MB, and Carruthers, J. "Crashworthy capability of composite material structures". *Composite structures* 37.2 (1997), pp. 109–134.

[190] Bambach, MR, Jama, HH, and Elchalakani, M. "Axial capacity and design of thin-walled steel SHS strengthened with CFRP". *Thin-Walled Structures* 47.10 (2009), pp. 1112–1121.

[191] Gameiro, Celina Pires, Cirne, Jose, Miranda, Victor, Pinho-da-Cruz, Joaquim, and Teixeira-Dias, Filipe. "Dynamic behaviour of cork and cork-filled aluminium tubes: Numerical simulation and innovative applications". *Holzforschung* 61.4 (2007), pp. 400–405.

[192] Coelho, RM, Sousa, RJ Alves de, Fernandes, FAO, and Teixeira-Dias, FMVH. "New composite liners for energy absorption purposes". *Materials & Design* 43 (2013), pp. 384–392.

[193] Paulino, M., Teixeira-Dias, F., Gameiro, C.P., and Cirne, J. "Hyperelastic and dynamical behaviour of cork and its performance in energy absorption devices and crashworthiness applications". *International Journal of Materials Engineering Innovation* 1.2 (2009), pp. 197–234.

[194] Reddy, TY and Al-Hassani, STS. "Axial crushing of wood-filled square metal tubes". *International journal of mechanical sciences* 35.3-4 (1993), pp. 231–246.

[195] Saito, H. and Kimpara, I. "Evaluation of impact damage mechanism of multi-axial stitched CFRP laminate". *Composites Part A: Applied Science and Manufacturing* 37.12 (2006), pp. 2226–2235.

[196] Sun, G., Li, G., Stone, M., and Li, Q. "A two-stage multi-fidelity optimization procedure for honeycomb-type cellular materials". *Computational Materials Science* 49.3 (2010), pp. 500–511.

[197] Hanssen, A.G., Langseth, M., and Hopperstad, O.S. "Static and dynamic crushing of square aluminum extrusions with aluminum foam filler". *International Journal of Impact Engineering* 24.4 (2000), pp. 347–383.

[198] Bi, J., Fang, H., Wang, Q., and Ren, X. "Modeling and optimization of foam-filled thin-walled columns for crashworthiness designs". *Finite Elements in Analysis and Design* 46.9 (2010), pp. 698–709.

[199] Alavi Nia, A. and Sadeghi, M.Z. "The effects of foam filling on compressive response of hexagonal cell aluminum honeycombs under axial loading-experimental study". *Materials and Design* 31.3 (2010), pp. 1216–1230.

[200] Santosa, S and Wierzbicki, Tomasz. "Crash behavior of box columns filled with aluminum honeycomb or foam". *Computers & Structures* 68.4 (1998), pp. 343–367.

[201] Langseth, M., Hopperstad, O.S., and Hanssen, A.G. "Crash behaviour of thin-walled aluminium members". *Thin-Walled Structures* 32.1-3 (1998), pp. 127–150.

[202] Hanssen, AG, Langseth, M, and Hopperstad, OS. "Optimum design for energy absorption of square aluminium columns with aluminium foam filler". *International Journal of Mechanical Sciences* 43.1 (2001), pp. 153–176.

[203] Song, H.-W., Wan, Z.-M., Xie, Z.-M., and Du, X.-W. "Axial impact behavior and energy absorption efficiency of composite wrapped metal tubes". *International Journal of Impact Engineering* 24.4 (2000), pp. 385–401.

[204] Toksoy, Ahmet Kaan and Güden, Mustafa. "The strengthening effect of polystyrene foam filling in aluminum thin-walled cylindrical tubes". *Thin-walled structures* 43.2 (2005), pp. 333–350.

[205] Seitzberger, Markus, Rammerstorfer, Franz G, Gradinger, R, Degischer, HP, Blaimschein, M, and Walch, Ch. "Experimental studies on the quasi-static axial crushing of steel columns filled with aluminium foam". *International Journal of Solids and Structures* 37.30 (2000), pp. 4125–4147.

[206] Reid, S. R. and Reddy, T. Y. "Axial crushing of foam-filled tapered sheet metal tubes". *International Journal of Mechanical Sciences* 28.10 (1986), pp. 643–656.

[207] Hanssen, A.G., Langseth, M., and Hopperstad, O.S. "Static and dynamic crushing of circular aluminium extrusions with aluminium foam filler". *International Journal of Mechanical Sciences* 24.4 (2000), pp. 475–570.

[208] Santosa, S.P., Wierzbicki, T., Hanssen, A.G., and Langseth, M. "Experimental and numerical studies of foam-filled sections". *International Journal of Impact Engineering* 24.5 (2000), pp. 509–534.

[209] Zarei, HR and Kröger, Matthias. "Optimization of the foam-filled aluminum tubes for crush box application". *Thin-Walled Structures* 46.2 (2008), pp. 214–221.

[210] Markaki, AE and Clyne, TW. "The effect of cell wall microstructure on the deformation and fracture of aluminium-based foams". *Acta Materialia* 49.9 (2001), pp. 1677–1686.

[211] Gibson, Lorna J and Ashby, Michael F. *Cellular solids: structure and properties*. Cambridge university press, 1999.

[212] Brezny, Rasto and Green, David J. "The effect of cell size on the mechanical behavior of cellular materials". *Acta metallurgica et materialia* 38.12 (1990), pp. 2517–2526.

[213] Chen, C, Lu, TJ, and Fleck, NA. "Effect of imperfections on the yielding of two-dimensional foams". *Journal of the Mechanics and Physics of Solids* 47.11 (1999), pp. 2235–2272.

[214] Bouix, Rémy, Viot, Philippe, and Lataillade, Jean-Luc. "Polypropylene foam behaviour under dynamic loadings: Strain rate, density and microstructure effects". *International journal of impact engineering* 36.2 (2009), pp. 329–342.

[215] Yi, Feng, Zhu, Zhengang, Zu, Fangqiou, Hu, Shisheng, and Yi, Pan. "Strain rate effects on the compressive property and the energy-absorbing capacity of aluminum alloy foams". *Materials Characterization* 47.5 (2001), pp. 417–422.

[216] Tagarielli, VL, Deshpande, VS, and Fleck, NA. "The high strain rate response of PVC foams and end-grain balsa wood". *Composites Part B: Engineering* 39.1 (2008), pp. 83–91.

[217] Tan, PJ, Reid, SR, Harrigan, JJ, Zou, Z, and Li, S. "Dynamic compressive strength properties of aluminium foams. Part I—experimental data and observations". *Journal of the Mechanics and Physics of Solids* 53.10 (2005), pp. 2174–2205.

[218] Xu, Shanqing, Ruan, Dong, and Lu, Guoxing. "Strength enhancement of aluminium foams and honeycombs by entrapped air under dynamic loadings". *International Journal of Impact Engineering* 74 (2014), pp. 120–125.

[219] Tan, PJ, Reid, SR, Harrigan, JJ, Zou, Z, and Li, S. "Dynamic compressive strength properties of aluminium foams. Part II—'shock'theory and comparison with experimental data and numerical models". *Journal of the Mechanics and Physics of Solids* 53.10 (2005), pp. 2206–2230.

[220] Onsalung, Nirut, Thinvongpituk, Chawalit, and Painthong, Kulachate. "The influence of foam density on specific energy absorption of rectangular steel tubes". *Energy Research Journal* 1.2 (2010), pp. 135–140.

[221] Thornton, PH, Mahmood, HF, and Magee, CL. "Energy absorption by structural collapse". In: *Structural crashworthiness*. 1983. Chap. 4, pp. 96–117.

[222] Sun, Guangyong, Li, Guangyao, Hou, Shujuan, Zhou, Shiwei, Li, Wei, and Li, Qing. "Crashworthiness design for functionally graded foam-filled thin-walled structures". *Materials Science and Engineering: A* 527.7 (2010), pp. 1911–1919.

[223] Gupta, Nikhil and Ricci, William. "Comparison of compressive properties of layered syntactic foams having gradient in microballoon volume fraction and wall thickness". *Materials Science and Engineering: A* 427.1 (2006), pp. 331–342.

[224] Mohsenizadeh, S, Alipour, R, Rad, M Shokri, Nejad, A Farokhi, and Ahmad, Z. "Crashworthiness assessment of auxetic foam-filled tube under quasi-static axial loading". *Materials & Design* 88 (2015), pp. 258–268.

[225] Carruthers, Joe J, Kettle, AP, and Robinson, AM. "Energy absorption capability and crashworthiness of composite material structures: a review". *Applied Mechanics Reviews* 51.10 (1998), pp. 635–649.

[226] Jacob, G.C., Fellers, J.F., Starbuck, J.M., and Simunovic, S. "Crashworthiness of automotive composite material systems". *Journal of Applied Polymer Science* 92.5 (2004), pp. 3218–3225.

[227] Soutis, C. "Fibre reinforced composites in aircraft construction". *Progress in Aerospace Sciences* 41.2 (2005), pp. 143–151.

[228] Hellard, Guy. "Composites in airbus a long story of innovations and experiences". In: *Composites in Airbus at Global Investor Forum*. 2008.

[229] Johnson, A.F. and David, M. "Failure mechanisms and energy absorption in composite elements under axial crush". *Key Engineering Materials* 488-489 (2012), pp. 638–641.

[230] Israr, H.A., Rivallant, S., and Barrau, J.J. "Experimental investigation on mean crushing stress characterization of carbon-epoxy plies under compressive crushing mode". *Composite Structures* 96 (2013), pp. 357–364.

[231] Jia, X., Chen, G., Yu, Y., Li, G., Zhu, J., Luo, X., Duan, C., Yang, X., and Hui, D. "Effect of geometric factor, winding angle and pre-crack angle on quasi-static crushing behavior of filament wound CFRP cylinder". *Composites Part B: Engineering* 45.1 (2013), pp. 1336–1343.

[232] Costas, M., Díaz, J., Romera, L.E., Hernández, S., and Tielas, A. "Static and dynamic axial crushing analysis of car frontal impact hybrid absorbers". *International Journal of Impact Engineering* 62 (2013), pp. 166–181.

[233] Huang, J. and Wang, X. "Numerical and experimental investigations on the axial crushing response of composite tubes". *Composite Structures* 91.2 (2009), pp. 222–228.

[234] Ramakrishna, S. and Hamada, Hiroyuki. "Energy Absorption Characteristics of Crash Worthy Structural Composite Materials". *Key Engineering Materials* 141-143 (1998).

[235] Farley, Gary L and Jones, Robert M. "Crushing characteristics of continuous fiber-reinforced composite tubes". *Journal of composite Materials* 26.1 (1992), pp. 37–50.

[236] Wierzbicki, Tomasz et al. "Axial resistance and energy absorption of externally reinforced metal tubes". *Composites Part B: Engineering* 27.5 (1996), pp. 387–394.

[237] Heimbs, Sebastian. "Energy absorption in aircraft structures". *International Workshop on Hydraulic Equipment and Support Systems for Mining* (2012).

[238] Rock West Composites. *Nomex ® panel*. `https://goo.gl/LQZbyd`.

[239] Hou, S., Li, Q., Long, S., Yang, X., and Li, W. "Design optimization of regular hexagonal thin-walled columns with crashworthiness criteria". *Finite Elements in Analysis and Design* 43.6-7 (2007), pp. 555–565.

[240] Aktay, L., Johnson, A.F., and Kröplin, B.-H. "Numerical modelling of honeycomb core crush behaviour". *Engineering Fracture Mechanics* 75.9 (2008), pp. 2616–2630.

[241] Yin, H., Wen, G., Hou, S., and Chen, K. "Crushing analysis and multiobjective crashworthiness optimization of honeycomb-filled single and bitubular polygonal tubes". *Materials and Design* 32.8-9 (2011), pp. 4449–4460.

[242] Schultz, J., Griese, D., Ju, J., Shankar, P., Summers, J.D., and Thompson, L. "Design of honeycomb mesostructures for crushing energy absorption". *Journal of Mechanical Design, Transactions of the ASME* 134.7 (2012).

[243] Heimbs, S, Middendorf, P, Maier, M, et al. "Honeycomb sandwich material modeling for dynamic simulations of aircraft interior components". In: *Proceedings of the 9th international LS-DYNA users conference. Dearborn (MI)*. 2006.

[244] Heimbs, S, Strobl, F, Middendorf, P, Gardner, S, Eddington, B, and Key, J. "Crash Simulation of an F1 Racing Car Front Impact Structure" (2009).

[245] Olympio, Kingnidé R and Gandhi, Farhan. "Flexible skins for morphing aircraft using cellular honeycomb cores". *Journal of intelligent material systems and structures* 21.17 (2010), pp. 1719–1735.

[246] Miller, W, Smith, C W, and Evans, K E. "Honeycomb cores with enhanced buckling strength". *Composite Structures* 93.3 (2011), pp. 1072–1077.

[247] Xue, Zhenyu and Hutchinson, John W. "Crush dynamics of square honeycomb sandwich cores". *International Journal for Numerical Methods in Engineering* 65.13 (2006), pp. 2221–2245.

[248] Belytschko, Ted, Liu, Wing Kam, Moran, Brian, and Elkhodary, Khalil. *Nonlinear finite elements for continua and structures*. John wiley & sons, 2013.

[249] Barbeiro, S. "Supraconvergence of a finite difference scheme for solutions in Hs(0, L)". *IMA Journal of Numerical Analysis* 25 (4 2005).

[250] Courant, Richard, Friedrichs, Kurt, and Lewy, Hans. "Über die partiellen Differenzengleichungen der mathematischen Physik". *Mathematische annalen* 100.1 (1928), pp. 32–74.

[251] Silberschmidt, Vadim V. *Dynamic deformation, damage and fracture in composite materials and structures*. Woodhead Publishing, 2016.

[252] Belytschko, T. "An overview of semidiscretization and time integration procedures". *Computational Methods for Transient Analysis* 1 (1983).

[253] *ABAQUS 6.16 Documentation*. Dassault Systèmes. 2016.

[254] Belytschko, Ted, Smolinski, Patrick, and Liu, Wing Kam. "Stability of multi-time step partitioned integrators for first-order finite element systems". *Computer Methods in Applied Mechanics and Engineering* 49.3 (1985), pp. 281–297.

[255] Daniel, William John Trevor. "A study of the stability of subcycling algorithms in structural dynamics". *Computer methods in applied mechanics and engineering* 156.1-4 (1998), pp. 1–13.

[256] Daniel, WJT. "Analysis and implementation of a new constant acceleration subcycling algorithm". *International Journal for Numerical Methods in Engineering* 40.15 (1997), pp. 2841–2855.

[257] Smolinski, P, Sleith, S, and Belytschko, T. "Stability of an explicit multi-time step integration algorithm for linear structural dynamics equations". *Computational Mechanics* 18.3 (1996), pp. 236–244.

[258] Yang, RJ, Tseng, L, Nagy, L, and Cheng, J. "Feasibility study of crash optimization". In: *ASME*. Vol. 69. 2. 1994, pp. 549–556.

[259] Fang, Jianguang, Sun, Guangyong, Qiu, Na, Kim, Nam H, and Li, Qing. "On design optimization for structural crashworthiness and its state of the art". *Structural and Multidisciplinary Optimization* 55.3 (2017), pp. 1091–1119.

[260] Liu, Yucheng. "Thin-walled curved hexagonal beams in crashes–FEA and design". *International Journal of Crashworthiness* 15.2 (2010), pp. 151–159.

[261] Ghamarian, Ali and Zarei, Hamidreza. "Crashworthiness investigation of conical and cylindrical end-capped tubes under quasi-static crash loading". *International journal of crashworthiness* 17.1 (2012), pp. 19–28.

[262] Zhang, Yong, Sun, Guangyong, Xu, Xipeng, Li, Guangyao, and Li, Qing. "Multiobjective crashworthiness optimization of hollow and conical tubes for multiple load cases". *Thin-Walled Structures* 82 (2014), pp. 331–342.

[263] Toksoy, Ahmet Kaan and Güden, Mustafa. "The optimisation of the energy absorption of partially Al foam-filled commercial 1050H14 and 6061T4 Al crash boxes". *International journal of crashworthiness* 16.1 (2011), pp. 97–109.

[18] Costas, M, Morin, D, Langseth, M, Romera, L, and Díaz, J. "Axial crushing of aluminum extrusions filled with PET foam and GFRP. An experimental investigation". *Thin-Walled Structures* 99 (2016), pp. 45–57.

[264] Mohammadiha, O and Beheshti, H. "Optimization of functionally graded foam-filled conical tubes under axial impact loading". *Journal of Mechanical Science and Technology* 28.5 (2014), pp. 1741–1752.

[265] Fang, Jianguang, Gao, Yunkai, An, Xiuzhe, Sun, Guangyong, Chen, Junning, and Li, Qing. "Design of transversely-graded foam and wall thickness structures for crashworthiness criteria". *Composites Part B: Engineering* 92 (2016), pp. 338–349.

[266] Hou, Shujuan, Zhang, Zhidan, Yang, Xujing, Yin, Hanfeng, and Li, Qing. "Crashworthiness optimization of new thin-walled cellular configurations". *Engineering Computations* 31.5 (2014), pp. 879–897.

[267] Esfahlani, SS, Shirvani, H, Shirvani, A, Nwaubani, S, Mebrahtu, H, and Chirwa, C. "Hexagonal honeycomb cell optimisation by way of metamodel techniques". *International Journal of Crashworthiness* 18.3 (2013), pp. 264–275.

[268] Tran, TrongNhan, Hou, Shujuan, Han, Xu, Tan, Wei, and Nguyen, Nhat-Tan. "Theoretical prediction and crashworthiness optimization of multi-cell triangular tubes". *Thin-Walled Structures* 82 (2014), pp. 183–195.

[269] Bisagni, Chiara, Lanzi, Luca, and Ricci, Sergio. "Optimization of helicopter subfloor components under crashworthiness requirements using neural networks". *Journal of Aircraft* 39.2 (2002), pp. 296–304.

[270] Astori, Paolo and Impari, Francesco. "Crash response optimisation of helicopter seat and subfloor". *International Journal of Crashworthiness* 18.6 (2013), pp. 570–578.

[271] Hernandez, S. "Métodos de diseño óptimo de estructuras". *Colegio de ICCP, Coleccion Seinor* 8 (1990).

[272] Zabaras, Nicholas, Ganapathysubramanian, Shankar, and Li, Qing. "A continuum sensitivity method for the design of multi-stage metal forming processes". *International Journal of Mechanical Sciences* 45.2 (2003), pp. 325–358.

[273] Forrester, Alexander, Keane, Andy, et al. *Engineering design via surrogate modelling: a practical guide*. John Wiley & Sons, 2008.

[274] Wang, G Gary and Shan, Songqing. "Review of metamodeling techniques in support of engineering design optimization". *Journal of Mechanical design* 129.4 (2007), pp. 370–380.

[275] Glover, Fred. "Future paths for integer programming and links to artificial intelligence". *Computers & operations research* 13.5 (1986), pp. 533–549.

[276] Glover, Fred. "Tabu search—part I". *ORSA Journal on computing* 1.3 (1989), pp. 190–206.

[277] Blum, Christian and Roli, Andrea. "Metaheuristics in combinatorial optimization: Overview and conceptual comparison". *ACM Computing Surveys (CSUR)* 35.3 (2003), pp. 268–308.

[278] Kirkpatrick, Scott, Gelatt, C Daniel, Vecchi, Mario P, et al. "Optimization by simulated annealing". *science* 220.4598 (1983), pp. 671–680.

[279] Holland, John H. *Adaptation in Natural and Artificial Systems: An Introductory Analysis with Applications to Biology, Control, and Artificial Intelligence*. MIT press, 1992.

[280] Storn, Rainer and Price, Kenneth. "Differential evolution–a simple and efficient heuristic for global optimization over continuous spaces". *Journal of global optimization* 11.4 (1997), pp. 341–359.

[281] Dorigo, Marco, Birattari, Mauro, and Stutzle, Thomas. "Ant colony optimization". *IEEE computational intelligence magazine* 1.4 (2006), pp. 28–39.

[282] Kennedy, James. "Particle swarm optimization". In: *Encyclopedia of machine learning*. 2011, pp. 760–766.

[283] Glover, Fred and Laguna, Manuel. "Tabu Search". In: *Handbook of Combinatorial Optimization*. 2013, pp. 3261–3362.

[284] Geem, Zong Woo, Kim, Joong Hoon, and Loganathan, Gobichettipalayam Vasudevan. "A new heuristic optimization algorithm: harmony search". *simulation* 76.2 (2001), pp. 60–68.

[285] Yang, Xin-She. *Nature-inspired metaheuristic algorithms*. Luniver press, 2010.

[286] Yang, Xin-She and Deb, Suash. "Cuckoo search via Lévy flights". In: *Nature & Biologically Inspired Computing, 2009. NaBIC 2009. World Congress on*. IEEE. 2009, pp. 210–214.

[287] McKay, M., Beckman, R., and Conover, W. "A comparison of three methods for selecting values of input variables in the analysis of output from a computer code". *Technometrics* 21.2 (1979), pp. 239–245.

[288] Matheron, Georges. "Principles of geostatistics". *Economic geology* 58.8 (1963), pp. 1246–1266.

[289] Krige, D. G. "A statistical approach to some basic mine valuation problems on the Witwatersrand". *Journal of the Chemical, Metallurgical and Mining Engineering Society of South Africa* 52(6) (1951), pp. 119–139.

[290] Friedman, J. H. "Multivariate adaptive regression splines". *Annals of Statistics* 19 (1991), pp. 1–141.

[291] Friedman, J.H. and Roosen, C.B. "An introduction to multivariate adaptive regression splines." *Statistical methods in medical research* 4.3 (1995), pp. 197–217.

[292] Nealen, A. "A short-as-possible introduction to the least squares, weighted least squares, and moving least squares methods for scattered data approximation and interpolation." *Technical report, Discrete Geometric Modeling Group, Technishe Universität, Berlin, Germany* (2004).

[293] Lancaster, P. and Salkauskas, K. "Surfaces generated by moving least squares methods". *Mathematics of Computation* 37.155 (1981), pp. 141–158.

[294] Holland, John H. *Adaptation in Natural and Artificial Systems: An Introductory Analysis with Applications to Biology, Control, and Artificial Intelligence*. MIT press, 1992.

[295] Mitchell, Melanie. *An introduction to genetic algorithms*. MIT press, 1998.

[296] Wahde, Mattias. *Biologically Inspired Optimization Methods: An Introduction*. WIT Press, 2008.

[19] Adams, B., Bauman, L., Bohnhoff, W., Dalbey, K., Ebeida, M., Eddy, J., Eldred, M., Hough, P., Hu, K., Jakeman, J., Swiler, L., and Vigil, D. *DAKOTA, A Multilevel Parallel Object-Oriented Framework for Design Optimization, Parameter Estimation, Uncertainty Quantification, and Sensitivity Analysis: Version 6.1.0 User's Manual*. Sandia National Laboratories. 2014.

[297] Eddy, J. E. and Lewis, K. "Effective Generation of Pareto Sets using Genetic Programming". *Proceedings of ASME Design Engineering Technical Conference* (2001).

3

Crushing analysis and crashworthiness optimization of hybrid energy absorbers enclosing GFRP honeycomb structures[1]

3.1 Introduction

One procedure traditionally used for absorbing and dissipating the energy during automobile impact scenarios consists in adding collapsible impact energy absorbers behind the bumper structures, as seen in section 2.2. These devices absorb and dissipate through plastic deformation a large amount of the energy involved in such an impact, thereby reducing the severity and consequences of the crash for the passengers. Nevertheless, not only the energy absorbed but also the mass and price of the element are factors taken into account during its design, seeing that weight-saving, fuel consumption and assembling price are other critical characteristics in vehicle structural design.

This chapter introduces the first of a series of hybrid energy absorber designs combining thin-walled metal square tubes and honeycomb composite structures (see figure 3.1). Devices are numerically modeled and simulated under axial

[1] Chapter adapted from the work published as:
J. Paz, J. Díaz, L. Romera, and M. Costas. "Crushing analysis and multi-objective crashworthiness optimization of GFRP honeycomb-filled energy absorption devices". *Finite Elements in Analysis and Design* 91 (2014), pp. 30–39.

(a) Pretest specimen. **(b)** Post-test deformation.

Figure 3.1: Hybrid energy absorber.

dynamic loads resembling those of an automobile frontal collision during the Euro NCAP tests. The numerical simulations are parametrized so that core height, cell size and materials' thicknesses can be chosen as design variables; aiming for the ultimate goal of optimization.

To understand the behavior of such devices under dynamic impact loads, three preliminary analyses are to be performed. The interaction effect between the parts and the comparison between a hollow tube with a hybrid specimen of the same mass are analyzed; later followed by a parameter study considering all four design parameters. Once stablished as a suitable candidate for crashworthiness enhancement, surrogate-based optimization techniques are used on the specimen considering passenger-related objective functions as mass, absorbed energy, peak load and specific energy absorption.

3.2 Model description

3.2.1 Specimen

The specimen chosen for this research is a combination of two individual elements. The first one is a square hollow tube made from a standard S-275 J0H steel, with properties detailed in table 3.1. The steel is modeled according to a Johnson-Cook strain-rate sensitive model, which yields to reliable solutions even if the material is subjected to various strain rates [20]. The model is a Mises plasticity model that also takes into account the strain-rate dependence, as well as temperature dependent effects. The constitutive equation of the steel model for yield stresses is:

$$\sigma_y = \left[A + B\left(\varepsilon_p^{eff}\right)^P\right]\left(1 + C\ln\dot{\varepsilon}\right)\left[1 - (T_H)^Q\right] \tag{3.1}$$

where A is the yielding stress, B modifies the hardening law amplitude, C affects the strain-rate dependency, P changes the shape of the hardening law, and Q adjusts the temperature dependency. Since the temperature dependency of the specimen is not taken into account, $(T_H)^Q = 0$.

E	σ_y^0	ν	ρ	A	B	C	P	$\dot{\varepsilon_0}$
210 GPa	275 MPa	0.3	78.5 kN/m^3	275 MPa	50 MPa	0.03	0.4	0.0001

Table 3.1: S-275 J0H steel properties and Mises plasticity model values for equation (3.1). Taken from [304].

The second part is the inner reinforcement, which has a smaller section than the tube so it can be placed within the steel structure. It is made up of a honeycomb structure made of Ultramid A3WG10 BK00564 (BASF), a glass-fiber-reinforced-polyamide. Its mechanical properties have been extracted from the manufacturer's data sheets [21] and are shown in table 3.2. These properties have also been implemented in the finite element model, as a linear, isotropic, elastic model with fragile failure. The short fibers of the composite are randomly

chopped into a polyamide matrix, thus obtaining an isotropic behavior. For the failure criterion, it is considered that no further damage can occur to the material after the failure strain ε_u is reached, so the elements are deleted after overpassing this value for the strain.

E	ν	ρ	σ_u	ε_u
10.16 GPa	0.4	15.5 kN/m^3	254 MPa	2.6%

Table 3.2: Material properties of Ultramid A3WG10 BK00564.

Since this investigation consists in a set of finite element analyses, the meshing of the model also needs to be detailed as it is an important factor for the results obtained. The mesh size varies according to each material and its attributes. In the steel tube, there has to be enough elements to allow the specimen to fold according to its natural crushing modes. This requires a moderate to high finite element density, but avoiding a very high density which would greatly increase computation times. The mesh size of the tube was set considering the previous work done by Costas et al. [232], where the mesh size was selected by taking into account the experimental folding process of a similar tube. In this research, a 4 mm mesh is implemented, trying to obtain an accurate steel folding process during the impact process. The honeycomb part has been meshed proportionally to the size of the cell, ranging from 1.6 mm to 3.5 mm, so that every cell wall has at least two elements and no more than six. Figure 3.2 represents a model already meshed accordingly and with the actual thickness of the elements. Both parts consist of four-node shell elements with 3 integration points through their thickness and a reduced integration scheme.

3.2.2 Design variables and objective functions

The standard energy absorption device that will be used during the rest of the chapter is now defined. For the sizing of the specimen, there are two design parameters and four design variables, presented in table 3.3. The two design

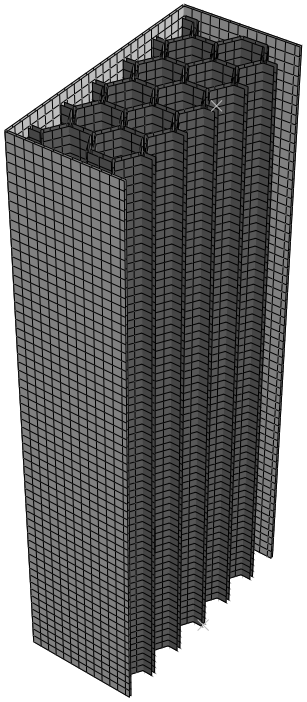

Figure 3.2: Three-dimensional cut of the finite element mesh of the specimen.

parameters are the height of the tube, which takes a value of 250 mm, and the edge of the square tube, equal to 100 mm.

The design variables chosen for this research are:

- T1: Thickness of the steel sheets.
- T2: Thickness of the GFRP honeycomb reinforcement.
- D: Diagonal length of a single honeycomb cell.
- H1: Height of the GFRP honeycomb reinforcement.

Table 3.3 gives insight on the upper and lower bounds of each variable, as well as their initial values and to which specimen part they belong to. For a

better understanding of the specimen, the measurements detailed in table 3.3 are depicted in figures 3.3 and 3.4.

		Bounds		
Part	Design Variable	Lower	Upper	Initial Design
Tube	T1	0.87	2.44	1.50
Honeycomb	T2	1.00	3.00	1.50
	D	8.00	20.00	20.00
	H1	220.00	250.00	250.00

Table 3.3: Characteristics of design variables from figures 3.3 and 3.4. All dimensions in millimeters.

The objective of this research is to find a set of optimum designs of the specimen previously described according to three different objective functions. These functions are the absorbed energy (E_a), the mass of the specimen (m) and the peak load (P_peak). The three metrics are obtained using a finite element simulation, where E_a and P_peak are obtained via the force-displacement curves.

Before making any calculations with the force-displacement curve, and according to the specialized literature in crash analysis [17], a standard SAE 600 filter [22] is applied. This removes the high-frequency noise from the curve with a cutoff frequency of 1000 Hz. Once the filter is used, the direct integration of the resulting force-displacement curve yields to the E_a:

$$E_a = \int_0^\delta F(z)\ dz\,, \tag{3.2}$$

with δ being the total axial crushing distance and $F(z)$ the value of the crushing force at the crushing length z.

The peak load P_peak is defined as

$$P_\mathrm{peak} = max\left\{F(z)\,\forall z \in [0,\delta]\right\} \tag{3.3}$$

These three objective functions have not been randomly chosen. The first reason is the nature of the design and its aim to improve the crashworthiness

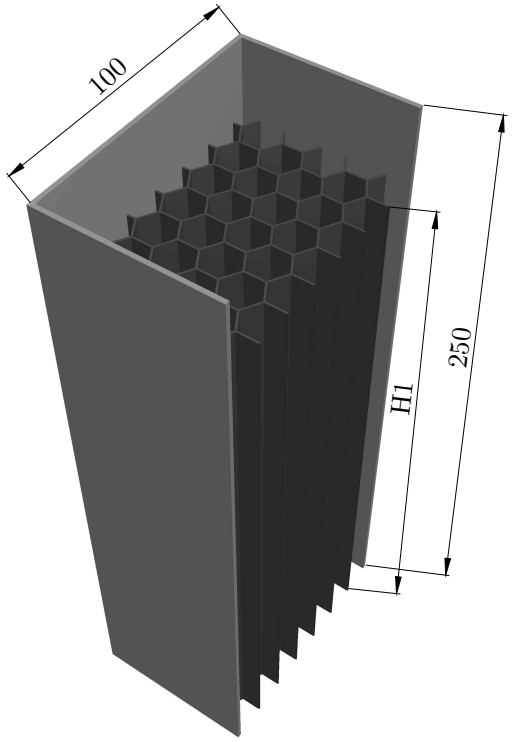

Figure 3.3: Three-dimensional cut of the specimen. All dimensions in millimeters.

of vehicles. The E_a can be easily improved by increasing the thicknesses of the materials or making the honeycomb cells smaller, but these actions would harm the other two objective functions m and P_{peak}, increasing both of them. An increase in the mass of the specimen translates into a higher mass of the vehicle, increasing its fuel consumption and reducing its performance. On the other hand, an increase in the P_{peak} means that the part is stiffer and needs more force to be crumpled, which translates into a dispersed damage throughout the whole chassis rather than local damage of the piece. Furthermore, the height of the honeycomb structure also has an effect on all three objective functions: besides augmenting the mass and the absorbed energy, since there is more material in the model, the initial peak force is increased as well. This happens because the initial peaks of the tube and the honeycomb occur at the same time, adding the

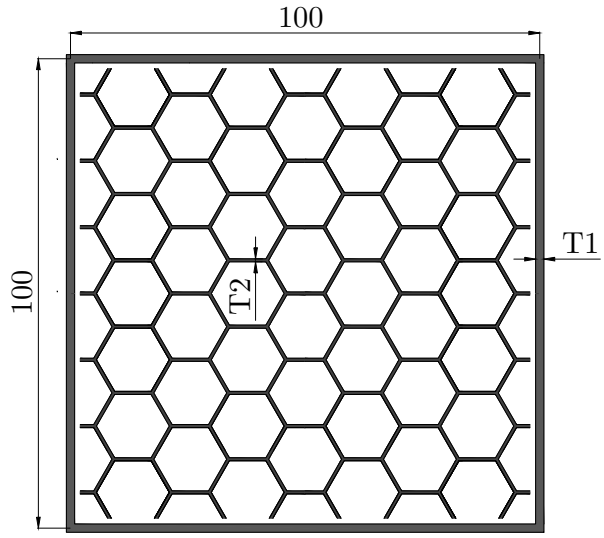

Figure 3.4: Top view of the specimen. All dimensions in millimeters.

forces of both peaks. When the height of the honeycomb is reduced, an offset between the peaks is observed, and the maximum total peak load is reduced.

The second reason for choosing these objective functions is purely computational. Traditionally, other researchers have swerved towards optimization of the specific energy absorption (SEA) and the load ratio (LR) [239] but it was found that during the optimization process these quantities have a more complicated comportment and a noisier nature for this model. Consequently, they were discarded from the optimization process and are only used during the parameter study and as indicators to compare different specimens.

3.2.3 Analysis settings

The simulations have been run with the specimen being crushed between two rigid plates. One plate is fixed, and the other impacts the specimen at a constant speed of 64 km/h (17.78 m/s). This maximum speed matches the Euro NCAP protocol for frontal impact testing [3]. When a maximum crushing length of $\delta = 180$ mm is reached the analysis stops, thus fixing stroke efficiency $St_{\mathrm{e}} = 0.72$

(see equation (2.6)). This limitation has been set in order to avoid the undesired bottom-out effect and contamination of the final energy absorption values.

The explicit module of the Abaqus 6.13 FEA package [305] was used for the evaluation of the samples. For this research, 600 data points have been used for the sampling, after considering the nature of the four design variables and the three objective functions. The complete crushing of each specimen was divided into 500 time steps, in which the FEA writes the variables' values. On the other hand, the surrogate based optimization procedure and the MOGA were implemented via DAKOTA framework in its version 5.4.1 [306]. The problems were first divided into 4 domains and each of them was computed in a separate processor with 3000 megabytes of RAM. All the complete analyses were run in a high performance computing (HPC) cluster with a theoretical peak performance of 7.6 TFLOP's.

3.3 Results and discussion

3.3.1 Initial results

The first calculations need to determine whether the objective functions selected comply with the initial expectations, since they will be used throughout the rest of the research. In order to judge the accuracy of the trend functions, the goodness of fit R^2, is looked into. This has been done for all objective functions (figure 3.5), obtaining values equal or higher than 0.95 for the three selected objective functions. It can be seen that the R^2 is lower for SEA and LR despite increasing the number of maximum basis functions used. Consequently, the option with E_{a}, m and P_{peak} as objective functions was verified to be better than the one with SEA and LR.

This indicator is only useful for the MARS approximation, since kriging always has an error equal to zero in the sampling points and therefore the R^2 value is 1.

In order to test the accuracy of the emulator we have evaluated for the three objective functions the root mean squared error (RMSE) metric together with a

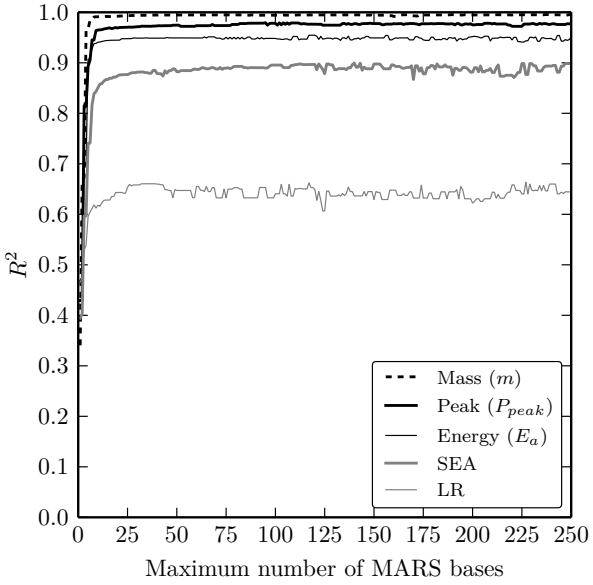

Figure 3.5: Variation of the R^2 indicator with the maximum number of MARS bases for different objective functions.

10-fold cross-validation strategy in order to find an adequate number of bases for the MARS model.

Figure 3.6 shows the evolution of this indicator as the maximum number of MARS basis functions is increased. After an approximate maximum of 25 MARS basis functions, the mean absolute error stabilizes for all functions. This justifies using a maximum number of 48 MARS bases for the next optimization steps, since the error is not significantly reduced after this value.

Initial calculations with the initial design parameters shown in table 3.3 have been conducted to prove that the resulting capabilities of the combined specimen are better than those of both parts analyzed separately and summed afterward. For this, the initial model was analyzed as a whole, along with both of its separate components. The response of the detached components was then added and compared with the initial specimen, as it can be seen in figure 3.7. The interaction effect accounts for an increase of 22% in the absorbed energy in this example,

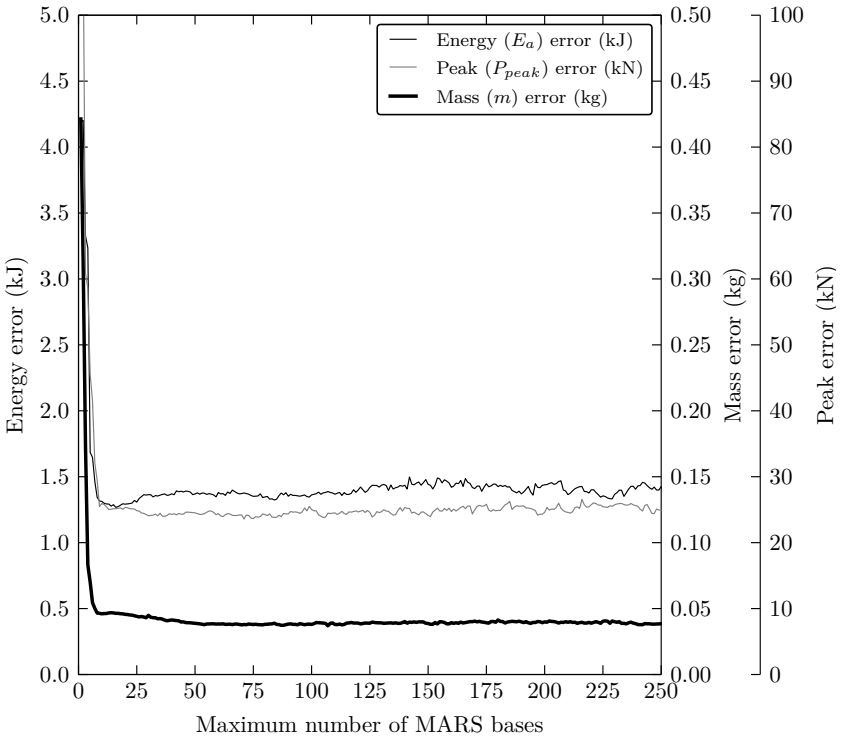

Figure 3.6: Influence of the maximum number of MARS maximum basis functions on the cross-validated mean absolute error for different objective functions.

with no significant variations in the peak load value. It is also noticeable that this effect is significant in the last part of the crushing of the specimen, after a crushing length of 9 cm. Whereas the energy absorbed by both separate parts amounts to 3.19 kJ in the last 9 cm of the crushing process; the tube filled with the honeycomb absorbs 6.06 kJ, nearly twice as much as the previous value. The more stable flattened response of the reinforced tube is produced by the higher energy dissipated compared to the empty tube, as more folds are developed during the crushing of the specimen (figure 3.8).

Another important effect is the behavior of the honeycomb structure alone. During various crumpling steps the absorbed energy corresponding to this element

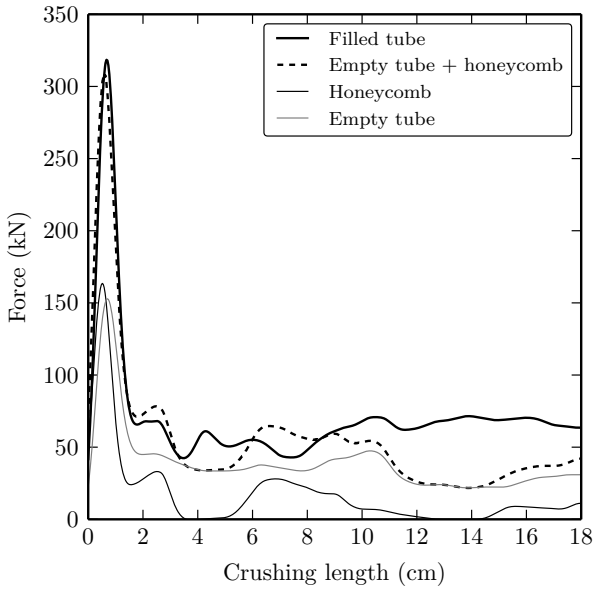

Figure 3.7: Force-displacement curves of the complete specimen, separate parts, and both parts added together.

is close to zero. This is caused by the absence of a casting, which would constrain the shattering of this piece and yield steadier results.

Further tests have also been carried out with different specimens. With a defined value for the mass, two tubes were crushed. One of them was empty, and the other tube had thinner walls but had a honeycomb structure inside. The results show that for this certain design the energy absorption value is 29.1% higher and the peak load is only increased by 8.6% compared to the empty tube (figure 3.9). This proves that filling the tube with a honeycomb structure can greatly improve the crashworthiness of the specimen without increasing the mass and, therefore, harming fuel consumption.

With all preliminary considerations taken into account, and seeing the improvement of both objective functions, the specimen is declared fit for analysis and undergoes a parameter study before the optimization process.

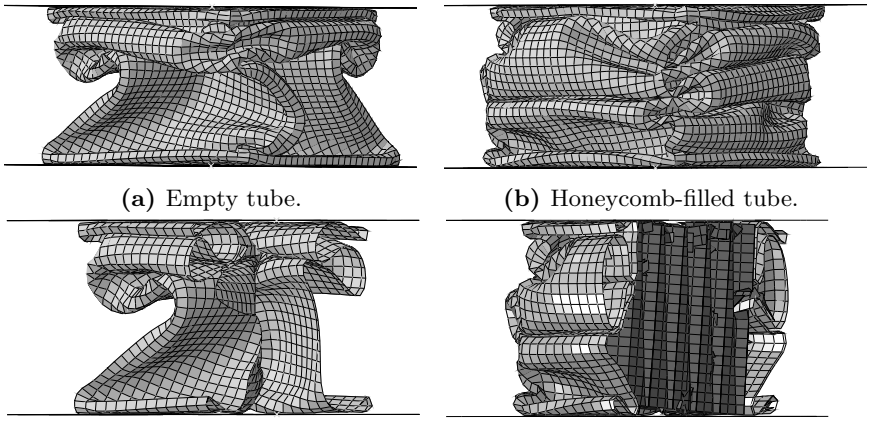

(a) Empty tube. **(b)** Honeycomb-filled tube.

(c) Empty tube. **(d)** Honeycomb-filled tube.

Figure 3.8: Post-test deformation and sectional cut of reinforced and hollow square steel tubes ($C/h = 50$).

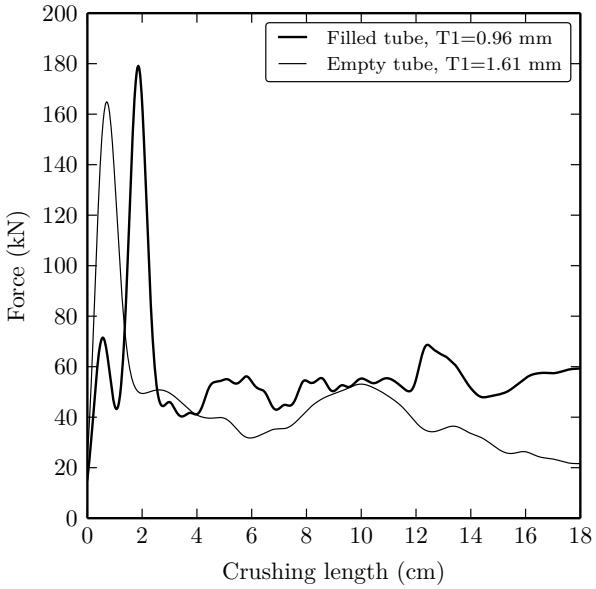

Figure 3.9: Force-displacement curves of the complete specimen and a hollow tube with equal mass.

3.3.2 Parameter study

As a last characterization procedure, a parameter study is performed to understand the effect of each design variable on the objective functions. The whole model was run manually, based on the initial design, varying one design variable at a time. Two indicators —SEA and maximum peak load —were used to see the influence of each variable in the performance of the specimen. From figures 3.10a to 3.10d, the influence of the four variables on two of the objective functions can be hinted.

The first design variable, the cell size, reduces the peak load when increased. This is understandable considering that the smaller the cell, is the greater the mass and stiffness of the inner core; thus increasing the initial force during the impact. For cell sizes larger than 14 mm, the peak load stabilizes, and small reductions in its value are observed. The other metric, the SEA, has a different comportment. Even though it does not vary excessively, a maximum value of 9.5 kJ/kg is obtained with a cell size of 14 mm. The optimum range for the SEA is found between 11 and 16 mm. For higher values of the cell size, the SEA absorption decreases drastically as seen in figure 3.10a.

The steel and honeycomb thicknesses affect the peak load function similarly. An increase in the thicknesses increases the peak load almost linearly, which fluctuates between 245 kN to 445 kN. The curve for the thickness of the steel is slightly steeper that the one for the honeycomb (see figures 3.10b and 3.10c), but the small difference can be obviated. Increasing the thicknesses also improves the SEA. For the steel, the improvement is over 20% (figure 3.10b), whereas the increase of T2 increases this metric by nearly 13% (figure 3.10c).

The last design variable, the height of the honeycomb core, has nearly no influence in the SEA indicator. On the other hand, the initial peak load is greatly affected. As the honeycomb height is linearly increased so does the peak load, but with an exponential-like trend (figure 3.10d). A decrease of only 10 mm in the variable leads to a peak load which is 66% the original value. In the variable's frontier, the lower value, 155 kN, is less than half the peak load of the higher

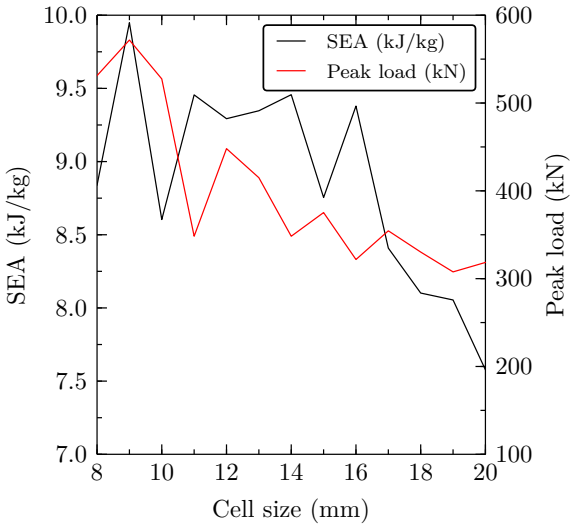

(a) *SEA* and peak load evolution with the cell size, D.

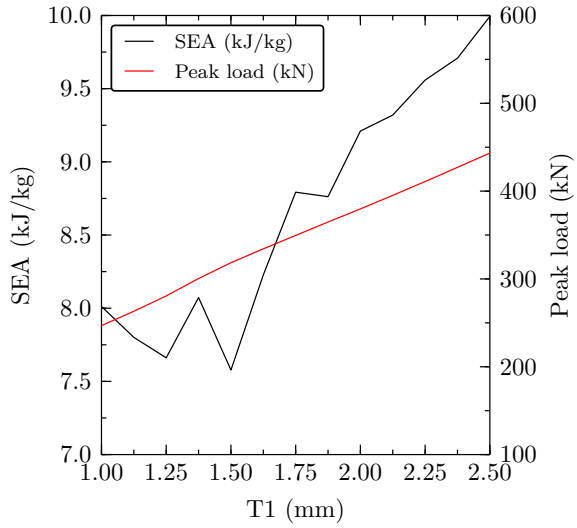

(b) *SEA* and peak load evolution with the steel thickness, T1.

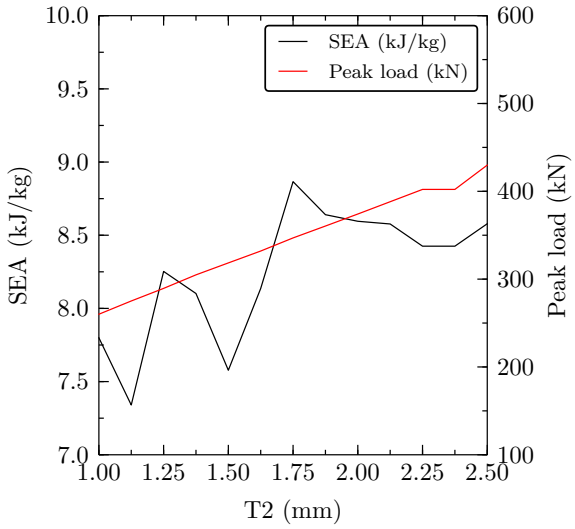

(c) SEA and peak load evolution with the honeycomb cell thickness, T2.

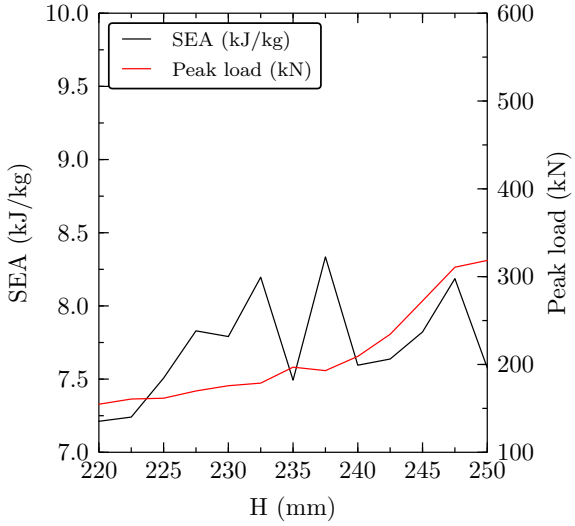

(d) SEA and peak load evolution with the honeycomb height, H1.

Figure 3.10: Parameter study results in term of SEA and peak load.

value, 319 kN. This results lead to think that the final specimen should have a honeycomb height closer to the 220 mm than to the 250 mm.

3.3.3 Optimization results

After running the optimization algorithm, the MOGA outputs a set of points that conform the Pareto front. There are two sets Pareto fronts, one obtained with MARS (figures 3.11a and 3.11b), and another one obtained using a Gaussian process (figures 3.11c and 3.11d). Although the function trends obtained from both methods are greatly resemble eachother, the Pareto fronts obtained with the Gaussian process have a less defined outline and the frontier is less clear. It is also noticeable that the Pareto sets from figures 3.11b and 3.11d have a noisier nature, caused by the strong slope discontinuities of the peak objective function and, in the case of the MARS model, because of the lower R^2 value in the approximation. Despite this, both Pareto fronts obtained with MARS have a clearly defined boundary, establishing a set of optimum designs. Therefore, this Pareto fronts are used during the rest of the research.

The two following tables show the values for the design variables and objective functions of different points from the Pareto front. Table 3.4 corresponds to points from the energy-mass Pareto front, and table 3.5 to points from the energy-peak load Pareto front.

Design variables (mm)				Objective functions		Indicator
D	T1	T2	H	E_a (kJ)	m (kg)	SEA (kJ/kg)
18.55	0.92	1.03	247.78	6.86	1.07	6.41
11.50	0.92	1.43	247.78	14.83	1.64	9.04
11.48	2.13	1.03	247.67	23.48	2.29	10.25
11.50	2.38	1.56	245.73	30.34	2.84	10.68
11.50	2.33	2.43	247.67	36.70	3.37	10.89
11.47	2.36	2.90	247.78	40.73	3.71	10.99

Table 3.4: Points from the energy-mass Pareto front shown in figure 3.11a.

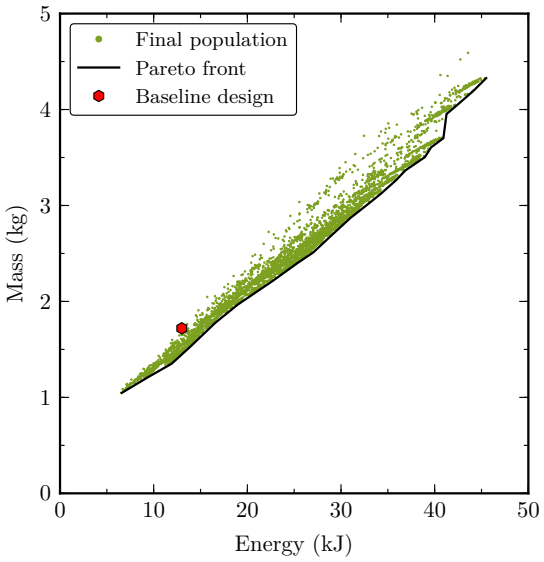

(a) $E_a - m$ Pareto front. MARS model.

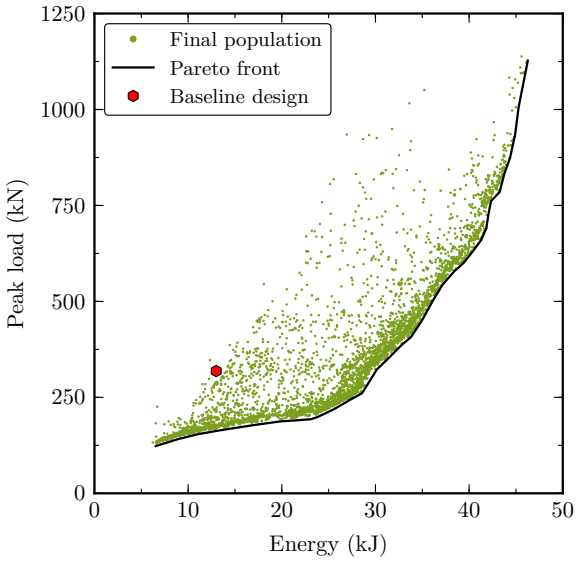

(b) $E_a - P_{peak}$ Pareto front. MARS model.

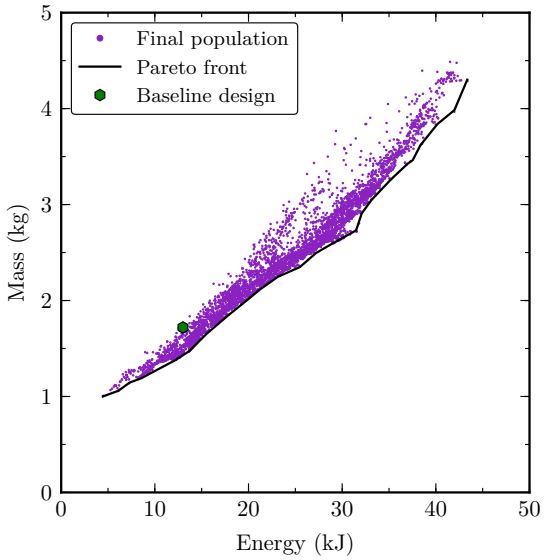

(c) $E_a - m$ Pareto front. Gaussian process.

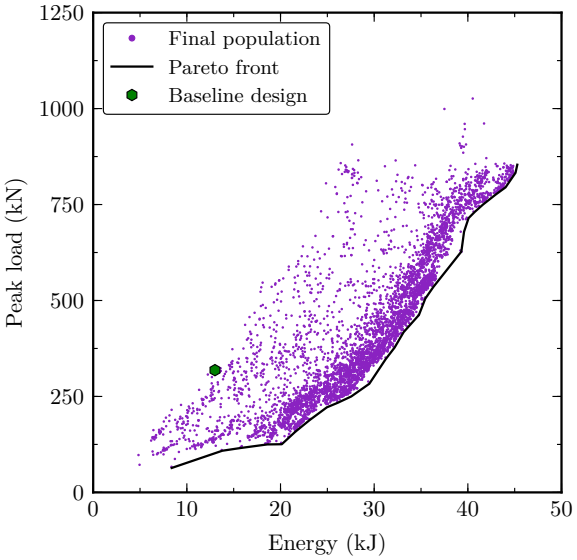

(d) $E_a - P_{peak}$ Pareto front. Gaussian process.

Figure 3.11: Pareto fronts obtained after multi-objective optimization.

Design variables (mm)				Objective functions	
D	T1	T2	H	E_a (kJ)	P_{peak} (kN)
19.89	0.96	1.10	233.84	6.62	130.44
14.80	1.80	1.01	235.18	15.55	179.55
14.48	2.44	1.02	235.08	23.66	205.74
14.29	2.44	1.63	235.58	28.91	280.62
14.21	2.44	2.72	234.27	34.53	440.08
10.73	2.44	2.94	235.92	41.88	690.49
8.21	2.44	2.97	238.46	44.83	928.50

Table 3.5: Points from the energy-peak load Pareto front shown in figure 3.11b.

The energy-mass Pareto front has a quasi-linear shape throughout the whole design space. Also, it is noted that the SEA indicator varies throughout the frontier, ranging from 6.4 kJ/kg for low energy values, to approximately 11 kJ/kg at the other end of the front. Compared to the initial specimen, which had a SEA of 7.6 kJ/kg, all models in the Pareto front that absorb more than 11 kJ have a higher SEA value. The small portion of designs that have a lower SEA confirm that most specimens improve the capabilities of the initial design. As seen in table 3.4, in order to increase the energy absorbed by the specimen the cell size is reduced, both thicknesses are increased, and the honeycomb height tends to match that of the steel tube. All of this also leads to a higher mass of the object, but increasing the SEA indicator.

The energy-peak load Pareto front starts with a linear tendency, and between the energy values of 19 kJ and 23 kJ the frontier becomes nearly horizontal. This means that in this small range the peak load is nearly stagnant even when the energy increases, an effect that was pursued in this research. After that, the frontier becomes steeper, so that a small increase of the absorbed energy demands a high peak load value increase, an undesirable effect for the model.

3.3.4 Optimum points

The initial design proposed in table 3.3 was analyzed and its results will be used as a reference for the optimum designs.

The algorithm used also provides the closest points to the utopia point, which constitute the optimum designs. Two optimum designs, designated as 1 and 2, were run again on the Abaqus software to check the fitness of the metamodel, with discordances between the surrogate and analysis lower than 6%. The force-displacement curves from the optimum designs are compared to the initial design, as shown in table 3.6.

			Optimum design (Improvement)	
	Parameter	Baseline	1	2
Design variable	D (mm)	20.00	13.13	13.31
	T1 (mm)	1.50	1.44	2.44
	T2 (mm)	1.50	1.03	1.53
	H (mm)	250.00	222.53	235.63
Objective function	E_a (kJ)	13.02	13.27 (1.9%)	29.50 (126.6%)
	m (kg)	1.72	1.68 (2.3%)	2.79 (-62.2%)
	P_{peak} (kN)	318.47	200.77 (37.0%)	298.67 (6.3%)
Indicator	SEA (kJ/kg)	7.57	7.90 (4.4%)	10.56 (39.5%)

Table 3.6: Comparison between initial design and optimum design[2]Positive values between brackets designate improvement of an objective function from the optimum over the baseline design.

The initial design has been optimized obtaining a peak load 37% smaller than the original one in the optimum design 1, with similar mass and energy absorption. It can be seen that the honeycomb height approaches the minimum value allowed, 220 mm, in order to reduce the maximum peak load. The thickness of the honeycomb also tends to the lower boundary value, with the other variables in the middle part of the design spectrum.

The optimum design 2 has a maximum peak load nearly as high as that of the initial design, but with a higher specific energy absorption. Even though the

mass is increased by 62.2%, the improvement of 126.6% in the energy absorption yields a SEA 39.5% higher than the one obtained for the initial design. In this model the steel thickness tends towards the maximum value, showing that an increase in the mass of the steel provides high specific energy absorption values. The other variables are in the middle of the design range, slightly higher than the values for the optimum design 1.

Figure 3.12 shows how the peak load from the initial design —which is the sum of the peak load from the tube and the honeycomb —splits into two peaks in the optimum designs, yielding to similar energy absorption values with smaller peak loads. The offset in the peaks is caused by the different height of both parts. After the peak load produced by the tube, the force decreases. When the peak load from the honeycomb occurs, the total force is not the sum of both peaks but the force from the honeycomb peak load and a lower value from the crushing of the tube. This second peak load is higher that the first one, which justifies the low honeycomb thicknesses of both optimum designs. If the value of the variable T2 were higher, the second peak load would be increased, and therefore so would the overall peak load. A utopian design would have both peaks equal, maximizing the area under the force-displacement curve and minimizing the maximum peak load.

3.4 Conclusions

This chapter attempts an improvement in the crashworthiness of a traditional energy absorption device, in order to increase fuel efficiency and occupant safety. For this, multi-objective structural optimization of a honeycomb-filled square tube are performed. Three objective functions —mass, absorbed energy and peak load —have been selected because of their contrasting nature and the high goodness of fit during the approximation. An initial study was carried out to determine the approximate number of multi-adaptive regression splines basis functions needed to resemble accurately the objective functions that had to be optimized. Pareto optimization was performed with a multi-objective genetic algorithm, obtaining two Pareto fronts. Results show that the initial design has

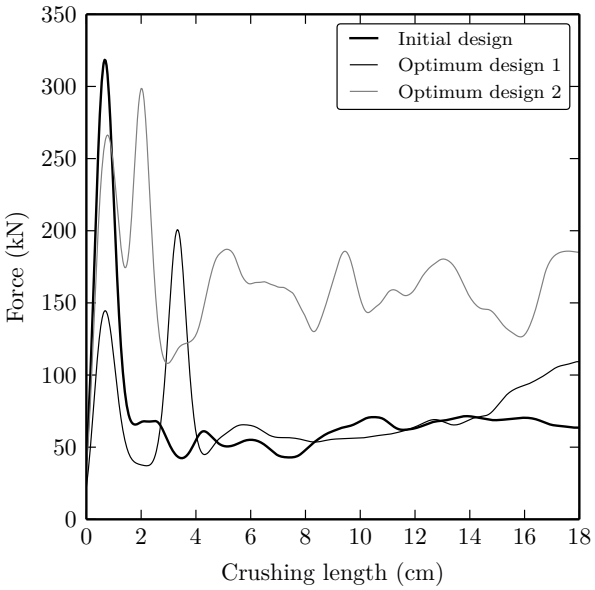

Figure 3.12: Force-displacement curves of the initial and optimum specimens.

been optimized obtaining a peak load 37% smaller than the peak load from the initial design, with similar mass and energy absorption. The initial design was also improved with a model that has a specific energy absorption 39.5% higher and a slightly smaller peak.

An initial model, the initial specimen, was selected as a reference to compare with the optimum designs which would be obtained. Also, some preliminary tests were carried out with this specimen. We proved that the interaction effect for the initial specimen accounts for 22% of the energy absorption, with no significant effects on the initial peak load. Another preliminary experiment compared the performance between an empty hollow tube and a specimen with equal mass and a glass-fiber reinforced polymer honeycomb structure inside. The latter option had an energy absorption 29.1% higher with a peak load increased by only 8.6% compared to the empty hollow tube.

The Pareto frontiers were obtained with MARS and a Gaussian process. The MARS model proved to be more adequate in this research, since it yields clearer and more stable Pareto fronts.

The energy-peak load Pareto front has a noisier nature than the energy-mass one since the peak load function has strong slope discontinuities and is approximated with a lower R^2 value than the mass function. The design variables from this model with the most influence in the peak load value are the honeycomb height and the honeycomb thickness, which greatly reduce the peak load as their value is also lowered.

The energy-mass Pareto front is clearer than the other Pareto front, being almost linear. The specific energy absorption increases as the absorbed energy and mass increase, obtaining values of up to 11 kJ/kg; when the initial model had a specific energy absorption value of 7.6 kJ/kg. The points from the energy-mass Pareto front tend to high values of the honeycomb part, therefore producing high values for the peak. Nevertheless, a reduction of this design variable would generate models with high energy absorption and lower peak load than the original model.

References

[3] European New Car Assessment Programme (Euro NCAP). *Frontal Impact Testing Protocol, Version 6.0.2*. Tech. rep. European New Car Assessment Programme (Euro NCAP), 2013.

[17] Huang, M. *Vehicle Crash Mechanics*. CRC Press, 2002.

[232] Costas, M., Díaz, J., Romera, L.E., Hernández, S., and Tielas, A. "Static and dynamic axial crushing analysis of car frontal impact hybrid absorbers". *International Journal of Impact Engineering* 62 (2013), pp. 166–181.

[239] Hou, S., Li, Q., Long, S., Yang, X., and Li, W. "Design optimization of regular hexagonal thin-walled columns with crashworthiness criteria". *Finite Elements in Analysis and Design* 43.6-7 (2007), pp. 555–565.

[20] Cook, G. R. and Johson, W. H. "A constitutive model and data for metals subjected to large strains, high strain rates and high temperatures". *Proceedings of Seventh International Symposium on Ballistics* (1983).

[304] Costas, M., Díaz, J., Romera, L., and Hernández, S. "A multi-objective surrogate-based optimization of the crashworthiness of a hybrid impact absorber". *International Journal of Mechanical Sciences* 88 (2014), pp. 46–54.

[21] BASF. *Ultramid (R) A3WG10 BK00564 Polyamide 66. Product information sheet*. 2012.

[22] *SAE Standard J211: Instrumentation for Impact Test*. Tech. rep. Safety Test Instrumentation Stds Comm, 1995.

[305] *ABAQUS 6.13 Documentation*. Dassault Systèmes. 2013.

[306] Adams, B., Bauman, L., Bohnhoff, W., Dalbey, K., Ebeida, M., Eddy, J., Eldred, M., Hough, P., Hu, K., Jakeman, J., Swiler, L., and Vigil, D. *DAKOTA, A Multilevel Parallel Object-Oriented Framework for Design Optimization, Parameter Estimation, Uncertainty Quantification, and Sensitivity Analysis: Version 5.4 Reference Manual*. Sandia National Laboratories. 2013.

4

Size and shape crashworthiness optimization of hybrid energy absorbers enclosing honeycomb and foam structures[1]

4.1 Introduction

There exist certain aircraft configurations that feature vertical struts connecting the cabin floor beams with the lower part of the main frames (see figure 4.1), offering higher structural strength under normal load situations. However, as seen in section 2.1.3.3, struts dissipate a limited amount of energy under dynamic loading. To address this limitation, this research focuses on the crashworthiness enhancement of standalone hybrid energy absorbers designed to work as vertical struts in aircraft structures. Two components are analyzed, with the first composed of an outer metallic tube filled with a honeycomb-like glass-fiber

[1] Chapter adapted from the work published as:
J. Paz, J. Díaz, L. Romera, and M. Costas. "Size and shape optimization of aluminum tubes with GFRP honeycomb reinforcements for crashworthy aircraft structures". *Composite Structures* 133 (2015), pp. 499–507;
and
J. Paz, L. Romera, and J. Díaz. "Crashworthiness optimization of aircraft hybrid energy absorbers enclosing honeycomb and foam structures". *AIAA Journal* 55.2 (2017), pp. 652–661.

reinforced polymer structure, and the second also featuring foam extrusions filling the honeycomb cells. Honeycomb structures from chapter 3 are upgraded, now featuring a cell design with variable size and shape. Hereafter, a description of the component's and methods employed is presented, as well as the results and conclusions derived from this work.

Figure 4.1: Airbus A300 fuselage section featuring vertical struts. Taken from [23].

4.2 Materials

Materials need to be selected according to structure's shape, loading conditions during service and it's energy absorption-to-weight efficiency. For the dynamic loads to which these absorbers will be subjected, metals as steel or aluminum show outstanding energy dissipation values though plastic deformation; while composite materials and foams have proved superb complementing the response

of thin-walled tubes. With this considerations, and in view of future applications in fuselage structures, the confining tube is made of an AA7075-T651 aluminum alloy used in aircraft designs. Moreover, the honeycomb inner structures are made from the glass-fiber reinforced polymer Ultramid A3WG10 BK00564 (BASF), while the polymeric foam ArmaFORM PET/W AC 135 from Armacell is used as a cell filler.

The aluminum strain-stress curves follow the modified Johnson-Cook [20] strain-rate sensitive model proposed by Børvik et al. [24]. Given the nature of this investigation, the temperature dependency is ruled out of the equation. Hence, the constitutive equation of the Mises plasticity model used to simulate the aluminum is defined as

$$\sigma_y = (A + Bp^n)\left(1 + \frac{\dot{p}}{\dot{p_0}}\right)^C , \tag{4.1}$$

where A is the material's yielding stress, B is the hardening law's amplitude modifier, p is the equivalent plastic strain, $\frac{\dot{p}}{\dot{p_0}}$ is the dimensionless plastic strain rate, and C is the strain-rate's dependency modifier. All material and model parameter values, taken from the work of Børvik et al. [25], are detailed in table 4.1. figure 4.2 provides the stress-strain curve for a model subjected to a strain rate of 0.035 s^{-1}.

E (GPa)	ν	ρ (kN/m^3)	A (MPa)	B (MPa)	n	C	$\dot{p_0}$
70.00	0.30	27.70	520.00	477.00	0.52	0.001	0.0005

Table 4.1: AA7075-T651 aluminum properties and Mises plasticity model values for equation (4.1). Taken from Børvik et al. [25].

The material constitutive model has been calibrated after the data recorded from the tensile tests by Costas et al. [18]. The expression shown in equation (4.2) was adjusted with its four parameters to fit the experimental data. The density and the Poisson's modulus have been extracted from the manufacturer's data sheets [21]. All data is listed in table 4.2.

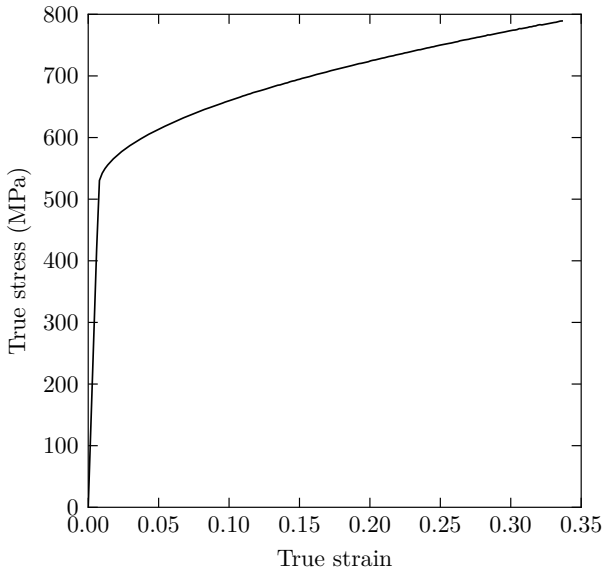

Figure 4.2: Stress-strain curve of the AA7075-T651 aluminum at a strain rate of 0.035 s^{-1}.

$$\sigma_y = \sigma_0 + \left[\sum_{j=1}^{k} Q_j \left(1 - e^{-b_j p}\right) \right], \tag{4.2}$$

where Q_j, b_j and σ_0 are material constants, and k is the number of terms used to approximate the material's response. For this material, $k = 2$, with a true strain at failure of 2.38%. figure 4.3 provides the numerical and experimental stress-strain curves for the GFRP model used.

E (GPa)	ν	ρ (kN/m^3)	σ_0 (MPa)	Q_1 (MPa)	Q_2 (MPa)	b_1	b_2
15.48	0.4	15.15	25.00	124.86	44.46	315.89	5748.46

Table 4.2: Material properties of Ultramid A3WG10 BK00564.

As for the foam, various material tests were performed by Costas et al. [18] in order to obtain its behavior under compressive loads. Despite being an orthotropic material, it was considered that the foam was loaded parallel to the extrusion

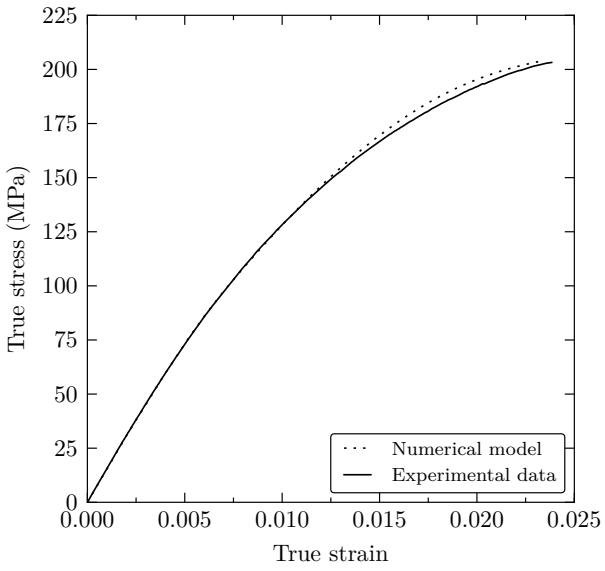

Figure 4.3: Numerical and experimental tensile stress-strain curves of the Ultramid A3WG10 BK00564 up to fracture at a strain rate of $3.25 \times 10^{-4} s^{-1}$

(or strong) direction. The mechanical properties used to model this material have been detailed in table 4.3. An isotropic foam hardening model proposed by Deshpande and Fleck [26] for metallic foams was used to model the foam's behavior. The yield surface f, which includes pressure dependency, is modeled by a Mises circle in the deviatoric stress plane and an ellipse centered in the meridional stress plane as

$$f = \sqrt{{\sigma_{\mathrm{eq}}}^2 + \alpha^2 \sigma_{\mathrm{H}}^2} - D = 0\,, \tag{4.3}$$

with σ_{eq} being the von Mises stress, σ_{H} the hydrostatic stress, α the shape factor of the yield ellipse that defines the relative magnitude of the axis, and D the size of the vertical axis of the yield ellipse.

Furthermore, a flow potential g was used to represent non-associated flow as

$$g = \sqrt{{\sigma_{\text{eq}}}^2 + \beta^2 \sigma_{\text{H}}^2} = 0\,, \tag{4.4}$$

where β represents the shape of the flow potential ellipse on the meridional stress plane, dependent on the plastic Poisson's ratio ν_{p}. figure 4.4 shows the crushable foam constitutive model with isotropic hardening along the meridional plane.

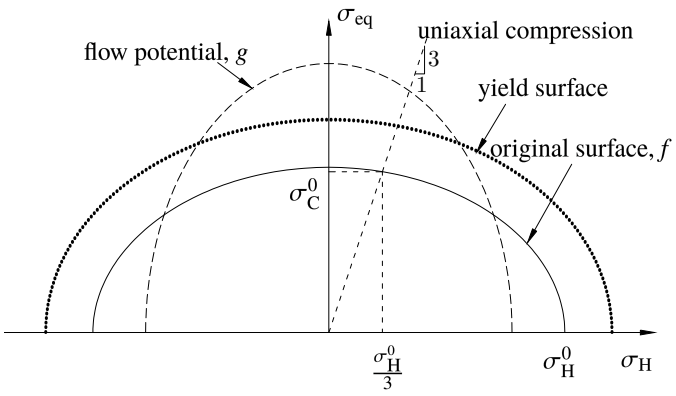

Figure 4.4: Yield surface and flow potential in the meridional plane for the crushable foam model with isotropic hardening.

Moreover, the true stress versus true strain foam curve is depicted in figure 4.5, showing the comparison of both the numerical and the analytical behavior of the material.

E	ν	ρ	α	β	ν_{p}
59.006 MPa	0.1	1.35 kN/m^3	0.729	1.7754	0.1109181

Table 4.3: Material properties of ArmaFORM PET/W AC 135.

4.3 Design variables and objective functions

Two similar specimens have been studied during this part of the research, with differences residing in the usage of foam and the cross-sectional inertia of the

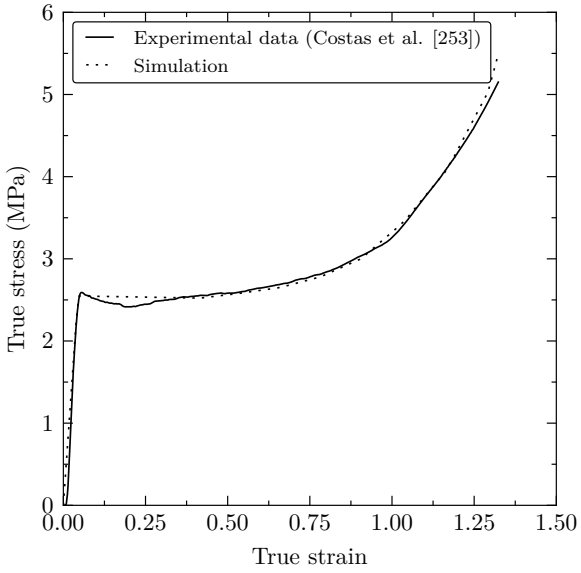

Figure 4.5: Stress-strain curve of the ArmaFORM PET/W AC 135.

tubes. Specimen A has a shorter tube edge and empty honeycomb cells, while the other device featuring foam extrusions as cell filler is referred to as specimen B.

4.3.1 Specimen A

Three design parameters and four design variables define the geometrical configuration of specimen A; being the height of the tube (500 mm), the edge-length of the tube (100 mm), and the height of the inner reinforcement (480 mm). The 20-millimeter height difference between the inner reinforcement and the tube assures an offset in the initial force peaks during the crushing process, resulting in a lower combined peak force [9].

On the other hand, the design variables chosen are the thickness of the aluminum plates (T1), the thickness of the GFRP honeycomb reinforcement (T2), the half-length of a single honeycomb cell (L1), and the honeycomb cell

shape modifier (S) (figures 4.6 and 4.7). This last variable is responsible for the honeycomb's shape optimization, and it is defined as

$$S = \frac{L2}{L1}\,. \tag{4.5}$$

The effect of the shape modifier variable is shown in figure 4.7. For a value of S=0 (figure 4.7a), the honeycomb cell is a regular hexagon. As the value of S increases, the cell shape tends to a rectangle with a length to width ratio of $1.73 : 1$, achieved for $S = 0.5$ (figure 4.7b). For values greater than $S = 0.5$, and with an upper boundary of $S = 0.75$, the cell shape resembles that of an hourglass, as shown in figure 4.7c.

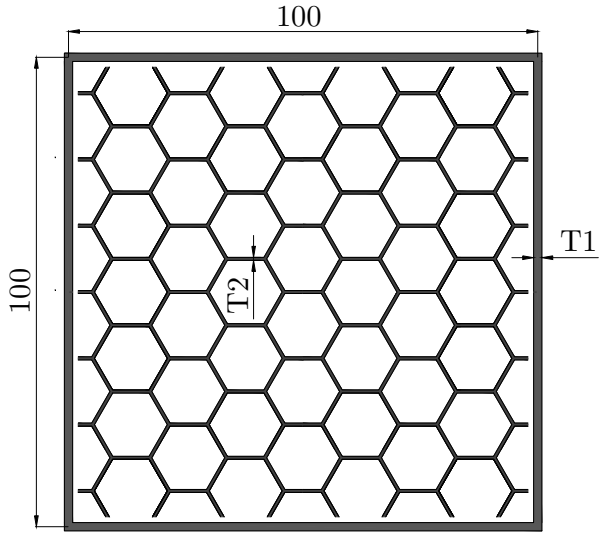

Figure 4.6: Top view of the specimen. All values in millimeters.

The initial values and upper and lower bounds of all design variables, as well as the description of which part they belong to, are listed in table 4.4.

Concerning the objective functions, different options have been considered. Simple metrics, such as the total energy absorbed or the mass of the structure, are usually taken into account. However, in an attempt to improve lightness

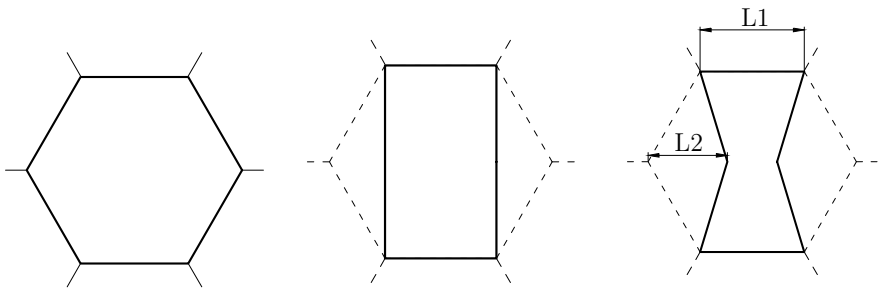

(a) Regular hexagon. S = 0. **(b)** Rectangular cell. S = 0.5. **(c)** Hourglass shape. 0.5 < S < 0.75.

Figure 4.7: Different honeycomb cell shape configurations.

		Bounds		
Part	Variable	Lower	Upper	Initial Value
Tube	T1	0.87	2.44	1.50
Honeycomb	T2	1.00	3.00	1.50
	L1	5.88	14.30	10.00
	S	0.00	0.75	0.00

Table 4.4: Bounds and initial values of design variables for specimen A. All dimensions in millimeters.

and robustness at a time, the maximization of the specific energy absorption ratio (SEA) has also been considered. Furthermore, and for the benefit of the passengers of the aircraft and its integrity, the peak force values are minimized. By doing so, the survivability odds increase, as well as reducing the damage to the craft and occupants. The four metrics selected are the absorbed energy (E_{a}), the mass of the specimen (m), the specific energy absorption (SEA) and the maximum force suffered during the crushing (P_{peak}).

All responses except the mass have been obtained from the force-displacement curves resulting from the crushing by means of finite element analysis, all limited to $\delta_{\max} = 0.4$ m or a stroke efficiency $St_{\mathrm{e}} = 0.8$. These data is post-processed

with a standard SAE 600 filter [22], as recommended by Huang [17], removing the high-frequency noise with a cutoff frequency of 1000 Hz.

The reason for choosing these objective functions derives from the necessity of a reliable crashworthiness optimization. As in any multi-objective optimization, the objective functions need to relate to different aspects of the model's capabilities. By maximizing the E_{a}, structural deformations are localized in the strut area, since less energy needs to be absorbed by other surrounding structures. Furthermore, reducing the element's mass decreases the building cost and fuel consumption as well. Nevertheless, single-objective optimization requires only one metric, and maximizing the SEA ratio would entail both a maximization of the E_{a} and a minimization of the specimen's mass. However, even though they provide important information about the model's responses, metrics that derive from ratios tend to have noisier behaviors in nonlinear problems, thus also justifying the use of the first two metrics as objective functions. Finally, the occupant's safety is always considered by reducing the maximum deceleration experienced at the end of the tube opposite to the impacting mass' strike, P_{peak}.

4.3.2 Specimen B

Specimen B is also defined by three design parameters and four design variables. A 500 mm hollow square tube is proposed, with a 150 mm edge. Both the honeycomb and foam reinforcements measure 50 mm less than the outer tube in order to reduce the combined peak force during the crushing process. The design variables are homologous to those from specimen A, being the thickness of the aluminum (T1) and GFRP (T2), as well as the cell's shape modifier (S) and size (L1). The initial values and bounds of all design variables, as well as the description of which part they belong to, are listed in table 4.5.

The foam shape adapts to that of the void left by the honeycomb cells. However, a one-millimeter gap is left between the honeycomb and foam opposing surfaces in order to facilitate the convergence of the numerical model as the foam has a void to slightly expand. This has no significant impact on the component's

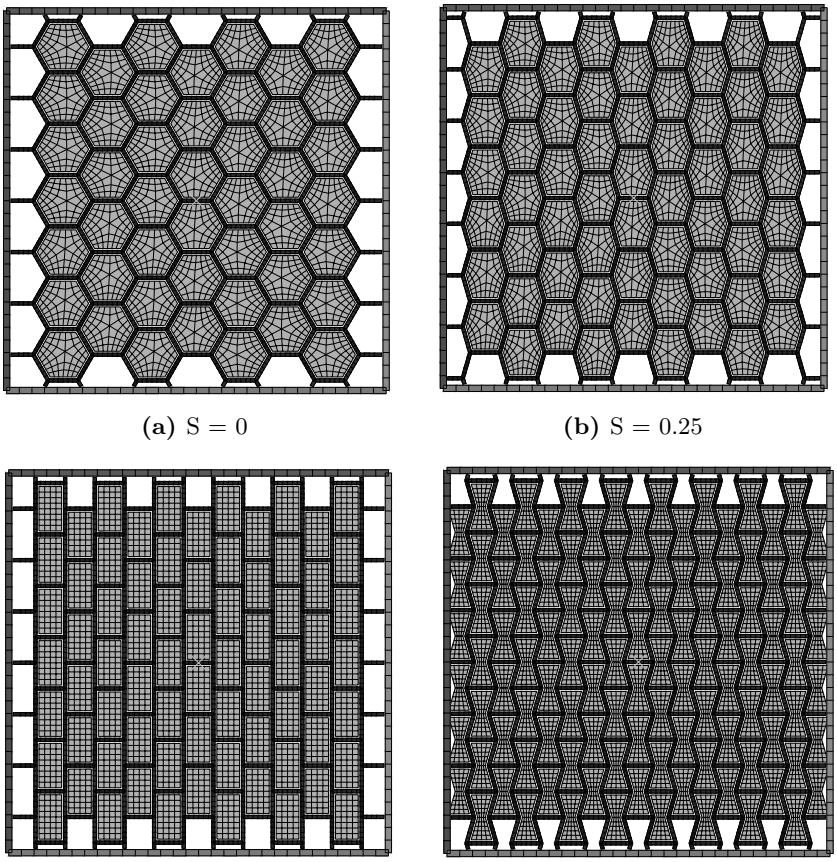

(a) S = 0 **(b)** S = 0.25

(c) S = 0.5 **(d)** S = 0.75

Figure 4.8: Significant cell shapes for specimen B.

		Bounds		
Part	Variable	Lower	Upper	Initial Value
Tube	T1	1.00	2.50	1.50
	T2	1.00	3.00	1.50
Honeycomb	L1	9.00	18.00	10.00
	S	0.00	0.75	0.00

Table 4.5: Bounds and initial values of design variables for specimen B. All dimensions in millimeters.

performance and, by doing so, the assembly of the component would be less demanding, since this gap eases the insertion of the foam into the cells.

Another design aspect that can be perceived in figure 4.8 is that the gaps between the honeycomb structure and the tube are empty when the full size foam structure cannot fit. This facilitates the modeling process and assembly of the component, in view of the fact that custom-cut pieces would increase the cost of the design and building processes.

A total number of five objective functions have been considered, three of them being simple metrics and the other two a combination of them. The first three functions are the energy absorbed, the component's mass and the peak crushing force. Furthermore, the specific energy absorption and a cost function (C_t) have been computed. This last function has been approximated by multiplying each part's mass by different estimated weight factors that consider the price of the materials. Hence, the component's cost is approximated according to:

$$C_\mathrm{t} = \lambda_\mathrm{a} m_\mathrm{a} + \lambda_\mathrm{g} m_\mathrm{g} + \lambda_\mathrm{f} m_\mathrm{f}\,, \tag{4.6}$$

where λ_a, λ_g and λ_f are the weight factors for, respectively, the aluminum, GFRP and foam; and m_a, m_g and m_f are their masses. Four weight combinations have been used (table 4.6), all of them with a fixed $\lambda_\mathrm{a} = 1.0$ and variable λ_g and λ_f. This variation in the weights is implemented to consider the cost fluctuation in the manufacturing process. For the first configuration, SC1, all weights are 1.0,

so that the C_t (and the optimization of this function) is identical as the mass of the component.

Configuration	λ_a	λ_g	λ_f
SC1	1.0	1.0	1.0
SC2	1.0	0.85	0.85
SC3	1.0	1.15	0.85
SC4	1.0	0.85	1.15

Table 4.6: Different weight factors for the cost function from equation (4.6).

With these five objective functions, the most significant aspects for the construction of a viable strut are considered: its effectiveness as an energy-absorption device (through the measurement of the E_a and *SEA*), the maximum deceleration transmitted to the surrounding structure (by monitoring P_{peak}), and its cost (C_t). As in the case of specimen A, $\delta_{max} = 0.4$ m.

4.3.3 Analysis settings

Concerning the mesh, different sizes were used throughout the model, according to the material's behavior and the part's shape. A mesh sensitivity analysis (table 4.7) showed that the outer tube and the honeycomb should be modeled with quadrilateral shell elements with reduced integration, with edges approximately four millimeters long. This mesh size ensures a stable collapse of the tube, with the same number of folds and similar absorbed energy obtained with finer meshes. The usage of solid elements for this parts is disregarded due to the large number of elements required for the analysis and the consequently high computational cost. For the foam, solid eight-node elements with reduced integration were used, with an edge of four millimeters, and distortion and enhanced hourglass controls to ensure convergence. A three-dimensional cut of the baseline meshed model is presented in figure 4.11.

The finite element simulation settings attempt to replicate the conditions in which the structure would be crushed, had it been implemented in a full-scale

Mesh size (mm)	Energy absorbed (kJ)
16	133.833
13	127.618
10	119.206
8	117.674
6	112.036
5	108.948
4	106.688
3	105.843
2	105.830

Table 4.7: Energy absorbed values for different mesh sizes.

fuselage. The first step of the process forces a two-millimeter triggering on the upper edges of the aluminum tube in order to obtain a regular collapse mode and reduce the initial peak force in the subsequent steps. figures 4.9a and 4.9b show the difference between two identical specimens with the only the non-triggered and triggered collapse schemes, with this last one having a more organized fold distribution. The initial peak force of the triggered specimen is also 31% lower (figure 4.10).

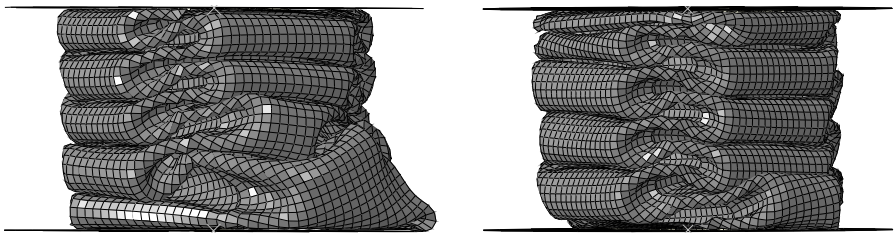

(a) Non-triggered collapse scheme. **(b)** Triggered collapse scheme.

Figure 4.9: Comparison of the collapse modes of specimen A.

To determine the impact velocity, the test conditions simulated by other authors are taken into account (table 4.8). Its diversity is relatively moderate, with values often between 6.5 m/s and 9.5 m/s. As for this set of experiments, specimen A is crushed at a constant velocity of 10 m/s, while specimen B is subjected to 15 m/s considering its increased stiffness due to the foam filler.

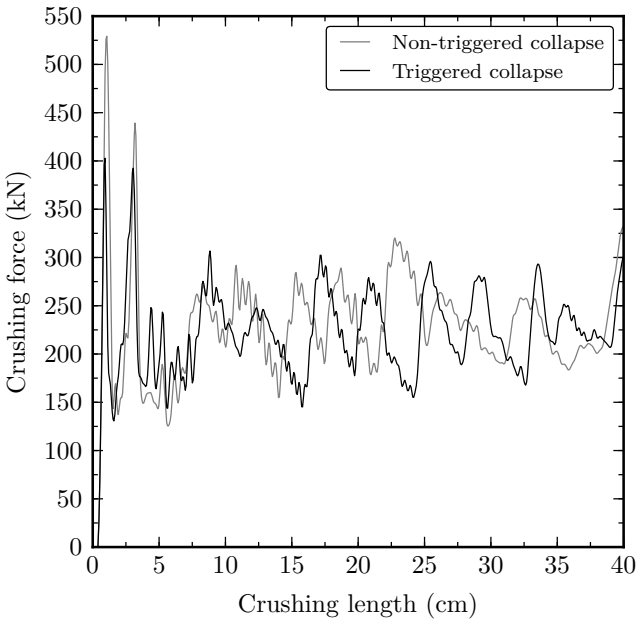

Figure 4.10: Force - displacement curves of the non-triggered and triggered collapse schemes for specimen A.

For the construction of the surrogate model, the MARS technique from chapter 3 is used together with the MLS approach, discarding Gaussian processes altogether. The samplings for the simulations with specimens A and B consist of 500 and 600 samples respectively, enough to obtain reasonably low values for the *RMSE* metric and over 0.9 for the R^2 indicator. Each sample has been run with the explicit module of the Abaqus 6.14 FEA package [33]. The software allows two different parallelization schemes: domain or loop parallelization. Preliminary tests showed that the domain parallelization with eight processors per sample resulted in competent computing times for the analysis, with simulations needing approximately six hours to complete. As for the optimization procedure, the genetic algorithm was tuned to achieve trustworthy data, yielding the best results with the settings from table 4.9 The construction of the surrogate model and the surrogate-based optimization procedures have been computed with the DAKOTA 6.1.0 framework [19]. Both the Abaqus and the DAKOTA softwares are run on a

Source	Impact velocity (m/s)
Zou et al. [27]	6.67
Heimbs et al. [28]	6.80
Zheng et al. [14]	7.00
Meng et al. [15]	7.40
Fasanella et al. [29]	7.74
Adams and Lankarani [30]	9.00
Adams et al. [31]	9.15
Jackson et al. [32]	9.45
Ren and Xiang [16]	24.5
Mean	9.75

Table 4.8: Experiment and impact velocity correlation for FEM simulations.

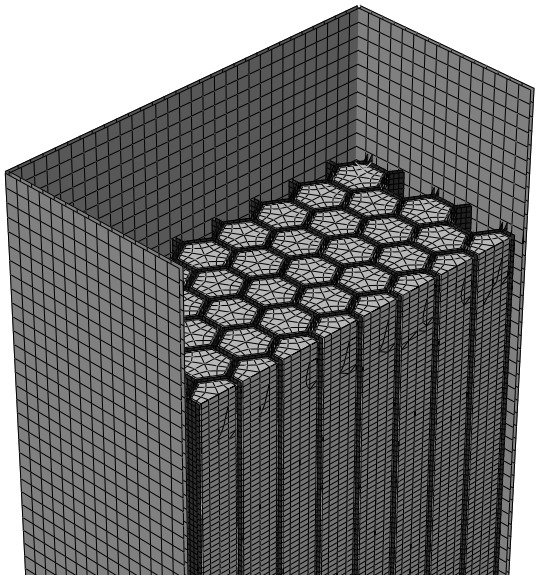

Figure 4.11: Three-dimensional cut of the baseline model for specimen B.

high performance computing cluster, with a theoretical peak performance of 7.6 TFLOPS.

Parameter	Value
Population size	500
Offset normal mutation rate	0.8
Two-point crossover probability	0.8
Elitism	50
Maximum allowed individuals	10^5

Table 4.9: Configuration parameters for the JEGA library optimization algorithms.

4.4 Results

4.4.1 Specimen A

4.4.1.1 Initial results

Results and their validity closely depend on the accuracy of the surrogate model. The R^2 and the root mean squared error (RMSE) metrics have been used to assess the accuracy of two surrogate models, with the RMSE being computed under a 10-fold cross-validation technique. table 4.10 compares a second order moving least squares model and a multivariate adaptive regression splines model with a maximum of 74 basis functions. The results show a better overall performance of the MLS model, with a higher R^2 and lower RMSE values than the MARS approximation. Therefore, the surrogate-based optimization is performed with the MLS model.

4.4.1.2 Single-objective optimization results

The first strategy applied was a single-objective optimization with the SEA as the objective function. This was performed both unconstrained and constrained with a peak force limit of 250 kN, as shown in table 4.11. With the design variables given by the algorithm for the optimum designs using the surrogate model, new models were calculated to check for consistency in the results, obtaining errors between the surrogate model and the FEA below 5%.

Method	Metric	R^2	RMSE	
MLS	m	0.9985	0.1307	kg
	E_a	0.9618	19.8514	kJ
	P_{peak}	0.9903	70.4558	kN
	SEA	0.8789	7.0793	kJ/kg
MARS	m	0.9938	0.1398	kg
	E_a	0.8127	21.0837	kJ
	P_{peak}	0.9367	81.2864	kN
	SEA	0.2026	6.8470	kJ/kg

Table 4.10: R^2 and RMSE values for the different metrics of two surrogate models for specimen A.

When no maximum force limit is specified, the optimum design tends to the highest thicknesses and cell size, with minor changes from the original cell shape. Compared with the initial design, the SEA is increased by 136.67%, but also harming the P_{peak} function by an increment of 46.14%. Still, the much smaller effect on the P_{peak} than on the SEA shows the advantage of this design over the initial specimen.

Given the importance of the P_{peak} function, a peak force limit value was set to 250 kN. The result is a specimen which betters the initial design's SEA by 65.34% while maintaining the constraint and reducing P_{peak} by 18.89%. The resulting cell shape (S = 0.27) differs noticeably from the regular hexagon, as depicted in figure 4.12.

In order to identify to which extent the size optimization is beneficial, the optimization was also computed fixing the cell with a regular hexagonal shape, thus eliminating this design variable from the optimization process. Results show a SEA value 16.30% higher for the non-regular honeycomb cell shape for an equal peak force constraint, with a comparison between the force-displacement evolution of the initial and both optimum designs offered in figure 4.15.

Furthermore, figure 4.13 depicts the objective function value evolution for the constrained optimization as the algorithm performs function evaluations. Starting from a value slightly over 25 kJ/kg, the SEA increases until the 1000th evaluation,

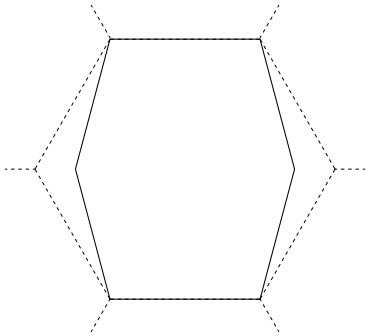

Figure 4.12: Cell shape of the optimum for the single-objective constrained optimization of specimen A.

where the objective function value is already near the global optimum. The objective function reaches its maximum at approximately the 2500th evaluation, thus justifying the use of surrogate models throughout this investigation.

Model	Design variables (mm)				Objective function	Constraint
	L1	T1	T2	S	SEA (kJ/kg)	P_{peak} (kN)
Initial	6.50	1.35	1.00	0.00	15.58	307.77
Unconstrained	14.27	2.99	2.55	0.07	36.88	449.76
Constrained	14.24	2.17	1.43	0.27	25.76	248.89
	14.27	1.98	1.46	0.00	22.15	241.95

Table 4.11: Single-objective optimization results of specimen A.

4.4.1.3 Multi-objective optimization results

The first multi-objective optimization performed to the surrogate model yields a Pareto frontier opposing SEA and P_{peak}, depicted in figure 4.16.

The SEA - P_{peak} frontier has been tabulated with some representative points in table 4.12. For low SEA and P_{peak} values, the specimen tends to low thicknesses of both components, with a large cell size and a significant shape variation

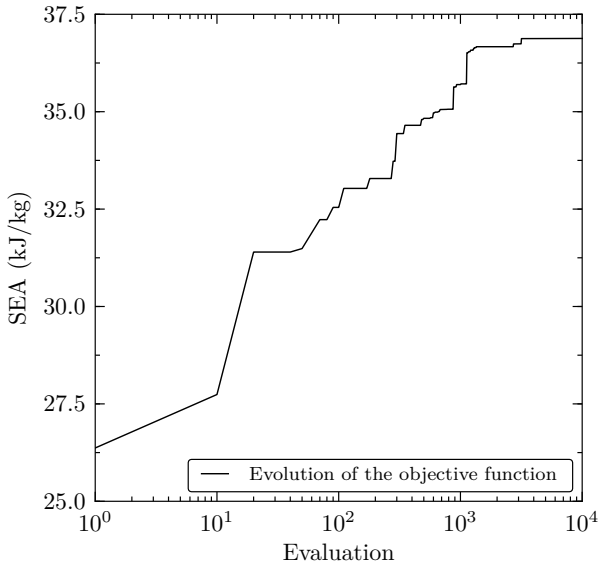

Figure 4.13: Objective function evolution.

compared to the regular hexagon. The trend observed as the objective function values increase is that of reducing the cell size, increasing the aluminum thickness and changing the cell towards the regular hexagonal shape. The performance of these specimens is remarkably convenient, since the SEA is significantly improved with little effect on the P_{peak}. However, the opposite effect occurs after the 26 kJ/kg threshold, when the honeycomb thickness increase noticeably harms the peak force, which had been kept below 250 kN. The right end of the Pareto front has again a lower slope, as the cell size and both thicknesses increase, and the cell shape is also slightly affected. The baseline model is strongly dominated by the results on the Pareto front, with designs that reduce its peak force by over 55% or increase the SEA up to 65%.

The Pareto front from figure 4.17 shows the trade-off between mass and energy absorbed, with some of its representative values listed in table 4.13. The evolution of the variables shows greater mass and energy absorbed as the cell size decreases and the thicknesses increase. The cell shape, always a non-regular hexagon, takes

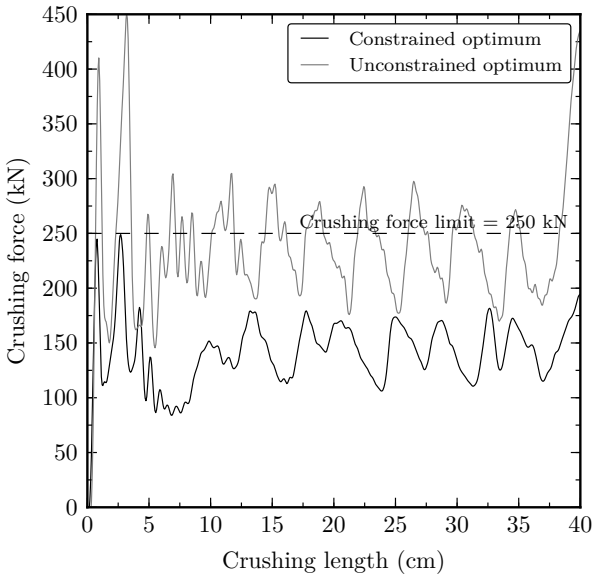

Figure 4.14: Force - displacement curves of the unconstrained and constrained optima of specimen A.

Design variables (mm)				Objective functions	
L1	T1	T2	S	SEA (kJ/kg)	P_{peak} (kN)
13.51	1.25	1.02	0.31	14.39	135.63
12.51	1.40	1.02	0.17	17.41	165.35
11.40	1.82	1.08	0.02	24.44	199.22
9.55	1.82	1.12	0.03	25.69	240.55
12.66	2.17	2.00	0.04	26.16	377.99
14.19	2.97	1.69	0.08	34.12	418.32
12.55	2.99	2.48	0.10	35.18	508.42

Table 4.12: Points from SEA - P_{peak} Pareto front of specimen A.

diverse values of S, ranging between 0.17 and 0.39 for the greater part of the design space. The section of the frontier for mass values below 5.5 kg has a pseudo-linear trend, maintaining a proportion between the energy absorption and the mass increase. In the last part of the front the utmost energy absorption

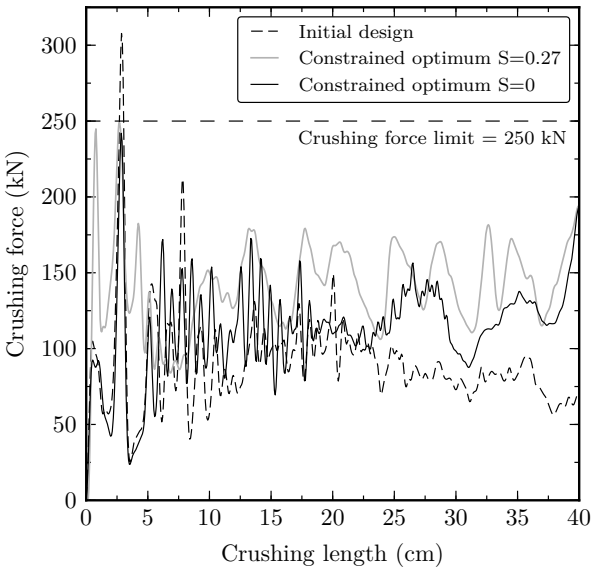

Figure 4.15: Force - displacement curves of the initial design constrained optima of specimen A.

is achieved with a hourglass cell shape, but significantly increasing the mass of the specimen. It is also remarkable the progress of the SEA, used in this case as an indicator. The highest values, in the vicinity of 31 kJ/kg, are obtained towards the middle and right end of the Pareto front, always with modified cell shapes, proving that the regular hexagonal honeycomb shape is not the most advantageous for these load cases.

4.4.2 Specimen B

4.4.2.1 Single-objective optimization

SEA optimization

In this case, the baseline model is optimized using the single-objective algorithm. Since the SEA includes both the energy absorbed by the component and its

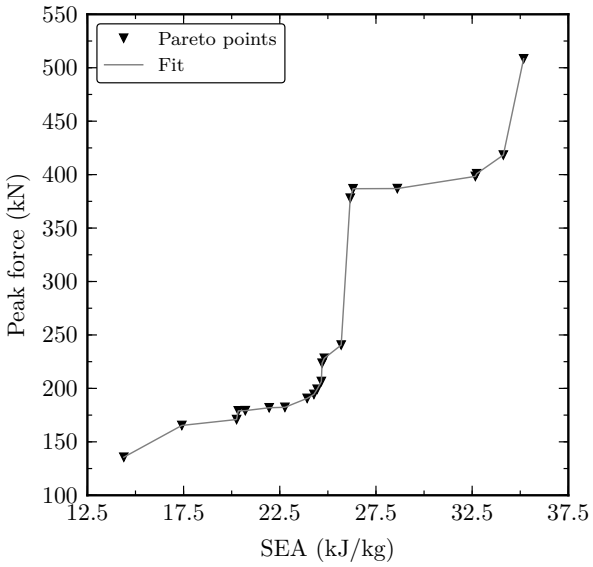

Figure 4.16: SEA - P_{peak} Pareto front of specimen A.

Design variables (mm)				Objective functions		Indicator
L1	T1	T2	S	m (kg)	E_{a} (kJ)	SEA (kJ/kg)
12.55	1.44	1.02	0.31	1.74	34.96	20.09
12.58	2.23	1.12	0.17	2.12	55.40	26.13
11.40	2.99	1.02	0.30	2.58	79.63	30.86
6.47	2.97	1.02	0.35	3.41	106.31	31.18
6.25	2.99	1.39	0.39	4.15	128.51	30.97
6.44	2.97	2.82	0.18	5.64	167.80	29.75
6.44	2.44	2.82	0.74	8.17	187.44	22.94

Table 4.13: Points from mass - E_{a} Pareto front of specimen A.

mass, it was chosen as the objective function. The first optimization performed yielded an optimum with a 26% higher specific energy absorption compared to the baseline model (table 4.14), a noticeable increase in the aluminum's thickness and a cell shape near the rectangle (figure 4.18). This shape is the most efficient for the component proposed, since it yields the lowest GFRP mass and, therefore,

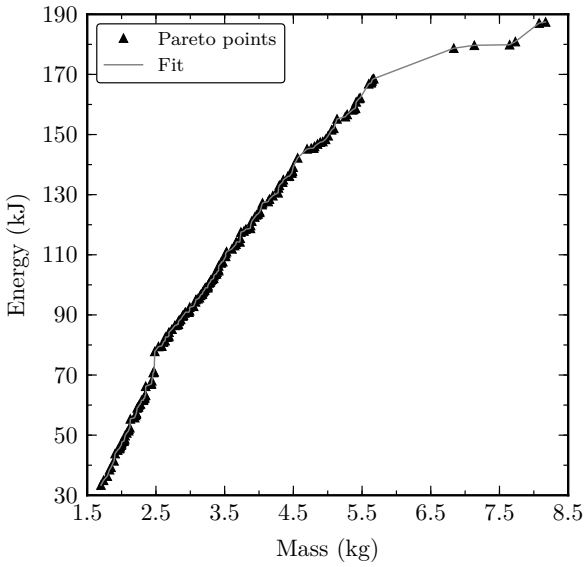

Figure 4.17: Mass - E_a Pareto front of specimen A.

allows for higher foam mass to fill the component. However, the peak force is also increased by 25% (figure 4.19) due to the thicker materials. In order to solve this problem, another *SEA* optimization is sought, but this time the value of P_{peak} is limited to 420 kN, which is lower than the peak force of the baseline model. The result is still an optimum with a *SEA* value 22% higher than that of the baseline model, but complying with the maximum crushing force limit. In this model, the cell size and the fiber's thickness are reduced, with a cell shape between the regular hexagon and the rectangle.

Furthermore, two *SEA* optimizations are performed on modified components. For the model with no foam, the optimum has a *SEA* value slightly lower than the baseline model with the foam, and 28% lower than the unconstrained optimum, thus proving the effectiveness of adding foam to the proposed component. For the model with no honeycomb and a single foam block inside, its *SEA* is the highest among the results obtained. However, the energy absorbed is less than 75 kJ, and without any changes in the tube's thickness boundaries, this value

cannot be surpassed, thus yielding efficient components but with no room for improvement through optimization techniques.

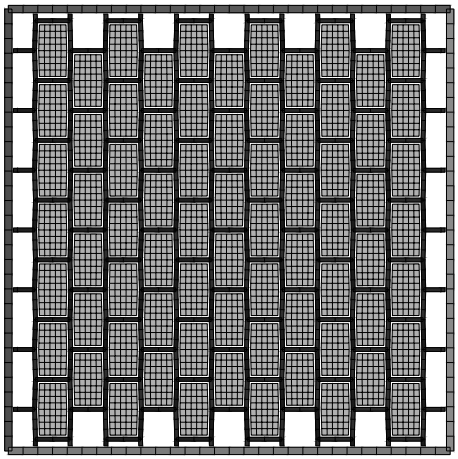

Figure 4.18: Top view of the optimum model for the single-objective *SEA* unconstrained optimization of specimen B.

Model	Design variables (mm)				Objective function	Constraint	Metric
	L1	T1	T2	S	*SEA* (kJ/kg)	P_{peak} (kN)	E_{a} (kJ)
Baseline	10.00	1.50	1.50	0.00	19.04	425.97	87.60
Unconstrained	11.72	2.47	1.28	0.48	24.04	532.25	125.99
Constrained	9.63	2.49	1.01	0.20	23.17	418.78	109.44
No foam	14.73	2.50	1.10	0.28	18.76	424.30	64.93
Only foam		2.50			27.82	377.50	74.36

Table 4.14: Single-objective *SEA* optimization results of specimen B.

Cost optimization

Another single-objective optimization is carried out, only this time the objective function is the cost of the component. The four configurations from table 4.6

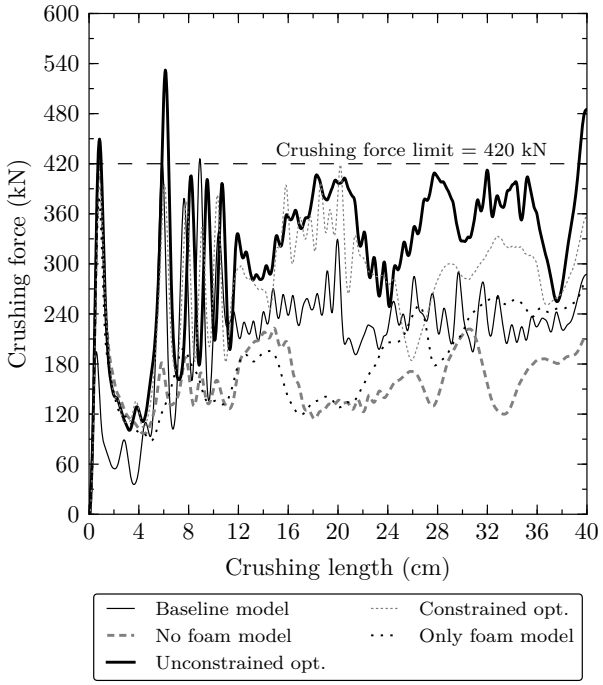

Figure 4.19: Baseline component compared to the model without foam, the model with only a foam filling, and the constrained and unconstrained optima of specimen B.

were used. The optimization procedure comprised the minimization of C_{t}, while complying with two boundary conditions:

$$P_{\mathrm{peak}} \in [254.00, 256.00] \tag{4.7}$$

$$SEA \in [19.50, 20.00] \tag{4.8}$$

The optima obtained are compared to the baseline model in table 4.15. It can be seen that the specific energy absorption of all models is similar, and even with a peak force constraint 40 % lower than the baseline model, the hypothetical cost of the component is lowered up to 40 %. This is achieved by increasing the cell size and reducing the GFRP thickness to the lowest value allowed, as well as minor cell shape variations for all four optimized combinations.

Model	Design variables (mm)				Objective function	Constraint	
	L1	T1	T2	S	C_t	*SEA* (kJ)	P_{peak} (kN)
Baseline	10.00	1.50	1.50	0.00	4.37	19.04	425.97
SC1 opt	17.71	1.88	1.00	0.26	3.31	19.69	254.77
SC2 opt	16.85	1.86	1.00	0.24	2.62	19.59	255.12
SC3 opt	16.68	1.82	1.00	0.14	2.97	19.53	255.07
SC4 opt	16.76	1.85	1.00	0.15	2.90	19.56	255.07

Table 4.15: Single-objective C_t optimization results of specimen B.

Finally, the C_t function evolution for the SC4 case along the genetic algorithm is monitored. As seen in figure 4.20, during the first 500 function evaluations, the values for C_t are rather disperse. However, after that point, they stabilize and range between the values of 2 and 5, with a thicker point-cloud around the 2.90 value, which, as seen in table 4.15, is the optimum.

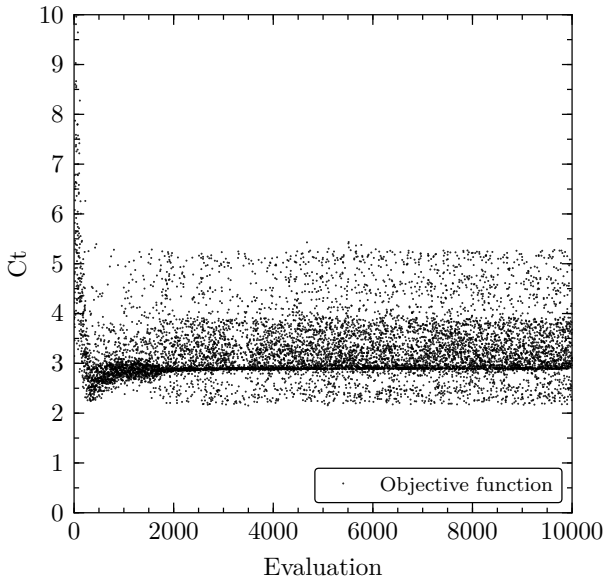

Figure 4.20: Evolution of the cost function during the single-objective optimization of specimen B for the SC4 case.

4.4.2.2 Multi-objective optimization

Three different multi-objective optimizations have been executed, all of them with two objective functions: m - E_a, *SEA* - P_{peak} and *SEA* - C_t.

Mass - E_a optimization

The two Pareto frontiers obtained from the optimization are presented in figure 4.21. As to further analyze the enhancement provided by the foam, the multi-objective optimization process is run on the metamodel without this material. The energy dissipation capability of components between two and three kg rapidly increases from 25 to nearly 75 kJ, reaching *SEA* values of 20 kJ. However, this efficiency decreases for specimens with higher mass as the Pareto front's slope is reduced, leading to 11-kilogram designs with *SEA*s lower than 12 kJ/kg. The behavior can be explained by understanding contribution of each part to the crushing process of the device. In the first region of the Pareto front, the efficiency gain can be attributed to the bracing effect of the inner reinforcement, increasing the number of folds developed as seen in chapter 3. However, once a certain stiffness of the core is reached, increased energy absorption entails thicker tube tube walls, challenging the design essence of a hybrid energy absorption device.

As an answer to this efficiency limitation if higher energy dissipation values were required, a similar optimization procedure was performed featuring foam blocks for increased absorption capabilities. The behavior of such absorbers is tabulated in table 4.16, where the *SEA* indicator is also presented. As the mass and energy absorbed increase, the cell size gradually decreases, since a smaller cell size enlarges the mass of the GFRP in the component, and, consequently, the energy absorbed. Moreover, the aluminum and the GFRP thicken. The aluminum thickness is on the upper boundary for components with a mass between 4.5 and 12 kg, thus showing its significant influence and behavior when seeking high *SEA* values. The cell shape swifts from the regular hexagon until it ultimately reaches the hourglass shape, since this configuration increases the GFRP mass of the

model, and therefore, the energy the component absorbs. However, the hourglass shape is not as efficient as the rectangular configuration, as revealed with the slight decrease of the *SEA*.

Concerning the *SEA* indicator, its value increases from 15 kJ/kg until reaching a maximum of 24 kJ/kg for components with a mass in the vicinity of five kilograms. After that, it progressively decreases again to values near 20 kJ/kg. This behavior shows the efficiency enhancement of components as their mass increases. However, the maximum value of 24 kJ/kg is obtained with a similar configuration to the one shown in section 4.4.2.1, with thick aluminum, low GFRP thickness, and a rectangular cell with an intermediate size.

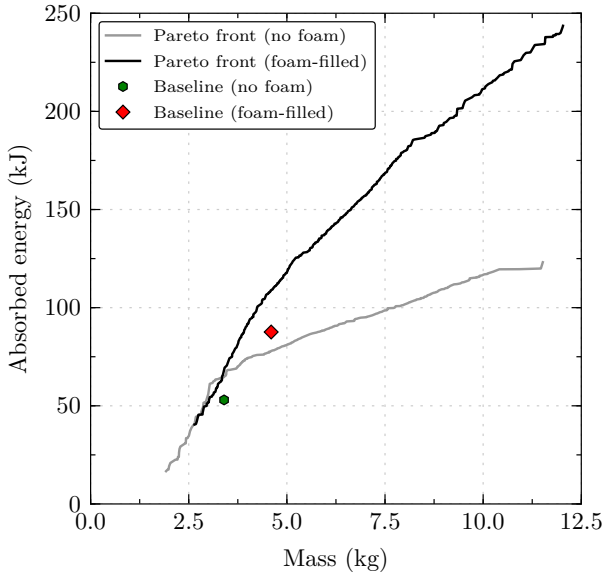

Figure 4.21: Mass - E_a Pareto fronts of specimen B. Designs with and without foam extrusions.

SEA - P_{peak} optimization

The second multi-objective optimization is the one that confronts *SEA* and P_{peak} (figure 4.22). Results are significantly non-linear, in contrast with the

Design variables (mm)				Objective functions		Indicator
L1	T1	T2	S	m (kg)	E_a (kJ)	*SEA* (kJ/kg)
17.81	1.08	1.17	0.10	2.65	40.46	15.29
15.24	1.97	1.02	0.31	3.60	74.96	20.80
16.37	2.49	1.02	0.54	4.47	106.54	23.83
11.68	2.49	1.23	0.47	5.15	123.55	24.00
9.17	2.49	1.80	0.31	6.65	151.07	22.70
9.17	2.49	2.82	0.16	8.26	185.71	22.50
9.57	2.49	2.69	0.62	10.05	211.73	21.08
9.16	2.49	2.89	0.73	12.03	243.61	20.24

Table 4.16: Points from mass - E_a Pareto front of specimen B.

mass - E_a Pareto frontier, mainly caused by the variation of the aluminum's thickness. As the tube thickens, the increase on the peak force is greater than the increase obtained for the *SEA* objective function due to the impact simulation's characteristics. Again, the cell size decreases to obtain higher *SEA* - and P_{peak} - values, but it never surpasses the 11.5 millimeter threshold, as it would harm both metrics. The thickness of the aluminum increases to its upper boundary, but the GFRP stays thin throughout the frontier, showing the greater contribution of the aluminum to high specific energy absorption values. This is caused by the differences between the collapse mechanisms of both materials, since the ductile nature of the metal allows the formation of folds and, therefore, a higher energy absorption without increasing the initial peak force. Lastly, the cell shapes that yield the highest *SEA* are those close to a rectangle, as it could also be seen in the mass - E_a front (table 4.16) and the single-objective *SEA* optimization, since other shapes introduce more GFRP in the component and reduce the mass of the foam.

SEA - C_t optimization

The last optimization confronts the *SEA* and the component's cost. Four Pareto fronts are obtained, since the four different cost weights combinations from table 4.6 were used. The graphs from figure 4.23 show this four frontiers, with

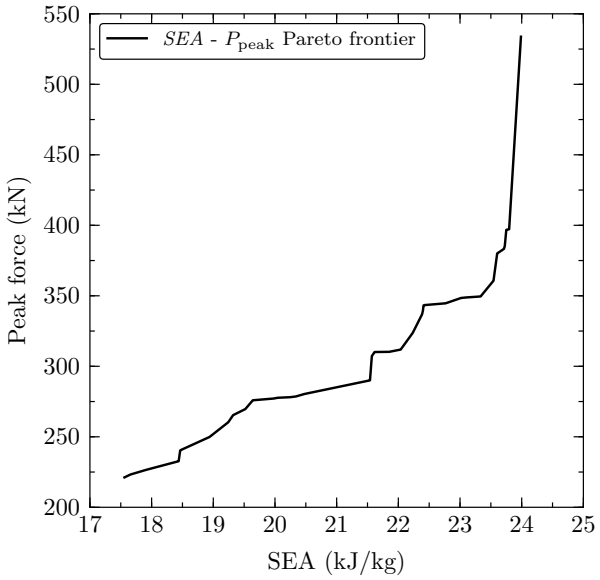

Figure 4.22: *SEA* - P_{peak} Pareto front of specimen B.

Design variables (mm)				Objective functions	
L1	T1	T2	S	*SEA* (kJ/kg)	P_{peak} (kN)
17.30	1.48	1.07	0.16	17.56	221.19
16.77	1.61	1.02	0.27	18.46	240.39
15.76	1.92	1.02	0.16	20.05	277.67
16.80	2.15	1.07	0.39	21.85	310.26
14.73	2.49	1.02	0.07	22.41	343.19
15.62	2.48	1.02	0.50	23.71	383.25
11.72	2.47	1.28	0.48	24.05	532.25

Table 4.17: Points from *SEA* - P_{peak} Pareto front of specimen B.

a noticeably similar shape, but showing a certain offset of the frontier using the SC2 weights. This happens due to the small (but reasonable) reduction of the weights used in the SC2 cost function. The combination named SC1, where $\lambda_{\text{a}} = \lambda_{\text{g}} = \lambda_{\text{f}} = 1.0$ has a special interest, since $Ct = m$, and the *SEA* - C_{t} front translates into a *SEA* - m frontier. As seen in table 4.18 and the variables'

evolution from figure 4.24, the cell size tends to the maximum allowed in order to obtain a higher *SEA*, as it introduces the least GFRP on the model. The same behavior can be appreciated for the aluminum's thickness which reaches the maximum for components with over 4 kg. However, the honeycomb laminates stay in the lower thickness boundary value throughout the whole frontier, as the GFRP's density is higher than that of the foam. Figures 4.25a to 4.25d show how the honeycomb's cell shape starts with a regular hexagon, tending towards the rectangular shape and even slightly surpassing this threshold in figure 4.25d for the highest *SEA* values, as expected after the results obtained in other Pareto fronts.

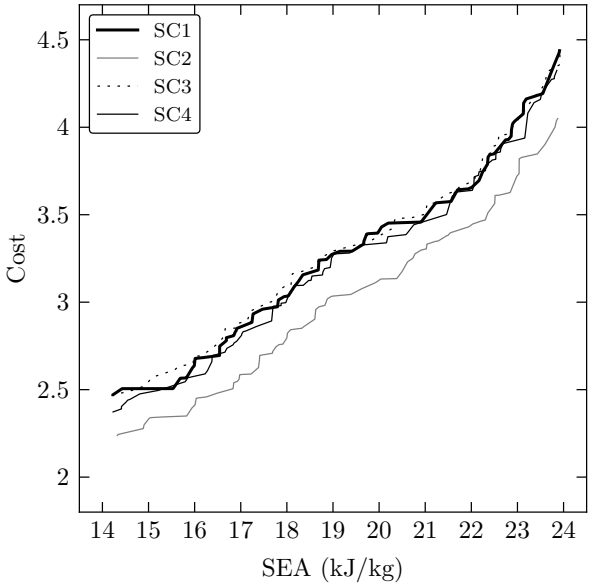

Figure 4.23: *SEA* - C_t Pareto front.

4.5 Conclusions

The research in this chapter focuses on the crashworthiness analysis and optimization of two thin-walled hybrid collapsible absorbers designed to work as

Design variables (mm)				Objective functions	
L1	T1	T2	S	*SEA* (kJ/kg)	C_t
16.26	1.01	1.05	0.01(*1)	14.24	2.47
17.48	1.42	1.05	0.16	17.24	2.88
17.91	1.87	1.07	0.31(*2)	19.67	3.34
17.91	2.24	1.05	0.36	22.01	3.66
17.91	2.49	1.06	0.41(*3)	23.12	4.07
17.51	2.50	1.05	0.55(*4)	23.91	4.44

Table 4.18: Points from *SEA* - C_t Pareto front of specimen B for SC1. Model with an * depicted in figures 4.25a to 4.25d.

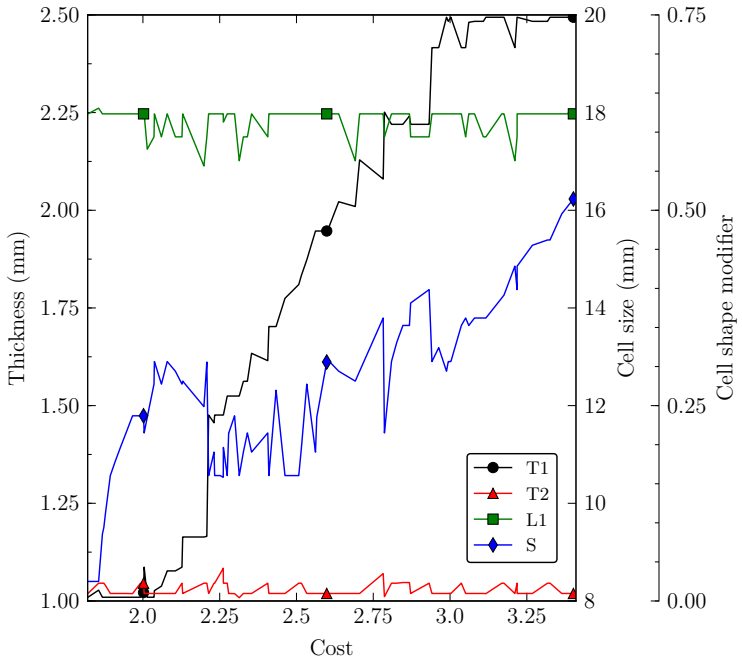

Figure 4.24: Variables' evolution for SC1 in the *SEA* - C_t Pareto front of specimen B.

struts located on the lower half of an aircraft's fuselage. The structures have been upgraded by adding foam extrusions and a GFRP-honeycomb as inner

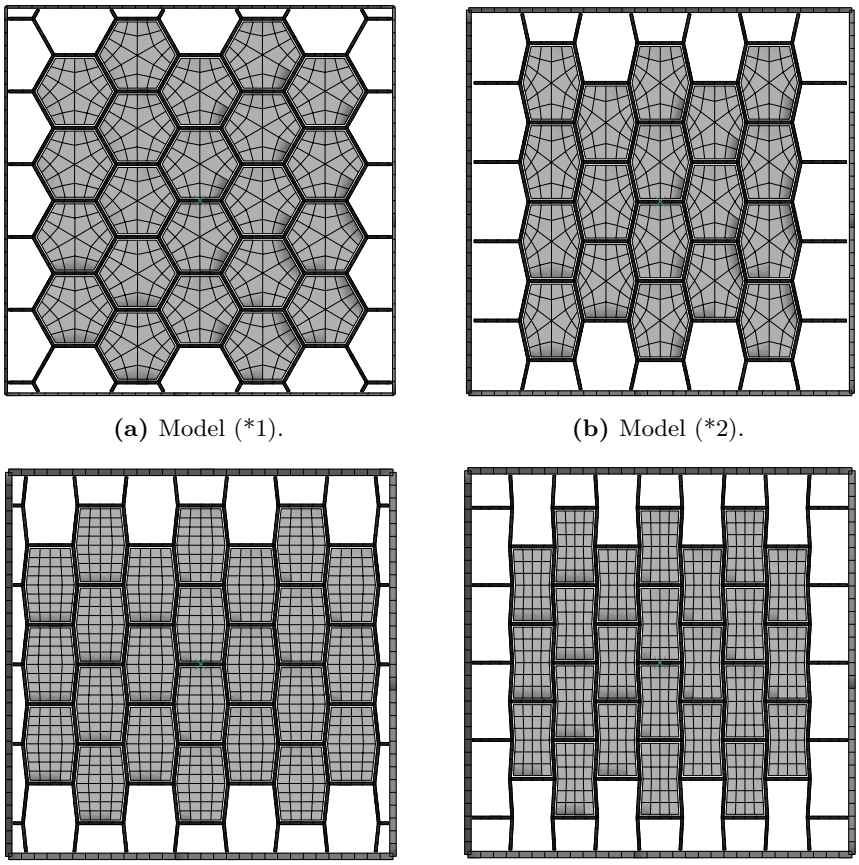

(a) Model (*1). **(b)** Model (*2).

(c) Model (*3). **(d)** Model (*4).

Figure 4.25: Component configuration for some points from the *SEA* - C_t Pareto frontier from table 4.18.

reinforcements, with variable thicknesses for the aluminum and the GFRP as well as the shape and size of the cell. From this research it was concluded that:

- The usage of triggers on the impacting edge of the thin-walled tube reduces over 30 % of the initial crushing loads, while also producing more stable collapse mechanisms.
- Single-objective optimization of the honeycomb's cell shape revealed that non-regular designs offered an energy absorption efficiency over 10 % higher than regular hexagons, with no increase in peak force values.
- Multi-objective optimization of the honeycomb-filled component showed that peak force of the initial designs can be lowered by 55 % whilst delivering a similar SEA performance; or boosting the later 65 % and still reducing the maximum force by almost 20 %.
- Foam extrusions filling the honeycomb cells have delivered SEA values 28 % higher with no harm on the maximum force response.
- As in devices without foam, optimization of the cell shape according to SEA delivered values of up to 24 kJ/kg with pseudo-rectangular cells instead of the 19 kJ/kg of the baseline specimen.
- Different multi-objective optimizations showed that best performances according to weight, energy absorption and maximum force criteria are delivered by specimens with large, non-regular thin-walled cells and high aluminum thicknesses.

References

[1] Laananen, DH and Winkelman, KL. "Analysis of energy-absorbing seat configurations for aircraft". *International journal of crashworthiness* 1.4 (1996), pp. 355–368.

[2] Snyder, Richard G. *Civil Aircraft Restraint Systems: State-of-the-Art Evaluation of Standards, Experimental Data, and Accident Experience*. Tech. rep. SAE Technical Paper, 1977.

[3] European New Car Assessment Programme (Euro NCAP). *Frontal Impact Testing Protocol, Version 6.0.2*. Tech. rep. European New Car Assessment Programme (Euro NCAP), 2013.

[4] Global NCAP. *List of NCAPS*. `https://goo.gl/dWvokW`.

[5] NASA. *1974 Cessna 172 drop test at NASA Langley's Landing and Impact Research Facility. August 26ht, 2015*. `https://goo.gl/x8U3hc`.

[6] Jackson, Karen E, Fasanella, Edwin L, Boitnott, Richard, McEntire, Joseph, and Lewis, Alan. "Occupant Responses in a Full-Scale Crash Test of the Sikorsky ACAP Helicopter". *Journal of the American Helicopter Society* 49.2 (2004), pp. 127–139.

[7] Jackson, Karen E, Boitnott, Richard L, Fasanella, Edwin L, Jones, Lisa E, and Lyle, Karen H. "A history of full-scale aircraft and rotorcraft crash testing and simulation at NASA Langley Research Center" (2004).

[8] *Barómetro de Seguridad Vehicular del Parque de Automoción*. Tech. rep. Fundación FITSA, 2007.

[9] Paz, J, Díaz, J, Romera, L, and Costas, M. "Crushing analysis and multi-objective crashworthiness optimization of GFRP honeycomb-filled energy absorption devices". *Finite Elements in Analysis and Design* 91 (2014), pp. 30–39.

[10] Paz, J., Díaz, J., Romera, L., and Costas, M. "Size and shape optimization of aluminum tubes with GFRP honeycomb reinforcements for crashworthy aircraft structures". *Composite Structures* 133 (2015), pp. 499–507.

[11] Paz, J., Romera, L., and Diaz, J. "Crashworthiness optimization of aircraft hybrid energy absorbers enclosing honeycomb and foam structures". *AIAA Journal* 55.2 (2017), pp. 652–661.

[12] Romera, L, Paz, J, Costas, M, Dıaz, J, and Hernandez, S. "Crashworthiness response of honeycomb metallic-GFRP energy absorption devices". *High Performance and Optimum Design of Structures and Materials. Ostend, Belgium.* 137 (2014), p. 225.

[13] Díaz, J., Costas, M., Romera, L., Paz, J., and Hernández, S. "Surrogate-based multi-objective optimization of glass-fiber-steel crash absorbers". *High Performance and Optimum Design of Structures and Materials. Ostend, Belgium.* 137 (2014), p. 225.

References

[9] Paz, J, Díaz, J, Romera, L, and Costas, M. "Crushing analysis and multi-objective crashworthiness optimization of GFRP honeycomb-filled energy absorption devices". *Finite Elements in Analysis and Design* 91 (2014), pp. 30–39.

[14] Zheng, Jianqiang, Xiang, Jinwu, Luo, Zhangping, and Ren, Yiru. "Crashworthiness design of transport aircraft subfloor using polymer foams". *International Journal of Crashworthiness* 16.4 (2011), pp. 375–383.

[15] Meng, F X, Zhou, Q, and Yang, J L. "Improvement of crashworthiness behaviour for simplified structural models of aircraft fuselage". *International Journal of Crashworthiness* 14.1 (2009), pp. 83–97.

[16] Ren, Yiru and Xiang, Jinwu. "The crashworthiness of civil aircraft using different quadrangular tubes as cabin-floor struts". *International Journal of Crashworthiness* 16.3 (2011), pp. 253–262.

[17] Huang, M. *Vehicle Crash Mechanics.* CRC Press, 2002.

[18] Costas, M, Morin, D, Langseth, M, Romera, L, and Díaz, J. "Axial crushing of aluminum extrusions filled with PET foam and GFRP. An experimental investigation". *Thin-Walled Structures* 99 (2016), pp. 45–57.

[19] Adams, B., Bauman, L., Bohnhoff, W., Dalbey, K., Ebeida, M., Eddy, J., Eldred, M., Hough, P., Hu, K., Jakeman, J., Swiler, L., and Vigil, D. *DAKOTA, A Multilevel Parallel Object-Oriented Framework for Design Optimization, Parameter Estimation, Uncertainty Quantification, and Sensitivity Analysis: Version 6.1.0 User's Manual*. Sandia National Laboratories. 2014.

[20] Cook, G. R. and Johson, W. H. "A constitutive model and data for metals subjected to large strains, high strain rates and high temperatures". *Proceedings of Seventh International Symposium on Ballistics* (1983).

[21] BASF. *Ultramid (R) A3WG10 BK00564 Polyamide 66. Product information sheet*. 2012.

[22] *SAE Standard J211: Instrumentation for Impact Test*. Tech. rep. Safety Test Instrumentation Stds Comm, 1995.

[23] *Airbus A300 Fuselage Section*. `https://goo.gl/aqcMBf`.

[24] Børvik, T., Hopperstad, O.S., Berstad, T.., and Langseth, M. "A computational model of viscoplasticity and ductile damage for impact and penetration". *European Journal of Mechanics, A/Solids* 20.5 (2001), pp. 685–712.

[25] Børvik, T., Hopperstad, O.S., and Pedersen, K.O. "Quasi-brittle fracture during structural impact of AA7075-T651 aluminium plates". *International Journal of Impact Engineering* 37.5 (2010), pp. 537–551.

[26] Deshpande, V.S. and Fleck, N.A. "Isotropic constitutive models for metallic foams". *Journal of the Mechanics and Physics of Solids* 48.6 (2000), pp. 1253–1283.

[27] Zou, Tianchun, Mou, Haolei, and Feng, Zhenyu. "Research on Effects of Oblique Struts on Crashworthiness of Composite Fuselage Sections". *Journal of Aircraft* 49.6 (2012), pp. 2059–2063.

[28] Heimbs, S., Strobl, F., and Middendorf, P. "Integration of a composite crash absorber in aircraft fuselage vertical struts". *International Journal of Vehicle Structures and Systems* (2011).

[29] Fasanella, E. L., Jackson, K. E., Sparks, C. E., and Sareen, A. K. "Water Impact Test and Simulation of a Composite Energy Absorbing Fuselage Section" (2011), pp. 1–15.

[30] Adams, A and Lankarani, HM. "A modern aerospace modeling approach for evaluation of aircraft fuselage crashworthiness". *International journal of crashworthiness* 8.4 (2003), pp. 401–413.

[31] Adams, A, Thorbole, C K, and Lankarani, H M. "Scale modelling of aircraft fuselage: an innovative approach to evaluate and improve crashworthiness". *International Journal of Crashworthiness* 15.1 (2010), pp. 71–82.

[32] Jackson, Karen E, Fasanella, Edwin L, and Kellas, Sotiris. "Development of a Scale Model Composite Fuselage Concept for Improved Crashworthiness". *Journal of Aircraft* 38.1 (2001), pp. 95–103.

[33] *ABAQUS 6.14 Documentation*. Dassault Systèmes. 2014.

5

Crash response of aircraft structures enhanced with crushable energy absorbers. Crashworthiness analysis and passenger injury assessment

5.1 Introduction

Crashworthiness tests and standards, such as those established by the Federal Aviation Administration (FAA) or by the Joint Airworthiness Requirements (JAR) [298], have noticeably increased the survival probabilities and reduced passenger injuries in crash scenarios. A crashworthiness improvement of an aircraft combines the improvement of both its structure and the materials, so that it exhibits exceptional crash resistance and energy-absorption capabilities for passenger protection. Section 2.1.3 presents different techniques used to improve the crashworthiness of an aircraft, such as modifying its response to failure or increasing the energy that can be absorbed by the structure. However, real tests and simulations are required to assess the actual improvements of the aircraft's response under impact and to obtain conclusive data on the structural response and the loads and accelerations transmitted to the passengers.

Confident with the knowledge gained in chapters 3 and 4, this part of the investigation swerves from the examination of collapsible energy absorbers on a standalone basis towards its analysis featured as vertical struts in a fuselage section from a commercial aircraft. For such a task, a numerical simulation of a Boeing 737-200 is first developed and verified with experimental data, constituting a benchmark to analyze the behavior of the energy absorbers during vertical impact scenarios. The fuselage section is then simulated both with and without the auxiliary fuel tank, analyzing the collapse process of both scenarios. The verified numerical model is later used to assess the performance of the fuselage and the five energy absorbers designed for programmed and progressive collapse, featured in the cargo compartment connecting the underfloor beams and the frames. As to understand the effects of using these devices on aircraft structures, hollow specimens are added to the fuselage and compared to the base model through energy-related responses, collapse evolution, as well as by biometric parameters predicting passenger injury levels.

5.2 Fuselage model description

The experimental drop test on which this investigation is based was performed in November of 2000 at the FAA William J. Hughes Technical Center (New Jersey, USA) [67]. In this test, a 3.048 m (10 ft) long section of a Boeing 737-200 was dropped from a height of 4.27 m (14 ft) as shown in figure 5.1. The initial impact against solid ground occurred at 9.144 m/s (30 ft/s), thus constituting a severe but survivable crash.

The fuselage was thoroughly instrumented to record both accelerations and strains at a significant number of locations. The obtained data is used to check the validity of the proposed numerical model. The acceleration-history plots were also studied in an Eiband diagram [125] at four different locations (see section 2.1.4.5), thus assessing the effects suffered by the passengers during the impact.

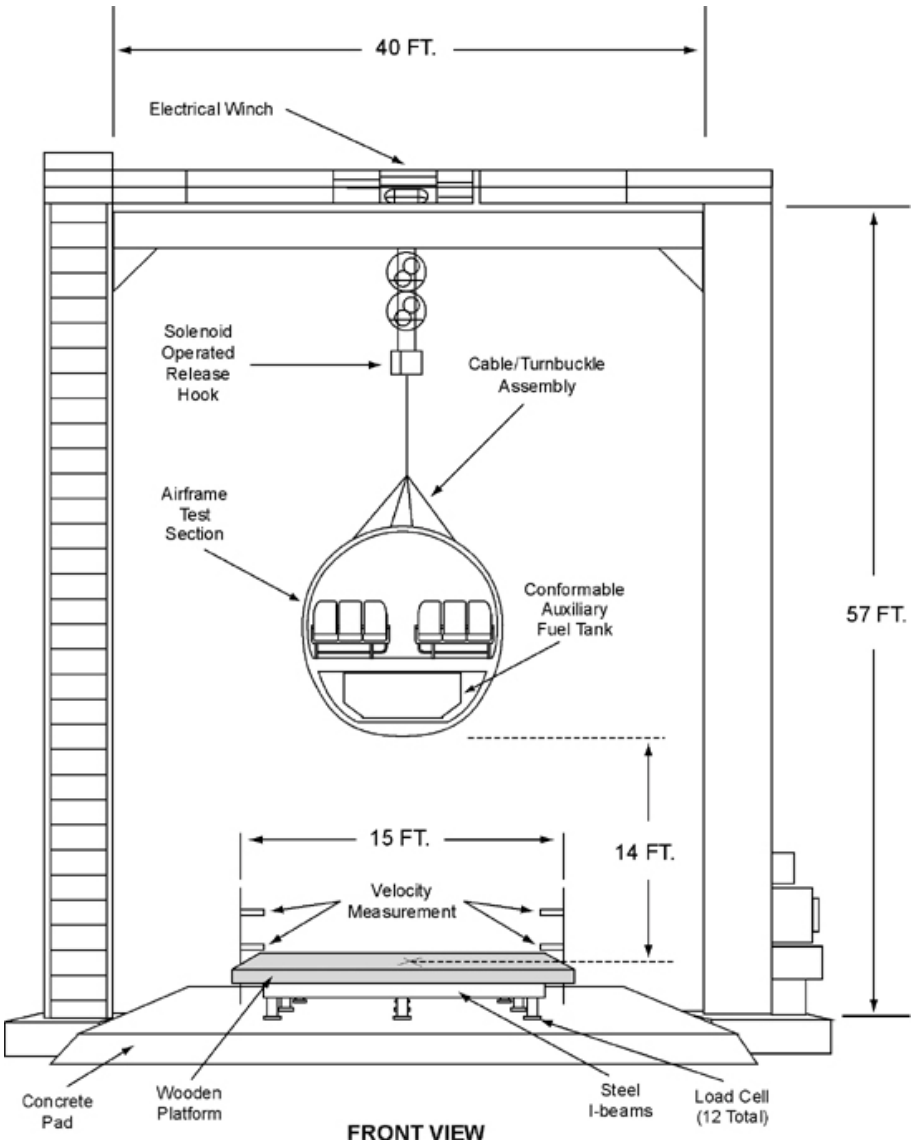

Figure 5.1: Dynamic drop test facility diagram as presented by Abromowitz et al. [299].

As previously mentioned, a finite element numerical model of a Boeing 737-200 fuselage section was developed and verified. Hereunder, the materials, numerical simulation parameters and analysis settings used for the simulation of the 10-foot vertical drop test are described in detail.

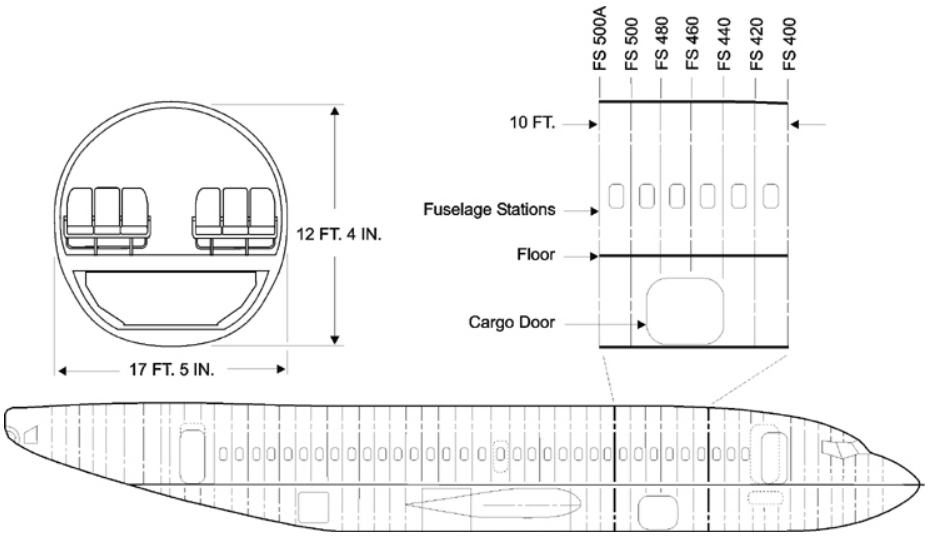

Figure 5.2: Boeing 737-200 test section. Taken from [299].

The specimen tested, and therefore, the numerical model proposed, is the fuselage section between stations FS400 and FS500A, as shown in figure 5.2. The model's main structures are the outer fuselage skin, seven evenly-spaced frames, the passenger floor and its seven supporting beams. In order to compensate for the loss of structural stiffness caused by removing the rest of the fuselage, two under-floor beams are added, one on each end of the section (stations FS400 and FS500A), as shown in figure 5.3. The specimen also includes the mass of six triple-occupant seats with 18 passengers as point masses along the inner and outer seat tracks. A mass of 1460.6 kg (3220 lb) accounts for the auxiliary full fuel tank in the under-floor compartment. The cargo door and its reinforced door frame are also part of this section, stiffening the lower right part of the fuselage, thus modifying the collapse mechanisms (e.g. making them non-symmetrical) and the monitored metrics during the actual test [48].

Figure 5.3: Boeing 737-200 test article. Taken from [67].

Once the original model is verified with the experimental results from Fasanella and Jackson [67], it is used as a benchmark and compared against a fuselage section with the vertical struts implemented. The struts are composed of 700 mm long aluminium tubes with an 80 mm width square cross-section and wall thicknesses of 2.5 and 1.2 mm for the top and bottom halves, respectively. This dimensions ensure its progressive collapse according to Abramowicz and Jones [143] for axially-dominated loading, as the minimum critical length for the tube is $L_{\text{cr}} = 984$ mm (see section 2.2.2.3, equation (2.59)). While the thinner region is designed to collapse first and trigger a stabilized folding mechanism, the thicker plates allow for higher energy absorption values in case it were required. The struts are rotated 45 ° along the vertical axis so that their inertia is highest in the transverse plane to avoid off-plane global buckling. Absorbers are connected to the fuselage frames and the cabin floor beams with pinned joints, which can rotate only in the transverse plane. A clearance of 2.04 m between struts is ensured so that the necessary capacity for the cargo containers and auxiliary fuel tanks is not compromised [300]. The struts span every meter along the longitudinal plane if attachment is feasible. In the section studied, only five struts were fitted due to the presence of the cargo door, as visible in figure 5.5.

5.2.1 Materials

The Boeing 737-200 test article studied is made from three different materials. AA7075-T6 aluminium alloy was used for the frames, under-floor beams and stringers. The vertical struts fitted for the second part of the research were also made from AA7075-T6. However, the fuselage skin and floor are made from AA2024-T3 aluminium. Both materials have been modelled according to the modified Johnson-Cook strain-rate sensitive plasticity models [20, 24] without temperature effects (see section 4.2). However, the test article was obtained from an used aircraft [67], consequently offering reduced values for the elastic and plastic parameters due to damage and fatigue as recommended by Fasanella and Jackson [66]. The values used for the Johnson-Cook plasticity models are detailed in table 5.1.

Parameter		AA2024-T3	AA7075-T6	Tank	Wood
General properties	E (GPa)	73.08	72.4	72.4	0.5
	ν	0.33	0.33	0.3	0.3
	ρ (kN/m^3)	2.78	2.78	4.94	1.2
Plasticity model	A (MPa)	302	413	682.6	-
	B (MPa)	550	600	-	-
	n	0.73	0.71	-	-
	C	$3 \cdot 10^{-4}$	$1 \cdot 10^{-4}$	-	-
	$\dot{\varepsilon_0}$	$5 \cdot 10^{-4}$	$5 \cdot 10^{-4}$	-	-

Table 5.1: Material properties of the AA2024-T3 [301], AA7075-T6 [302] aluminium alloys, the tank material [67] and the impacting block.

The fuel tank is a significant feature, therefore capable of noteworthy effects on the collapse mechanism of the fuselage. The properties for the tank material were taken from Fasanella and Jackson [67] and also detailed in table 5.1. Finally, the impacting surface used in the test was made from wood, with material properties listed in table 5.1.

5.2.2 Numerical simulation

The fuselage section was developed using the Abaqus CAE package (ver. 2016) and represented all the significant structural features of the test specimen, including the skin stiffeners, the cargo door and its stiffening beams (see figures 5.4 and 5.7b), the mass of seats and passengers and the filled auxiliary fuel tank. A total of 12 accelerometers recorded data from the experimental and numerical articles, two of which are chosen for the verification of the simulation, shown in figure 5.4 as locations **1** and **2**. Location **1** is the data extraction point on the left side of the station FS420 and **2** the point on the right; both measured at the fuselage floor. The data points **1b** and **2b** are vertically aligned with the location of an energy absorber, and its metrics are also monitored to ensure that the use of the energy absorbers doesn't lead to excessive acceleration. Furthermore, a connector was developed for the model with vertical struts, providing a linkage between absorber and frame. These parts were designed with the same aluminum alloy and are rigidly connected to the tubes. A detailed view of the energy absorbers and connectors is shown in figure 5.5.

Quadrilateral shell elements with reduced integration (S4R) were used to model the skin and floor, frames, under-floor beams and tank panels. The usage of shell elements represents more accurately the actual behavior of the specimen and allows for an accurate representation of plastic hinges, whereas beam elements would not reproduce local buckling and crippling. However, the omega-shaped longitudinal stringers are modeled as 2-node linear beam elements (B31) in order to reduce the number of elements in the model and the computational cost, with no significant effect on the results. Figure 5.6 provides a close view of these structures, offering shape-rendered structural details as the beam section or shell thickness display. The passenger-seat blocks are approximated with evenly distributed lumped masses. Solid eight-node elements with reduced integration (C3D8R) were used for the impacting surface's mesh.

Windows were also added to the model with simplified right-angled corners and the subsequent frame stiffeners as shown in figure 5.7a. Following other authors' approach, rivets and fasteners throughout the fuselage are modeled

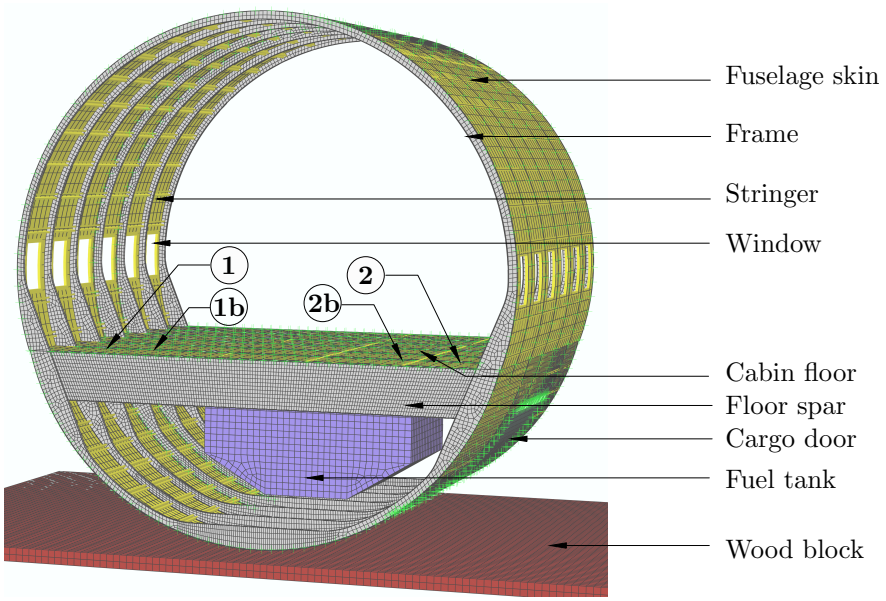

Figure 5.4: Numerical model in Abaqus 2016.

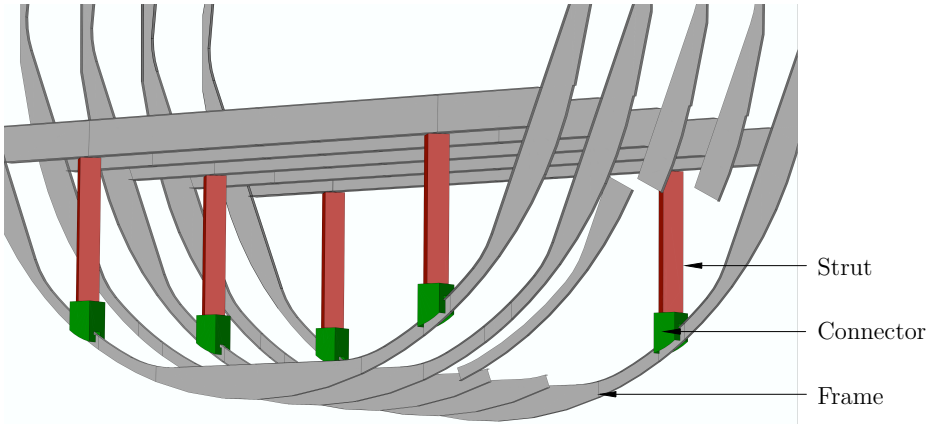

Figure 5.5: Detail of the energy absorbers and the connecting part developed.

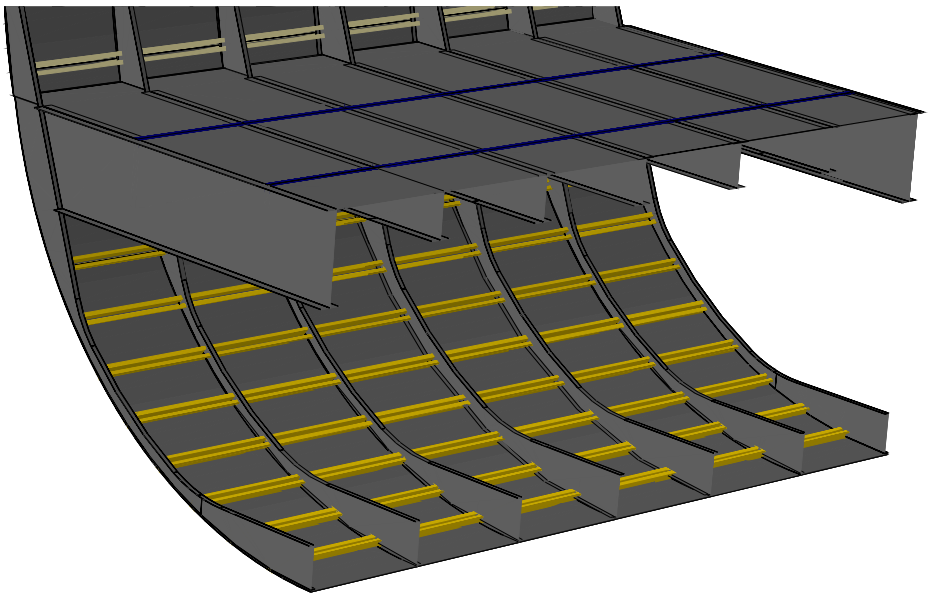

Figure 5.6: Detail of the lower aircraft structures.

as rigid connectors in the software [48, 107], avoiding the increased computer effort required for considering failure and damage processes in these elements. Other complex geometry and features, including cutouts, joints and doublers were excluded from the model, since their implementation would heavily increase the computational cost while not significantly affecting the overall behavior of the model. The 404 gallons of water filling the tank were considered by adding point inertias distributed inside the tank, thus neglecting the water sloshing effects produced in the experimental test.

The final model dimensions, material thicknesses, cross-section profiles and sectional inertias were obtained through reverse engineering from technical drawings and a tuning process considering know static and dynamic simulations. Table 5.2 offers a detailed list of the values adopted that yielded the closest response to the experiments.

The mesh sizes were selected after performing a mesh study as in previous chapters, seeking to obtain the best trade-off between computational time and

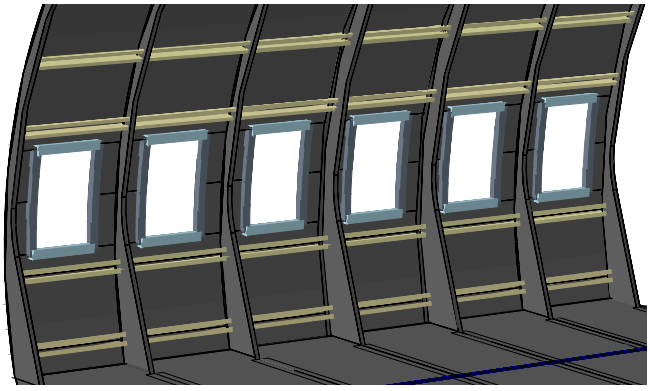

(a) Windows and upper fuselage structures.

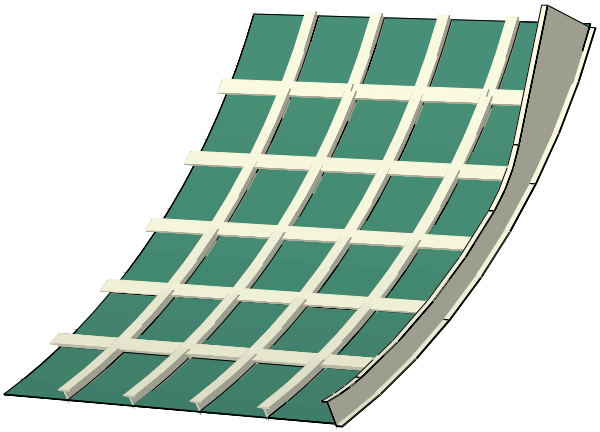

(b) Cargo door and reinforcing structures.

Figure 5.7: Detail of cargo door and upper fuselage structures.

Item	Thickness (mm)	Profile section	Inertia (cm^4)
Fuselage skin	2	-	-
Floor	2	-	-
Fuel tank	0.8	-	-
Floor spar	2.5	I	417.924
Frames (thin)	3	Z	10.801
Frames (thick)	3	Z	56.851
Stringers	2	Omega	3.328

Table 5.2: Geometrical properties of significant fuselage structures.

accuracy. A total of 77 289 nodes and 65 391 elements compose the finite element model of the fuselage section, with 2863 beam elements, 43 328 shell elements and 19 200 solid elements. Energy absorbers and connectors require finer meshes than those of the main structures, reducing the mesh seed dimension by one order of magnitude; increasing overall number of elements increases to 94 496. An image of the fuselage section's mesh is also shown in figure 5.4. The total number and type of elements for each part of the specimen are listed in table 5.3.

Item	Element type	Element no.	Avg. size (mm)
Fuselage	S4R	9959	75
Fuel tank	S4R	3150	50
Frames	S4R	30 219	20
Stringers	B31	2863	75
Impacting surface	C3D8R	19 200	50
Occupants and seats	Point masses	20	-
Vertical struts	S4R	4872	5
Connector	S4R	949	8

Table 5.3: Type, number and size of the finite elements used.

The tested section has a total mass of 3691.9 kg, whereas the tuned finite element model weighs 3700 kg. A detailed list of the mass of each part is provided in table 5.4. When the energy absorbers and connectors are added, the mass of

the fuselage increases by 11.07 kg (0.3%), corresponding to 1.14 and 1.07 kg from each strut and connector, respectively.

Item	Test article	Simulation
Fuselage	616.9	640
Tank	1464.7	1460
Occupants and seats	1610.3	1600
Total weight	3691.9	3700

Table 5.4: Comparison of masses (in kg) between the test article and the computer model.

For the impacting surface, a solid block with a thickness of 100 mm and similar dimensions to those of the wood used in the test was included. General contact properties were also added to the model, with a friction coefficient of 0.04.

Four different crash tests and a static case with internal pressure are presented in the following paragraphs, with the latter only being used for verification purposes. The impact against solid ground is used both for verification and obtaining crashworthiness metrics. Moreover, once the model is verified, an additional hard-landing scenario of the fuselage without the auxiliary fuel tank is developed and analyzed. The behavior and collapse mechanisms of the fuselage section differ when the tank is removed from the sub-cargo area [30], thus making this scenario also of significant interest. The two hard-landing tests are repeated with the vertical energy absorbing struts, with and without the auxiliary fuel tank, as to understand their effect on the global aircraft crash mechanics.

5.2.3 Analysis settings

Three different analyses are performed. The first one is a static case with an internal pressure of 45 kPa (6.5 psi). The fuselage section model is fixed at the bottom and complies with a symmetry boundary condition at the top of the fuselage. This load case is only used for the verification of the developed

numerical model, comparing stress and deformation values the expected from analyses and experiments.

For the four hard-landing scenarios, the impact conditions match those of the experimental test, with an initial impact velocity of 9.144 m/s.

5.3 Results and discussion

5.3.1 Verification

5.3.1.1 Internal pressure static load

The first result used for the verification of the developed model are obtained from a static loading case with internal pressure on a fuselage without the auxiliary fuel tank. According to the results presented in the report from Jeong et al. [303], the maximum radial displacement under the considered load should be slightly under 4 mm. In the model studied, the total displacement is that of 3.8 millimeters, thus within the experimental boundary. The results are shown in figure 5.8.

5.3.1.2 Hard landing impact

The tuned fuselage was tested and used for verification of the finite element model developed. After the analysis of the model, different considerations were made to assess whether the finite element model had a similar behavior to the original test specimen.

A qualitative comparison between the real and numerical specimens was performed at different time values during the simulation. Figure 5.9 shows three front views of both at 20, 60 and 100 ms. The images show significant resemblances between the collapse mechanisms of the numerical and analytical models, with similar locations of the frames' plastic hinges, the asymmetry caused

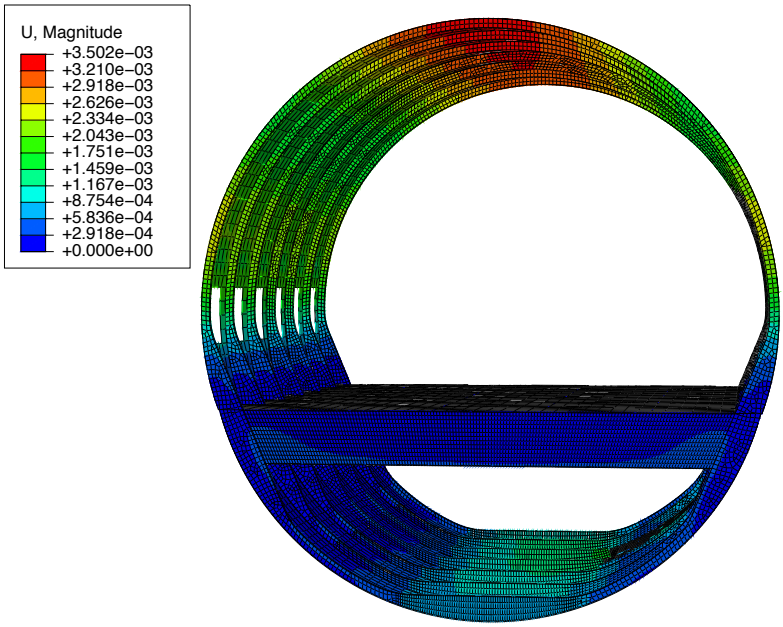

Figure 5.8: Radial displacements obtained in the static load case. All displacements in meters.

by the presence of the cargo door and an almost equal deformation of the sub-floor structures.

Furthermore, the final deformation on both the right and left sides of the floor was measured. The asymmetry of the fuselage due to the presence of the cargo door yields a maximum deformation of 58 cm compared to the 55 cm obtained experimentally on the right side. For the left side, the numerical deformation is 52.7 cm, whereas the test specimen yielded a value of 52.5 cm.

The velocity and acceleration responses were also monitored for both sides of the fuselage floor. The graphs in figures 5.10 and 5.11 show the comparison between the velocity and acceleration, filtered with a 48-Hz four-pole Butterworth low-pass filter forwards and backwards as performed by Fasanella and Jackson [67], for the two data extraction locations. All four graphs show a significant resemblance with the analytic results, matching the velocity slope changes and

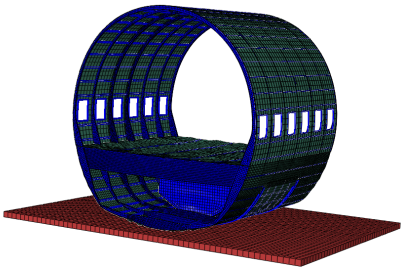

(a) Front view of FEM at 20 ms.

(b) Front view of specimen at 20 ms.

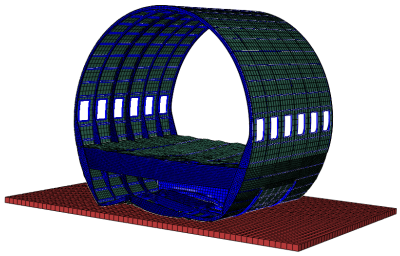

(c) Front view of FEM at 60 ms.

(d) Front view of specimen at 60 ms.

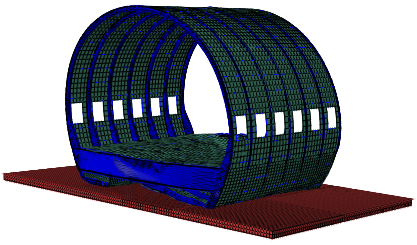

(e) Front view of FEM at 100 ms.

(f) Front view of specimen at 100 ms.

Figure 5.9: Comparison between the real [67] and numerical specimens at 20 ms, 60 ms and 100 ms.

the peak acceleration values throughout the entire simulation and with differences in peak values under 15%.

Finally, the model energies are monitored to ensure that the analysis settings do not induce high artificial energy values for stabilization and convergence purposes (see figure 5.12). For this model and impact conditions, the artificial energy is less than 9% of the internal energy of the model, thus being well under the recommended maximum of 10-15% for similar crashworthiness numerical simulations [253].

The results obtained from the hard-landing scenario have been compared to the numerical verification from Fasanella and Jackson [67], which display a similar fitness of the acceleration and velocity graphs to the ones here presented. Considering this and a final examination of the static and the hard-landing simulation results, the numerical model here proposed is regarded as a verified specimen. Therefore, the implementation and study of the energy absorbers can be performed.

5.3.2 Effect of the energy absorbers

Once the model is verified, the vertical struts were added and the data obtained was compared to that from the original fuselage section. The vertical struts are tested for a fuselage section with the auxiliary fuel tank and for another section without it.

In order to assess the improvement obtained from the usage of the energy absorbers, the Eiband diagram is used together with the acceleration responses for two locations on the left side of the fuselage, **1** and **1b** (see figure 5.4), and the two symmetrically opposed on the right side, **2** and **2b**. This diagram exhibits a depiction of the vertical acceleration loads at the floor level, although the loads experienced by passengers at those locations in a real event would be lower due to factors like the usage of seat restraints and cushion damping.

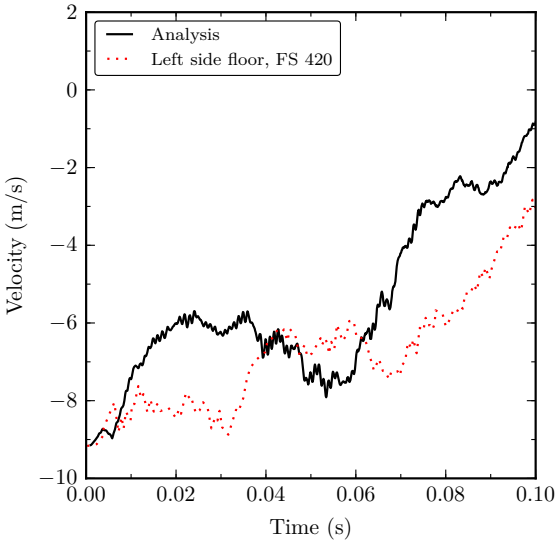

(a) Left floor velocity (location **1**).

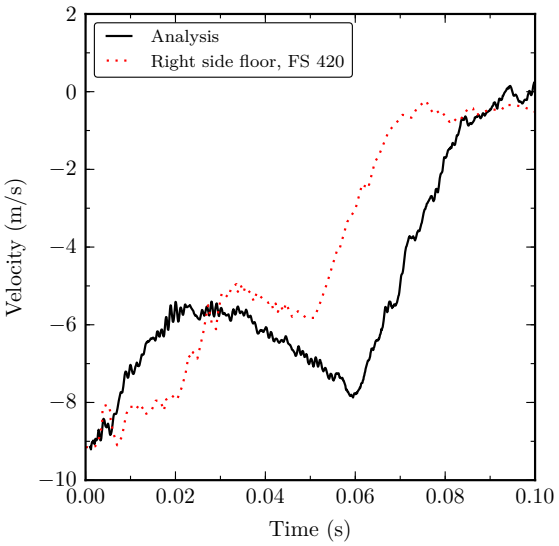

(b) Right floor velocity (location **2**).

Figure 5.10: Left and right floor velocities. Analytic and numerical results.

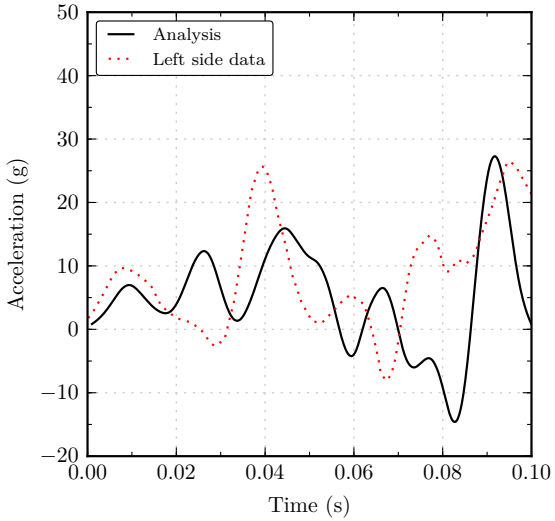

(a) Left floor acceleration (location **1**).

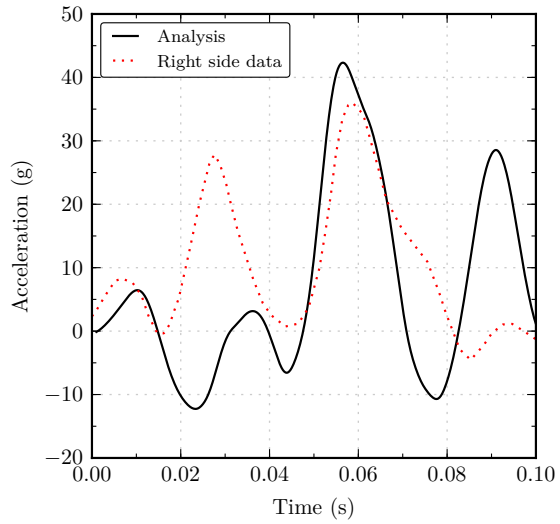

(b) Right floor acceleration (location **2**).

Figure 5.11: Left and right floor accelerations. Analytic and numerical results

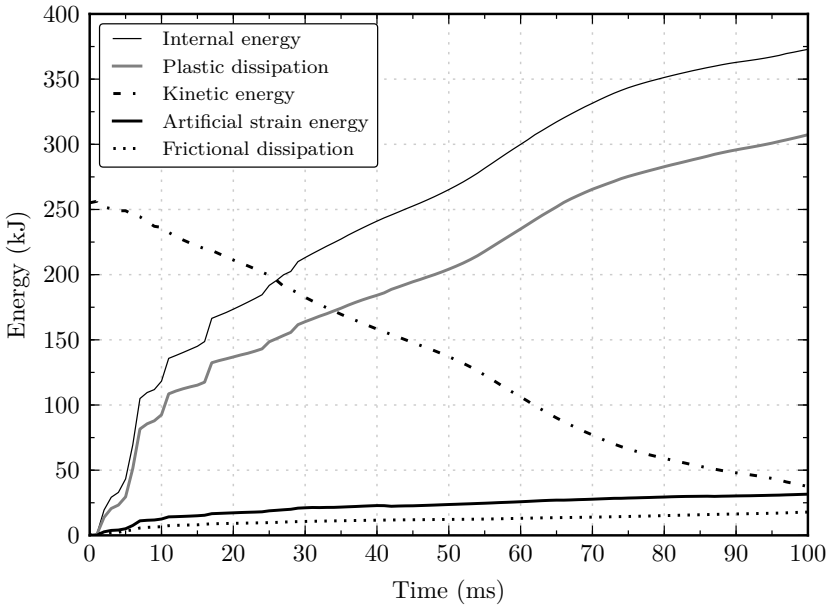

Figure 5.12: Model energies throughout the simulation.

5.3.2.1 Fuselage with auxiliary fuel tank

The effect of struts on the acceleration response for the fuselage sections with the auxiliary fuel tank was analyzed and depicted in figure 5.13. Results show a similar trend on location **1**, but with lower acceleration values for the model with the energy absorbers throughout most of the simulation, as well as reducing the peak acceleration by 25%. However, on location **1b** the responses differ significantly between both scenarios, even though the acceleration peaks are almost identical.

The Eiband diagram in figure 5.14 is used to compare the plausible injuries at the locations monitored. After implementing the energy absorbers to the model, the injury rating is lowered on location **1**, even though the outcome for location **1b** is slightly more harmful.

Moreover, figures 5.15a and 5.15b elucidate the behavior offered by the energy absorber proposed at location **1b**. The crash response in figure 5.15b shows a

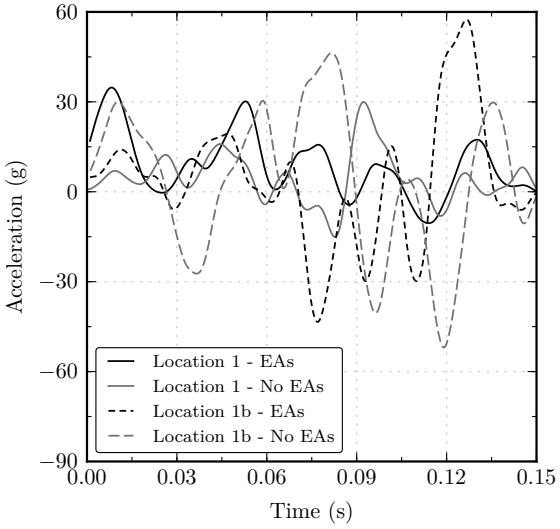

(a) Accelerations at locations **1** and **1b**.

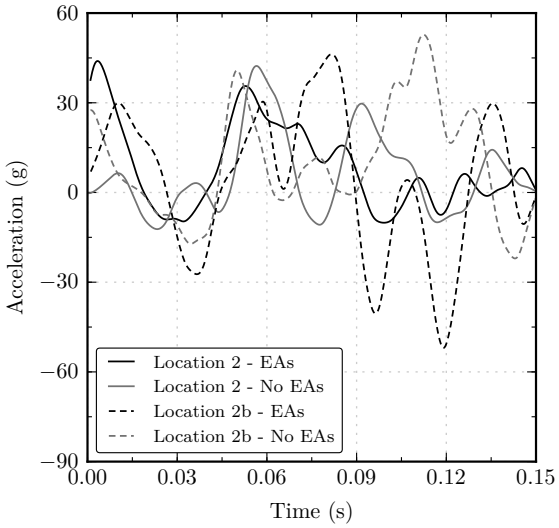

(b) Accelerations at locations **2** and **2b**.

Figure 5.13: Aircraft acceleration responses with the auxiliary fuel tank, with and without energy absorbers.

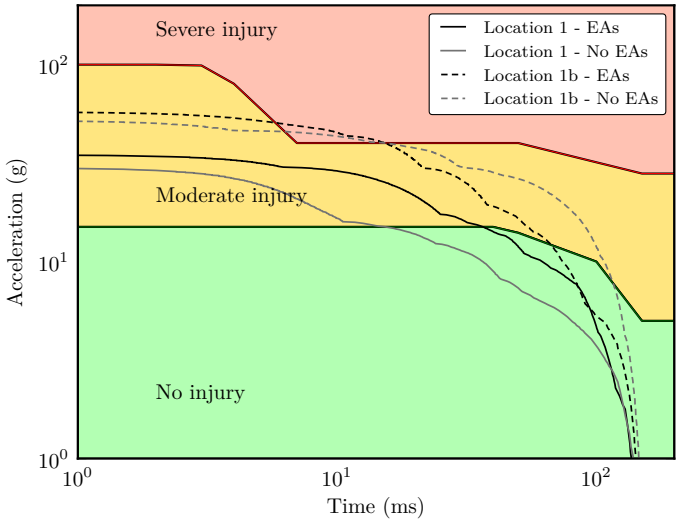

(a) Vertical acceleration loads at locations **1** and **1b**.

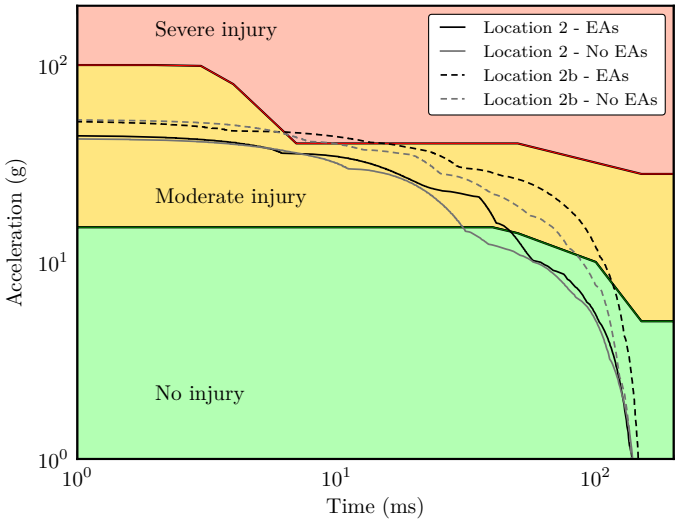

(b) Vertical acceleration loads at locations **2** and **2b**.

Figure 5.14: Vertical acceleration loads in Eiband diagram. Fuselage with the auxiliary fuel tank, with and without energy absorbers.

low initial peak of 40 kN for the initiation of the strut's collapse, followed by a crushing force in the range of 20 - 30 kN throughout most of the crushing. However, after 90 ms the vertical strut ceases to absorb and dissipate energy as the fuselage's cargo compartment stops collapsing.

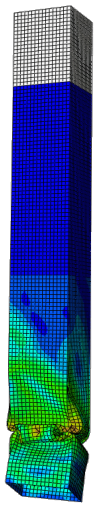

(a) Final deformation of strut under location **1b**.

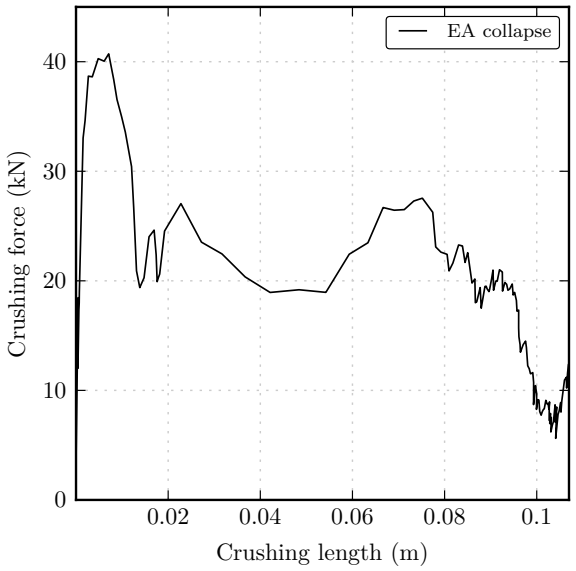

(b) Response of strut under location **1b**.

Figure 5.15: Vertical strut after impact and response.

5.3.2.2 Fuselage without auxiliary fuel tank

In the event of a hard-landing scenario without the auxiliary fuel tank, the contribution of the energy absorbers is even more significant than in the previous case. A closer examination to the collapse evolution of the main structures reveals how the collision with the ground crushes the sub-cargo area after 20 ms, as shown in figure 5.16a. Another 20 ms into the simulation, the main frames experience high localized deformation at the struts' insertion areas, forming two plastic hinges on each frame that allow for a flattening of this region (see figure 5.16b).

Although the lower part of the struts undergoes some deformation before this point, it is only after $50-60$ ms that absorbers fully collapse under post-buckling conditions, developing between one or two folds as seen in figure 5.16c. Finally, figure 5.16d reveals how the floor spars bend near the middle section while struts crushing continues until the specimen completely comes to a halt.

Figure 5.17 offers the post-test final deformation for two fuselage sections without the auxiliary fuel tank. When comparing figure 5.17a and figure 5.17b, it is clear that the absence of a fuel tank results in a higher deformation of the sub-cargo area. However, the vertical struts not only ensure a higher sub-cargo area after the impact, but they also delay the bottom-out effect observed in figure 5.17a, and therefore, lower acceleration loads are transmitted to the passengers in the final 50 ms of the crushing process (figure 5.18). The location where the plastic hinges form in main frames is also affected, as bending occurs where the struts are inserted rather than on the outer regions of the frame.

The acceleration graphs from figure 5.18 compare the acceleration felt at locations **1** and **1b** both with and without energy absorbers. The earliest 50 - 60 ms show that the fuselage with the energy absorbers undergoes higher acceleration loads than the original configuration. This is caused by the presence of the struts, which initiate the collapse for high triggering loads to ensure a correct behavior during the normal flight operation conditions.

As the crushing continues, the original specimen bottoms-out and the lowest section of the frames hits the underfloor beams, resulting in acceleration peaks of over 90 g's. However, since the section with the energy absorbers experiences a more controlled collapse and the energy absorbers dissipate up to 6% of the fuselage's kinetic energy through plastic deformation, the acceleration peaks at less than 45 g's, 50% less than in the original specimen.

Moreover, the contribution offered by the energy absorbers is ever best perceived in the Eiband diagram from figure 5.19. In the scenario with no vertical struts, the acceleration loads experienced on both locations can lead to severe injuries, mainly caused during the latest stages of the impact. However, in the enhanced section, the injuries are on the "moderate injury" region due to the

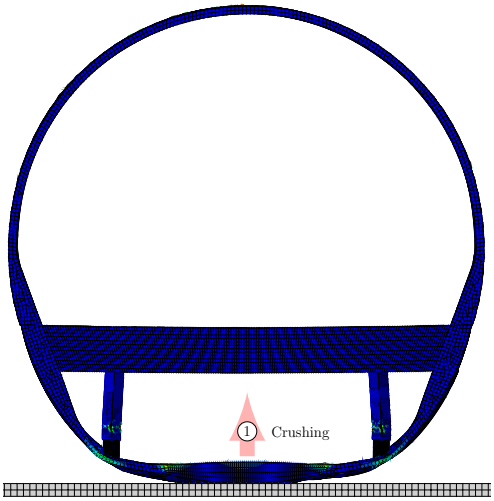

(a) Fuselage 20 ms after collision. Crushing of the sub-cargo area.

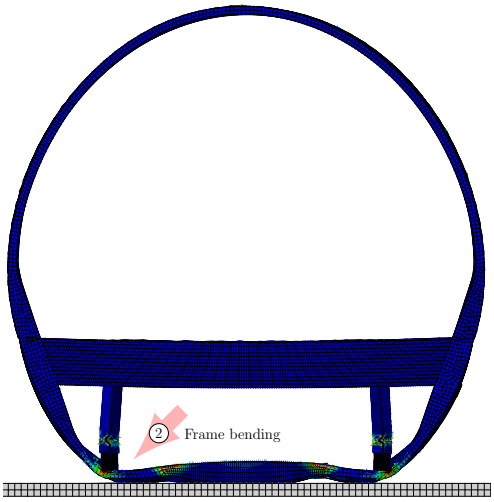

(b) Fuselage 40 ms after collision. Frame bending and formation of plastic hinges.

Figure 5.16: Aircraft collapse evolution of main structures.

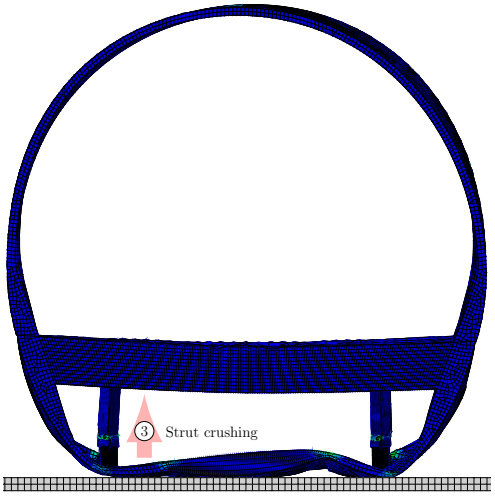

(c) Fuselage 60 ms after collision. Strut crushing.

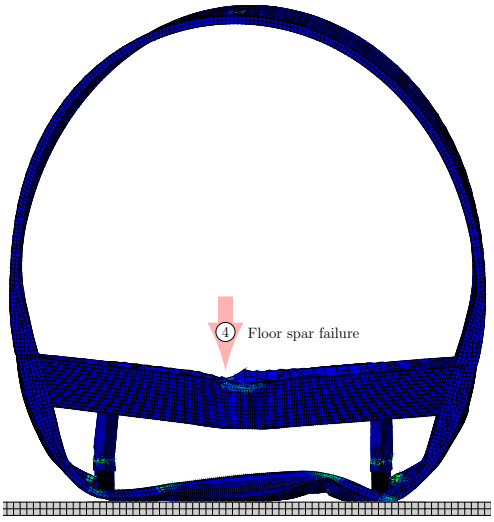

(d) Fuselage 80 ms after collision. Collapse of the floor spars.

Figure 5.16: *(Continued).*

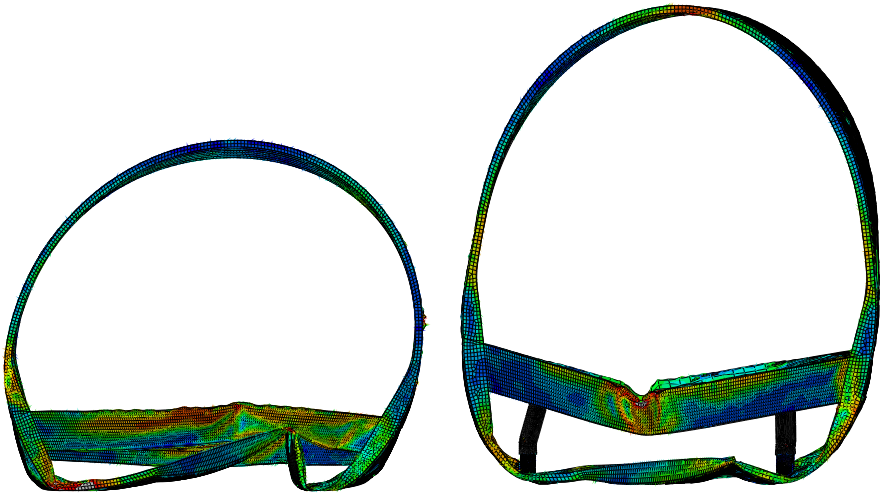

(a) Final deformation of the specimen without energy absorbers.

(b) Final deformation of the specimen with energy absorbers.

Figure 5.17: Final deformation of the specimen without the auxiliary fuel tank, without and with energy absorbers.

more stable collapse mechanism obtained and the energy dissipated by the energy absorbers.

5.4 Conclusions

For this research, crushable metallic energy absorbers are developed and studied under axial impact loads on aircraft structures. For that, a 10-foot long fuselage section from a Boeing 737-200 with an auxiliary fuel tank is empirically developed from reverse engineering and adjusted with data from static and dynamic experiments. Crashworthiness metrics are evaluated before and after the implementation of the energy absorbers to determine their overall effect on the aircraft. The following conclusions are drawn:

- For the fuselage numerical model verification, the qualitative comparison at different steps of the crushing process shows homologous collapse mecha-

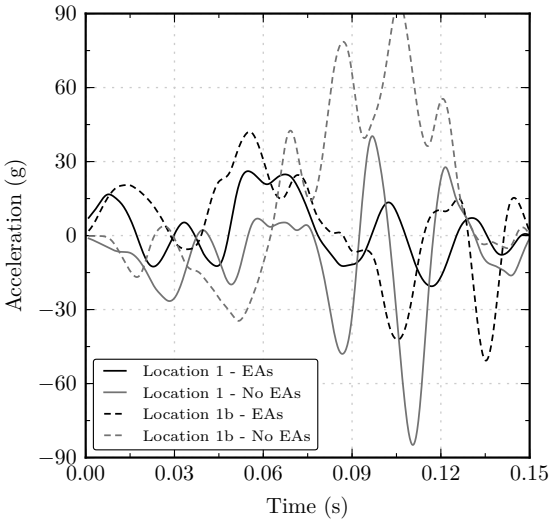

(a) Accelerations at locations **1** and **1b**.

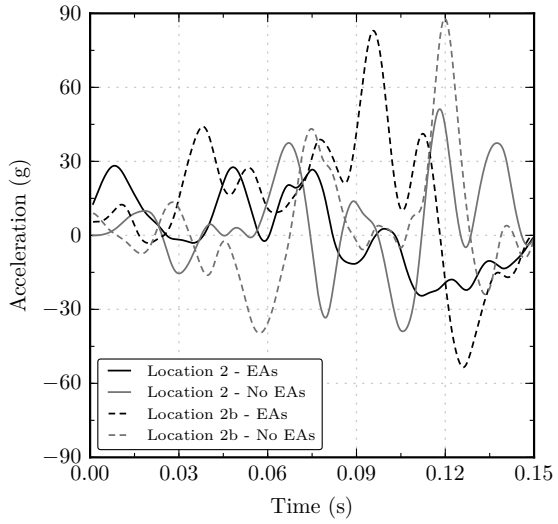

(b) Accelerations at locations **2** and **2b**.

Figure 5.18: Aircraft acceleration responses without the auxiliary fuel tank, with and without energy absorbers.

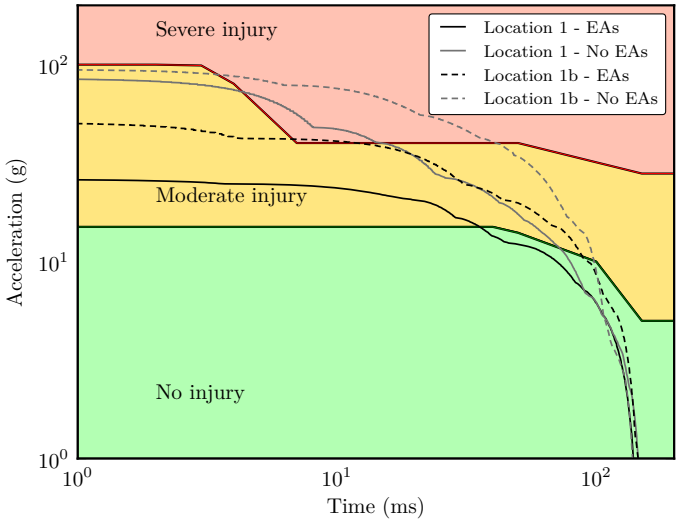

(a) Vertical acceleration loads at locations **1** and **1b**.

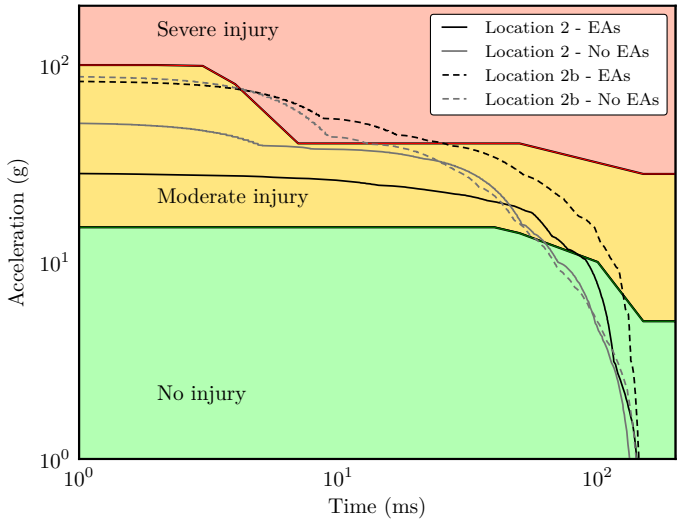

(b) Vertical acceleration loads at locations **2** and **2b**.

Figure 5.19: Vertical acceleration loads in Eiband diagram. Fuselage without the auxiliary fuel tank, with and without energy absorbers.

nisms between the experimental and tuned numerical models. The vertical speed and acceleration loads at two locations in the fuselage station FS420 also deliver results with sensible agreement with experimental data.

- An Eiband diagram determine that injury ratings on the occupants, are more harmful in the scenario without the auxiliary fuel tank, as the acceleration loads are well in the severe injury region with acceleration peaks of over 90 g's. The tank betters the overall behavior of the fuselage through progressively folding and plastic dissipation.
- The addition of crushable energy absorbers enhances the crashworthiness performance of the aircraft. For the model with the fuel tank, peak acceleration is lowered by 25% at the original measuring location, without noticeable detriment of the response over the vertical strut's location.
- In the event of an impact without the auxiliary fuel tank, the usage of the energy absorbers reduces the peak acceleration by over 50% and provides a softer acceleration profile. Furthermore, the usage of vertical struts lowers the injury criteria from severe to moderate on both locations and ensures a bigger survivable space in the under-floor compartment.

References

[48] Byar, Alan and Tan, Tein-Min. "A crashworthiness study of a Boeing 737 fuselage section". PhD thesis. Drexel University Philadelphia, PA, 2003.

[66] Fasanella, Edwin L and Jackson, Karen E. "Best practices for crash modeling and simulation" (2002).

[67] Fasanella, Edwin L and Jackson, Karen E. "Crash simulation of vertical drop tests of two Boeing 737 fuselage sections". In: *U.S. Army Research Laboratory, Vehicle Technology Center, Langley Research Center*. 2002.

[107] Schatrow, Paul and Waimer, Matthias. "Investigation of a crash concept for CFRP transport aircraft based on tension absorption". *International journal of crashworthiness* 19.5 (2014), pp. 524–539.

[125] Eiband, A Martin. "Human tolerance to rapidly applied accelerations: a summary of the literature". *National Aeronautics and Space Administration (NASA)* (1959).

[143] Abramowicz, W. and Jones, N. "Transition from initial global bending to progressive buckling of tubes loaded statically and dynamically". *International Journal of Impact Engineering* 19.5-6 (1997), pp. 415–437.

[253] *ABAQUS 6.16 Documentation*. Dassault Systèmes. 2016.

[20] Cook, G. R. and Johson, W. H. "A constitutive model and data for metals subjected to large strains, high strain rates and high temperatures". *Proceedings of Seventh International Symposium on Ballistics* (1983).

[24] Børvik, T., Hopperstad, O.S., Berstad, T.., and Langseth, M. "A computational model of viscoplasticity and ductile damage for impact and penetration". *European Journal of Mechanics, A/Solids* 20.5 (2001), pp. 685–712.

[30] Adams, A and Lankarani, HM. "A modern aerospace modeling approach for evaluation of aircraft fuselage crashworthiness". *International journal of crashworthiness* 8.4 (2003), pp. 401–413.

[298] De Florio, F. *Airworthiness: An Introduction to Aircraft Certification*. Oxford, 2006.

[299] Abromowitz, Allan, Smith, Timothy G, and Vu, Tong. "Vertical drop test of a narrow-body transport fuselage section with a conformable auxiliary fuel tank onboard". *2000.* (2000).

[300] Airplanes, Boeing Commercial. *737 Airplane Characteristics for Airport Planning. D6-58325-6*. 2013.

[301] Kay, Gregory. *Failure modeling of titanium 6AI-4V and aluminum 2024-T3 with the Johnson-Cook material model*. Office of Aviation Research, Federal Aviation Administration, 2003.

[302] Brar, NS, Joshi, VS, and Harris, BW. "Constitutive Model Constants for Al7075-t651 and Al7075-t6". In: *Shock Compression of Condensed Matter 2009: Proceedings of the American Physical Society Topical Group on Shock Compression of Condensed Matter*. Vol. 1195. 1. AIP Publishing. 2009, pp. 945–948.

[303] Jeong, David Y, Roach, Dennis P, Canha, Joseph V, Brewer, John C, and Flournoy, Thomas H. *Strain Fields in Boeing 737 Fuselage Lap Splices. Field and Laboratory Measurements with Analytical Correlations.* Tech. rep. DTIC Document, 1995.

6

Optimization of hybrid energy absorbers for crashworty aircraft designs

6.1 Introduction

The present chapter seeks a further enhancement of the fuselage section from chapter 5 by combining the usage and optimization of hybrid collapsible energy absorbers with full-scale aircraft dynamic simulations. The Boeing 737-200 fuselage section studied, an aircraft model conceived in the mid 1960s, was not designed according to nowadays crashworthiness standards. Therefore, it becomes a suitable candidate to be fitted with four hybrid energy absorbers similarly-conceived as those in chapter 4 acting as crushable vertical struts. These devices are composed of a hollow aluminum tube, a star-shaped GFRP inner skeleton and foam extrusions. The aircraft undergoes a hard landing scenario, and the effect on the passengers of a baseline absorber is monitored with crashworthiness metrics. Seeking a better response from the craft, the absorbers are parametrized with variable tube edge and thickness, GFRP thickness and core height. Considering the ultimate goal of surrogate-based optimization, a MLS metamodel is built using the LHS technique. Later on, the vertical struts are optimized using single- and multi-objective genetic algorithms according to biometric and crashworthiness criteria, considering peak acceleration loads at two locations, the injury level expected and the structure's weight.

6.2 Components description

6.2.1 Description of test article

For the following study, the verified hard landing scenario from chapter 5 is analyzed. The aircraft is dropped from a height of 4.27 meters, impacts the ground at 9.144 m/s, constituting a severe but survivable crash. Two scenarios were studied in that part of the investigation, either including or excluding the auxiliary fuel tank in the cargo area. Since the latter case delivered the most harmful results —the fuel tank dissipates a significant amount of the vertical kinetic energy, as seen in section 5.3.2.2 —this simulation is chosen as the baseline for structural enhancement.

6.2.2 Model description

Seeking the crashworthiness improvement of the craft, honeycomb-filled energy absorbers as those developed in chapter 4 are added to the model. However, after several preliminary tests, they proved too rigid for the impact conditions of this study, developing only one fold at the most and barely deforming in the post-buckling region as seen in figures 6.1a and 6.1b. Moreover, little energy was dissipated, resulting in low sub-floor deformation on account of excessive acceleration peak loads and significantly drawing the Eiband graph into the severe-injury region. Following the same concept, a version of the hybrid absorbers offering lower stiffness and complexity was considered, also combing metal, GFRP and foam structures. These devices, inspired by the designs from Costas et al. [18], are now composed of an outer aluminum tube filled with a star-shaped structure and foam extrusions filling the triangular cells in-between the composite plates. Since the overall amount of GFRP (the stiffest reinforcing material) is significantly reduced with the skeleton configuration, the absorbers require lower initial triggering loads to undergo progressive collapse.

The square-sectioned tube is 200 millimeters long as it provides enough crush stroke; and it is connected to the fuselage via vertical beams stiffer than the tube

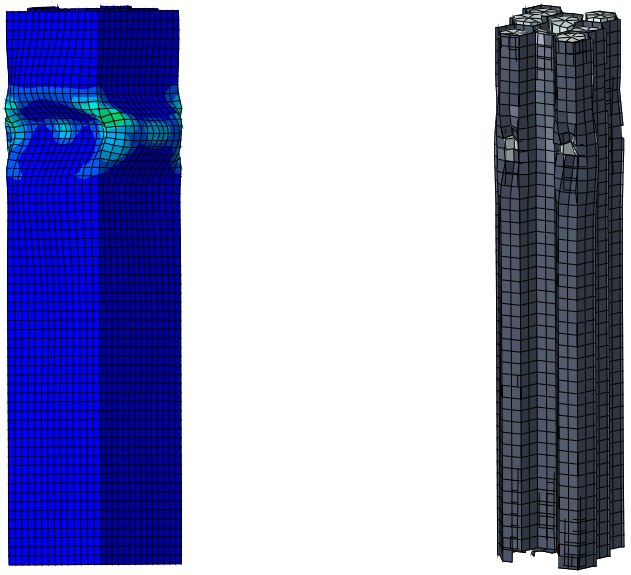

(a) Outer tube deformation. **(b)** Inner reinforcement.

Figure 6.1: Post-test deformation of honeycomb- and foam-filled hybrid energy absorber featured as vertical strut.

to ensure its collapse under impact conditions. They are rotated 45 ° degrees along the vertical axis to reduce global buckling along the longitudinal direction. Two rigid plates are welded to the top and bottom ends of the tube to distribute the vertical load along the edges. The complete assembly of this device is shown in figure 6.2.

Furthermore, a two-millimeter trigger is implemented on the lower tube end to reduce high initial peak forces and ease a stable collapse of the structure [18]. Figure 6.3 shows the trigger locations and displacement direction implemented on the tube.

The tube's inner core is made from an intertwined four-plate star-shaped structure and triangular foam extrusions filling the gap between tube and reinforcement. As done in previous simulations with hybrid absorbers, a one millimeter gap is left between the core and tube to avoid computational instabilities, while easing a hypothetical manufacturing process.

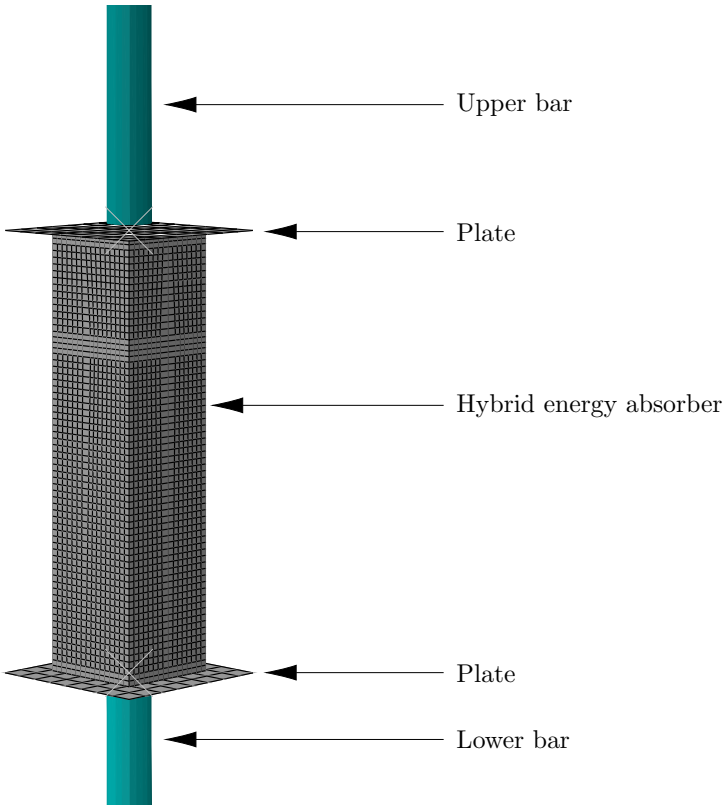

Figure 6.2: Mesh detail of hybrid energy absorber with load-transmitting bars and rigid plates.

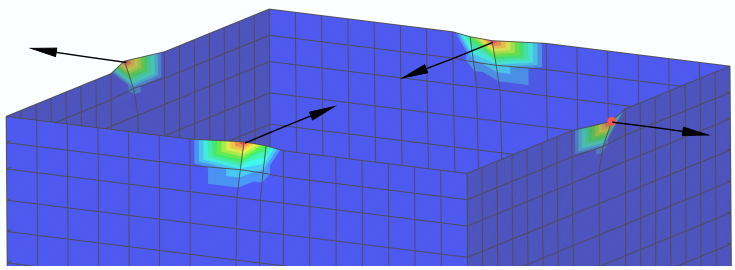

Figure 6.3: Two-millimeter trigger on lower edges of HEA.

A three dimensional cut of the hybrid absorber is presented in figure 6.4, where two of the design variables are shown. In the meshed top view from figure 6.5 the inner core configuration and the final two variables are also represented.

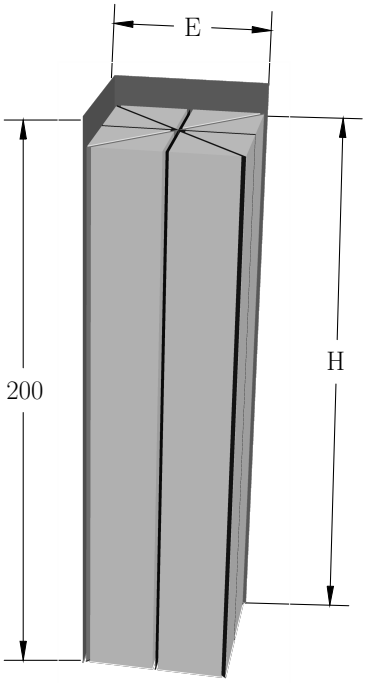

Figure 6.4: Three-dimensional cut of the hybrid energy absorber.

6.2.3 Materials

The fuselage section is made from two different metals. An aluminum AA7075-T6 alloy was used for the frames, under-floor beams and stringers. However, the fuselage skin and floor are made from the aluminum AA2024-T3 alloy. Both materials have been modeled according to the modified Johnson-Cook strain-rate sensitive plasticity model, with equal parameters as in section 5.2.1.

The hybrid energy absorption devices are made with three different materials. The outer tube is made from the AA7075-T6 aluminum alloy used in the fuselage.

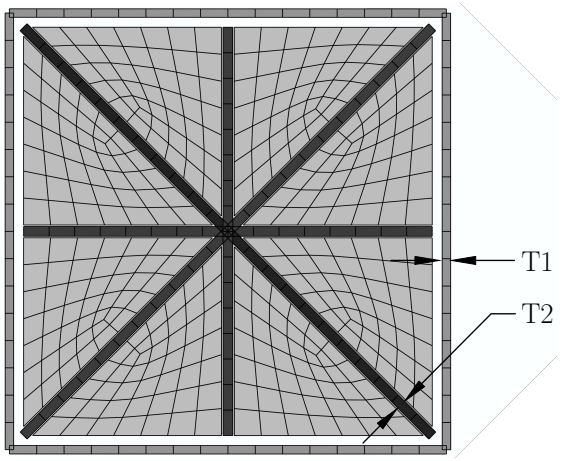

Figure 6.5: Top view of meshed specimen.

The glass-fiber-reinforced polyamide Ultramid A3WG10 BK00564 from BASF is used for the inner plates and a polymeric foam from Armacell (ArmaFORM PET/W AC 135) fills the void cells. Both materials have identical properties as those presented and characterized in section 4.2.

6.2.4 Numerical simulation

The fuselage section and energy absorbers were developed using the Abaqus CAE module in its version 6.16. Shell elements were used to model the skin and floor, frames and under-floor beams for a more accurate behavior of the model, as seen in the longitudinal cut from figure 6.6. However, the omega-section longitudinal stringers are computed as beam elements in order to reduce the number of nodes and computing times, with no significant effect on the results. The passenger-seat blocks are approximated with evenly distributed point masses. A more detailed description of the model can be found in chapter 5.

This specimen is enhanced by adding four[1] vertical struts evenly spaced every two meters in the longitudinal direction and 2.04 meters transversally, ensuring the necessary area for standard aircraft cargo containers [300] as shown in figure 6.6. Since material properties influence the correct mesh size, different values are taken for each component. A sensitivity analysis was performed, in which accurate behavior of the absorber and computational time were considered. Relying on the mesh sensitivity results from chapter 4, the tube and GFRP are modeled with shell elements four millimeters long with four nodes and reduced integration; while the foam is meshed by solid eight-node elements with reduced integration, with an edge of five millimeters, and distortion and enhanced hourglass controls to ensure convergence (see figures 6.2 and 6.5).

6.2.5 Surrogate-based optimization

The initial hybrid absorbers constitute what is referenced as the baseline model. However, even if it betters the original results, changes in certain design characteristics could improve even more the baseline design. In this research, surrogate-based optimization techniques are applied to the hybrid absorber's design to improve different crashworthiness metrics.

6.2.5.1 Design variables and objective functions

In any optimization process, the design variables and objective functions must be established in the early stages. In the aforementioned model, all design variables affect the hybrid energy absorber's design. The tube has variable edge length (E) and material thickness (T1), the GFRP plates can also vary in thickness (T2), and the inner core can be constructed with different heights (H) since slightly shorter reinforcement helps avoid high initial peak forces. These variables, upper and lower bounds, and initial design values are shown in table 6.1.

[1]Only four absorbers are fitted, as the central fuselage station coincides with cargo door structures that interfere with the attaching of the device. The strut opposite to the cargo door is also removed to preserve symmetry.

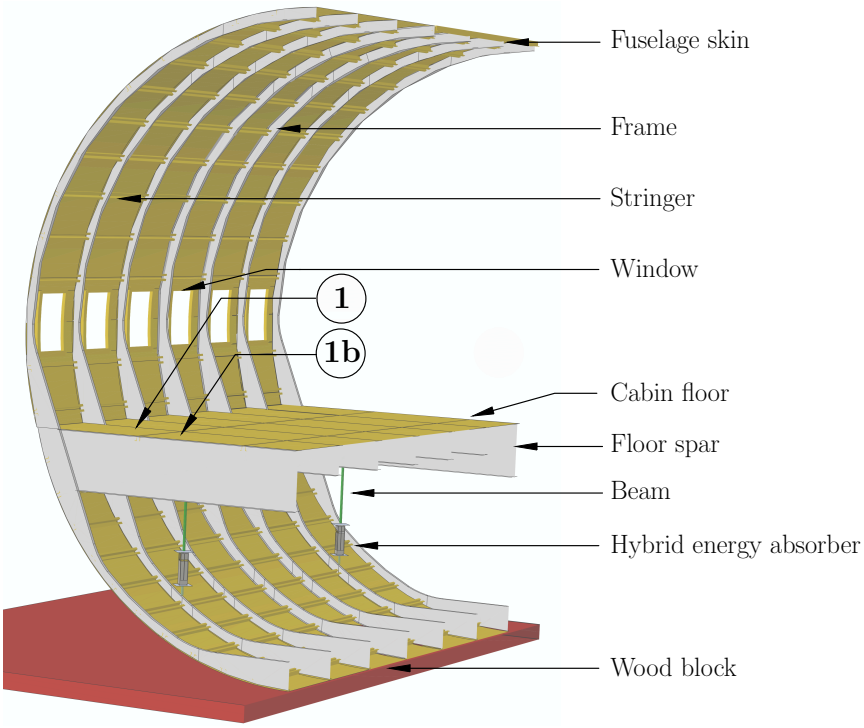

Figure 6.6: Numerical model in Abaqus 2016.

As for the objective metrics, four are also chosen. Acceleration trends are extracted from two locations on the cabin floor. The peak acceleration at the data extraction point 1 is identified by ${A_1}^{\max}$, while the peak load at location **1b**, ${A_{1\mathrm{b}}}^{\max}$, refers to a point vertically coincident with one of the vertical struts location (see figure 6.6). Thus, struts with high stiffness would be identified, as high initial peak crushing loads could increase peak acceleration loads at location **1b** as with the honeycomb-filled specimen.

Moreover, an integration of the acceleration loads over time is done for the evaluation of injury criteria on an Eiband diagram, denoted by ${A_1}^{\mathrm{avg}}$. The lower the area under this curve is, the safer the occupants are, thus being selected as another objective metric. Given the important role of weight reduction in the

Part	Variable	Bounds		Initial Value
		Lower	Upper	
Tube	T1	1.20	2.50	1.50
	E	40.00	80.00	50.00
Core	T2	1.00	3.00	2.00
	L	150.0	190.0	170.0

Table 6.1: Bounds and initial values of design variables. All dimensions in millimeters.

aircraft industry, the mass of the hybrid energy absorber was taken into account, constituting the fourth and last monitored response.

6.2.5.2 Sampling strategy

To perform optimization in this simulation, traditional methods are discarded due to the problems that arise in such a non-linear problem. To address this, surrogate-based optimization is chosen, given its robustness and efficiency. First, once the model with hybrid energy absorbers is parametrized, a LHS strategy is used over the design space. Using the Dakota software as a sampling generator, a total of 600 numerical simulations were computed parallelized with the domain scheme on 16-node CPUs. Considering the amount of simulations computed, every time-saving strategy was deemed vital for efficient sampling execution. The numerical model and output databases were lightened, limiting high-frequency outputs to few nodes. General variables as stresses or strains were requested every millisecond of the 100 ms simulation, while accelerations at the monitored nodes were extracted every 0.1 ms. Even though the usage of mass-scaling was discarded given the effect of inertias in the simulation, subcycling techniques were employed on the smaller elements from the hybrid absorbers. By using this method, the original stable time increment $\Delta t_{\text{fus}} = 1.29$ μs was not hindered by the increment required for the absorbers, $\Delta t_{\text{hea}} = 0.36$ μs, leading to an average time saving of over ten hours (27 %) per simulation. All samples were divided into 15 domains using the Abaqus parallelization scheme and computed on 20 CPUs from a high performance computing (HPC) cluster with a theoretical

peak performance of 7.6 TFLOPS; yielding a computational sampling time of approximately 26 natural days.

6.2.5.3 Surrogate model and optimization

After the sampling is completed, the surrogate model can be constructed. Several methods exist, although the MLS approach is selected given its performance in previous investigations. In order to judge the model's fitness, the R^2 and *RMSE* indicators are looked into. However, the predictive capabilities of the model also need assessing. For this, the *RMSE* is also computed using a 10-fold cross validation strategy.

Once a reliable and trustworthy surrogate model is obtained, optimization can be performed. The usage of algorithms with a need for derivative or gradient information is discarded, as local minima could lead to misleading results. Genetic algorithms, however, have delivered outstanding results in surrogate-based optimization

Two genetic algorithms are used for the optimization task: a single-objective genetic algorithm (SOGA) and a multi-objective genetic algorithm (MOGA), both from the JEGA library [297]. While the results obtained from the SOGA are one single point, the MOGA provides a set of points - the Pareto frontier - which represents a trade-off between the functions considered. The parameters chosen for the genetic algorithms which yielded the best results are detailed in table 6.2.

Parameter	Value
Population size	750
Offset normal mutation rate	0.5
Two-point crossover probability	0.7
Elitism	100
Maximum allowed individuals	10^6

Table 6.2: Configuration parameters for the JEGA library optimization algorithms.

Once the different optima are obtained, each one is again computed to assess whether the surrogate-based optimization produced reliable results.

6.3 Results

6.3.1 Surrogate model fitness

Checking the fitness of the surrogate model approximation is essential for obtaining accurate results in the optimization. Different polynomial orders were tried, with third order yielding the best approximation. Table 6.3 shows the R^2 and *RMSE* values for the MLS surrogate for each of the objective functions.

	Metrics		
Objective function	R^2	RMSE	RMSE (C-V*)
${A_1}^{\max}$	0.90	4.86 g	6.09 g
${A_{1b}}^{\max}$	0.94	2.89 g	3.75 g
${A_1}^{\text{avg}}$	0.92	1.01 g	1.29 g
Mass	0.99	0.042 kg	0.052 kg

Table 6.3: MLS surrogate model fitness. C-V* refers to the cross-validation value of RMSE.

The R^2 indicator is equal or higher than 0.9 for all functions, with also providing *RMSE* values lower than 10% of typical values for the noisier metric, ${A_1}^{\max}$. The *RMSE* is also evaluated with the 10-fold cross validation strategy, with values less than 50 % higher than the original error. The surrogate approximation is considered valid for the optimization process.

6.3.2 Baseline model

As a first approach, the baseline model is analyzed. Results show a significant improvement on the peak acceleration values at both locations (shown in table 6.4).

However, when studying the post-test deformation of the absorber in figure 6.7 it only shows one complete fold, hinting that the baseline design is slightly stiffer than desired. Therefore, the bounds from table 6.1 were set tending towards values that reduced the axial stiffness of the specimen. Figure 6.7 also reveals how the foam extrusions recover the elastic deformation after the fuselage rebound phase, as the absorber's crushing plates moderately separate.

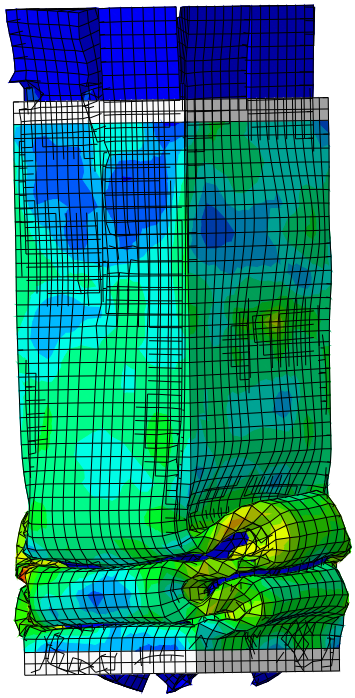

Figure 6.7: Post-impact deformation of HEA under location **1b**.

6.3.3 Single-objective optimization

Unconstrained and constrained single-objective optimization is performed using a genetic algorithm. This process is performed over the surrogate model, hence computational times ranged between 3 to 6 minutes, mainly depending on the number of individuals needed for convergence. A reasonable set of initial design

variables is assigned to a baseline model, which gives insight on the specimen's effect on the fuselage and serves as a measure for the optimization contributions.

Starting with the ${A_{1b}}^{max}$ as an objective function, optimization is applied. Results show that the metric is indeed optimized, reducing the peak acceleration by over 50%. However, this is achieved by selecting an absorber with a low stiffness, as both material thicknesses and the absorber's edge tend to the lower bounds, with the consequent low mass value (table 6.4). This leads to an excellent acceleration damping at location **1b**, while peak values at location **1** are only improved by 22% as no boundary was defined.

As a means to repress excessive accelerations and heavy specimens, the optimization is again computed with constraints for ${A_1}^{max}$ and the specimen's mass. The problem is now formulated as

$$\min({A_{1b}}^{max}) \tag{6.1}$$

while enforcing

$$\begin{aligned} \text{mass} &\leqslant 5.00\,\text{kg} \\ {A_1}^{max} &\leqslant 40.00\,\text{g} \end{aligned}$$

Sample	Variables (mm)				Responses		
	T1	E	T2	H	${A_{1b}}^{max}$	${A_1}^{max}$	Mass
Original	-	-	-	-	78.60 g	87.32 g	-
Baseline	2.00	65.00	3.00	180.0	42.61 g	67.90 g	6.13 kg
Unconstrained	1.51	40.01	1.12	179.0	24.93 g	64.76 g	4.75 kg
Constrained	2.17	47.94	1.62	159.9	27.97 g	39.80 g	4.99 kg

Table 6.4: Design variables and response metrics of original fuselage without absorbers, with baseline absorbers, and with the single-objective optimum specimen designs.

When both constraints are activated, results are more sensible and practical than the previous. The strut's edge and inner core height stay close to the lower boundary, given their effect on the initial peak acceleration when the absorber crushing initiates. In turn, both thicknesses are increased, yielding a design with

more energy absorption capabilities. Thus, both constraints are fulfilled, and the acceleration at location **1b** is still improved by 34%. Design values and the responses obtained for the baseline and optima have been tabulated in table 6.4.

The acceleration trends at location **1** are shown in figure 6.8. The constrained optimum not only shows lower acceleration peaks, but also values which do not exceed 25 g's for most of the simulation. That, in turn, is translated into lower injury levels, as shown in the Eiband diagrams from figures 6.9a and 6.9b.

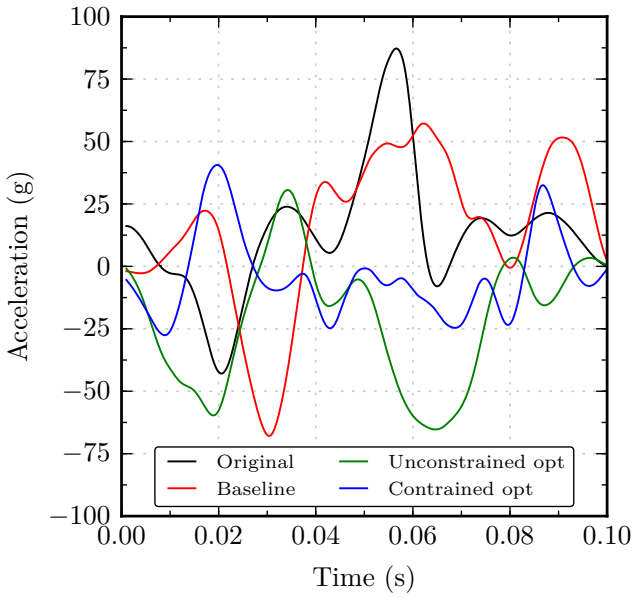

Figure 6.8: Acceleration history of original, baseline and optimum models at location **1**.

Moreover, the area under the passenger floor is less compromised in the enhanced fuselage, an important factor not only for passenger safety but also when transporting hazardous and valuable cargo. In the end, the post-test distance to the ground at location **1**, previously 0.61 m, is increased to 1.01 m (67% more) in the optimum, as shown in figures 6.10a and 6.10b. The rise of the

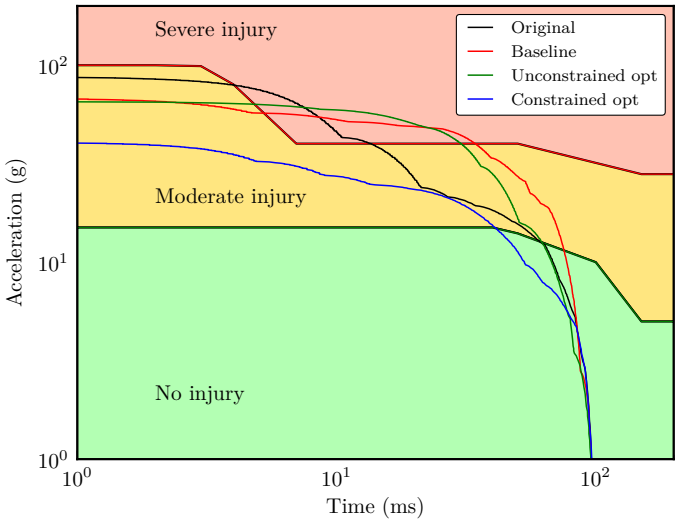

(a) Eiband injury criteria at location **1**.

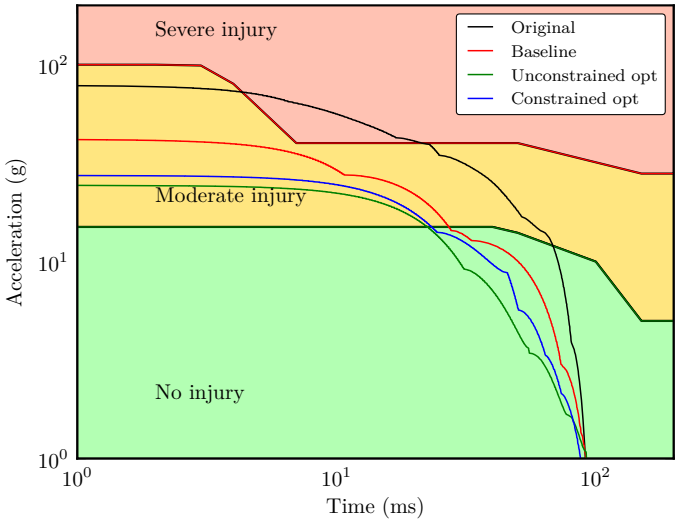

(b) Eiband injury criteria at location **1b**.

Figure 6.9: Eiband diagrams for vertical accelerations at locations 1 and 1b.

hinge formed on the lower left area is also constrained by the struts, reducing the risk of impact with the passenger floor and avoiding the resulting peak seen in figure 6.8.

6.3.4 Multi-objective optimization

Single-objective optimization expectedly improves the original and baseline designs, especially when other constraints are enforced. However, if optimality is sought on two or more metrics, multi-objective optimization is used. Here, two procedures are presented, one with two objective functions and another with all four metrics. First, the absorber is optimized for minimum acceleration peak loads at two locations. Results are expressed as a Pareto front, which has been detailed in table 6.5.

Variables (mm)				Responses		
T1	E	T2	H	${A_{1b}}^{max}$ (g)	${A_1}^{max}$ (g)	Mass (kg)
2.40	52.88	2.28	153.73	31.71	35.64	5.25
2.16	47.94	1.63	159.83	27.97	36.64	5.00
1.32	55.58	1.18	189.94	26.77	55.52	5.19
1.56	56.45	1.35	184.60	26.57	56.38	5.24
1.58	54.72	1.71	188.47	25.89	63.51	5.31
1.79	50.54	1.81	182.08	24.91	70.30	5.43

Table 6.5: Design variables and response metrics of Pareto front.

A deeper look at the Pareto values from figure 6.11 shows that ${A_1}^{max}$ values are in the same magnitude order but higher than those at ${A_{1b}}^{max}$, as expected from previous investigations [49]. This could be caused by the load distribution during the initial crushing states, where the main frames absorb most of the kinetic energy. Thus, when a data extraction location is closer to the frame, acceleration peaks tend to be higher. The response from location **1b** is damped by the absorber, which not only dissipates kinetic energy energy but also avoids vibration of the passenger floor structures. Looking at the variables and metrics evolution, the thickness of the GFRP tends the low boundary value, as thin plates are sufficient to enable the interaction effect between all three components

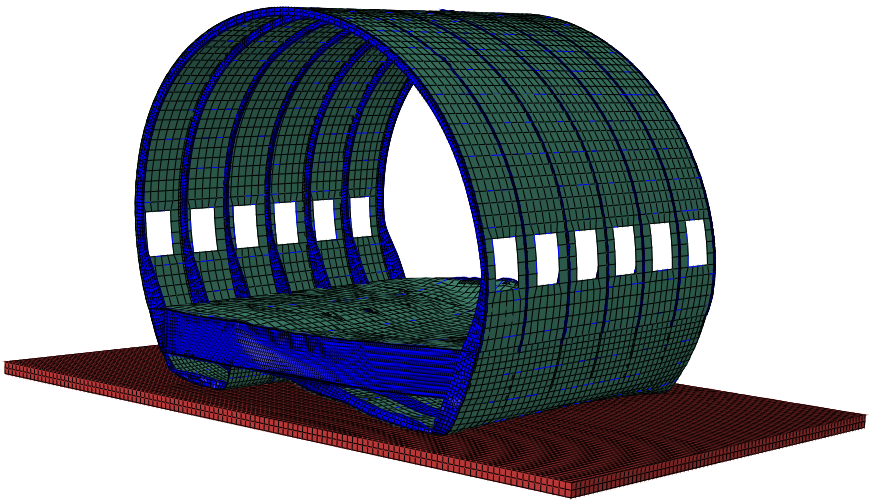

(a) Original fuselage section.

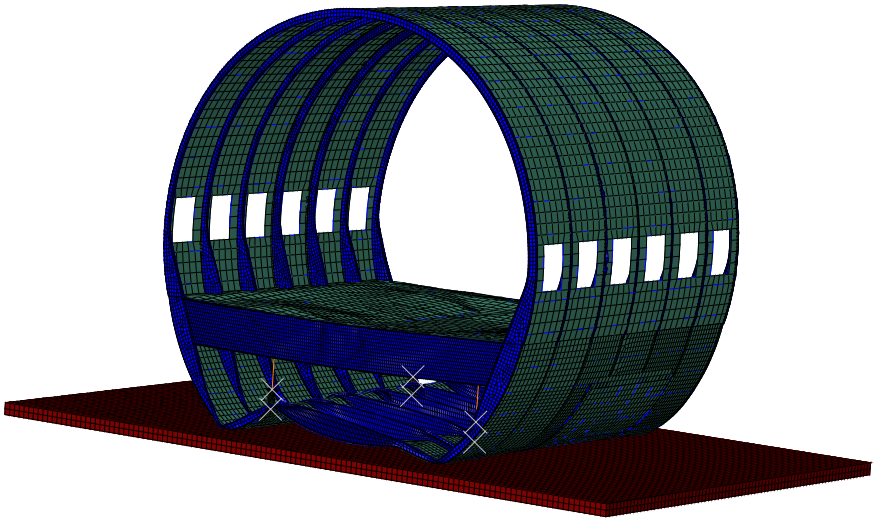

(b) Fuselage section with HEAs.

Figure 6.10: Deformation comparison of crushed fuselage section with and without HEAs.

given the high density and stiffness of the composite. Also, the tube's edge is always kept on the lower half of the design space (under 60 mm), as surpassing that value would entail higher masses and peak loads resulting from absorbers being too rigid.

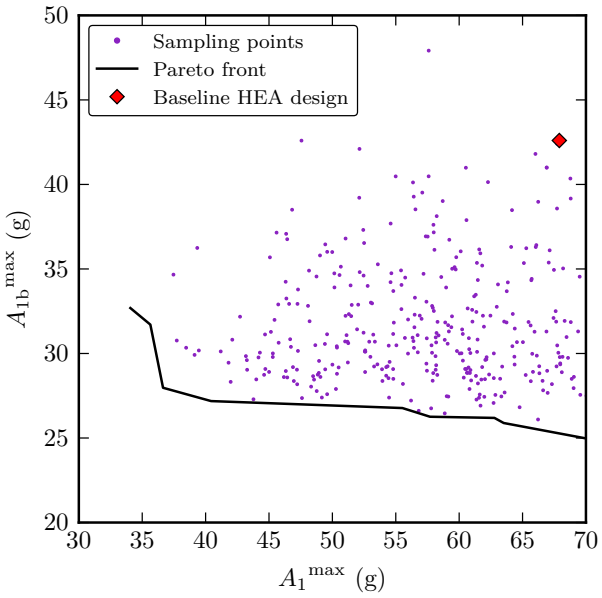

Figure 6.11: Pareto front and sampling values for $A_1{}^{max}$ and $A_{1b}{}^{max}$.

As a last approach, optimization with all four metrics is performed. Rather than requesting a Pareto frontier, the closest specimen to the utopia point is provided. The optimum has nearly matched acceleration peaks, both under the 35 g frontier. The overall reduction of the peak load is over 50% on both data extraction points when compared to the original fuselage section. Injury levels are reduced from severe to moderate at both locations, as shown in the Eiband diagram from figure 6.12. The injury curves from the optimum do not reach the severe injury region as opposed to the original, and enter the no injury area earlier. Moreover, mass is reduced from the initial 6.13 kg to designs between 5 and 5.5 kg. In addition, the cargo area is maintained, reducing the risk of sub-floor piercing through the passenger floor with the consequent occupant injury.

It should also be noted that results from the optimization procedures reveal a peculiar behavior on the acceleration trends for ${A_1}^{\max}$ and ${A_{1b}}^{\max}$; offering discordances between the two of up to 45 g's. While the objective metrics offered by the optimization closely resemble those in a finite element simulation with similar design variables (the discordances measured were less than 5 %); there may be some inaccuracies in the fuselage model used, mainly build on a reverse-engineering basis. However, coupling between full-scale impact simulations and surrogate-based optimization has been successfully performed, proving itself as and outstanding tool in aircraft crashworthiness design.

Variables (mm)				Responses			
T1	E	T2	H	${A_{1b}}^{\max}$	${A_1}^{\max}$	Mass	${A_1}^{\text{avg}}$
2.33	49.30	1.38	173.68	32.69 g	34.06 g	5.00 kg	13.22 g

Table 6.6: Design variables and response metrics of the closest specimen to utopia point.

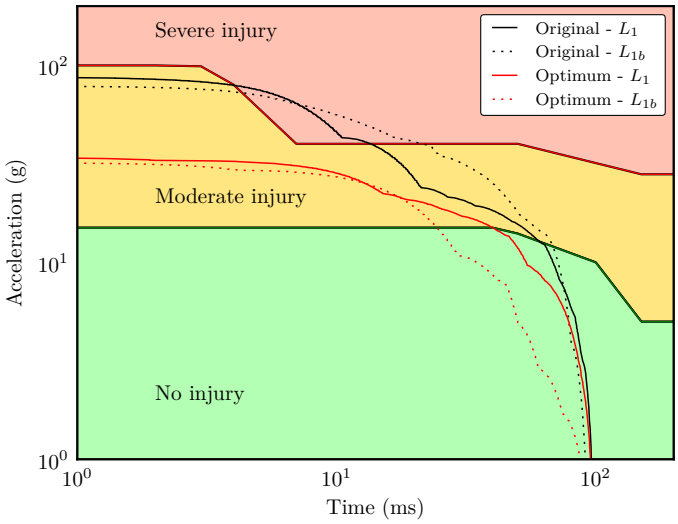

Figure 6.12: Eiband injury criteria of original fuselage and HEA optimum from table 6.6.

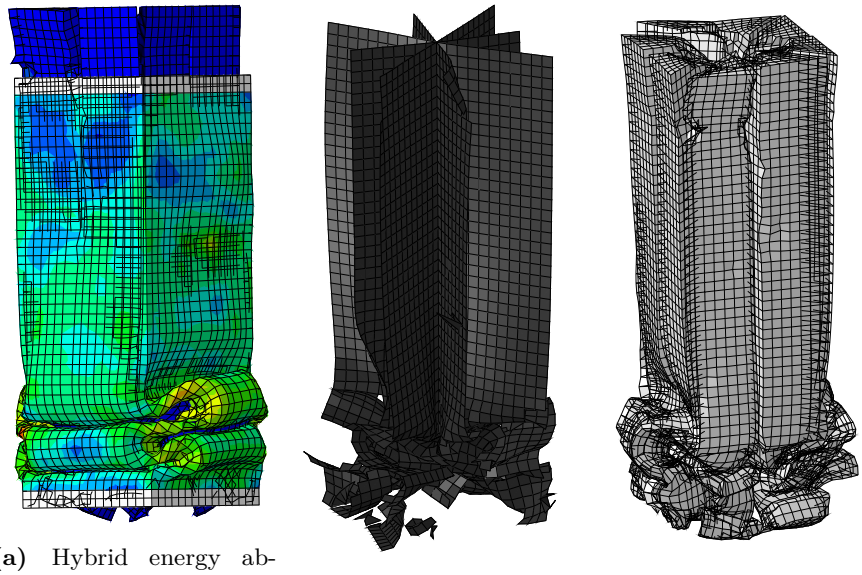

(a) Hybrid energy absorber. Full specimen.

(b) Composite skeleton.

(c) Foam extrusions.

Figure 6.13: Post-test deformation of hybrid energy absorber under location **1b** for model in table 6.6. Complete specimen and inner core.

As to assess the performance of the hybrid absorbers during the simulation, the post-test deformation from figure 6.13, corresponding to the hybrid energy absorber under location **1b** for the model closest to the utopia point, is analyzed. In the full specimen from figure 6.13a, the outer tube exhibits the formation of three complete plastic folds, corresponding to a crushing stroke of 60 mm with folds lengths in the neighborhood of 20 mm. Considering that the crushing initiates from the lower end of the tube, the GFRP skeleton is primarily affected in the homologous region. Figure 6.13b reveals significant damage on the lowest part of the structure, while the rest still maintains structural integrity for further energy absorption if it were required. Finally, figure 6.13c shows the foam extrusions after crushing and elastic strain recovery, almost reaching pre-test dimensions.

After extracting the force-displacement curve of the aforementioned absorber and treating it with a SAE 600 filter, it is presented in figure 6.14. The graph

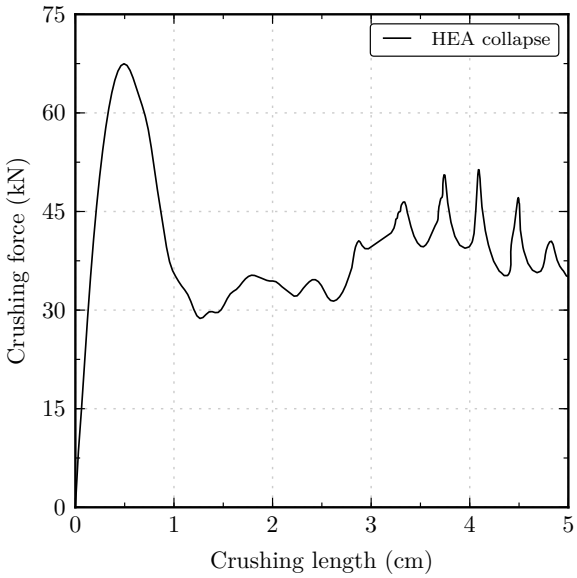

Figure 6.14: Force-displacement evolution of energy absorber from figure 6.13.

clearly reveals two sets of local maximums along the curve, the first one nearly reaching 70 kN while the others peak at 50 kN. These values correspond to the initial and secondary fold formations, with the latter 30 % lower as is typical with this type of absorbers. However, the force plateau observed one centimeter into the crushing process differs with what was expected from the results with the analysis of standalone absorbers. This behavior can be explained by relating to the crushing evolution of the device as featured in the fuselage, since there exist certain periods when no force is transmitted to the specimens. The total crushing length is slightly over 5 cm, leading to a stroke efficiency of $St_e \approx 0.25$. Considering the stroke efficiency achieved by similar components ($St_e = 0.8$ in chapter 4), it is judged that more folds could have developed if the impact conditions were more severe. Still, the final internal energy[2] dissipation from the absorbers is over 5 % (approximately 8 kJ) of that from the whole model, as shown in figure 6.15. This graph also reveals how their contribution is mainly

[2]Internal energy is computed in Abaqus as the sum of recoverable strain energy, plastic dissipation energy, energy dissipated by creep, viscoelasticity and swelling, and the artificial strain energy.

relevant around 50 ms into the impact, where they undergo collapse after the triggering load is reached. Thus, the hybrid absorbers only collapse during 10 % of the analysis time, maintaining structural integrity to provide support for frames and floor beams to avoid further cargo-area deformation.

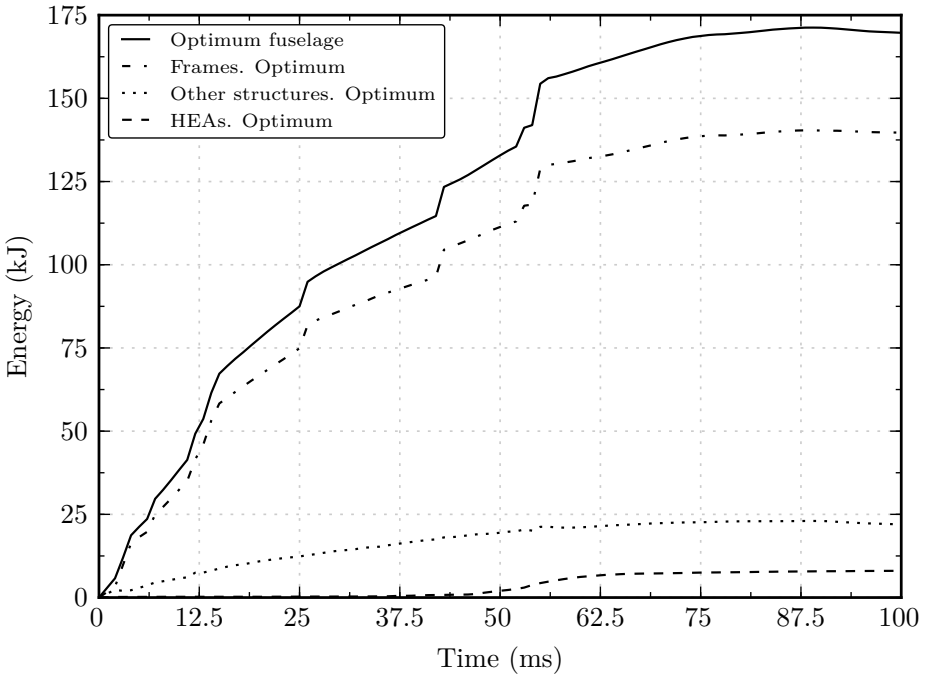

Figure 6.15: Internal energy for model in table 6.6, divided by significant structural components.

Exploiting the capabilities of numerical simulations over experimental procedures, energy values and trends are further looked into. The artificial-to-internal energy ratio, always under 10 %, still complies with the recommended limits for dynamic impact simulations [253]. Moreover, a comparison between the original fuselage with the optimum from table 6.6 in terms of energy absorption by plastic deformation reveals a significant disparity on the frames' performance (see figure 6.16). While these structures originally absorb 76 kJ, this value increases over 55 % to reach the 120 kJ mark in the enhanced fuselage, translated into a global difference of 50 kJ. By relating the results from this energy analysis with

the post-test deformations from figure 6.10, it can be observed how the overall structural behavior of the aircraft is modified; with the collapse evolution after adding the struts showing a higher usage of the frames plastic capabilities in addition of the energy dissipated by the devices.

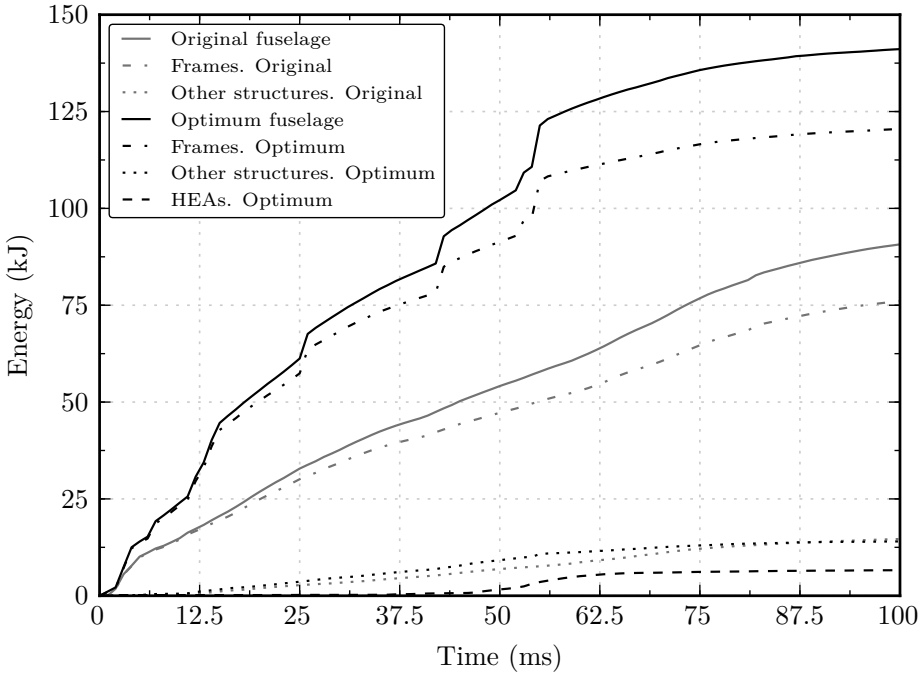

Figure 6.16: Energy dissipation by plastic deformation for original model and optimum from table 6.6.

6.4 Conclusions

In the research developed throughout this chapter, four vertical hybrid energy absorbers are added to work as crushable vertical struts in a fuselage. The following conclusions can be withdrawn:

- A drop test simulation of a Boeing 737-200 fuselage enhanced with a baseline hybrid absorber was performed. The absorber, composed by a square aluminum tube filled with GFRP plates and foam extrusions, delivers lower peak acceleration loads at the two data extraction locations when implemented in the aircraft.

- Four variables from the baseline absorber geometric design are parametrized for executing a 600-model Latin Hypercube Sampling and the following construction of a Moving Least Squares surrogate model. This model delivers a satisfactory approximation, with low $RMSE$ and R^2 values over 0.9 for all objective functions considered: peak acceleration at two locations (${A_1}^{\max}$ and ${A_{1b}}^{\max}$), injury criteria (${A_1}^{avg}$) and mass of the specimen.

- Single-objective optimization is performed with and without the usage of constraints. Unconstrained optimization reduced accelerations at the optimized location by over 50%, but best results were delivered when applying a constraint for the acceleration at the remaining point. By enforcing constraints, accelerations are reduced by over 50% at both locations when compared to the original fuselage, while maintaining the absorber's mass under 5 kg.

- Multi-objective optimization is also performed, with two and four objective functions. A Pareto front was obtained for ${A_1}^{\max}$ and ${A_{1b}}^{\max}$, where all designs improve the original and baseline fuselages. Also, trends in the variables show how low thickness values for the composite can still deliver high energy absorption values, as the interaction effect between all materials is still enabled. At the closest to the utopia point, the fuselage exhibits acceleration peaks under 35 g's at both locations, while maintaining a mass of only 5 kg.

- The usage of energy absorbers was also found to substantially affect the collapse process of the fuselage, bettering its overall response. The cargo area is less compromised, avoiding piercing of sub-floor structures with the passenger floor and maintaining a safer survivable area. In addition to the 8 kJ from the hybrid struts, the modified frames' collapse yields and overall increase in plastic dissipation of over 50 kJ.

References

[49] Siromani, Deepak. *Crashworthy design and analysis of aircraft structures.* Drexel University, 2013.

[253] *ABAQUS 6.16 Documentation.* Dassault Systèmes. 2016.

[18] Costas, M, Morin, D, Langseth, M, Romera, L, and Díaz, J. "Axial crushing of aluminum extrusions filled with PET foam and GFRP. An experimental investigation". *Thin-Walled Structures* 99 (2016), pp. 45–57.

[297] Eddy, J. E. and Lewis, K. "Effective Generation of Pareto Sets using Genetic Programming". *Proceedings of ASME Design Engineering Technical Conference* (2001).

[300] Airplanes, Boeing Commercial. *737 Airplane Characteristics for Airport Planning. D6-58325-6.* 2013.

7

Summary, conclusions and future research

This chapter concludes the present investigation, not without offering a brief summary of the work done, the conclusions from each of the studied topics and future lines continuing the work done.

7.1 Summary

This research versed on blueprinting, characterizing the behavior and improving hybrid energy absorbers intended for the crashworthiness enhancement of aircraft designs. The specimens were modeled and analyzed through high-end finite element simulations; while the usage of sampling, metamodeling and optimization algorithms allowed to improve selected responses of the initial designs. In a later stage, a fuselage drop-test was also developed, tuned and verified to assess absorber's performance in a representative impact scenario; which to the author's knowledge, no such study has been performed up to date.

The absorbers from chapter 3 revealed that the usage of honeycomb reinforcing structures constitutes an effective manner of enhancing thin-walled crushable tubes. Moreover, surrogate-based optimization techniques were successfully applied, delivering reliable and outstanding results. The characteristics of honeycombs are explored deeper in the models from chapter 4, were cell shape is first introduced as a variable. Later on, the addition of foam extrusions is also judged according to its crashworthiness enhancement of the component.

The accurate contribution of collapsible absorbers featured as aircraft vertical struts was measured in chapter 5. The dynamic experiment was modeled with a finite element code and thoroughly verified with experimental data. An in-depth analysis of the simulation also showed the structural crushing behavior and energy absorption characteristics of the main components. In chapter 6, hybrid energy absorbers are added to the aircraft section from chapter 5 for improved occupant protection. While honeycomb-reinforced devices proved too rigid in such an impact scenario, a GFRP skeleton and foam extrusions were used as core structures. The four absorbers added to the fuselage, with variable edge length, core height and material's thicknesses, undergo surrogate-based metaheuristic optimization techniques as part of the full scale simulation; ultimately seeking lowered injury levels and minimum mass values.

7.2 Conclusions

The conclusions extracted from this work are now presented, first offering the comprehensive knowledge gained followed by a particularization on a chapter basis. Considering the overall investigation, it can be stated that:

- Multi- and single-objective optimization techniques have been consistently and successfully applied on crashworthiness dynamic simulations all throughout the research. Traditionally hindering characteristics, including large non-linearities, noisy data, strain-rate dependency of materials or fracture processes, have been effectively overcome with the usage of surrogate-based optimization and genetic algorithms.

- Honeycomb reinforcements for thin-walled collapsible tubes have proved outstanding in enhancing the component response. Superior crashworthiness behaviors were obtained for novel designs with non-regular cell shapes and foam blocks filling cell voids.

- A full-scale fuselage section, developed though reverse engineering and response-tuning from experimental data, was used as a benchmark for

testing the effects of featuring collapsible absorbers as vertical struts. The addition of these structures substantially modifies the aircraft collapse mechanisms, ultimately dissipating over 50% more energy than the original structural design.

From the investigation on the dynamic axial crushing of hybrid steel specimens, it was concluded that:

- The usage of honeycomb reinforcements on steel tubes delivers energy absorption values over nearly 30 % higher than a thicker-walled tube with equal mass.
- The interaction effect during the crushing of honeycomb-filled specimens can account for more than 20 % of the total energy dissipated by the component.
- Optimization of the initial design showed the existence of specimens with peak force values a third lower while maintaining similar values of mass and energy absorption; or specific energy absorption rates 39.5 % higher with similar force maximums.
- Peak force values are lowered when the honeycomb height and its plate thickness are reduced, with no significant harm on the specific energy absorption values.
- Honeycomb components prove outstanding as structural reinforcement for axially-crushed thin-walled metallic tubes, offering a more controlled collapse process and higher energy absorption efficiency than single-component configurations.

The second set of designs studied featured aluminum tubes, honeycombs with variable cell shape and foam extrusions. The author reached the following conclusions from its analysis:

- The usage of triggers on the impacting edge of the thin-walled tube reduces over 30 % of the initial crushing loads, while also producing more stable collapse mechanisms.

- Single-objective optimization of the honeycomb's cell shape revealed that non-regular designs offered an energy absorption efficiency over 10 % higher than regular hexagons, with no increase in peak force values.

- Multi-objective optimization of the honeycomb-filled component showed that peak force of the initial designs can be lowered by 55 % whilst delivering a similar *SEA* performance; or boosting the later 65 % and still reducing the maximum force by almost 20 %.

- Foam extrusions filling the honeycomb cells have delivered *SEA* values 28 % higher with no harm on the maximum force response.

- For devices featuring foam extrusions, optimization of the cell shape according to *SEA* performance delivered values of up to 24 kJ/kg for pseudo-rectangular cells instead of the 19 kJ/kg from the baseline specimen.

- Different multi-objective optimizations showed that best performances according to weight, energy absorption and maximum force criteria are delivered by specimens with large, non-regular thin-walled cells and high aluminum thicknesses.

After the development and validation of the fuselage drop-test simulation, the following conclusions were extracted:

- Aircraft vertical impact scenarios with and empty cargo region result in more severe injury levels than those with an auxiliary fuel tank located in the cargo area.

- The addition of hollow aluminum crushable tubes as vertical struts can reduce peak acceleration values by 25 % in a section with a fuel tank, and by over 50 % without this component.

- Energy absorbers also maintain intact a greater part of the survivable volume, avoiding the bottoming-out of the sub-cargo area and object-intrusion on the passenger cabin.
- Injury levels on an Eiband diagram are reduced from severe to moderate when crushable absorbers are fitted.

The last part of this investigation led to the hereunder conclusions

- Hybrid energy absorbers composed of aluminum, glass-fiber reinforced polymers and foam can reduce acceleration loads by over 20 g's in a fuselage vertical drop test.
- Optimization techniques offered designs with acceleration maximums reduced by 50 % at the two monitored passenger locations. Mass was also considered as an objective function, yielding weight savings of over one kilograms per device.
- The analysis of the design variables after optimization reveals that tube sections with low inertia and thin GFRP plates are preferred, as those designs offer the best ratio between mass and acceleration damping.
- The addition of hybrid energy absorbers as vertical struts modifies the overall structural collapse process, yielding plastic dissipation values over 55 % higher mainly rooted in a higher usage of the frames plastic capabilities. The contribution of the absorbers is 8 kJ (5 %) of the final plastic energy absorption.

7.3 Future research

The outcomes of this work may be continued and further analyzed along many research paths, some of which are now presented:

- The current material characterization has sufficed for accurately matching dynamic numerical simulations with experimental data. However, a broad

campaign could be run for determining the strain-rate properties of the materials used, bringing simulation and experiment ever closer.

- Regarding the design of energy absorbers, further crashworthiness enhancements may be found exploring new material combinations and novel structural arrangements. Bi-material tubes made from metals and composites have shown excellent crushing behavior, while multi-corner tubes deliver specific energy absorption values 50 % higher than traditional cross-sections.
- The impact conditions of the fuselage featuring energy absorbers can be widened for a deeper understanding of their performance, studying different impact velocities, surfaces or angles. More data recording points at the fuselage may be processed, capturing locations with higher injury risk and reducing it accordingly.
- Explore other variants for featuring crushable absorbers in the fuselage model, including their positioning along the longitudinal and transversal directions or their angle with the vertical axis, as other authors have proved its effect on the aircraft's crashworthiness. Hybrid honeycomb- and foam-filled belly sections are also yet to be studied.
- Concerning the techniques used, new metamodeling and optimization algorithms could be used seeking faster and more accurate results.

Appendices

A

Extended summary in Spanish

Hereunder an extended summary in Spanish is presented, as to comply with the content regulations from the Universidade da Coruña.

A.1 Introducción y objetivos

La sociedad actual está cada vez más concienciada con las consecuencias derivadas de los accidentes de tráfico y otros medios de transporte. Ingenieros y diseñadores han desarrollado numerosos sistemas de seguridad activa que ayudan a reducir el número de colisiones en todos los medios de transporte. En el caso de los vehículos, centralitas electrónicas distribuídas a lo largo del coche son programadas con algoritmos para evitar el bloqueo de frenos o maximizar la tracción de las ruedas dependiendo de las condiciones de agarre; mientras que los sistemas electrónicos de ayuda al pilotaje han facilitado cada vez más el control de las aeronaves. Sin embargo, cuando el impacto es inevitable, es necesario un sistema estructural diseñado adequadamente que pueda reducir los daños sufridos por los ocupantes. El diseño de las estructuras atendiendo a criterios de impacto busca el colapso progresivo de los componentes estructurales con el fin de disipar altas cantidades de energía cinética, manteniendo a los pasajeros protegidos en una célula quasi-indeformable.

En el caso de los automóviles, ya es común el uso de aceros de alta resistencia en puertas y pilares-B, aumentando la protección ante impactos laterales. La

zona frontal de algunos modelos ya incluye elementos unidos a los raíles frontales que han sido diseñados para un colapso y absorción de energía progresivos. Para las aeronaves, por su parte, existen propuestas con extrusiones de espuma en parte inferior de la zona de carga para atenuar las deceleraciones durante impactos, soportes verticales que se delaminan progresivamente o cuadernas con mecanismos biela-tirante que aumentan la energía disipada y reducen los daños causados por un impacto vertical. Dentro del amplio rango de los elementos para protección ante impacto, uno de los diseños analizados más en detalle es el de los absorbedores colapsables, con especial énfasis en los tubos de pared delgada.

El mecanismo de colapso de estos elementos ha sido estudiado desde la década de 1960, cuando se caracterizaron el comportamiento de tubos huecos de sección circular y cuadrada. Un dimensionamiento correcto de las proporciones entre altura, espesor e inercia de la sección origina un modo de colapso basado en la generación de pliegues (pandeos locales del material) que exhibe una disipación de energía constante durante más de tres cuartos de la longitud total del tubo. A la vista de este comportamiento, numerosos autores han experimentando con variedad de secciones, materiales, y refuerzos interiores; obteniendo valores de absorción de energía varias veces superior a los diseños huecos originales.

Así, uno de los principales objetivos de este trabajo es el diseño y caracterización del comportamiento de sistemas híbridos de absorción de energía orientados a su uso en aplicaciones industriales. Tubos metálicos cuadrados son complementados con estructuras internas hechas de materiales compuestos y espumas, buscando una mejora en su comportamiento ante cargas dinámicas de impacto. Entre los refuerzos existentes, se presta especial atención a las estructuras de nidos de abeja, estudiando su respuesta al variar el tamaño y la forma de sus celdas. Además, se analiza el uso de la espuma como único material reforzando el tubo y rellenando las celdas huecas, caracterizando el incremento de la rigidez estructural aportada por este elemento así como su penalización en la masa.

La segunda parte de esta investigación busca demostrar la respuesta mejorada que aporta el uso de los absorbedores de energía en un caso de impacto representativo. Para ello, se modela con procesos de ingeniería inversa el impacto vertical de una sección de fuselage de un Boeing 737-200 con el software de elementos finitos

Abaqus 2016 en su versión de cálculo Explicit. Posteriormente se comparan y ajustan los resultados de la simulación numérica con los datos expermientales del ensayo original, prestando especial atención a la evolución de las curvas de aceleraciones y velocidades, así como los niveles de deformación en distintos instantes de tiempo. Diversos indicadores biométricos son utilizados para medir los niveles de daño estimado en los ocupantes, como las aceleraciones máximas o la integración de las aceleraciones en un diagrama de daño de Eiband. Finalmente, se añaden absorbedores híbridos de energía al fuselage, conectando las vigas que soportan la cabina con la zona inferior de las cuadernas. La simulación aporta información sobre el comportamiento global de la estructura que permite evaluar el beneficio real ofrecido por estos elementos.

A.2 Metodología y modelos

Una de las bases de este trabajo reside en el uso de métodos de optimización como herramienta para diseñar estructuras más eficientes. En este caso, y dada la naturaleza altamente ruidosa y no-linear de las simulaciones con las que se trabaja, la optimización se ayuda del uso de modelos subrogados. Estos métodos reemplazan las funciones ruidosas, no derivables y con discontinuidades en otras con un comportamiento homólogo pero notablemente más suave, constituyendo el metamodelo o modelo subrogado. Para ello, se realiza primero un muestreo eficiente que ofrezca suficiente información de como responde el modelo ante los cambios en las variables de diseño. A lo largo de este trabajo se usa el método de los hipercubos latinos (LHS), ya que maximiza la información aportada por cada muestra evitando la superposición de los valores de las variables. Esta información es tratada por otro algoritmo que genera las funciones necesarias para obtener el metamodelo. Dos modelos basados en la conjunción de splines y funciones polinómicas han servido para este propósito, los "multivariate adaptive regression splines" (MARS) y los "moving least squares" (MLS) respectivamente. Los metamodelos representarán a partir de ahora a los modelos numéricos, por lo que debe establecerse si son eficaces en ello. El uso de métricas estadísticas de error, como la bondad de ajuste R^2 o el error medio cuadrático RMSE, permite discernir

si este modelo se corresponde con las respuestas de la simulación. Además, el cálculo de estos indicadores con técnicas de validación cruzada permite estimar la capacidad predictiva y el nivel de aproximación aportado por los metamodelos.

Cuando la bondad de ajuste del modelo subrogado cumple con los requisitos establecidos, este puede ser luego optimizado en cuestión de minutos usando algoritmos genéticos. Estos procedimientos, inpirados en la evolución genética, crean generaciones de individuos que combinan y mutan dando lugar a generaciones posteriores. Un ajuste adecuado de sus parámetros biométricos aporta gran robustez ante los mínimos locales, recurrentes en este tipo de modelos.

La optimización realizada se puede dividir según tres grados de complejidad, obteniendo cada vez más información y mayor control sobre las respuestas aportadas por el modelo. Inicialmente se realiza optimización mono-objetivo de una función como la energía absobida o la *SEA*, añadiendo posteriormente diversos límites a respuestas como la masa o la fuerza máxima durante el ensayo. Finalemente se realiza optimización multi-objetivo, calculando frentes de Pareto compuestos por modelos que no pueden mejorar su respuesta en una función sin empeorar su valor en otras. Así, se obtiene una gran variedad de diseños, con un comportamiento óptimo pero adaptables a distintas necesidades estructurales.

Otra parte de esta investigación consiste en el modelado de un ensayo dinámico del impacto de un fuselaje ante una superficie de madera. El modelo consiste en una sección de 3700 kg y tres metros de largo, impactando el suelo a 9.144 m/s. Elementos como la piel o las cuadernas son representados con elementos lámina con el fin de capturar más fielmente el pandeo local y otros mecanismos complejos de colapso. Sin embargo, los rigidizadores longitudinales se modelan con elementos barra, reduciendo así en número de grados de libertad del modelo y agilizando los tiempos de cálculo de las simulaciones. El comportamiento de la estructura se analiza según criterios de deformación tras el ensayo, daño resultante en los pasajeros y absorción de energía de los componentes. De este modo, se analiza si la presencia o ausencia de ciertos componentes resulta en configuraciones que son más peligrosas para los ocupantes.

Se utiliza estudio preliminar con tubos huecos de aluminio para determinar la sensibilidad de la aeronave ante la implementación de estos elementos. Finalmente se añaden los absorbedores híbridos de energía al fuselaje, compuestos de tubos cuadrados de aluminio de sección variable rellenos de una estructura de láminas de GFRP interconectadas y con extrusiones de espuma. Estos elementos se disponen espaciados cada metro en dirección longitudinal y 2.04 en transversal, cumpliendo con las dimensiones de un contenedor de carga estándar. Con esta simulación parametrizada se genera un nuevo modelo subrogado, usando como variables de diseño el espesor y lado del tubo, la altura del relleno y el espesor de las láminas de GFRP. Este metamodelo se someterá a optimización, buscando minimizar la masa de los elementos a la vez que se mejoran varios indicadores biométricos de daño en pasajeros como el diagrama de lesiones de Eiband.

A.3 Resultados y discusión

Los resultados del análisis del componente compuesto por el tubo de acero y un nido de abeja regular de GFRP confirman los beneficios aportados por estos rellenos, obteniendo valores de absorción de energía por unidad de masa (*SEA*) un 28 % superiores que en componentes vacíos. También se ha cuantificado el efecto de interacción entre los elementos del componente, pudiendo suponer hasta un 22 % de la energía total disipada por el espécimen. A nivel del relleno, la disminución del tamaño de las celdas también aporta un mejora del comportamiento ofreciendo un valor de *SEA* más alto cuando se reduce el lado del hexágono bajo 15 mm. El uso de la optimización permitió reducir valores de fuerza máxima 33 % manteniendo valores similares de *SEA* y masa, así como obtener conjuntos de diseños con valores simultáneamente óptimos de energía absorbida y masa, o *SEA* y pico de fuerza.

Con el segundo conjunto de modelos se estudian ciertas mejoras y su aporte al comportamiento ante impacto del componente. Así, el acero es substituído por aluminio de alta ductilidad, puede aumentar la energía absorbida al entorno de los 100 kJ; mientras que la variacón de la forma regular de la celda por otras de forma pseudo-rectangular mejora la *SEA* otro 15 %. Por último, se demuestra que

el uso de extrusiones de espuma como relleno de las celdas permite la obtención de diseños con valores de *SEA* de 23 kJ/kg, manteniendo la fuerza máxima bajo el umbral de 420 kN. Al igual que en el apartado anterior, la optimización basada en subrogados permite obtener diferentes diseños que mejoran la respuesta de una o más funciones objetivo.

A la hora de ajustar y validar el fuselaje, se analiza la evolución de las aceleraciones y velocidades durante el impacto, obteniendo una excelente concordancia entre los valores numéricos y los experimentales. Las gráficas capturaron fielmente los cambios de pendiente y los valores máximos en las curvas, con mínimas discordancias. Además, se halló que la ausencia del tanque de combustible, responsable de la disipación de una gran cantidad de energía cinética, resultaba en una mayor deformación de las estructuras principales con deceleraciones más bruscas y su consecuente aumento en el nivel de lesiones en los ocupantes.

Una vez se ha validado la respuesta del modelo numérico, se evalúa la efectividad de la implementación de sistemas colapsables de energía de pared delgada. En una primera iteración se estimó la respuesta del fuselaje con cinco tubos huecos verticales en la zona de carga. Estos contribuyeron un 6 % a la disipación de energía y redujeron las aceleraciones máximas en 45 g's. Además, al evitar el impacto de las zonas inferiores del fuselaje con el suelo de la cabina de pasajeros, el nivel de daño en los pasajeros disminuyó de severo a moderado en varias localizaciones de medida.

Para finalizar, se optimizó la respuesta ante impacto de un fuselaje con absorbedores híbridos de energía. La parametrización de los modelos permitió variar las dimensiones del tubo, el relleno de espuma y láminas de GFRP y los espesores de los materiales. El muestreo para la generación del metamodelo requirió 600 simulaciones a escala real para obtener valores de R^2 superiores a 0.9, mientras que el RMSE se mantuvo con valores reducidos incluso tras la aplicación de las técnicas validación cruzada. Los resultados de la optimización con algoritmos evolutivos ofrecen modelos con la rigidez necesaria para desarrollar entre tres y cinco pliegues, absorbiendo la energía necesaria para reducir las aceleraciones máximas a tan sólo 36 g's en lugar de los más de 85 g's originales. Consecuentemente, el nivel de daño disminuye en consonancia de severo a moderado según los diagra-

mas de Eiband. Los diseños óptimos tendieron hacia inercias seccionales bajas y láminas delgadas de GFRP, ofreciendo para estas condiciones el compromiso más eficiente entre amortiguamiento y masa. Además, la optimización multi-objetivo considera a la masa como función de respuesta, por lo que los diseños obtenidos aportan menos de un 1% (unos 10 kg por cada metro de fuselaje) al peso total de una aeronave.

A.4 Conclusiones y futuras líneas de investigación

Las conclusiones extraídas durante las diversas etapas de este trabajo se exponen a continuación.

De la investigación sobre el impacto axial de elementos híbridos de absorción de energía se concluye que:

- El uso de rellenos con forma de nido de abeja ofrece valores de absorción de energía casi un 30 % superiores a los de un tubo hueco de igual masa.
- El efecto de interacción durante el aplastamiento de tubos rellenos de nido de abeja puede suponer más de un 20 % de la energía total disipada por el componente.
- La optimización del diseño inicial mostró la existencia de modelos con igual masa y valores máximos de fuerza reducidos un tercio; o absorción específica de energía un 39.5 % superior manteniendo el mismo pico de fuerza.
- Los valores máximos de fuerza se reducen con el acortamiento del relleno y la disminución del espesor del nido de abeja, sin afectar a la absorción específica de energía.

Tras el análisis del segundo conjunto de componentes estudiados, con tubos de aluminio, nidos de abeja con celdas de forma variable y extrusiones de espuma, se ha llegado a las siguiente conslusiones:

- La implementación de pequeñas inestabilidades en el borde del tubo que recibe el impacto puede reducir las fuerzas máximas iniciales en más de un 30 % y facilitar un colapso más estable.

- El uso de optimización mono-objetivo mostró que los diseños irregulares de celdas pueden incrementar la absorción de energía espacífica en un 10 % sin aumentar los valores de fuerza máxima.

- La optimización multi-objetivo del diseño inicial permitió obtener componentes con un incremento del 65 % en la absorción específica de energía mientras que se redujo el pico de fuerza un 20 %.

- El análisis de la evolución de las variables de diseño mostró valores más altos de *SEA* para espesores gruesos de acero, mientras que el espesor del GFRP, el tamaño de la celda y la altura del refuerzo interno provocan aumentos de la *SEA* al reducir su magnitud.

- La implementación de extrusiones de espuma en los huecos de las celdas aumenta la absorción de energía por unidad de masa en un 28 % sin afectar al pico de fuerza máximo.

Tras el desarrollo y validación de la simulación de impacto vertical de la sección de fuselaje, se han extraído estas conclusiones:

- Las situaciones de impacto en las que la zona de carga de la aeronave está vacía resultan en niveles de daño superiores a casos con el tanque de combustible auxiliar.

- El uso de tubos huecos de aluminio en la zona de carga orientados a funcionar como soportes verticales reducen las aceleraciones máximas un 25 % en la sección con tanque de combustible y 50 % en el fuselaje sin este.

- Los absorbedores de energía mantienen intacta una mayor parte del volumen de supervivencia, evitando el impacto de la zona de carga con el suelo de la cabina y la intrusión de objetos extraños.

- El nivel de daño según el diagrama de Eiband se reduce con el uso de absorbedores de energía colapsables.

La última parte de la investigación ha culminado con las siguientes conclusiones:

- La implementación de absorbedores híbridos de energía compuestos por aluminio, GFRP y espuma puede reducir las aceleraciones durante un impacto de una sección de fuselaje en más de 20 g's.
- La optimización multi-objetivo de los absorbedores ha revelado que es posible reducir los picos de aceleración en el fuselaje por debajo de los 50 g's, manteniendo la masa de los elementos en menos de 5 kg.
- Las variables de diseño tienden hacia valores reducidos de espesor de GFRP y baja inercia en la sección del tubo, ya que estos componentes ofrecen el mejor compromiso entre atenuamiento de aceleraciones y masa.
- El análisis del colapso de las estructuras principales revela que los absorbedores disipan la energía antes usada para la formación de rótulas plásticas en las cuadernas, reduciendo las deformaciones finales y manteniendo así el espacio de supervivencia necesario en la zona de carga.

Por último, el autor estima interesante la exploración de las siguientes líneas de investigación directamente relacionadas con este trabajo:

- Realización de ensayos experimentales con los absorbedores híbridos de energía y posterior validación de las simulaciones numéricas.
- Elección y prueba de nuevas combinaciones de rellenos, estructuras o materiales que mejoren aún más los resultados obtenidos en este estudio.
- Estudio de otros escenarios de impacto de fuselaje, como el caso de amerizaje o la existencia de una componente horizontal en la velocidad inicial, analizando los indicadores biométricos y el comportamiento de los absorbedores híbridos de energía.

- Adaptación de los componentes aquí estudiados para su aplicación en otras industrias del transporte.

B

Extended summary in Galician

Hereunder an extended summary in Galician is presented, as to comply with the content regulations from the Universidade da Coruña.

B.1 Introdución e obxectivos

A sociedade actual está cada vez máis concienciada coas consecuencias derivadas dos accidentes de tráfico e outros medios de transporte. Enxeñeiros e deseñadores desenvolveron numerosos sistemas de seguridade activa que axudan a reducir o número de colisións en todos os medios de transporte. No caso dos vehículos, centraliñas electrónicas distribuídas por todo o coche son programadas con algoritmos para evitar o bloqueo dos freos ou maximizar a tracción das rodas dependendo das condicións do firme; mentres que os sistemas electrónicos de axuda á pilotaxe facilitan cada vez máis o control das aeronaves en calquera circunstancia ambiental. Porén, cando o impacto é inevitable, é necesario un sistema estrutural deseñado adecuadamente que permita reducir os danos que sufren os ocupantes. O deseño das estruturas atendendo a criterios de impacto busca o colapso progresivo de elementos co fin de disipar altas cantidades de enerxía cinética, mantendo os pasaxeiros protexidos nunha célula quasi-indeformable.

No caso dos automóbiles, xa é común o uso de aceiros de alta resistencia en portas e pilares B, aumentando a protección ante impactos laterais. A zona frontal de algúns modelos xa inclúe elementos unidos ós raís frontais deseñados para un

colapso e absorción de enerxía controlados. Para as aeronaves existen propostas con bloques de espuma na zona de carga para atenuar as deceleracións durante impactos, soportes verticais que se delaminan progresivamente ou cadernas con mecanismos biela-tirante que aumentan a disipación e reducen os danos causados por un impacto vertical. Dentro do amplo rango dos elementos estruturais para protección, un dos deseños analizados máis en detalle é o dos absorbedores colapsables, con especial énfase nos tubos de parede delgada.

O mecanismo de colapso destes elementos estúdase dende a década de 1960, cando se caracterizou o comportamento de tubos ocos de sección circular e cadrada. O dimensionamento correcto das proporcións entre altura, espesor e inercia da sección pode orixinar un modo de colapso basado na xeración de pregaduras (pandeos locais do material) que exhibe unha disipación de enerxía constante durante máis de tres cuartos da lonxitude total do tubo. Observando este comportamento, numerosos autores experimentaron con variedade de seccións, materiais, e reforzos interiores; obtenendo valores de absorción de enerxía varias veces superior ós deseños ocos orixinais.

Así, un dos principais obxectivos de este traballo é o deseño e caracterización do comportamento de sistemas híbridos de absorción de enerxía orientados a un uso en aplicacións industriais. Tubos metálicos cadrados son complementados con estruturas internas de materiaies compostos e espumas, buscando unha mellora no seu comportamento ante cargas dinámicas de impacto. Entre os reforzos existentes, préstase especial atención ás estruturas de niño de abella, estudando a súa resposta ó variar o tamaño e a forma das celas. Ademáis, analízase o uso da espuma como único material reforzando o tubo e enchendo as celas ocas, caracterizando o incremento da rixidez estrutural aportada por este elemento, así como a penalización na masa.

A segunda parte de esta investigación busca demostrar a resposta mellorada que aporta o uso dos absorbedores de enerxía nun caso de impacto representativo. Para isto, modélase o impacto vertical dunha sección de fuselaxe dun Boeing 737-200 co software de elementos finitos Abaqus 2016 na súa versión de cálculo Explicit. Posteriormente, compáranse os resultados da simulación numérica cos datos expermientais do ensaio orixinal, prestando especial atención á evolución

das curvas de aceleracións e velocidades, así como ós niveis de deformación en distintos instantes de tempo. Diversos indicadores biométricos son utilizados para medir os niveis de dano estimado nos ocupantes, como as aceleracións máximas ou a integración das aceleracións nun diagrama de dano de Eiband. Finalmente, engádense absorbedores híbridos de enerxía á fuselaxe, conectando as vigas que soportan a cabina coa zona inferior das cadernas. A simulación aportará información sobre o comportamento global da estrutura e calcularase o beneficio real ofrecido polos elementos híbridos de absorción de enerxía.

B.2 Metodoloxía e modelos

Unha das bases de este traballo reside no uso de métodos de optimización como ferramenta para deseñar estruturas máis eficientes. Neste caso, e dada a natureza altamente ruidosa e non-linear das simulacións coas que se traballa, a optimización axúdase do uso de modelos surrogados. Estes métodos reemplazan as funcións ruidosas, non derivables e con discontinuidades noutras cun comportamento homólogo pero máis suave, constituíndo un metamodelo ou modelo surrogado. Para isto, realízase primeiro un mostreo eficiente que ofreza suficiente información de como responde o modelo ante os cambios nas variables de deseño. Ó longo deste traballo, úsase o método dos hipercubos latinos (LHS), xa que maximiza a información aportada por cada mostra evitando a superposición dos valores das variables. Esta información é tratada por outro algoritmo que xera as funcións necesarias para obter o metamodelo. Dous modelos basados na conxunción de splines e funcións polinómicas foron usados para este propósito, os "multivariate adaptive regression splines" (MARS) e os "moving least squares" (MLS) respectivamente. Os metamodelos representarán a partires de agora ós modelos numéricos, polo que debe establecerse se son eficaces nelo. O uso de métricas estadísticas de error, como a bondade de axuste R^2 ou o error medio cadrático RMSE, permite discernir se este modelo corresponde coas respostas da simulación. Ademáis, o cálculo destes indicadores con técnicas de validación cruzada permitirán estimar a capacidade predictiva e o nivel de aproximación aportado polos metamodelos.

Cando a bondade de axuste do modelo surrogado cumpre cos requisitos establecidos, este pode ser optimizado en cuestión de minutos usando algoritmos xenéticos. Estes procedementos, inpirados na evolución xenética, crean xeracións de individuos que se combinan e mutan dando lugar a xeracións posteriores. Un axuste adecuado dos seus parámetros biométricos aporta gran robustez ante os mínimos locais, recurrentes neste tipo de modelos.

A optimización realizada pódese dividir en tres grados de complexidade, obtendo cada vez máis información e maior control sobre as respostas aportadas polo modelo. Inicialmente realizouse optimización mono-obxectivo dunha función como a enerxía absorbida ou a *SEA*, engadindo posteriormente diversos límites a respostas como a masa ou a forza máxima durante o ensaio. Finalmente, realízase optimización multi-obxectivo, ofrecendo frentes de Pareto compostos por modelos que non poden mellorar a súa resposta nunha función sen empeorar o seu valor noutras. Así, obtéñense unha gran variedade de deseños cun comportamento óptimo sendo adaptables a distintas necesidades estruturais.

Outra parte de esta investigación consiste no modelado dun ensaio dinámico do impacto dunha fuselaxe ante unha superficie de madeira. O modelo consiste nunha sección de 3700 kg e tres metros de longo, impactando o chan a 9.144 m/s. Elementos como a pel ou as cadernas son representados con elementos lámina co fin de capturar máis fielmente o pandeo local e outros mecanismos complexos de colapso. Sen embargo, os rixidizadores lonxitudinais modélanse con elementos barra, reducindo así o número de graos de liberdade do modelo e axilizando os tempos de cálculo das simulacións. O comportamento da estrutura analízase segundo criterios de deformación tras o ensaio, dano resultante nos pasaxeiros e absorción de enerxía dos compoñentes. Deste modo, analizarase se a presenza ou ausencia de certos compoñentes resultará en configuracións máis perigosas para os ocupantes.

Un estudo preliminar con tubos ocos de aluminio é usado para determinar a sensibilidade das aeronaves ante a implementación destes elementos. Finalmente engádense os absorbedores híbridos de enerxía á fuselaxe, compostos de tubos cadrados de aluminio de sección variable recheos dun esqueleto de GFRP e bloques de espuma. Estes elementos dispóñense espaciados cada metro en dirección

lonxitudinal e 2.04 en transversal, cumprindo coas dimensións dun contenedor de carga estándar. Con esta simulación parametrizada xérase un novo modelo surrogado, usando como variables de deseño o espesor e lado do tubo, a altura do recheo e o espesor das láminas de GFRP. Este metamodelo someterase a optimización, buscando minimizar a masa dos elementos á vez que se melloran varios indicadores biométricos de dano en pasaxeiros como o diagrama de lesións de Eiband.

B.3 Resultados e discusión

Os resultados da análise do compoñente composto polo tubo de aceiro e un niño de abella regular de GFRP confirman os beneficios aportados por estes recheos, obtendo valores de *SEA* un 28 % superiores que en compoñentes baleiros. Tamén se cuantificou o efecto de interacción entre os elementos do compoñente, puidendo supoñer ata un 22 % da enerxía total disipada polo espécimen. A nivel de recheo, a diminución do tamaño das celas tamén aporta unha mellora do comportamento, ofrecendo un valor de *SEA* máis alto cando se reduce o lado do héxagono baixo os 15 mm. O uso da optimización permitiu reducir valores de forza máxima 33 % mantendo valores similares de *SEA* e masa, así como obter conxuntos de deseños con valores simultáneamente óptimos de enerxía absorbida e masa, ou *SEA* e pico de forza.

Co segundo conxunto de modelos estúdanse certas melloras e o seu aporte ó comportamento ante impacto do compoñente. Así, o aceiro é substituído por aluminio de alta ductilidade, podendo aumentar a enerxía absorbida ó entorno dos 100 kJ; mentres que a variación da forma regular da cela por outras de forma pseudo-rectangular mellora a *SEA* outro 15 %. Por último, demóstrase que o uso de bloques de espuma como recheo das celas permite a obtención de deseños con valores de *SEA* de 23 kJ/kg, mantendo a forza máxima baixo o umbral de 420 kN. Igual que no apartado anterior, a optimización basada en surrogados permite obter diferentes deseños que melloran a resposta dunha ou máis funcións obxectivo.

Á hora de validar a fuselaxe, analízase a evolución das aceleracións e velocidades durante o impacto, obtendo unha excelente concordancia entre os valores numéricos e os experimentais. As gráficas capturaron fielmente os cambios de pendente e os valores máximos nas curvas con mínimas discordancias. Ademáis, atopouse que a ausencia do tanque de combustible, responsable da disipación dunha gran cantidade de enerxía cinética, resultaba nunha maior deformación das estruturas principais con deceleracións máis bruscas e o seu consecuente aumento no nivel de lesións nos ocupantes.

Unha vez existe a suficiente confianza na resposta do modelo numérico, evalúase a efectividade da implementación de sistemas colapsables de enerxía de parede delgada. Nunha primeira iteración estimouse a resposta da fuselaxe con cinco tubos ocos verticais na zona de carga. Estes contribuíron un 6 % á disipación de enerxía e a reducir as aceleracións máximas en 45 g's. Ademáis, evitanto o impacto das zonas inferiores da fuselaxe co chan da cabina de pasaxeiros, o nivel de danos diminuíu de severo a moderado en varias localizacións de medida.

Para finalizar, optimizouse a resposta ante impacto dunha fuselaxe con absorbedores híbridos de enerxía. A parametrización dos modelos permitiu variar as dimensións do tubo, o recheo de espuma e láminas de GFRP e espesores dos materiais. O mostreo para a xeración do metamodelo precisou de 600 simulacións a escala real para obter valores de R^2 superiores a 0.9, mentres que o RMSE mantívose con valores reducidos incluso tras a aplicación das técnicas validación cruzada. Os resultados da optimización con algoritmos evolutivos ofreceu modelos que presentaban a rixidez necesaria para desenvolver entre tres e cinco pregaduras, absorbendo a enerxía necesaria para que se diminuíran as aceleracións máximas a tan só 36 g no canto dos máis de 85 g orixinais. Consecuentemente, o nivel de dano reduciuse en consonancia de severo a moderado segundo os diagramas de Eiband. Os deseños óptimos tenderon cara inercias seccionais baixas e láminas delgadas de GFRP, ofrecendo nestas condicións o compromiso máis eficiente entre amortiguamento e masa. Ademáis, a optimización multi-obxectivo considera a masa como función de resposta, polo que os deseños obtidos aportan menos dun 1% (uns 10 kg por cada metro da fuselaxe) ó peso total dunha aeronave.

B.4 Conclusións e futuras liñas de investigación

As conclusións extraídas durante as diversas etapas de este traballo expóñense a continuación.

Da investigación sobre o impacto axial de elementos híbridos de absorción de enerxía, extraeuse que:

- O uso de recheos con forma de niño de abella ofrece valores de absorción de enerxía casi 30 % superiores ós dun tubo oco da mesma masa.
- O efecto de interacción durante o aplastamento de tubos recheos de niños de abella pode supoñer máis dun 20 % da enerxía total disipada polo compoñente.
- A optimización do deseño inicial mostrou a existencia de modelos con igual masa e valores máximos de forza reducidos un tercio; coa absorción específica de enerxía un 39.5 % superior mantendo o mismo pico de forza.
- Os valores máximos de forza redúcense co acortamento do recheo e a diminución do espesor do niño de abella, sen afectar á absorción específica de enerxía.

Tras a análise do segundo conxunto de compoñentes estudados, con tubos de aluminio, niños de abella con celas de forma variable e bloques de espuma, chegouse ás seguinte conslusións:

- A implementación de pequenas inestabilidades no borde do tubo que recibe o impacto pode reducir as forzas máximas iniciais en máis dun 30 % e facilitar un colapso máis estable.
- O uso da optimización mono-obxectivo mostrou que os deseños irregulares de celas poden incrementar a absorción de enerxía específica nun 10 % sen aumentar os valores de forza máxima experimentados.

- A optimización multi-obxectivo do deseño inicial permitiu obter compoñentes cun incremento do 65 % na absorción específica de enerxía, mentres que reduce o pico de forza nun 20 %.
- A análise da evolución das variables de deseño mostrou valores máis altos de *SEA* para espesores altos de aluminio, mentres que o espesor do GFRP, o tamaño da cela e a altura do reforzo interno provocan un aumento da *SEA* ó reducir a súa magnitude.
- A implementación de bloques de espuma nos ocos das celas aumenta a absorción de enerxía por unidade de masa nun 28 % sen afectar ó pico de forza máximo.

Tras desenvolver e validar a simulación do impacto vertical da sección de fuselaxe, extraéronse estas conclusións:

- As situacións de impacto nos que a zona de carga da aeronave está baleira resultan en niveis de dano superiores a casos co tanque de combustible auxiliar.
- O uso de tubos ocos de aluminio na zona de carga orientados a funcionar como soportes verticais reducen as aceleracións máximas un 25 % na sección con tanque de combustible e ata 50 % na fuselaxe sen este.
- Os absorbedores de enerxía manteñen intacta unha maior parte do volumen de supervivencia, evitando o impacto da zona de carga co chan da cabina e a intrusión de obxectos estraños.
- O nivel de dano según o diagrama de Eiband redúcese co uso de absorbedores de enerxía colapsables.

A última parte da investigación rematou coas seguintes conclusións:

- A implementación de absorbedores híbridos de enerxía compostos por aluminio, GFRP e espuma pode reducir as aceleracións durante un impacto dunha sección de fuselaxe en máis de 20 g's.

- A optimización multi-obxectivo dos absorbedores mostrou que é posible reducir os picos de aceleración na fuselaxe por debaixo dos 50 g's, mantendo a masa dos elementos en menos de 5 kg.
- As variables de deseño tenden cara valores reducidos de espesor de GFRP e baixa inercia na sección do tubo, xa que estes compoñentes ofrecen o mellor compromiso entre atenuamento de aceleracións e masa.
- A análise do colapso das estruturas principais revela que os absorbedores disipan a enerxía antes usada para a formación de rótulas plásticas nas cadernas e modifican a súa xeración, reducindo as deformacións finais e mantendo así o espacio de supervivencia necesario na zona de carga.

Por último, o autor estima interesante a exploración das seguintes liñas de investigación directamente relacionadas con este traballo:

- Realización de ensaios experimentais con absorbedores híbridos de enerxía e posterior validación das simulacións numéricas.
- Elección e proba de novas combinacións de recheos, estruturas ou materiais que melloren aínda máis os resultados obtidos neste estudo.
- Estudo doutros escenarios de impacto da fuselaxe, como o caso de amerizaxe ou a existencia dunha compoñente horizontal na velocidade inicial, analizando os indicadores biométricos e o comportamento dos absorbedores híbridos de enerxía.
- Adaptación dos compoñentes aquí estudados para a súa aplicación noutras industrias do transporte.

Bibliography

[1] Laananen, DH and Winkelman, KL. "Analysis of energy-absorbing seat configurations for aircraft". *International journal of crashworthiness* 1.4 (1996), pp. 355–368.

[2] Snyder, Richard G. *Civil Aircraft Restraint Systems: State-of-the-Art Evaluation of Standards, Experimental Data, and Accident Experience*. Tech. rep. SAE Technical Paper, 1977.

[3] European New Car Assessment Programme (Euro NCAP). *Frontal Impact Testing Protocol, Version 6.0.2*. Tech. rep. European New Car Assessment Programme (Euro NCAP), 2013.

[4] Global NCAP. *List of NCAPS*. `https://goo.gl/dWvokW`.

[5] NASA. *1974 Cessna 172 drop test at NASA Langley's Landing and Impact Research Facility. August 26ht, 2015*. `https://goo.gl/x8U3hc`.

[6] Jackson, Karen E, Fasanella, Edwin L, Boitnott, Richard, McEntire, Joseph, and Lewis, Alan. "Occupant Responses in a Full-Scale Crash Test of the Sikorsky ACAP Helicopter". *Journal of the American Helicopter Society* 49.2 (2004), pp. 127–139.

[7] Jackson, Karen E, Boitnott, Richard L, Fasanella, Edwin L, Jones, Lisa E, and Lyle, Karen H. "A history of full-scale aircraft and rotorcraft crash testing and simulation at NASA Langley Research Center" (2004).

[8] *Barómetro de Seguridad Vehicular del Parque de Automoción*. Tech. rep. Fundación FITSA, 2007.

[9] Paz, J, Díaz, J, Romera, L, and Costas, M. "Crushing analysis and multi-objective crashworthiness optimization of GFRP honeycomb-filled energy absorption devices". *Finite Elements in Analysis and Design* 91 (2014), pp. 30–39.

[10] Paz, J., Díaz, J., Romera, L., and Costas, M. "Size and shape optimization of aluminum tubes with GFRP honeycomb reinforcements for crashworthy aircraft structures". *Composite Structures* 133 (2015), pp. 499–507.

[11] Paz, J., Romera, L., and Diaz, J. "Crashworthiness optimization of aircraft hybrid energy absorbers enclosing honeycomb and foam structures". *AIAA Journal* 55.2 (2017), pp. 652–661.

[12] Romera, L, Paz, J, Costas, M, Dıaz, J, and Hernandez, S. "Crashworthiness response of honeycomb metallic-GFRP energy absorption devices". *High Performance and Optimum Design of Structures and Materials. Ostend, Belgium.* 137 (2014), p. 225.

[13] Díaz, J., Costas, M., Romera, L., Paz, J., and Hernández, S. "Surrogate-based multi-objective optimization of glass-fiber-steel crash absorbers". *High Performance and Optimum Design of Structures and Materials. Ostend, Belgium.* 137 (2014), p. 225.

[34] De Haven, Hugh. *Mechanical analysis of survival in falls from heights of fifty to one hundred and fifty feet.* Tech. rep. 1980.

[35] De Haven, Hugh. *Accident survival-airplane and passenger automobile.* Crash Injury Research Project, 1952.

[36] Shanahan, Dennis F. "Basic principles of crashworthiness". *Pathological Aspects and Associate Biodynamics in Aircraft Accident Investigation* (2004).

[37] *Ferrari's F310B cockpit.* `https://goo.gl/sGxXMN`.

[38] National Transportation Safety Board. *2014–2015 US Transportation Fatalities.* `https://goo.gl/VNAJLt`.

[39] Unknown. *AG-1 Airplane*. Digital: Cushing Memorial Library and Archives, Texas A & M University, College Station, Texas; Physical: Graphic Services, Texas A & M University. Available electronically from `https://goo.gl/FdYimq`.

[40] Waldock, William D. "A brief history of" Crashworthiness". In: *1997 SAFE Association Symposium, Phoenix, AZ*. 1997.

[41] Larkins, Bill. *Beech 35 N3188V Jan1949*. `https://flic.kr/p/hX3Zvf`.

[42] Clark, John C. *Summary report on the National Transportation Safety Board's general aviation crashworthiness project findings*. Tech. rep. SAE Technical Paper, 1987.

[43] "Airworthiness Standards: Transport Category Airplanes". *Title 14, Federal Aviation Administration Code of Federal Regulations, Part 23, Washington D. C.* (2012).

[44] Research and Innovative Technology Administration, Bureau of Transportation Statistics. *Transportation Statistics Annual Report 2015*. Tech. rep. U.S. Department of Transportation, Washington DC, 2016.

[45] O'Neill, Brian. "Preventing passenger vehicle occupant injuries by vehicle design—a historical perspective from IIHS". *Traffic injury prevention* 10.2 (2009), pp. 113–126.

[46] Fasanella, Edwin L., Widmayer, E., and Robinson, Martha P. "Structural analysis of the controlled impact demonstration of a jet transport airplane." *Journal of Aircraft* 24.4 (1987), pp. 274–280.

[47] Waimer, M, Kohlgrüber, D, Hachenberg, D, and Voggenreiter, H. "The kinematics model–a numerical method for the development of a crashworthy composite fuselage design of transport aircraft". In: *Sixth triennial international aircraft fire and cabin safety research conference*. 2010.

[48] Byar, Alan and Tan, Tein-Min. "A crashworthiness study of a Boeing 737 fuselage section". PhD thesis. Drexel University Philadelphia, PA, 2003.

[49] Siromani, Deepak. *Crashworthy design and analysis of aircraft structures*. Drexel University, 2013.

[50] Noor, Ahmed K and Carden, Huey D. "Computational methods for crashworthiness" (1993).

[51] Hajela, P and Lee, Eoo. "Topological optimization of rotorcraft subfloor structures for crashworthiness considerations". *Computers & structures* 64.1-4 (1997), pp. 65–76.

[52] Lahey, Robert S, Miller, Mark P, and Reymond, Michael. "MSC/NASTRAN Reference Manual, Version 68". *The MacNeal-Schwendler Corporation* (1994).

[53] Gamon, MA. *KRASH User's Manual: Thoery Volume I.* Tech. rep. FAA-RD-77-1891, Lockheed-California Company, 1979.

[54] Kindervater, CM, Kohlgrüber, D, and Lützenburger, M. "Crash simulation methodologies for aircraft structures used within european crashworthiness research" (1998).

[55] Walton, Andrew, Whayeb, Shakir, and Sadeghi, Majid. *The Air Accident Investigation Tool.* Tech. rep. Second International KRASH User's Seminar, Cranfield Impact Centre, 1995.

[56] Gamon, Max A, Wittlin, Gil, and LaBarge, Bill L. *KRASH 85 User's Guide-Input/Output Format.* Tech. rep. FAA-RD-77-1891, Lockheed-California Company, 1985.

[57] Maia, Leandro Guimarães and Oliveira, Paulo Henriques Iscold Andrade de. *A review of finite element simulation of aircraft crashworthiness.* Tech. rep. SAE Technical Paper, 2005.

[58] Hallquist, John O and Whirley, Robert G. "DYNA3D User's Manual". *LLNL, Livermore, CA, UCID-19592* (1989).

[59] Welch, RE, Bruce, RW, and Belytschko, Ted. *Finite element analysis of automotive structures under crash loadings.* National Highway Traffic Safety Administration, 1976.

[60] Belytschko, T and Marchertas, AH. "Nonlinear finite-element method for plates and its application to dynamic response of reactor fuel subassemblies". *Journal of Pressure Vessel Technology* 96.4 (1974), pp. 251–257.

[61] Hallquist, John O et al. "LS-DYNA keyword user's manual". *Livermore Software Technology Corporation* 970 (2007).

[62] MSC DYTRAN User's Manual. "DB/CD". *Los Angeles, USA: MSC Corporation* (2002).

[63] PAM-CRASH. "Solver Reference Manual". *ESI Group Software product company. Rungis (France)* (2000).

[64] Altenhof, William, Paonessa, Saverio, Zamani, Nader, and Gaspar, Robert. "An experimental and finite element investigation into the energy absorption characteristics of a steering wheel armature in an impact". *International journal of impact engineering* 27.2 (2002), pp. 197–212.

[65] Fasanella, EL, Boitnott, RL, Lyle, KH, and Jackson, KE. "Full-scale crash test and simulation of a composite helicopter". *International journal of crashworthiness* 6.4 (2001), pp. 485–498.

[66] Fasanella, Edwin L and Jackson, Karen E. "Best practices for crash modeling and simulation" (2002).

[67] Fasanella, Edwin L and Jackson, Karen E. "Crash simulation of vertical drop tests of two Boeing 737 fuselage sections". In: *U.S. Army Research Laboratory, Vehicle Technology Center, Langley Research Center*. 2002.

[68] Belytschko, T. "Partitioned and adaptive algorithms for explicit time integration". In: *Nonlinear Finite Element Analysis in Structural Mechanics*. 1981, pp. 572–584.

[69] Plewa, Tomasz, Linde, Timur, and Weirs, V Gregory. "Adaptive mesh refinement-theory and applications". *Lecture notes in computational science and engineering* 41 (2005), pp. 3–5.

[70] *MADYMO Dummy models brochure*. TASS International. 2018.

[71] Obergefell, Louise A, Gardner, Thomas R, Kaleps, Ints, and Fleck, John T. *Articulated Total Body Model Enhancements. Volume 2. User's Guide*. Tech. rep. HARRY G ARMSTRONG AEROSPACE MEDICAL RESEARCH LAB WRIGHT-PATTERSON AFB OH, 1988.

[72] Happee, R, Janssen, AJ, Fraterman, E, Monster, JW, Happee, R, and Automotive, TNO. "Application of MADYMO occupant models in LS-DYNA/MADYMO coupling". In: *4th European LS-DYNA Users Conference*. 2003, pp. 3–10.

[73] Fountain, M A, Koppens, W P, and Lupker, H A. "Flexible body modelling in MADYMO". *Proceedings of the 6th International MADYMO Users' Meeting* (1996), pp. 175–186.

[74] Kindervater, CM, Kohlgruber, D, and Johnson, Allen. "Composite vehicle structural crashworthiness-A status of design methodology and numerical simulation techniques". *International Journal of Crashworthiness* 4.2 (1999), pp. 213–230.

[75] Waimer, Matthias, Feser, Thomas, Schatrow, Paul, and Schueler, Dominik. "Crash concepts for CFRP transport aircraft–comparison of the traditional bend frame concept versus the developments in a tension absorbers concept". *International journal of crashworthiness* 23.2 (2018), pp. 193–218.

[76] Lyle, Karen H, Jackson, Karen E, and Fasanella, Edwin L. "Simulation of aircraft landing gears with a nonlinear dynamic finite element code". *Journal of Aircraft* 39.1 (2002), pp. 142–147.

[77] Zhangping, Luo and Jinwu, Xiang. "Crashworthiness performance evaluation to helicopter landing gear by finite element simulation". *Acta Aeronautica et Astronautica Sinica* 24 (2003), pp. 216–219.

[78] Xue, P., Wang, L., and Qiao, C.F. "Crashworthiness study on fuselage section and struts under cabin floor". *International Journal of Protective Structures* 2.4 (2011), pp. 515–526.

[79] Nicholson, Colin R, Turnour, Stephen R, and Chapman, Helen E. *The design and testing of buckling monocoque seating structures for aircraft*. Tech. rep. SAE Technical Paper, 1999.

[80] Cheng, ZQ, Pilkey, Walter D, Balandin, Dmitry V, Bolotnik, Nikolai N, Crandall, Jeffrey R, and Shaw, C Gregory. "Optimal control of helicopter seat cushions for the reduction of spinal injuries". *International journal of crashworthiness* 6.3 (2001), pp. 321–338.

[81] Desjardins, Stanley P. "The evolution of energy absorption systems for crashworthy helicopter seats". *Journal of the American Helicopter Society* 51.2 (2006), pp. 150–163.

[82] Hooper, SJ and Ellis, DR. "Aviation safety and crashworthy seat design". *International journal of crashworthiness* 2.1 (1996), pp. 39–54.

[83] Federal Aviation Administration, Advisory circular 23.562-1. *Dynamic Testing of Part 23 Airplane Seat/Restraint System and Occupant Protection*. 1989.

[84] Federal Aviation Regulations. *Part 23 Airworthiness Standards: Normal, Utility, Acrobatic and Commuter Category Airplanes*. 1991.

[85] Federal Aviation Administration, Advisory circular 25.562-1A. *Dynamic Evaluation of Seat Restraint Systems and Occupant Protection on Transport Airplanes*. 1996.

[86] Federal Aviation Regulations. *Part 25-Airworthiness Standards: Transport Category Airplanes*. 1970.

[87] Mahé, M, Ribet, H, and Le Page, F. "Composite fuselage crash FE modelling dedicated to enhance the design in correlation with full scale drop test". *Mécanique & industries* 2.1 (2001), pp. 5–17.

[88] Carden, Huey D and Hayduk, Robert J. *Aircraft subfloor response to crash loadings*. Tech. rep. SAE Technical Paper, 1981.

[89] Wiggenraad, JFM. *Development of a crashworthy composite fuselage structure for a commuter aircraft*. 1999.

[90] McCarthy, MA and Wiggenraad, JFM. "Numerical investigation of a crash test of a composite helicopter subfloor structure". *Composite structures* 51.4 (2001), pp. 345–359.

[91] Kindervater, C. M. and Georgi, H. "Composite strength and energy absorption as an aspect of structural crash resistance". *Structural Crashworthiness and Failure* (1993).

[92] Delsart, David, Joly, Didier, Mahe, Michel, and Winkelmuller, Gérard. "Evaluation of finite element modelling methodologies for the design of crashworthy composite commercial aircraft fuselage". *Office National d'Etudes et de recherches aerospatiales* 188 (2004).

[93] Littell, Justin D, Jackson, Karen E, Annett, Martin S, Seal, Michael D, and Fasanella, Edwin L. "The Development of Two Composite Energy Absorbers for Use in a Transport Rotorcraft Airframe Crash Testbed (TRACT 2) Full-Scale Crash Test". In: *Proceedings of the 71st Annual American Helicopter Society Forum, Virginia Beach, VA, Mat.* 2015, pp. 5–7.

[94] Duan, Shuyong, Tao, Yourui, Han, Xu, Yang, Xujing, Hou, Shujuan, and Hu, Zhangping. "Investigation on structure optimization of crashworthiness of fiber reinforced polymers materials". *Composites Part B: Engineering* 60 (2014), pp. 471–478.

[95] Sokolinsky, Vladimir S, Indermuehle, Kyle C, and Hurtado, Juan A. "Numerical simulation of the crushing process of a corrugated composite plate". *Composites Part A: Applied Science and Manufacturing* 42.9 (2011), pp. 1119–1126.

[96] Kermanidis, Th, Labeas, G, Apostolopoulos, C, and Michielseif, Louis. "Numerical simulation of composite structures under impact". *WIT Transactions on The Built Environment* 35 (1970).

[97] McCarthy, MA, Harte, CG, Wiggenraad, JFM, Michielsen, ALPJ, Kohlgrueber, D, and Kamoulakos, A. "Finite element modelling of crash response of composite aerospace sub-floor structures". *Computational Mechanics* 26.3 (2000), pp. 250–258.

[98] Waimer, Matthias, Siemann, MH, and Feser, Thomas. "Simulation of CFRP components subjected to dynamic crash loads". *International Journal of Impact Engineering* 101 (2017), pp. 115–131.

[99] Farley, Gary L. "Crash energy absorbing subfloor beam structure". *Journal of the American Helicopter Society* 32.4 (1987), pp. 28–38.

[14] Zheng, Jianqiang, Xiang, Jinwu, Luo, Zhangping, and Ren, Yiru. "Crashworthiness design of transport aircraft subfloor using polymer foams". *International Journal of Crashworthiness* 16.4 (2011), pp. 375–383.

[100] Jackson, KE. "Impact testing and simulation of a crashworthy composite fuselage concept". *International Journal of Crashworthiness* 6.1 (2001), pp. 107–122.

[101] Bisagni, Chiara. "Computational Fluid and Solid Mechanics 2003 || Development of a crashworthy subfloor concept for a commuter aircraft". In: 2003.

[15] Meng, F X, Zhou, Q, and Yang, J L. "Improvement of crashworthiness behaviour for simplified structural models of aircraft fuselage". *International Journal of Crashworthiness* 14.1 (2009), pp. 83–97.

[102] Heimbs, S, Mehrens, T, Middendorf, P, Maier, M, and Schumacher, A. "Numerical Determination of the Nonlinear Effective Mechanical Properties of Folded Core Structures for Aircraft Sandwich Panels". *6th European LS-DYNA Users' Conference* (2011), pp. 1–14.

[103] Jackson, Karen E and Fuchs, Yvonne T. "Comparison of ALE and SPH simulations of vertical drop tests of a composite fuselage section into water" (2008).

[104] Ren, Yiru and Xiang, Jinwu. "A comparative study of the crashworthiness of civil aircraft with different strut configurations". *International Journal of Crashworthiness* 15.3 (2010), pp. 321–330.

[105] Heimbs, Sebastian, Hoffmann, Marco, Waimer, Matthias, Schmeer, Sebastian, and Blaurock, Jörg. "Dynamic testing and modelling of composite fuselage frames and fasteners for aircraft crash simulations". *International Journal of Crashworthiness* 18.4 (2013), pp. 406–422.

[106] Waimer, Matthias, Kohlgrüber, Dieter, Keck, Rüdiger, and Voggenreiter, Heinz. "Contribution to an improved crash design for a composite transport aircraft fuselage—development of a kinematics model and an experimental component test setup". *CEAS Aeronautical Journal* 4.3 (2013), pp. 265–275.

[107] Schatrow, Paul and Waimer, Matthias. “Investigation of a crash concept for CFRP transport aircraft based on tension absorption”. *International journal of crashworthiness* 19.5 (2014), pp. 524–539.

[108] Gransden, Derek I and Alderliesten, René. “Development of a finite element model for comparing metal and composite fuselage section drop testing”. *International Journal of Crashworthiness* 22.4 (2017), pp. 401–414.

[109] Schatrow, Paul and Waimer, Matthias. “Crash concept for composite transport aircraft using mainly tensile and compressive absorption mechanisms”. *CEAS Aeronautical Journal* 7.3 (2016), pp. 471–482.

[110] Kindervater, Christof M, Johnson, Alastair F, Kohlgrüber, Dieter, Lützenburger, Marius, and Pentecote, Nathalie. “Crash and impact simulation of aircraft structures-hybrid and FE based approaches”. In: *European congress on computational methods in applied sciences and engineering. Barcelona, Spain: ECCOMAS*. 2000.

[111] Lyle, Karen H, Stockwell, Alan E, and Hardy, Robin C. “Application of probability methods to assess airframe crash modeling uncertainty”. *Journal of aircraft* 44.5 (2007), pp. 1568–1573.

[112] Kumakura, Ikuo, Minegishi, Masakatsu, Iwasaki, Kazuo, and HOSOKAWA, Takefumi. “Impact simulation of simplified structural models of aircraft fuselage”. *SAE transactions* 109.1 (2000), pp. 1238–1243.

[113] Shoji, Hirokazu, Minegishi, Masakatsu, and Aoki, Takahira. “Channel Section Short Column with Fixed Ends under Axial Impact Load”. In: *47th AIAA / ASME / ASCE / AHS / ASC Structures, Structural Dynamics, and Materials Conference*. 2006, p. 1760.

[114] Yiru, Ren, Jinwu, Xiang, Zhangping, Luo, and Jianqiang, Zheng. “Effect of Cabin-floor Oblique Strut on Crashworthiness of Typical Civil Aircraft Fuselage Section”. *Acta Aeronautica Et Astronautica Sinica* 2 (2010), p. 012.

[115] Kumakura, I., Minegishi, M., and Iwasaki, K. “Impact simulation of simplified structural models of aircraft fuselage”. *2000 World Aviation Conference* (2000).

[116] Shoji, H., Minegishi, M., and Aoki, T. "Impact characteristics estimation of channel section short column under axial impact load". *Structural Dynamics and Materials Conference* 4 (2007), pp. 3967–3976.

[16] Ren, Yiru and Xiang, Jinwu. "The crashworthiness of civil aircraft using different quadrangular tubes as cabin-floor struts". *International Journal of Crashworthiness* 16.3 (2011), pp. 253–262.

[117] Heimbs, S and Middendorf, P. "Design, analysis and testing of a composite crash absorber for aeronautic applications". In: *3rd ECCOMAS thematic conference on the mechanical response of composites*. 2011, pp. 537–544.

[118] Perez Galan, J. L., Climent, H., and Le Page, F. "Non-linear response of metallic and composite aeronautical fuselage structures under crash loads and comparison with full scale test". In: *European Congress on Computational Methods in Applied Sciences and Engineering, ECCOMAS, Barcelona*. 2000.

[119] Ezra, Arthur A. "An assessment of energy absorbing devices for prospective use in aircraft impact situations". In: *Dynamic response of structures*. Pergamon Press. 1972.

[120] Calladine, CR. "An investigation of impact scaling theory" (1983).

[121] Booth, E, Collier, D, and Miles, J. *Impact scalability of plated steel structures*. 1983.

[122] SAE, SAE. "J211-1 Instrumentation for Impact Test—Part 1—Electronic Instrumentation". *SAE International* (2007).

[17] Huang, M. *Vehicle Crash Mechanics*. CRC Press, 2002.

[123] Costas Piñó, Miguel. "Crashworthiness analysis and design optimization of hybrid impact energy absorbers" (2015).

[124] Desjardins, SP, Zimmerman, RE, Bolukbasi, AO, and Merritt, NA. "Aircraft crash survival design guide". *US Army Aviation Systems Command TR* 89 (1989).

[125] Eiband, A Martin. "Human tolerance to rapidly applied accelerations: a summary of the literature". *National Aeronautics and Space Administration (NASA)* (1959).

[126] Henn, Hans-Wolfgang. "Crash tests and the head injury criterion". *Teaching mathematics and its applications* 17.4 (1998), pp. 162–170.

[127] King, Albert I. "Fundamentals of impact biomechanics: part I-biomechanics of the head, neck, and thorax". *Annual review of biomedical engineering* 2.1 (2000), pp. 55–81.

[128] Stronge, William James. *Impact mechanics*. Cambridge university press, 2004.

[129] Alghamdi, AAA. "Collapsible impact energy absorbers: an overview". *Thin-walled structures* 39.2 (2001), pp. 189–213.

[130] Johnson, W. "Metallic energy dissipating systems". *Appl. Mech. Rev.* 31 (1978), pp. 277–288.

[131] Bisagni, Chiara. "Crashworthiness of helicopter subfloor structures". *International Journal of Impact Engineering* 27.10 (2002), pp. 1067–1082.

[132] White, M.D. and Jones, N. "Experimental quasi-static axial crushing of top-hat and double-hat thin-walled sections". *International Journal of Mechanical Sciences* 41.2 (1999), pp. 179–208.

[133] White, M.D., Jones, N., and Abramowicz, W. "A theoretical analysis for the quasi-static axial crushing of top-hat and double-hat thin-walled sections". *International Journal of Mechanical Sciences* 41.2 (1999), pp. 209–233.

[134] Marsolek, J and Reimerdes, H-G. "Energy absorption of metallic cylindrical shells with induced non-axisymmetric folding patterns". *International Journal of Impact Engineering* 30.8 (2004), pp. 1209–1223.

[135] Ahmad, Zaini and Thambiratnam, David Pathmaseelan. "Application of foam-filled conical tubes in enhancing the crashworthiness performance of vehicle protective structures". *International journal of crashworthiness* 14.4 (2009), pp. 349–363.

[136] Lu, Guoxing and Yu, TX. *Energy absorption of structures and materials*. Elsevier, 2003.

[137] Alexander, J. M. "An approximate analysis of the collapse of thin cylindrical shells under axial loading". *Quarterly Journal of Mechanics and Applied Mathematics* 13.1 (1960), pp. 10–15.

[138] Wierzbicki, Tomasz and Abramowicz, Wlodzimierz. "On the crushing mechanics of thin-walled structures". *Journal of Applied mechanics* 50.4a (1983), pp. 727–734.

[139] Abramowicz, W and Wierzbicki, T. "Axial crushing of multicorner sheet metal columns". *Journal of Applied Mechanics* 56.1 (1989), pp. 113–120.

[140] Abramowicz, Wlodzimierz and Jones, Norman. "Dynamic progressive buckling of circular and square tubes". *International Journal of Impact Engineering* 4.4 (1986), pp. 243–270.

[141] Pugsley, A.G. "On the crumpling of thin tubular struts". *Quarterly Journal of Mechanics and Applied Mathematics* 32.1 (1979), pp. 1–7.

[142] Singace, A.A. and Elsobky, H. "Further experimental investigation on the eccentricity factor in the progressive crushing of tubes". *International Journal of Solids and Structures* 33.24 (1996), pp. 3517–3538.

[143] Abramowicz, W. and Jones, N. "Transition from initial global bending to progressive buckling of tubes loaded statically and dynamically". *International Journal of Impact Engineering* 19.5-6 (1997), pp. 415–437.

[144] Kinkead, AN. "Analysis for inversion load and energy absorption of a circular tube". *The Journal of Strain Analysis for Engineering Design* 18.3 (1983), pp. 177–188.

[145] Al-Hassani, STS, Johnson, W, and Lowe, WT. "Characteristics of inversion tubes under axial loading". *Journal of Mechanical Engineering Science* 14.6 (1972), pp. 370–381.

[146] Thomas, SG, Reid, SR, and Johnson, W. "Large deformations of thin-walled circular tubes under transverse loading—I: an experimental survey of the bending of simply supported tubes under a central load". *International journal of mechanical sciences* 18.6 (1976), 325in3327–326in6333.

[147] DeRuntz, John A and Hodge, PG. "Crushing of a tube between rigid plates". *Journal of Applied Mechanics* 30.3 (1963), pp. 391–395.

[148] Reddy, T Yella and Reid, SR. "Lateral compression of tubes and tube-systems with side constraints". *International Journal of Mechanical Sciences* 21.3 (1979), pp. 187–199.

[149] Wu, Lan and Carney, John F. "Initial collapse of braced elliptical tubes under lateral compression". *International Journal of Mechanical Sciences* 39.9 (1997), pp. 1023–1036.

[150] Reid, SR. "Plastic deformation mechanisms in axially compressed metal tubes used as impact energy absorbers". *International Journal of Mechanical Sciences* 35.12 (1993), pp. 1035–1052.

[151] Guillow, SR, Lu, G, and Grzebieta, RH. "Quasi-static axial compression of thin-walled circular aluminium tubes". *International Journal of Mechanical Sciences* 43.9 (2001), pp. 2103–2123.

[152] Sadeghi, MM. "Design of heavy duty energy absorbers". *Structural Impact and Crashworthiness,* 2 (1984), pp. 588–604.

[153] Reid, SR. "Metal tubes as impact energy absorbers". *Metal forming and impact mechanics* (1985), p. 249.

[154] Hull, D. "A unified approach to progressive crushing of fibre-reinforced composite tubes". *Composites science and technology* 40.4 (1991), pp. 377–421.

[155] Hamada, H. and Ramakrishna, S. "A FEM method for prediction of energy absorption capability of crashworthy polymer composite materials". *Journal of Reinforced Plastics and Composites* 16.3 (1997), pp. 226–242.

[156] Andrews, KRF, England, GL, and Ghani, E. "Classification of the axial collapse of cylindrical tubes under quasi-static loading". *International Journal of Mechanical Sciences* 25.9-10 (1983), pp. 687–696.

[157] Wang, B and Lu, G. "Mushrooming of circular tubes under dynamic axial loading". *Thin-walled structures* 40.2 (2002), pp. 167–182.

[158] Tang, Zhiliang, Liu, Shutian, and Zhang, Zonghua. "Analysis of energy absorption characteristics of cylindrical multi-cell columns". *Thin-Walled Structures* 62 (2013), pp. 75–84.

[159] Zhang, Xiong and Huh, Hoon. "Crushing analysis of polygonal columns and angle elements". *International Journal of Impact Engineering* 37.4 (2010), pp. 441–451.

[160] Yamashita, Minoru, Gotoh, Manabu, and Sawairi, Yasuhiko. "Axial crush of hollow cylindrical structures with various polygonal cross-sections: Numerical simulation and experiment". *Journal of Materials Processing Technology* 140.1 (2003), pp. 59–64.

[161] Reddy, Sekhar, Abbasi, Milad, and Fard, Mohammad. "Multi-cornered thin-walled sheet metal members for enhanced crashworthiness and occupant protection". *Thin-Walled Structures* 94 (2015), pp. 56–66.

[162] Fan, Z, Lu, G, and Liu, K. "Quasi-static axial compression of thin-walled tubes with different cross-sectional shapes". *Engineering Structures* 55 (2013), pp. 80–89.

[163] Postlethwaite, HE and Mills, B. "Use of collapsible structural elements as impact isolators, with special references to automotive applications". *Journal of strain analysis* 5.1 (1970), pp. 58–73.

[164] Grzebieta, RH and Murray, NW. "The static behaviour of struts with initial kinks at their centre point". *International Journal of Impact Engineering* 3.3 (1985), pp. 155–165.

[165] Kumakura, Ikuo, Minegishi, Masakatsu, Iwasaki, Kazuo, Shoji, Hirokazu, Yoshimoto, Norio, Terada, Hiroyuki, Sashikuma, Hirofumi, Isoe, Akira, Yamaoka, Toshihiro, Katayama, Noriaki, et al. *Vertical drop test of a transport fuselage section*. Tech. rep. SAE Technical Paper, 2002.

[166] Heimbs, S, Strobl, F, Middendorf, P, and Guimard, JM. "Composite crash absorber for aircraft fuselage applications". *WIT Transactions on the built environment* 113 (2010), pp. 3–14.

[167] Baroutaji, Ahmad, Sajjia, Mustafa, and Olabi, Abdul-Ghani. "On the crashworthiness performance of thin-walled energy absorbers: Recent advances and future developments". *Thin-Walled Structures* 118 (2017), pp. 137–163.

[168] Mamalis, AG and Johnson, W. "The quasi-static crumpling of thin-walled circular cylinders and frusta under axial compression". *International Journal of Mechanical Sciences* 25.9-10 (1983), pp. 713–732.

[169] Guler, Mehmet A, Cerit, Muhammed E, Bayram, Bertan, Gerceker, Bora, and Karakaya, Emrah. "The effect of geometrical parameters on the energy absorption characteristics of thin-walled structures under axial impact loading". *International Journal of Crashworthiness* 15.4 (2010), pp. 377–390.

[170] Mamalis, AG, Johnson, W, and Viegelahn, GL. "The crumpling of steel thin-walled tubes and frusta under axial compression at elevated strain-rates: some experimental results". *International Journal of Mechanical Sciences* 26.11 (1984), pp. 537–547.

[171] Zhang, Xiong and Zhang, Hui. "Energy absorption of multi-cell stub columns under axial compression". *Thin-Walled Structures* 68 (2013), pp. 156–163.

[172] Zhang, Xiong, Wen, Zhuzhu, and Zhang, Hui. "Axial crushing and optimal design of square tubes with graded thickness". *Thin-Walled Structures* 84 (2014), pp. 263–274.

[173] Salehghaffari, S, Tajdari, M, Panahi, M, and Mokhtarnezhad, F. "Attempts to improve energy absorption characteristics of circular metal tubes subjected to axial loading". *Thin-Walled Structures* 48.6 (2010), pp. 379–390.

[174] Singace, Abduljalil Abdulla and El-Sobky, Hobab. "Behaviour of axially crushed corrugated tubes". *International Journal of Mechanical Sciences* 39.3 (1997), pp. 249263267–261265268.

[175] Eyvazian, Arameh, Habibi, Meisam K, Hamouda, Abdel Magid, and Hedayati, Reza. "Axial crushing behavior and energy absorption efficiency of corrugated tubes". *Materials & Design (1980-2015)* 54 (2014), pp. 1028–1038.

[176] Menouer, A, Baleh, R, Djebbar, A, and Abdul-Latif, A. "New generation of energy dissipating systems based on biaxial buckling". *Thin-Walled Structures* 85 (2014), pp. 456–465.

[177] Daimler. *The new smart fortwo 2014: smart fortwo bodyshell*. `https://goo.gl/4Fb2SD`.

[178] Jones, Norman. *Structural impact*. Cambridge university press, 2011.

[179] Reid, S. R., Reddy, T. Y., and Gray, M. D. "Static and dynamic axial crushing of foam-filled sheet metal tubes". *International Journal of Mechanical Sciences* 28.5 (1986), pp. 295–322.

[180] Calladine, Chris R. *Theory of shell structures*. Cambridge University Press, 1989.

[181] Ohokubo, Y, Akamatsu, T, and Shirasawa, K. "Mean crushing strength of closed-hat section members SAE paper 740040". *Automotive Engineering Comgress, Detroit* (1974).

[182] Aya, N and Takahashi, K. "Energy Absorbing Characteristics of Body Structures (Part 1)". *Transactions of Society of Automotive Engineers of Japan* 7 (1974), pp. 60–66.

[183] Magee, CL and Thornton, PH. *Design considerations in energy absorption by structural collapse*. Tech. rep. SAE Technical Paper, 1978.

[184] Macaulay, MA and Redwood, RG. "Small scale model railway coaches under impact". *The Engineer* 218 (1964), pp. 1041–1046.

[185] Dewalt, WJ and Herbein, WC. "Energy Absorption by Compression of Aluminum Tubes". *Alcoa Research Laboratories Engineering Design Division, Report* 12-72 (1972), p. 23.

[186] Abramowicz, W. and Jones, N. "Dynamic axial crushing of square tubes". *International Journal of Impact Engineering* 2.2 (1984), pp. 179–208.

[187] Cowper, G Rr and Symonds, Paul Southworth. *Strain-hardening and strain-rate effects in the impact loading of cantilever beams*. Tech. rep. Brown Univ Providence Ri, 1957.

[188] Karagiozova, D and Alves, Marcılio. "Transition from progressive buckling to global bending of circular shells under axial impact—-Part I: Experimental and numerical observations". *International Journal of Solids and Structures* 41.5 (2004), pp. 1565–1580.

[189] Mamalis, AG, Robinson, M, Manolakos, DE, Demosthenous, GA, Ioannidis, MB, and Carruthers, J. "Crashworthy capability of composite material structures". *Composite structures* 37.2 (1997), pp. 109–134.

[190] Bambach, MR, Jama, HH, and Elchalakani, M. "Axial capacity and design of thin-walled steel SHS strengthened with CFRP". *Thin-Walled Structures* 47.10 (2009), pp. 1112–1121.

[191] Gameiro, Celina Pires, Cirne, Jose, Miranda, Victor, Pinho-da-Cruz, Joaquim, and Teixeira-Dias, Filipe. "Dynamic behaviour of cork and cork-filled aluminium tubes: Numerical simulation and innovative applications". *Holzforschung* 61.4 (2007), pp. 400–405.

[192] Coelho, RM, Sousa, RJ Alves de, Fernandes, FAO, and Teixeira-Dias, FMVH. "New composite liners for energy absorption purposes". *Materials & Design* 43 (2013), pp. 384–392.

[193] Paulino, M., Teixeira-Dias, F., Gameiro, C.P., and Cirne, J. "Hyperelastic and dynamical behaviour of cork and its performance in energy absorption devices and crashworthiness applications". *International Journal of Materials Engineering Innovation* 1.2 (2009), pp. 197–234.

[194] Reddy, TY and Al-Hassani, STS. "Axial crushing of wood-filled square metal tubes". *International journal of mechanical sciences* 35.3-4 (1993), pp. 231–246.

[195] Saito, H. and Kimpara, I. "Evaluation of impact damage mechanism of multi-axial stitched CFRP laminate". *Composites Part A: Applied Science and Manufacturing* 37.12 (2006), pp. 2226–2235.

[196] Sun, G., Li, G., Stone, M., and Li, Q. "A two-stage multi-fidelity optimization procedure for honeycomb-type cellular materials". *Computational Materials Science* 49.3 (2010), pp. 500–511.

[197] Hanssen, A.G., Langseth, M., and Hopperstad, O.S. "Static and dynamic crushing of square aluminum extrusions with aluminum foam filler". *International Journal of Impact Engineering* 24.4 (2000), pp. 347–383.

[198] Bi, J., Fang, H., Wang, Q., and Ren, X. "Modeling and optimization of foam-filled thin-walled columns for crashworthiness designs". *Finite Elements in Analysis and Design* 46.9 (2010), pp. 698–709.

[199] Alavi Nia, A. and Sadeghi, M.Z. "The effects of foam filling on compressive response of hexagonal cell aluminum honeycombs under axial loading-experimental study". *Materials and Design* 31.3 (2010), pp. 1216–1230.

[200] Santosa, S and Wierzbicki, Tomasz. "Crash behavior of box columns filled with aluminum honeycomb or foam". *Computers & Structures* 68.4 (1998), pp. 343–367.

[201] Langseth, M., Hopperstad, O.S., and Hanssen, A.G. "Crash behaviour of thin-walled aluminium members". *Thin-Walled Structures* 32.1-3 (1998), pp. 127–150.

[202] Hanssen, AG, Langseth, M, and Hopperstad, OS. "Optimum design for energy absorption of square aluminium columns with aluminium foam filler". *International Journal of Mechanical Sciences* 43.1 (2001), pp. 153–176.

[203] Song, H.-W., Wan, Z.-M., Xie, Z.-M., and Du, X.-W. "Axial impact behavior and energy absorption efficiency of composite wrapped metal tubes". *International Journal of Impact Engineering* 24.4 (2000), pp. 385–401.

[204] Toksoy, Ahmet Kaan and Güden, Mustafa. "The strengthening effect of polystyrene foam filling in aluminum thin-walled cylindrical tubes". *Thin-walled structures* 43.2 (2005), pp. 333–350.

[205] Seitzberger, Markus, Rammerstorfer, Franz G, Gradinger, R, Degischer, HP, Blaimschein, M, and Walch, Ch. "Experimental studies on the quasi-static axial crushing of steel columns filled with aluminium foam". *International Journal of Solids and Structures* 37.30 (2000), pp. 4125–4147.

[206] Reid, S. R. and Reddy, T. Y. "Axial crushing of foam-filled tapered sheet metal tubes". *International Journal of Mechanical Sciences* 28.10 (1986), pp. 643–656.

[207] Hanssen, A.G., Langseth, M., and Hopperstad, O.S. "Static and dynamic crushing of circular aluminium extrusions with aluminium foam filler". *International Journal of Mechanical Sciences* 24.4 (2000), pp. 475–570.

[208] Santosa, S.P., Wierzbicki, T., Hanssen, A.G., and Langseth, M. "Experimental and numerical studies of foam-filled sections". *International Journal of Impact Engineering* 24.5 (2000), pp. 509–534.

[209] Zarei, HR and Kröger, Matthias. "Optimization of the foam-filled aluminum tubes for crush box application". *Thin-Walled Structures* 46.2 (2008), pp. 214–221.

[210] Markaki, AE and Clyne, TW. "The effect of cell wall microstructure on the deformation and fracture of aluminium-based foams". *Acta Materialia* 49.9 (2001), pp. 1677–1686.

[211] Gibson, Lorna J and Ashby, Michael F. *Cellular solids: structure and properties*. Cambridge university press, 1999.

[212] Brezny, Rasto and Green, David J. "The effect of cell size on the mechanical behavior of cellular materials". *Acta metallurgica et materialia* 38.12 (1990), pp. 2517–2526.

[213] Chen, C, Lu, TJ, and Fleck, NA. "Effect of imperfections on the yielding of two-dimensional foams". *Journal of the Mechanics and Physics of Solids* 47.11 (1999), pp. 2235–2272.

[214] Bouix, Rémy, Viot, Philippe, and Lataillade, Jean-Luc. "Polypropylene foam behaviour under dynamic loadings: Strain rate, density and microstructure effects". *International journal of impact engineering* 36.2 (2009), pp. 329–342.

[215] Yi, Feng, Zhu, Zhengang, Zu, Fangqiou, Hu, Shisheng, and Yi, Pan. "Strain rate effects on the compressive property and the energy-absorbing capacity of aluminum alloy foams". *Materials Characterization* 47.5 (2001), pp. 417–422.

[216] Tagarielli, VL, Deshpande, VS, and Fleck, NA. "The high strain rate response of PVC foams and end-grain balsa wood". *Composites Part B: Engineering* 39.1 (2008), pp. 83–91.

[217] Tan, PJ, Reid, SR, Harrigan, JJ, Zou, Z, and Li, S. "Dynamic compressive strength properties of aluminium foams. Part I—experimental data and observations". *Journal of the Mechanics and Physics of Solids* 53.10 (2005), pp. 2174–2205.

[218] Xu, Shanqing, Ruan, Dong, and Lu, Guoxing. "Strength enhancement of aluminium foams and honeycombs by entrapped air under dynamic loadings". *International Journal of Impact Engineering* 74 (2014), pp. 120–125.

[219] Tan, PJ, Reid, SR, Harrigan, JJ, Zou, Z, and Li, S. "Dynamic compressive strength properties of aluminium foams. Part II—'shock'theory and comparison with experimental data and numerical models". *Journal of the Mechanics and Physics of Solids* 53.10 (2005), pp. 2206–2230.

[220] Onsalung, Nirut, Thinvongpituk, Chawalit, and Painthong, Kulachate. "The influence of foam density on specific energy absorption of rectangular steel tubes". *Energy Research Journal* 1.2 (2010), pp. 135–140.

[221] Thornton, PH, Mahmood, HF, and Magee, CL. "Energy absorption by structural collapse". In: *Structural crashworthiness*. 1983. Chap. 4, pp. 96–117.

[222] Sun, Guangyong, Li, Guangyao, Hou, Shujuan, Zhou, Shiwei, Li, Wei, and Li, Qing. "Crashworthiness design for functionally graded foam-filled thin-walled structures". *Materials Science and Engineering: A* 527.7 (2010), pp. 1911–1919.

[223] Gupta, Nikhil and Ricci, William. "Comparison of compressive properties of layered syntactic foams having gradient in microballoon volume fraction and wall thickness". *Materials Science and Engineering: A* 427.1 (2006), pp. 331–342.

[224] Mohsenizadeh, S, Alipour, R, Rad, M Shokri, Nejad, A Farokhi, and Ahmad, Z. "Crashworthiness assessment of auxetic foam-filled tube under quasi-static axial loading". *Materials & Design* 88 (2015), pp. 258–268.

[225] Carruthers, Joe J, Kettle, AP, and Robinson, AM. "Energy absorption capability and crashworthiness of composite material structures: a review". *Applied Mechanics Reviews* 51.10 (1998), pp. 635–649.

[226] Jacob, G.C., Fellers, J.F., Starbuck, J.M., and Simunovic, S. "Crashworthiness of automotive composite material systems". *Journal of Applied Polymer Science* 92.5 (2004), pp. 3218–3225.

[227] Soutis, C. “Fibre reinforced composites in aircraft construction”. *Progress in Aerospace Sciences* 41.2 (2005), pp. 143–151.

[228] Hellard, Guy. “Composites in airbus a long story of innovations and experiences”. In: *Composites in Airbus at Global Investor Forum*. 2008.

[229] Johnson, A.F. and David, M. “Failure mechanisms and energy absorption in composite elements under axial crush”. *Key Engineering Materials* 488-489 (2012), pp. 638–641.

[230] Israr, H.A., Rivallant, S., and Barrau, J.J. “Experimental investigation on mean crushing stress characterization of carbon-epoxy plies under compressive crushing mode”. *Composite Structures* 96 (2013), pp. 357–364.

[231] Jia, X., Chen, G., Yu, Y., Li, G., Zhu, J., Luo, X., Duan, C., Yang, X., and Hui, D. “Effect of geometric factor, winding angle and pre-crack angle on quasi-static crushing behavior of filament wound CFRP cylinder”. *Composites Part B: Engineering* 45.1 (2013), pp. 1336–1343.

[232] Costas, M., Díaz, J., Romera, L.E., Hernández, S., and Tielas, A. “Static and dynamic axial crushing analysis of car frontal impact hybrid absorbers”. *International Journal of Impact Engineering* 62 (2013), pp. 166–181.

[233] Huang, J. and Wang, X. “Numerical and experimental investigations on the axial crushing response of composite tubes”. *Composite Structures* 91.2 (2009), pp. 222–228.

[234] Ramakrishna, S. and Hamada, Hiroyuki. “Energy Absorption Characteristics of Crash Worthy Structural Composite Materials”. *Key Engineering Materials* 141-143 (1998).

[235] Farley, Gary L and Jones, Robert M. “Crushing characteristics of continuous fiber-reinforced composite tubes”. *Journal of composite Materials* 26.1 (1992), pp. 37–50.

[236] Wierzbicki, Tomasz et al. “Axial resistance and energy absorption of externally reinforced metal tubes”. *Composites Part B: Engineering* 27.5 (1996), pp. 387–394.

[237] Heimbs, Sebastian. "Energy absorption in aircraft structures". *International Workshop on Hydraulic Equipment and Support Systems for Mining* (2012).

[238] Rock West Composites. *Nomex ® panel*. `https://goo.gl/LQZbyd`.

[239] Hou, S., Li, Q., Long, S., Yang, X., and Li, W. "Design optimization of regular hexagonal thin-walled columns with crashworthiness criteria". *Finite Elements in Analysis and Design* 43.6-7 (2007), pp. 555–565.

[240] Aktay, L., Johnson, A.F., and Kröplin, B.-H. "Numerical modelling of honeycomb core crush behaviour". *Engineering Fracture Mechanics* 75.9 (2008), pp. 2616–2630.

[241] Yin, H., Wen, G., Hou, S., and Chen, K. "Crushing analysis and multiobjective crashworthiness optimization of honeycomb-filled single and bitubular polygonal tubes". *Materials and Design* 32.8-9 (2011), pp. 4449–4460.

[242] Schultz, J., Griese, D., Ju, J., Shankar, P., Summers, J.D., and Thompson, L. "Design of honeycomb mesostructures for crushing energy absorption". *Journal of Mechanical Design, Transactions of the ASME* 134.7 (2012).

[243] Heimbs, S, Middendorf, P, Maier, M, et al. "Honeycomb sandwich material modeling for dynamic simulations of aircraft interior components". In: *Proceedings of the 9th international LS-DYNA users conference. Dearborn (MI)*. 2006.

[244] Heimbs, S, Strobl, F, Middendorf, P, Gardner, S, Eddington, B, and Key, J. "Crash Simulation of an F1 Racing Car Front Impact Structure" (2009).

[245] Olympio, Kingnidé R and Gandhi, Farhan. "Flexible skins for morphing aircraft using cellular honeycomb cores". *Journal of intelligent material systems and structures* 21.17 (2010), pp. 1719–1735.

[246] Miller, W, Smith, C W, and Evans, K E. "Honeycomb cores with enhanced buckling strength". *Composite Structures* 93.3 (2011), pp. 1072–1077.

[247] Xue, Zhenyu and Hutchinson, John W. "Crush dynamics of square honeycomb sandwich cores". *International Journal for Numerical Methods in Engineering* 65.13 (2006), pp. 2221–2245.

[248] Belytschko, Ted, Liu, Wing Kam, Moran, Brian, and Elkhodary, Khalil. *Nonlinear finite elements for continua and structures*. John wiley & sons, 2013.

[249] Barbeiro, S. "Supraconvergence of a finite difference scheme for solutions in Hs(0, L)". *IMA Journal of Numerical Analysis* 25 (4 2005).

[250] Courant, Richard, Friedrichs, Kurt, and Lewy, Hans. "Über die partiellen Differenzengleichungen der mathematischen Physik". *Mathematische annalen* 100.1 (1928), pp. 32–74.

[251] Silberschmidt, Vadim V. *Dynamic deformation, damage and fracture in composite materials and structures*. Woodhead Publishing, 2016.

[252] Belytschko, T. "An overview of semidiscretization and time integration procedures". *Computational Methods for Transient Analysis* 1 (1983).

[253] *ABAQUS 6.16 Documentation*. Dassault Systèmes. 2016.

[254] Belytschko, Ted, Smolinski, Patrick, and Liu, Wing Kam. "Stability of multi-time step partitioned integrators for first-order finite element systems". *Computer Methods in Applied Mechanics and Engineering* 49.3 (1985), pp. 281–297.

[255] Daniel, William John Trevor. "A study of the stability of subcycling algorithms in structural dynamics". *Computer methods in applied mechanics and engineering* 156.1-4 (1998), pp. 1–13.

[256] Daniel, WJT. "Analysis and implementation of a new constant acceleration subcycling algorithm". *International Journal for Numerical Methods in Engineering* 40.15 (1997), pp. 2841–2855.

[257] Smolinski, P, Sleith, S, and Belytschko, T. "Stability of an explicit multi-time step integration algorithm for linear structural dynamics equations". *Computational Mechanics* 18.3 (1996), pp. 236–244.

[258] Yang, RJ, Tseng, L, Nagy, L, and Cheng, J. "Feasibility study of crash optimization". In: *ASME*. Vol. 69. 2. 1994, pp. 549–556.

[259] Fang, Jianguang, Sun, Guangyong, Qiu, Na, Kim, Nam H, and Li, Qing. "On design optimization for structural crashworthiness and its state of the art". *Structural and Multidisciplinary Optimization* 55.3 (2017), pp. 1091–1119.

[260] Liu, Yucheng. "Thin-walled curved hexagonal beams in crashes–FEA and design". *International Journal of Crashworthiness* 15.2 (2010), pp. 151–159.

[261] Ghamarian, Ali and Zarei, Hamidreza. "Crashworthiness investigation of conical and cylindrical end-capped tubes under quasi-static crash loading". *International journal of crashworthiness* 17.1 (2012), pp. 19–28.

[262] Zhang, Yong, Sun, Guangyong, Xu, Xipeng, Li, Guangyao, and Li, Qing. "Multiobjective crashworthiness optimization of hollow and conical tubes for multiple load cases". *Thin-Walled Structures* 82 (2014), pp. 331–342.

[263] Toksoy, Ahmet Kaan and Güden, Mustafa. "The optimisation of the energy absorption of partially Al foam-filled commercial 1050H14 and 6061T4 Al crash boxes". *International journal of crashworthiness* 16.1 (2011), pp. 97–109.

[18] Costas, M, Morin, D, Langseth, M, Romera, L, and Díaz, J. "Axial crushing of aluminum extrusions filled with PET foam and GFRP. An experimental investigation". *Thin-Walled Structures* 99 (2016), pp. 45–57.

[264] Mohammadiha, O and Beheshti, H. "Optimization of functionally graded foam-filled conical tubes under axial impact loading". *Journal of Mechanical Science and Technology* 28.5 (2014), pp. 1741–1752.

[265] Fang, Jianguang, Gao, Yunkai, An, Xiuzhe, Sun, Guangyong, Chen, Junning, and Li, Qing. "Design of transversely-graded foam and wall thickness structures for crashworthiness criteria". *Composites Part B: Engineering* 92 (2016), pp. 338–349.

[266] Hou, Shujuan, Zhang, Zhidan, Yang, Xujing, Yin, Hanfeng, and Li, Qing. "Crashworthiness optimization of new thin-walled cellular configurations". *Engineering Computations* 31.5 (2014), pp. 879–897.

[267] Esfahlani, SS, Shirvani, H, Shirvani, A, Nwaubani, S, Mebrahtu, H, and Chirwa, C. "Hexagonal honeycomb cell optimisation by way of metamodel techniques". *International Journal of Crashworthiness* 18.3 (2013), pp. 264–275.

[268] Tran, TrongNhan, Hou, Shujuan, Han, Xu, Tan, Wei, and Nguyen, Nhat-Tan. "Theoretical prediction and crashworthiness optimization of multi-cell triangular tubes". *Thin-Walled Structures* 82 (2014), pp. 183–195.

[269] Bisagni, Chiara, Lanzi, Luca, and Ricci, Sergio. "Optimization of helicopter subfloor components under crashworthiness requirements using neural networks". *Journal of Aircraft* 39.2 (2002), pp. 296–304.

[270] Astori, Paolo and Impari, Francesco. "Crash response optimisation of helicopter seat and subfloor". *International Journal of Crashworthiness* 18.6 (2013), pp. 570–578.

[271] Hernandez, S. "Métodos de diseño óptimo de estructuras". *Colegio de ICCP, Coleccion Seinor* 8 (1990).

[272] Zabaras, Nicholas, Ganapathysubramanian, Shankar, and Li, Qing. "A continuum sensitivity method for the design of multi-stage metal forming processes". *International Journal of Mechanical Sciences* 45.2 (2003), pp. 325–358.

[273] Forrester, Alexander, Keane, Andy, et al. *Engineering design via surrogate modelling: a practical guide*. John Wiley & Sons, 2008.

[274] Wang, G Gary and Shan, Songqing. "Review of metamodeling techniques in support of engineering design optimization". *Journal of Mechanical design* 129.4 (2007), pp. 370–380.

[275] Glover, Fred. "Future paths for integer programming and links to artificial intelligence". *Computers & operations research* 13.5 (1986), pp. 533–549.

[276] Glover, Fred. "Tabu search—part I". *ORSA Journal on computing* 1.3 (1989), pp. 190–206.

[277] Blum, Christian and Roli, Andrea. "Metaheuristics in combinatorial optimization: Overview and conceptual comparison". *ACM Computing Surveys (CSUR)* 35.3 (2003), pp. 268–308.

[278] Kirkpatrick, Scott, Gelatt, C Daniel, Vecchi, Mario P, et al. "Optimization by simulated annealing". *science* 220.4598 (1983), pp. 671–680.

[279] Holland, John H. *Adaptation in Natural and Artificial Systems: An Introductory Analysis with Applications to Biology, Control, and Artificial Intelligence*. MIT press, 1992.

[280] Storn, Rainer and Price, Kenneth. "Differential evolution–a simple and efficient heuristic for global optimization over continuous spaces". *Journal of global optimization* 11.4 (1997), pp. 341–359.

[281] Dorigo, Marco, Birattari, Mauro, and Stutzle, Thomas. "Ant colony optimization". *IEEE computational intelligence magazine* 1.4 (2006), pp. 28–39.

[282] Kennedy, James. "Particle swarm optimization". In: *Encyclopedia of machine learning*. 2011, pp. 760–766.

[283] Glover, Fred and Laguna, Manuel. "Tabu Search". In: *Handbook of Combinatorial Optimization*. 2013, pp. 3261–3362.

[284] Geem, Zong Woo, Kim, Joong Hoon, and Loganathan, Gobichettipalayam Vasudevan. "A new heuristic optimization algorithm: harmony search". *simulation* 76.2 (2001), pp. 60–68.

[285] Yang, Xin-She. *Nature-inspired metaheuristic algorithms*. Luniver press, 2010.

[286] Yang, Xin-She and Deb, Suash. "Cuckoo search via Lévy flights". In: *Nature & Biologically Inspired Computing, 2009. NaBIC 2009. World Congress on*. IEEE. 2009, pp. 210–214.

[287] McKay, M., Beckman, R., and Conover, W. "A comparison of three methods for selecting values of input variables in the analysis of output from a computer code". *Technometrics* 21.2 (1979), pp. 239–245.

[288] Matheron, Georges. "Principles of geostatistics". *Economic geology* 58.8 (1963), pp. 1246–1266.

[289] Krige, D. G. "A statistical approach to some basic mine valuation problems on the Witwatersrand". *Journal of the Chemical, Metallurgical and Mining Engineering Society of South Africa* 52(6) (1951), pp. 119–139.

[290] Friedman, J. H. "Multivariate adaptive regression splines". *Annals of Statistics* 19 (1991), pp. 1–141.

[291] Friedman, J.H. and Roosen, C.B. "An introduction to multivariate adaptive regression splines." *Statistical methods in medical research* 4.3 (1995), pp. 197–217.

[292] Nealen, A. "A short-as-possible introduction to the least squares, weighted least squares, and moving least squares methods for scattered data approximation and interpolation." *Technical report, Discrete Geometric Modeling Group, Technishe Universität, Berlin, Germany* (2004).

[293] Lancaster, P. and Salkauskas, K. "Surfaces generated by moving least squares methods". *Mathematics of Computation* 37.155 (1981), pp. 141–158.

[294] Holland, John H. *Adaptation in Natural and Artificial Systems: An Introductory Analysis with Applications to Biology, Control, and Artificial Intelligence*. MIT press, 1992.

[295] Mitchell, Melanie. *An introduction to genetic algorithms*. MIT press, 1998.

[296] Wahde, Mattias. *Biologically Inspired Optimization Methods: An Introduction*. WIT Press, 2008.

[19] Adams, B., Bauman, L., Bohnhoff, W., Dalbey, K., Ebeida, M., Eddy, J., Eldred, M., Hough, P., Hu, K., Jakeman, J., Swiler, L., and Vigil, D. *DAKOTA, A Multilevel Parallel Object-Oriented Framework for Design Optimization, Parameter Estimation, Uncertainty Quantification, and Sensitivity Analysis: Version 6.1.0 User's Manual*. Sandia National Laboratories. 2014.

[297] Eddy, J. E. and Lewis, K. "Effective Generation of Pareto Sets using Genetic Programming". *Proceedings of ASME Design Engineering Technical Conference* (2001).

[20] Cook, G. R. and Johson, W. H. "A constitutive model and data for metals subjected to large strains, high strain rates and high temperatures". *Proceedings of Seventh International Symposium on Ballistics* (1983).

[304] Costas, M., Díaz, J., Romera, L., and Hernández, S. "A multi-objective surrogate-based optimization of the crashworthiness of a hybrid impact absorber". *International Journal of Mechanical Sciences* 88 (2014), pp. 46–54.

[21] BASF. *Ultramid (R) A3WG10 BK00564 Polyamide 66. Product information sheet*. 2012.

[22] *SAE Standard J211: Instrumentation for Impact Test*. Tech. rep. Safety Test Instrumentation Stds Comm, 1995.

[305] *ABAQUS 6.13 Documentation*. Dassault Systèmes. 2013.

[306] Adams, B., Bauman, L., Bohnhoff, W., Dalbey, K., Ebeida, M., Eddy, J., Eldred, M., Hough, P., Hu, K., Jakeman, J., Swiler, L., and Vigil, D. *DAKOTA, A Multilevel Parallel Object-Oriented Framework for Design Optimization, Parameter Estimation, Uncertainty Quantification, and Sensitivity Analysis: Version 5.4 Reference Manual*. Sandia National Laboratories. 2013.

[23] *Airbus A300 Fuselage Section*. `https://goo.gl/aqcMBf`.

[24] Børvik, T., Hopperstad, O.S., Berstad, T.., and Langseth, M. "A computational model of viscoplasticity and ductile damage for impact and penetration". *European Journal of Mechanics, A/Solids* 20.5 (2001), pp. 685–712.

[25] Børvik, T., Hopperstad, O.S., and Pedersen, K.O. "Quasi-brittle fracture during structural impact of AA7075-T651 aluminium plates". *International Journal of Impact Engineering* 37.5 (2010), pp. 537–551.

[26] Deshpande, V.S. and Fleck, N.A. "Isotropic constitutive models for metallic foams". *Journal of the Mechanics and Physics of Solids* 48.6 (2000), pp. 1253–1283.

[27] Zou, Tianchun, Mou, Haolei, and Feng, Zhenyu. "Research on Effects of Oblique Struts on Crashworthiness of Composite Fuselage Sections". *Journal of Aircraft* 49.6 (2012), pp. 2059–2063.

[28] Heimbs, S., Strobl, F., and Middendorf, P. "Integration of a composite crash absorber in aircraft fuselage vertical struts". *International Journal of Vehicle Structures and Systems* (2011).

[29] Fasanella, E. L., Jackson, K. E., Sparks, C. E., and Sareen, A. K. "Water Impact Test and Simulation of a Composite Energy Absorbing Fuselage Section" (2011), pp. 1–15.

[30] Adams, A and Lankarani, HM. "A modern aerospace modeling approach for evaluation of aircraft fuselage crashworthiness". *International journal of crashworthiness* 8.4 (2003), pp. 401–413.

[31] Adams, A, Thorbole, C K, and Lankarani, H M. "Scale modelling of aircraft fuselage: an innovative approach to evaluate and improve crashworthiness". *International Journal of Crashworthiness* 15.1 (2010), pp. 71–82.

[32] Jackson, Karen E, Fasanella, Edwin L, and Kellas, Sotiris. "Development of a Scale Model Composite Fuselage Concept for Improved Crashworthiness". *Journal of Aircraft* 38.1 (2001), pp. 95–103.

[33] *ABAQUS 6.14 Documentation*. Dassault Systèmes. 2014.

[298] De Florio, F. *Airworthiness: An Introduction to Aircraft Certification*. Oxford, 2006.

[299] Abromowitz, Allan, Smith, Timothy G, and Vu, Tong. "Vertical drop test of a narrow-body transport fuselage section with a conformable auxiliary fuel tank onboard". *2000.* (2000).

[300] Airplanes, Boeing Commercial. *737 Airplane Characteristics for Airport Planning. D6-58325-6*. 2013.

[301] Kay, Gregory. *Failure modeling of titanium 6AI-4V and aluminum 2024-T3 with the Johnson-Cook material model*. Office of Aviation Research, Federal Aviation Administration, 2003.

[302] Brar, NS, Joshi, VS, and Harris, BW. "Constitutive Model Constants for Al7075-t651 and Al7075-t6". In: *Shock Compression of Condensed Matter 2009: Proceedings of the American Physical Society Topical Group on Shock Compression of Condensed Matter*. Vol. 1195. 1. AIP Publishing. 2009, pp. 945–948.

[303] Jeong, David Y, Roach, Dennis P, Canha, Joseph V, Brewer, John C, and Flournoy, Thomas H. *Strain Fields in Boeing 737 Fuselage Lap Splices. Field and Laboratory Measurements with Analytical Correlations.* Tech. rep. DTIC Document, 1995.